

# **WELDABILITY OF BORATED STAINLESS STEEL-(SS 304B4)**

*By*

**M.Divya**

Enrollment No: ENGG02201304006

**Indira Gandhi Centre for Atomic Research, Kalpakkam-603102,  
India**

*A thesis submitted to the  
Board of Studies in Engineering Sciences*

*In partial fulfillment of requirements  
for the Degree of*

**DOCTOR OF PHILOSOPHY**

*of*

**HOMI BHABHA NATIONAL INSTITUTE**



**July, 2019**

# Homi Bhabha National Institute<sup>1</sup>

## Recommendations of the Viva Voce Committee

As members of the Viva Voce Committee, we certify that we have read the dissertation prepared by **M. Divya** entitled “**Weldability of Borated Stainless Steel-SS 304B4**” and recommend that it may be accepted as fulfilling the thesis requirement for the award of Degree of Doctor of Philosophy.

---

Chairman - Name & Signature with date **Dr.Velusamy. K** 

---

Guide / Convener - Name & Signature with date **Dr. Shaju K Albert** 

---

Examiner - Name & Signature with date **Prof. Murugaiyan**  
**Amirthalingam** 

---

Member 1- Name & Signature with date **Dr. R.Mythili** 

---

Member 2- Name & Signature with date **Dr.Vani Shankar** 

---

Member 3- Name & Signature with date **Prof.G.D.Janaki Ram** 

---

Final approval and acceptance of this thesis is contingent upon the candidate's submission of the final copies of the thesis to HBNI.

I/We hereby certify that I/we have read this thesis prepared under my/our direction and recommend that it may be accepted as fulfilling the thesis requirement.

**Date:** 09/07/2020

**Place:** Kalpakkam

  
**Signature**

**Guide**

<sup>1</sup> This page is to be included only for final submission after successful completion of viva voce.

## STATEMENT BY AUTHOR

This dissertation has been submitted in partial fulfillment of requirements for an advanced degree at Homi Bhabha National Institute (HBNI) and is deposited in the Library to be made available to borrowers under rules of the HBNI.

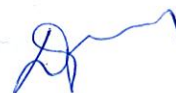
Brief quotations from this dissertation are allowable without special permission, provided that accurate acknowledgement of source is made. Requests for permission for extended quotation from or reproduction of this manuscript in whole or in part may be granted by the Competent Authority of HBNI when in his or her judgment the proposed use of the material is in the interests of scholarship. In all other instances, however, permission must be obtained from the author.



( M.Divya)

## DECLARATION

I, hereby declare that the investigation presented in the thesis has been carried out by me. The work is original and has not been submitted earlier as a whole or in part for a degree / diploma at this or any other Institution / University.



(M.Divya)

## List of Publications arising from the thesis

### Journal

1. "Liquation cracking susceptibility of partially melted zone in 304B4 SS multipass weldments", **Divya. M**, Shaju K Albert and Rajinikanth. V, *Welding in the World*, **2019**, 63, 1101–1113, DOI :10.1007/s40194-019-00738-9.
2. "Characterization of Eutectic Borides formed during Solidification of Borated Stainless Steel 304B4", **Divya. M**, Albert. S. K and Thomas Paul. V, "Welding in the world", **2019**, online,1-13, DOI :10.1007/s40194-019-00786-1
3. "Weldability Study on SS 304B4 Joined using Boron Containing Austenitic Stainless Steel Consumable", **Divya. M** and Albert. S. K *Journal of Welding and Joining*, **2018**, 36(6), 60-70. DOI: <https://doi.org/10.5781/JWJ.2018.36.6.9>.
4. "Dilution effects on weld metal microstructure and liquation cracking susceptibility of 304B4 SS joined using E309 electrode" **Divya. M**, Albert. S. K, *Journal of Manufacturing Processes*, **2018**, 34, 540–554, DOI:10.1016/j.jmapro.2018.06.034.
5. "Weldability studies on borated stainless steel using Vareststraint and Gleeble tests", Srinivasan. G, **Divya. M**, Das. C. R, Albert. S. K, Bhaduri. A. K, Lauf. S, Stubenrauch. S and Klenk. A, *Welding In the World*, **2015**, 59, 119–126.

### Conferences

1. "Hot cracking susceptibilities of SS 304B4 base metal and weld joint", **Divya. M** and Dr. Shaju K Albert, IIW International congress,**2017**. Chennai.
2. "A Study of Solidification and liquation cracking in AISI 304B4 Stainless Steel base and weld metal", **Divya. M**, Albert. S. K, Das. C. R and Bhaduri. A. K, *National Welding Seminar-2015*,Jamshedpur.



(M.Divya)

## **DEDICATIONS**

*To my beloved parents who introduced me to this world and to Dr. Shaju K. Albert  
who introduced me to the beautiful borated stainless steels.*

## **ACKNOWLEDGEMENTS**

I express my deepest gratitude to Dr.Shaju.K.Albert (AD, MEG), for motivating, mentoring and guiding me to accomplish this research work. His constant perusal for scientific excellence and perfection has helped me to shape this thesis. I thank Dr.A.K.Bhaduri, Director, IGCAR for permitting me to take up this work for PhD thesis. I sincerely thank the DC committee Dr.K.Velusamy (Chairman), Dr.Vani Shankar, Dr.R.Mythili and Prof.G.D.Janaki Ram (IIT, Madras) for giving valuable suggestions and encouragements during the DC committee meetings. I am very grateful to Dr. Chittaranjan Das (Head, MJS) for his support and motivation. I am very thankful to Dr.C.Ravishankar (MJS), Dr.S.Raju (Head, PMD) Dr.V.Thomas Paul, (PMD), Mr.K.Rangan (IIT, Madras), Mrs.N.Sreevidya (MJS), Mr.M.Arul (MJS) for their various technical help. I express my sincere gratitude to Dr. J.Christopher (CSS) for his guidance in learning Thermo-Calc software. I would like to extend my sincere gratitude to my friends Mrs.G.Shanthi (MMS), Mrs.J.Vanaja (CSS), Dr.Gopa (MJS), Mr.P.Vasantharaja (AWPMS) and Mr.Yatindra Kumar (MMS) supporting at all difficult times and creating a lively atmosphere. I would like to thank all my other colleagues in the MJS and MDTD for their motivation and encouragements. It is my great privilege to acknowledge (Late) Prof. D.R.G.Achar, IIT Madras who introduced me to the field of Welding science. I am highly indebted to my parents and teachers for motivating me for studies which inculcated great interest in me to pursue research. I would like to acknowledge the sacrifices made by my mother Mrs. M. Lakshmi by taking care of my family in my absence. Last but not the least, my heartfelt thanks to my daughters Parnitha Subhi, Thanuja and husband Mr.R.Amirthalingam for bearing my absence at home and co-operating with me which geared me to finish my thesis.

# CONTENTS

	<b>Page No.</b>
<b>SUMMARY</b> .....	<b>viii</b>
<b>LIST OF FIGURES</b> .....	<b>x</b>
<b>LIST OF TABLES</b> .....	<b>xx</b>
<b>CHAPTER 1 BACKGROUND AND MOTIVATION</b> .....	<b>1</b>
1.1 Introduction.....	<b>1</b>
1.2 Aim and Objective.....	<b>4</b>
1.3 Organization of Thesis.....	<b>6</b>
<b>CHAPTER 2 LITERATURE REVIEW</b> .....	<b>9</b>
2.1 Borated stainless steels and its applications.....	<b>9</b>
2.2 Microstructures of borated stainless steels.....	<b>12</b>
2.3 Evolution of phases on melting and re-solidification of borated stainless steels.....	<b>13</b>
2.4 Microstructure of 304B4 weldment.....	<b>16</b>
2.5 Weldability .....	<b>18</b>
2.5.1 Theory of weld solidification cracking.....	<b>20</b>
2.5.2 Metallurgical factors responsible for weld solidification cracking .....	<b>21</b>
2.5.3 Mechanisms of HAZ liquation cracking.....	<b>28</b>
2.5.4 Factors influencing the liquation cracking susceptibility.....	<b>31</b>
2.6 Methods for evaluation of hot cracking.....	<b>33</b>
2.6.1 The Varestraint Test.....	<b>36</b>
2.6.2 Hot Ductility Test.....	<b>39</b>

2.7	Weldability of Borated Stainless Steel – SS 304B4 ..	43
2.8	Research gaps in weldability study of borated stainless steels.....	46
2.9	Scope of the Thesis.....	48
<b>CHAPTER 3</b>	<b>MATERIALS AND EXPERIMENTAL DETAILS.....</b>	<b>49</b>
3.1	Introduction.....	49
3.2	Materials.....	49
3.3	Procedures for weld pad fabrication.....	50
3.4	Hot cracking test procedures.....	52
	3.4.1 Varestraint test specimens.....	52
	3.4.2 Varestraint test procedure.....	53
	3.4.3 Hot ductility experiments.....	60
3.5	Differential scanning calorimetry experiments.....	64
3.6	Metallography.....	65
3.7	Optical microscopy.....	65
3.8	Scanning electron microscopy (SEM).....	66
3.9	X-ray diffraction studies (XRD).....	66
3.10	Transmission electron microscopy (TEM).....	66
3.11	Electron probe micro analysis (EPMA).....	67
3.12	Mechanical property evaluation.....	67
3.13	Solidification simulations.....	68
3.14	Scheil’s solidification simulation.....	69

<b>CHAPTER 4</b>	<b>HOT CRACKING SUSCEPTIBILITY OF SOLUTION ANNEALED AND FUSED 304B4 SS .....</b>	<b>71</b>
4.1	Introduction.....	71
4.2	Results.....	72
4.2.1	Equilibrium transformations-Thermo-Calc Simulation.....	72
4.2.2	Non-equilibrium transformations.....	73
4.2.3	Phase transformations in 304B4 base metal during thermal cycle.....	77
4.2.4	Phase transformations in fused 304B4 during thermal cycle.....	79
4.2.5	Microstructure of SS 304B4 base metal.....	80
4.2.6	Microstructure of 304B4 fusion zone.....	83
4.2.7	Hot cracking susceptibility.....	87
4.2.7.1	SS 304B4 Base metal.....	87
4.2.7.2	Fused SS 304B4.....	91
4.2.8	Microstructural features of hot cracks in Varestraint tested specimens.....	95
4.2.8.1	Transvarestraint tested specimens of SS 304B4 base metal.....	95
4.2.8.2	Spot Varestraint tested specimens of SS 304B4 base metal.....	96
4.2.8.3	Spot Varestraint tested specimens of fused SS 304B4 .....	97
4.2.9	Microstructures of hot ductility tested specimens.....	98
4.2.9.1	SS 304B4 base metal.....	98
4.2.9.2	Fused SS 304B4 .....	100
4.2.10	Fracture surfaces of hot ductility tested	

specimens.....	101
4.2.10.1 SS 304B4 base metal specimens.....	101
4.2.10.2 Fused SS 304B4 specimens.....	102
4.2.11 Electron Probe Micro Analysis (EPMA) of Hot ductility tested specimens.....	103
4.3 Discussions.....	107
4.3.1 Equilibrium and non equilibrium transformations in SS 304B4 .....	107
4.3.2 Influence of non equilibrium transformation on hot cracking susceptibility.....	110
4.3.3 Effect of back filling in hot cracks formed in SS 304B4 .....	111
4.3.4 Mechanism of liquation cracking in PMZ.....	112
4.4 Summary.....	119
<b>CHAPTER 5 WELD METAL LIQUATION CRACKING IN SS 304B4 WELD JOINT PREPARED USING E309 ELECTRODE.....</b>	<b>121</b>
5.1 Introduction.....	121
5.2 Preparation of spot vareststraint test specimens .....	122
5.3 Results.....	123
5.3.1 Microstructures of different zones of SS 304B4 weld joint prepared using E309 electrode.....	123
5.3.2 Microstructural features of 309 weld metal diluted by base metal.....	124
5.3.3 Dilution of weld metal by the base metal in the weld joint made using E309 electrode.....	125
5.3.4 Ferrite number (FN).....	128
5.3.5. Scheil's solidification simulation.....	129
5.3.6 Effect of base metal dilution in weld metal on	

its liquation cracking susceptibility.....	130
5.3.7 Macroscopic cracking characteristics	131
5.3.8. Microstructures of specimens after spot varestraint test.....	133
5.3.9 Brittleness Temperature Range (BTR).....	135
5.3.10 Qualitative analysis of microchemistry of borides.....	138
5.4 Discussion.....	138
5.4.1 Effect of base metal dilution on weld metal.....	138
5.4.2 Cracking susceptibility.....	139
5.4.3 Effect of delta ferrite on liquation cracking susceptibility.....	142
5.4.4 Effect of sulphur, phosphorus and silicon on liquation cracking susceptibility.....	143
5.5 Summary.....	144
<b>CHAPTER 6 HOT CRACKING SUSCEPTIBILITY OF THE WELD METAL IN SS 304B4 WELD JOINT PREPARED USING BORON ADDED E308 ELECTRODE.....</b>	<b>146</b>
6.1 Introduction.....	146
6.2 Varestraint test specimens .....	147
6.3 Results.....	148
6.3.1 Microstructure of 308BRN weld metal.....	148
6.3.2 Hot cracking susceptibility.....	149
6.3.3 Microstructures of Varestraint tested specimens.....	151
6.3.4 Micro chemical analysis of re-fused zone using electron probe micro analyzer (EPMA).	153
6.3.5 Solidification simulation.....	154

6.4	Discussion.....	154
6.5	Summary.....	159
<b>CHAPTER 7</b>	<b>MECHANICAL PROPERTIES OF SS 304B4 WELD JOINTS PREPARED USING E309 AND E308BRN ELECTRODES.....</b>	<b>161</b>
7.1	Introduction.....	161
7.2	Results.....	162
	7.2.1 Tensile properties.....	162
	7.2.2 Impact properties.....	165
	7.2.3 Microhardness survey across the weldments	166
7.3	Discussion.....	167
7.4	Summary.....	171
<b>CHAPTER 8</b>	<b>MODIFIED WELDING PROCEDURE TO REDUCE HOT CRACKING IN SS 304B4 WELD JOINT PREPARED USING E309 ELECTRODE.....</b>	<b>173</b>
8.1	Introduction.....	173
8.2	Modified welding procedure for joining SS 304B4 using E309 electrode .....	174
8.3	Preparation of spot vareststraint test specimen from the weld joints prepared with buttering .....	176
8.4	Results.....	177
	8.4.1 Microstructure of the weld joint prepared after buttering.....	177
	8.4.2 Quantitative analysis of cracking susceptibility	179
	8.4.3 Microstructures of specimens after spot Vareststraint test.....	181
8.5	Discussion.....	182
8.6	Summary.....	184

<b>CHAPTER 9</b>	<b>CONCLUSIONS, CONTRIBUTIONS AND SCOPE FOR FUTURE RESEARCH.....</b>	<b>186</b>
9.1	Conclusions.....	186
9.2	Contributions.....	189
9.3	Scope of future research.....	190
	<b>REFERENCES.....</b>	<b>191</b>
	<b>LIST OF ABBREVIATIONS &amp; ACRONYMS....</b>	<b>203</b>

## SUMMARY

Borated stainless steels belongs to a class of austenitic stainless steel which contain 0.2 to 2 wt.% of boron in it. These steels are widely used for applications that require absorption of neutrons in nuclear reactors and nuclear waste management facilities. This is because neutron absorption cross section of B<sup>10</sup> isotope present in natural boron is very high. Hence, in the nuclear reactors, to protect the structural materials in and around the core from neutron bombardment, neutron shields made of borated stainless steels are placed around the components. In general neutron shields made from borated stainless steels are fabricated by welding.

Weldability of borated stainless steels is poor due to formation of low melting eutectics of austenite and boride during last stages of solidification. Hence, in the available literature, it is recommended to use borated stainless steels containing 0.5 to 2 wt.% of boron for better weldability. However, the recommendations are based on weldability tests performed on base metals. In practical conditions, during fabrication of neutron shields using SS 304B4 (1.2 wt.% B) for intermediate heat exchangers (IHX) of prototype fast breeder reactor (PFBR), extensive cracking of welds were encountered even though recommended E309 electrode was used. Finally, the neutron shields were fabricated by using special electrodes containing boron. Therefore, this study was taken up to understand the mechanism of cracking in these steels during welding so that a suitable solution to mitigate cracking in the steels can be identified.

In the present work solidification and liquation cracking sensitivity of SS 304B4 and its weld joint prepared using standard E309 electrode is investigated. The solidification and liquation cracking susceptibility in this study were evaluated using transverse and spot Varestraint tests respectively. In addition to this, liquation

cracking susceptibility of SS 304B4 base metal and partially melted SS 304B4 were also confirmed through “Gleeble<sup>TM</sup>” based hot ductility tests. The mechanisms behind hot cracking in the weld joints were identified by detailed microstructural characterizations of tested specimens. It is found that base metal dilution in weld metal plays a significant role in controlling the hot cracking susceptibility of the weld joints prepared using borated stainless steels and boron free consumable. The cracking tendency is found to be very high at certain regions of the weld metal. The boron content in these regions of the weld metal was found in the range of 0.2 to 0.4 wt.% which falls in the highly crack susceptible regime as reported in the literature. Further, the volume fraction of eutectic liquid present in this region is very low which impeded backfilling of cracks. Moreover, it is found that chemistry of borides formed on re-melting of borated stainless steels during welding is highly rich in Fe and increased the solidification range which further complimented cracking susceptibility. Alternatively, a special purpose electrode containing ~1 wt.% boron considered for welding borated stainless steels was also investigated for its hot cracking susceptibility. The results showed that the weld joints prepared from this electrodes are also not completely immune to hot cracking whereas, susceptible for cracking on application of higher restraint forces. Also, it is found that the weld metal suffers from poor impact properties due to continuous network of interdendritic borides. Based on the results obtained from this study, an alternate procedure for welding SS 304B4 using standard E309 electrode which shows better impact properties and also likely to have reduced cracking susceptibility than the boron containing electrode is proposed. Further, low susceptibility for liquation cracking in SS 304B4 weld joint prepared using the proposed welding procedure is demonstrated.

## LIST OF FIGURES

Figure No.	Title	Page No.
<b>CHAPTER 1</b>		
Fig.1.1	(a) Photograph of actual IHX taken during fabrication (b) Schematic of IHX along with position of neutron shield made from borated stainless steel with respect to neutron flux in the reaction.....	2
Fig.1.2	Schematic representation of macrostructure of SS 304B4 weld joint prepared using E309 electrode.....	5
<b>CHAPTER 2</b>		
Fig.2.1	Microstructures of SS 304B4 in annealed condition (a) Grade A (powder metallurgy route) (b) Grade B (ingot metallurgy route).....	12
Fig.2.2	Microstructures of borated stainless steel in annealed condition (a) 304B4 (~1.24 wt.%B) SS grade B (b) 304B6 (~1.7 wt.%B) Grade B.....	13
Fig.2.3	DTA thermograms obtained for different types of borated stainless steel (a) Type1 (b) Type 2 (c) Type 3.....	14
Fig.2.4	Microstructures of different zones of 304B4 SS weldment (a) taken from autogeneous bead on plate welds made using GTAW process (b) taken from weldment prepared using E308L and SMAW process.....	17
Fig.2.5	Schematic of a weld joint showing various types of hot cracks formed during welding.....	18
Fig.2.6	Schematic representation of micro segregation in welds (a) phase diagram of an alloy system (b) compositions of solid and liquid during solidification (c) composition profiles of solid and liquid during solidification.....	22

Fig.2.7	Schematic of a solute segregation during solidification of a sub grain in a weld metal.....	23
Fig.2.8	Effect of composition on crack susceptibility: (a) weld (b) crack susceptibility.....	24
Fig.2.9	Schematic representation of penetration mechanism occurring in the HAZ.....	29
Fig.2.10	Mechanism of segregation occurring in HAZ liquation cracking.....	30
Fig.2.11	Statistics on utility of different types of hot cracking tests for weldability studies based on literature citations.....	35
Fig.2.12	Statistics on the utility of different types of Varestraint tests for weldability studies based on citations.....	36
Fig.2.13	Schematic representation of different type of Varestraint tests (a) Longitudinal Varestraint test (b) Transverse Varestraint test (c) Spot Varestraint test.....	38
Fig.2.14	Schematic representation of vacuum chamber in which test specimen is loaded in a “Gleeble <sup>TM</sup> ” machine.....	40
Fig.2.15	Schematic representation of hot ductility curves and locations of NDT, NST and DRT are indicated in the figure.....	41

### CHAPTER 3

Fig.3.1	Schematic figure of weld joint prepared using E309 and E308BRN from which Varestraint specimens were extracted.....	50
Fig.3.2	Schematic of (a) Longitudinal varestraint test specimen (b) Transverse Varestraint Test specimen.....	52
Fig.3.3	Schematic of Varestraint test set up used for hot cracking experiments.....	53

Fig.3.4	Macrostructure of Spot Varestraint tested specimen showing the fusion zone and partially melted zone. Cracks that are considered for calculation of TCL and MCL are marked.....	56
Fig.3.5	Schematic representation of procedure involved during BTR determination (a) acquiring weld thermal profile (b) determination of BTR.....	59
Fig.3.6	Sketches and dimensions of specimens used for hot ductility experiments (a) determination of Nil Strength Temperature (NST) (b) determination of Nil ductility Temperature (NDT) and Ductility Recovery temperature (DRT).....	60
Fig.3.7	Schematic representation of load and temperature cycle experienced by 304B4 specimens during hot ductility experiments thermal cycle for (a) NST (b) NDT (c) DRT (d) Partial melting in hot ductility specimens.....	62
Fig.3.8	Drawings of specimens used for (a) Tensile test (b) Charpy “V” notch impact test.....	68

#### CHAPTER 4

Fig.4.1	Pseudo-binary phase diagram of SS 304B4 generated using “Thermo-Calc™”, version 6 using TCFE8 database	73
Fig.4.2	Non-equilibrium solidification simulation of SS 304B4 using Scheil’s module.....	74
Fig.4.3	Scheil’s solidification simulation of liquid phase in the interdendritic regions of PMZ in re-melted 304B4 SS of composition (19.84 wt.% Cr-11.53wt.% Ni-1.77 wt.% B - 0.025 wt.% C-0.357wt.% Si-0.031wt.% P-65wt.% Fe).....	76
Fig. 4.4	<i>On heating and On cooling</i> DSC profile of SS 304B4 base metal heating up to its melting point and cooled down at 10 K/min.....	77

Fig.4.5	<i>On heating and on cooling</i> DSC profile of fused 304B4 SS heated up to its melting point and cooled thereafter at 10K/min.....	79
Fig.4.6	Microstructure of 304B4 SS base metal (solution annealed) obtained using optical microscope.....	81
Fig.4.7	Microstructure of primary borides extracted from 304B4 SS base metal by electrolytic dissolution of matrix obtained using SEM. EDS spectrum of the boride is inset in the figure.....	81
Fig.4.8	XRD profile obtained for base metal borides indicating that it is Cr <sub>2</sub> B type of boride.....	82
Fig.4.9	(a) TEM image of 304B4 SS base metal borides extracted by electrolytic dissolution (b) TEM/EDS taken on the extracted base metal borides.....	82
Fig.4.10	(a) Microstructure of re-melted 304B4 showing austenite dendrites and interdendritic eutectic borides (b) SEM image of re-melted 304B4 showing borides of different morphologies.....	83
Fig.4.11	(a)Image of the porous mass of eutectic network left out after anodic dissolution and XRD analysis of (b) Interdendritic borides and (c) Intradendritic borides present in the re-melted 304B4 SS .....	84
Fig.4.12	(a) TEM image of interdendritic borides (b), TEM/EDS analysis of borides shown in (a),(c) TEM image intradendritic spheroidal borides (d),TEM/ EDS analysis of boride shown in (c).....	85
Fig.4.13	Macrostructure of (a) Longitudinal Varestraint specimen tested at 4% augmented strain (b) Transverse Varestraint specimen tested at 4% augmented strain showing solidification cracks in the fusion zone (c) Spot Varestraint specimen tested at 4% augmented strain showing hot cracks.....	87

Fig.4.14	(a)Total Crack Length Vs % Augmented strain (b) Maximum Crack Length Vs % Augmented strain obtained from 304B4 SS base metal TVT specimens.....	88
Fig.4.15	(a) Total Crack length Vs % Augmented strain (b) Maximum Crack Length Vs % Augmented Strain obtained from 304B4 base metal SVT specimens.....	89
Fig.4.16	Hot ductility curve obtained for 304B4 SS base metal from hot ductility experiments carried out using “Gleeble <sup>TM</sup> ,” thermomechanical simulator.....	90
Fig.4.17	Schematic of re-melted 304B4 SS specimen with bead on plate weld used for SVT.....	92
Fig.4.18	Macrostructure of spot Varestraint specimen tested at 4% augmented strain showing hot cracks.....	92
Fig.4.19	(a) Total Crack Length Vs %Augmented Strain (b) Maximum Crack Length Vs %augmented strain obtained for re-fused 304B4 SS specimens from SVT.....	93
Fig.4.20	Hot ductility curve obtained for re-melted 304B4 SS from hot ductility experiments using “Gleeble <sup>TM</sup> ,” thermo mechanical simulator.....	94
Fig.4.21	Microstructure of 304B4 SS specimens subjected to TVT showing prominent backfilled cracks in the fusion zone.....	95
Fig.4.22	Microstructure of 304B4 SS specimen (a) subjected to augmented strain during SVT showing PMZ formed in the base metal region and back filled cracks (b) not subjected to strain during SVT.....	96
Fig.4.23	Microstructure of fused 304B4 SS specimen subjected to SVT shows hot crack extending from re-fused zone to the PMZ formed in the fused region (b) microstructure of PMZ formed on fused 304B4 SS not subjected to augmented strain.....	97

Fig.4.24	Microstructures of (a) 304B4 base metal (b) hot ductility tested base metal specimens at NDT (1165°C), (c) NST (1220°C), (d) Above DRT (1150°C), (e) At DRT (1125°C).....	98
Fig.4.25	Fig.4.25 Microstructures of hot ductility tested re-melted 304B4 SS specimen (a) NDT (1165°C) (b) NST (1214°C) (c) above DRT (1100°C) (d) at DRT (1075°C).....	100
Fig.4.26	Fracture surfaces of SS 304B4 base metal specimens tested at (a) NST (b) NDT (c) DRT.....	102
Fig.4.27	Fracture surfaces of hot ductility tested fused 304B4 specimens (a) NST (b) NDT (c) (DRT).....	102
Fig.4.28	Elemental mapping performed using WDS/EPMA on (a) SS 304B4 base metal (b) SS 304B4 specimen tested at NST (c) SS 304B4 specimen on cooling from NST (d) fused SS 304B4 specimens tested at NST.....	104-107
Fig.4.29	Schematic representation of thermal cycle and phase transformations experienced by various regions of 304B SS PMZ with respect to the weld thermal cycle and its corresponding microstructures (a) 304B4 SS base metal (b) PMZ in base metal (c) unaffected region of 304B4 SS bead on plate weld (d) PMZ in bead on plate weld formed during spot Varestraint test .....	114
Fig.4.30	Microstructure of PMZ formed on 304B4 SS bead on plate weld (a) after applying 2% strain during spot varestraint test (b) without applying strain.....	118

## CHAPTER 5

Fig.5.1	Schematic representation of extraction of Varestraint test specimens from 304B4 SS weld joint prepared using E309 electrode and location of spot Varestraint test conducted on the specimens.....	122
Fig.5.2	Schematic of 304B4 SS weld joint. Microstructure of various zones of 304B4 SS weld joint prepared using 309	

	electrode (b) base metal PMZ (c) 304B4 unmixed zone (d) 309 weld metal affected by base metal dilution (e) undiluted 309 weld metal.....	123
Fig.5.3	Fig.5.3 Microstructure of 309 weld metal affected by base metal dilution. The image shows the weld interface at the right side and weld center towards the left. Bright contrast is austenite, grey contrast is delta ferrite and dark contrast is eutectic phase.....	124
Fig.5.4	Schematic of SS 304B4 weld joint prepared using E309 electrode showing the locations of spot Varestraint test, direction of spot EDS analysis and different zones in the weld metal diluted by base metal.....	125
Fig.5.5	Semi quantitative spot EDS analysis of elements : Fe, Cr, Ni across the weld interface shows percentage of base metal dilution in sides P, Q and R of weld metal affected by base metal dilution.....	126
Fig.5.6	Shows ferrite number measured across weld metal interface from base metal to weld center.....	128
Fig.5.7	Comparison of solidification temperature range of SS 304B4 base metal to that of weld metal affected by base metal dilution and undiluted 309 weld metal simulated using Schiel's solidification model.....	129
Fig.5.8	Plot of (a) Total Crack Length Vs % augmented strain (b) Maximum Crack Length Vs % augmented strain obtained for 309 weld metal diluted by base metal.....	131
Fig.5.9	(a) Macro-cracks observed on (a) weld metal affected by base metal dilution (b) undiluted 309 weld metal.....	133
Fig.5.10	Microstructures of spot Varestraint tested Type B specimens of weld metal diluted by base metal.(a) Microstructure at P-side (close to weld interface) (b) Microstructure at Q side (slightly away from the interface) (c) Microstructure of side R (opposite to P side).....	134

Fig.5.11	Microstructure of undiluted 309 weld metal (Type A) taken from Varestraint tested specimen.....	135
Fig.5.12	(a) Schematic representation specimen preparation for fractography (b) top view of crack surface of 309 weld metal PMZ obtained from hot crack tested specimen of weld metal diluted by base metal. Regions 1& 2 shows typical “egg crate” fracture morphology pertaining to liquation of grain boundaries and region 3 shows interdendritic fracture typical of ductility dip cracking.....	137
Fig.5.13	SEM image of side Q of 309 weld metal diluted by base metal shows thin films of eutectics along MGB and spot EDS on the eutectic reveals segregation of impurity elements along with Cr borides.....	138

## CHAPTER 6

Fig.6.1	Schematic of extraction of hot crack specimens from the weld joint used for (a) Transvarestraint (TVT) (b) longitudinal varestraint test (LVT) showing the direction of autogenous TIG welding and loading during testing.....	147
Fig.6.2	(a) Microstructure of 308BRN weldment at low magnification and (b) high magnification image of 308BRN weld metal microstructure.....	148
Fig.6.3	(a) Macrostructure of longitudinal varestraint tested specimen (b) plot of total crack length (TCL) vs % augmented strain.....	149
Fig.6.4	Macrostructure of transvarestraint tested specimen (b) Total Crack Length (b) (c) Maximum Crack Length (MCL) obtained from crack length measurements carried out on transvarestraint tested specimens extracted from 304B4 SS joined using E308BRN plotted against % augmented strain.....	150
Fig.6.5	Microstructures obtained from 308BRN weld joint specimens after transvarestraint tested specimens at (a) 4% augmented strain (low magnification) (b) 4% augmented strain (high magnification) (c) 1% augmented	

	strain.....	152
Fig.6.6	Elemental mapping performed on 308BRN weld metal using EPMA shows Fe rich eutectic borides present in the interdendritic regions.....	153
Fig.6.7	Temperature vs fraction of liquid curves generated for 308BRN weld metal using Scheil's solidification simulation module.....	154
Fig.6.8	Plot of widths of the longest crack observed in the transverse restraint tested specimen at various % augmented strain.....	157
Fig.6.9	Microstructures of fusion zone of v-restraint test specimens (a) 304B4 SS base metal (b) 308BRN weld metal.....	158

## CHAPTER 7

Fig.7.1	Schematic representation of cross weld tensile and impact specimens extracted from the weld joints.....	162
Fig.7.2	Stress-strain curves of 304B4 SS base metal, 304B4 SS weld joints prepared using E308BRN and E309 electrodes tested at room temperature.....	163
Fig.7.3	Microstructures at the fracture location of (a) E308BRN weld joint (b) E309 weld joint specimens taken after room temperature tensile test.....	164
Fig.7.4	Fracture surface of (a) E308BRN weld joint (b) E309 weld joint specimens taken after room temperature impact test.....	165
Fig.7.5	Microhardness profiles taken across weld joints prepared using E308BRN and E309 electrodes.....	166
Fig.7.6	SEM image of tensile tested specimens extracted from E309 weld joint showing voids in the interdendritic regions near the fracture location.....	169

Fig.7.7	Microstructure of 309 weld metal taken adjacent to fracture location on impact tested specimen.....	170
---------	---	-----

**CHAPTER 8**

Fig.8.1	Schematic representation of modified welding procedure adopted for welding 304B4 SS using E309 electrode.....	175
---------	---	-----

Fig.8.2	Schematic representation of locations on weld pad prepared after buttering from which spot varestraint test specimens were extracted and spot varestraint test was conducted.....	176
---------	---	-----

Fig.8.3	(a) Macrostructure of 304B4 SS weld joint prepared using modified welding procedure (b) Microstructure of PMZ formed on 304B4 SS base metal (c) Microstructure of UMZ formed next to PMZ Microstructures of 309 butter layer (d) near (e) far away from 304B4 SS base metal-309 butter layer interface (interface -1) (f) Microstructure of interface between 309 butter layer and 309 weld metal (interface2) (g) Microstructure of 309 weld metal.....	178
---------	--	-----

Fig.8.4	(a) Macrostructure of spot Varestraint tested specimen extracted from weld joint prepared using E309 after buttering, Plots of (b) Total Crack Length (TCL) vs % augmented strain (c) Maximum Crack Length (MCL) vs % augmented strain of weld joints prepared using E309 with, without buttering and undiluted 309 weld metal.....	180
---------	---	-----

Fig.8.5	(a) Macrostructure of spot Varestraint tested specimens showing a liquation crack taken at low magnification (b) Microstructure of the liquation crack present in 309 weld metal taken at high magnification (c) Polarized light contrast microstructure of 309 weld metal showing MGBs taken at the crack tips and the inset to the figure shows features pertaining to eutectic films along the MGB at high magnification (d) Polarized light contrast microstructure of 309 weld metal showing austenite and delta ferrite at the location where liquation cracks are not present.....	181
---------	---	-----

## LIST OF TABLES

<b>Table No:</b>	<b>Title</b>	<b>Page No:</b>
<b>CHAPTER 2</b>		
Table 2.1	Chemical composition of borated stainless steels as per ASTM A887.....	9
Table 2.2	Mechanical properties requirements of borated stainless steels as per ASTM 887.....	10
<b>CHAPTER 3</b>		
Table 3.1	Chemical composition of 304B4 SS base metal used in the study in wt.%.....	50
Table 3.2	Chemical compositions in wt.% of undiluted weld metal of E309 and E308BRN electrodes used in the present study.....	50
Table 3.3	Welding parameters used for weld pad fabrication using E309 and E308BRN electrode using SMAW process.....	51
Table 3.4	Welding parameters used during Transverse, Longitudinal and Spot vareststraint test.....	55
Table 3.5	Summary of Vareststraint experiments designed in this study.	58
<b>CHAPTER 4</b>		
Table 4.1	Summary of transformation temperatures of 304B4 SS base metal, fused 304B4 and interdendritic liquid present in fused 304B4 SS.....	80
Table 4.2	Comparison of types of borides present in 304B4 SS base metal and fused 304B4 SS with predicted using “Thermo-Calc <sup>TM</sup> ” and that reported in literature.....	86
Table 4.3	Summary of hot ductility test results of 304B4 SS base	

	metal.....	91
Table 4.4	Summary of hot ductility test results of re-melted SS 304B4.	94

**CHAPTER 5**

Table-5.1	Semi quantitative EDS analysis of various regions of 309 weld metal affected by base metal dilution in wt.%.....	127
-----------	--	-----

# CHAPTER 1

## BACKGROUND AND MOTIVATION

### 1.1 Introduction

Borated stainless steels are a class of austenitic stainless steels (SS) that contain 0.2 to 2 wt.% boron dispersed in the form of borides in an austenite matrix. These steels are covered by ASTM specification A887, that specify eight boron levels (AISI 304B to 304B7) [1]. The intentional boron addition in these steels provides up to three times higher neutron absorption capacity relative to SS 304. This is because natural boron contains ~18 % of B<sup>10</sup> isotope which is an effective neutron absorber [2]. These steels find applications in the nuclear industry for construction of nuclear fuel transportation casks, spent fuel storage racks, absorber rods for nuclear criticality control and neutron shields for structural components. In India, AISI 304B4 SS plates containing ~1.24 wt.% boron was chosen for fabrication of neutron shields for Intermediate Heat Exchangers (IHX) for the Indian Prototype Fast Breeder Reactor (PFBR) [3].

PFBR is a 500 MWe demonstration plant, now at final stages of completion at Kalpakkam for commercial power production using FBR technology. In this reactor there are four Intermediate Heat Exchangers (IHXs) placed inside the reactor vessel. The purpose of IHX is to transfer the heat extracted by the primary sodium from the reactor core to the secondary sodium. The secondary sodium in turn transfers the heat to water to generate steam in the steam generator to rotate the turbine.

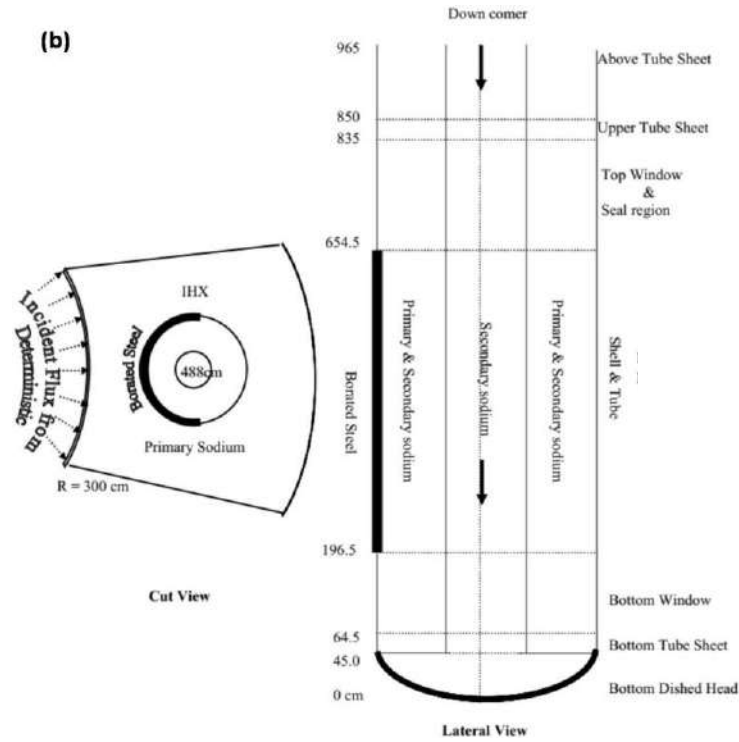


Fig.1.1 (a) Photograph of actual IHX taken during fabrication (b) Schematic of IHX along with position of neutron shield made from borated stainless steel with respect to neutron flux in the reaction [5].

The IHX was fabricated by welding process which was extremely challenging due to very tight tolerances and stringent specifications [4]. The vertical outer shell in the IHX

facing the core is enclosed by a neutron shield made of borated stainless steel conforming to ASTM A887 [1] as shown in Fig.1.1 [5].

The purpose of neutron shields is to reduce induced radioactivity in the secondary sodium which flows in to steam generator situated outside the reactor vessel. The most challenging task faced during fabrication of IHX was welding 10 and 28 mm thick 304B4 SS neutron shields around the shell in bottom portion of IHX [4].

In general, weldability of borated stainless steels is poor due to their high susceptibility to hot cracking. Hot cracking is a phenomenon that occurs in weldments due to segregation of impurity or alloying elements in the liquid metal present along the interdendritic/intergranular regions resulting in increased solidification temperature range for the weld and cracking of the joint under the action of shrinkage stresses developed during final stages of solidification. It is to be noted that in this steel boron is an intentional alloying element. Also, it is well known that boron is almost insoluble in austenite phase and hence gets partitioned to the liquid phase which leads to formation of low melting eutectic phases that accumulate at interdendritic spaces during last stages of solidification. The presence of interdendritic eutectic phases increases the susceptibility of the welds to hot cracking. However, it is reported in the literature that borated stainless steels with boron content in the range of 0.5-2 wt.% are immune to hot cracking under moderate restraint forces. This is attributed to effective backfilling of the hot cracks by the eutectic liquid formed in the fusion zone [6]. Welding consumable recommended for SS 304B4 is standard E309 as it solidifies in the primary ferritic mode thus utilizing the beneficial effects of delta ferrite in reducing hot cracking [4].

In the fabrication of neutron shields for IHX of PFBR, though E309 welding consumable was chosen to weld AISI 304B4 - to minimize the risk of hot cracking - extensive cracks were observed especially in the thick section joints. During subsequent procedure qualification for these joints, more than 100 weld test coupons produced with 10 different grades of consumables showed cracks and fissures in the welds. Finally, fabrication was carried out using a specially developed boron containing consumable which does not conform to any standard classification of austenitic welding consumables [2,3].

## **1.2 Aim and Objective**

The difficulties encountered during fabrication of the neutron shields for IHX of PFBR revealed that the current understanding of hot cracking behavior of boron containing stainless steel during fusion welding is far from complete. Hence, this systematic study on weldability of AISI 304B4 SS to understand its hot cracking behavior using both standard E309 and non standard boron added welding consumables (E308BRN) was undertaken.

It is realized that severe cracking in weld joints produced using E309 could be due to base metal dilution in the weld metal. Base metal dilution can introduce boron in fusion zone and its concentration can vary depending on the dilution ratio - being high close to the fusion boundary and less at the weld centre.

Further, depending on the melting and mixing of the base metal/previously deposited weld metal, different zones can be identified in the fusion zone of a multipass weld joint made of SS 304B4 using E309 electrode, as shown in Fig.1.2.

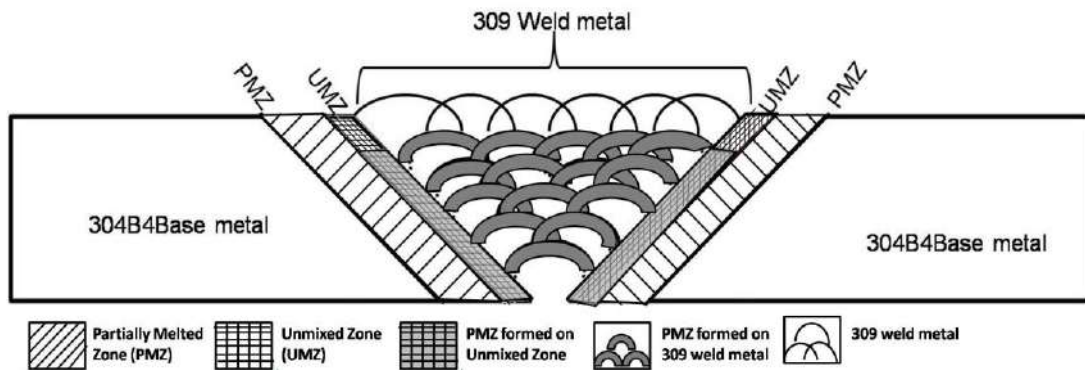


Fig.1.2 Schematic representation of macrostructure of 304B4 SS weld joint prepared using E309 electrode.

These five zones differ in their microstructure and micro constituents which can greatly influence hot cracking susceptibility of the weld joint as a whole. Hence, hot cracking studies conducted just on SS 304B4 base metal alone is not sufficient to assess the weldability of the steel. In contrast, when welding consumables containing boron is used, effect of dilution from base metal on weld metal would be negligible. However, high concentration of boron in the weld metal would increase the volume fraction of eutectic phase improving the back filling of cracks during solidification but adversely affecting the mechanical properties due to its increased boride content.

Accordingly, the broad aim of the present work is to understand the hot cracking behavior during welding of SS 304B4 steel with boron free as well as boron added consumables and study the mechanical properties of the weld joints. Based on the results obtained, recommend a procedure that can reduce the risk of cracking during actual fabrication. Specifically, to achieve these aims the following investigations were undertaken.

1. Study of solidification cracking behavior of 304B4 austenitic stainless steel.

2. Evaluation of liquation cracking susceptibility of partially melted zone (PMZ) formed in SS 304B4 base metal and Un-Mixed-Zone (UMZ) (re-solidified 304B4 SS) formed in weld joint prepared using 309 electrode.
3. Evaluation of liquation cracking susceptibility of weld metal diluted by SS 304B4 base metal and undiluted 309 weld metal present in weld joint prepared by 309 electrode using spot Varestraint test.
4. Estimation of hot ductility of AISI 304B4 base metal and PMZ produced by thermal simulation by determining Nil Strength Temperature, Nil Ductility Temperature and Ductility Recovery Temperatures using “Gleeble<sup>TM</sup>” thermo mechanical simulator and correlating the hot ductility behavior with liquation cracking test results obtained from Varestraint experiments.
5. Extensive characterizations of the fusion zone microstructure of the weld joints to understand the mechanism of cracking and correlation of the cracking results with microstructure.
6. The study of the cracking behavior of weld joints produced using boron added welding consumable and comparison of the results with those obtained from weld joint prepared using 309 electrode.
7. Recommendation of a procedure to bring down the risk of hot cracking during welding of borated stainless steel and its experimental demonstration.

### **1.3 Organization of thesis**

The thesis is organized in the following manner.

**Chapter 1:** Introduction and background of the present work and objectives of the study are given in this chapter.

**Chapter 2:** A complete review of current status on various studies carried out on borated stainless steels and its weldability aspects are presented. Based on this, gap areas are identified and accordingly, scope of the work is defined.

**Chapter 3:** In this chapter, the experimental set up used for the study is described in detail. Also, various characterization facilities utilized for microstructural and micro chemical analysis of tested specimens are described.

**Chapter 4:** This chapter explains the solidification and liquation cracking susceptibility of SS 304B4 base metal and re-melted SS 304B4 based on the results from Vareststraint and hot ductility experiments. The mechanisms behind the variation in their tendencies for cracking are also presented.

**Chapter 5:** Hot cracking studies conducted on SS 304B4 weld joint prepared using E309 electrode are given in this chapter. PMZ formed in previously deposited weld metal diluted by base metal and undiluted 309 weld metal are evaluated specifically and the micro mechanisms responsible for cracking in this region are identified.

**Chapter 6:** In this chapter the hot cracking susceptibility of boron added electrode which can be used as an alternate consumable for welding SS 304B4 is described.

**Chapter 7:** A comparison of mechanical properties between the weld joints prepared using boron free and boron added consumables is reported in this chapter so that for

selection of the consumables for welding borated stainless steel, in addition to susceptibility to hot cracking, mechanical property can also be considered.

**Chapter 8:** Based on the results presented in the previous chapters, a procedure that would significantly reduce hot cracking while welding SS 304B4 using standard E309 electrode is presented here. Results of the hot cracking tests carried out on the weld joints produced using this procedure indeed confirm that this procedure can bring down the risk of hot cracking during welding.

**Chapter 9:** This chapter provides major conclusions derived from the present study and scope for future work on welding of borated stainless steel.

## CHAPTER 2

### LITERATURE REVIEW

#### 2.1 Borated stainless steels and its applications

Borated stainless steels are a special class of austenitic stainless steels with intentional alloying additions of 0.2 to 2 wt.% of boron. These steels are classified under ASTM standard A887-89 [1]. Under this specification, the borated stainless steels are classified in to 8 groups depending on its boron content as given in Table 2.1.

Table 2.1 Chemical compositions of borated stainless steels as per ASTM A887 [1].

S.No:	Basic Composition (all types)		Boron content	
	Element	Concentration (wt.%)	Type of steel	(wt.%)
1	C	0.08 max	304B	0.20-0.29
2	Mn	2.00 max	304B1	0.30-0.49
3	P	0.045 max	304B2	0.50-0.74
4	S	0.030 max	304B3	0.75-0.99
5	Si	0.75 max	304B4	1.00-1.24
6	Cr	18.00-20.00	304B5	1.25-1.49
7	Ni	12.00-15.00	304B6	1.50-1.74
8	Other	0.010 max N	304B7	1.75-2.25

Each grade is further classified into A and B types depending on the route through which it is produced. Type A steels are produced via powder metallurgy route whereas type B steels are produced by ingot solidification method. In the finished product form, they differ in their mechanical properties. Requirements for these properties for type A and B steels as per the ASTM standard are shown in Table 2.1. Basically, the superior mechanical properties possessed by type A steels are due to the spheroidal morphology of the Cr<sub>2</sub>B type of borides distributed in the austenite matrix. In the powder metallurgy route, inert gas atomized alloy powder is compacted to full density by hot isostatic

pressing, hot rolled, annealed and water quenched. This process yields much finer, less elongated and more uniform distribution of borides in the matrix than those can be achieved through ingot solidification route [7].

Table 2.2 Requirements of mechanical properties for borated stainless steels as per ASTM A887\* [1].

S.No:	Type	Grade	Elongation in 50 mm (2 in.) min %	Hardness, max .		Charpy V- Notch J (ft-lb)
				Brinell	Rockwell B	
1	304B	A	40.0	201	92	88(65)
		B	40.0	201	92	54(40)
2	304B1	A	40.0	201	92	81(60)
		B	35.0	201	92	47(35)
3	304B2	A	35.0	201	92	65 (48)
		B	27.0	201	92	22 (16)
4	304B3	A	31.0	201	92	52(38)
		B	19.0	201	92	14(10)
5	304B4	A	27.0	217	95	41(30)
		B	16.0	217	95	-
6	304B5	A	24.0	217	95	31(23)
		B	13.0	217	95	-
7	304B6	A	20.0	241	100	22(16)
		B	9.0	241	100	-
8	304B7	A	17.0	241	100	14(10)
		B	6.0	241	100	-

\*Minimum yield and tensile strength requirements for all Types and Grades are 205 and 515MPa respectively.

It is to be noted from the table that there is no impact property requirement specified for grade B category steels of 304B4 to 304B7 as the boron content of these steels are high. Major application of this steel is in nuclear industries because, B<sup>10</sup>, which is present as much as 18% in natural boron is an efficient neutron absorber [8]. The absorption cross section of B<sup>10</sup> is 3800 barns for thermal neutron and 1 barn for the fast neutron spectrum - values that are considered to be high. Hence, borated stainless steels

offer an economically viable route for better neutron shielding of structural components in nuclear reactors. It may also be mentioned that borated stainless steels have up to three times higher efficiency for neutron absorption as compared to plain austenitic stainless steels. Control rods, burnable poison and neutron shielding plates are some of the components made of borated stainless steel that are used in nuclear reactors [9, 10]. Borated stainless steels also find applications in nuclear waste disposal and in reprocessing plants for storage, transportation and containment of radioactive substances. Casks made of the steel are used to transport spent fuel from a wet or dry storage facility to a permanent location, namely, a monitored retrievable storage (MRS) regional site or a permanent repository. These steels are also used in International Thermonuclear Experimental Reactor (ITER) project under construction in France. The material is used in inner wall thermal neutron shielding for the fusion reactor. In the ITER vacuum vessel, 40 millimeter-thick plates made out of borated stainless steel containing about two weight percent boron (AISI 304B7) is proposed for neutron shielding [11].

Several advanced versions of borated stainless steels with improved neutron absorption capabilities are also being developed to cater to various requirements of the nuclear industry. Some steels contain enriched  $B^{10}$  isotope, which offers a higher neutron absorption cross section for given total boron content. The use of  $B^{10}$  isotope enrichment enables use of less boron for equivalent neutron absorption along with improved ductility and impact toughness. Use of varying amounts of two neutron absorbing elements - boron and gadolinium (Gd) in austenitic stainless steel is also an option available to increase neutron absorption. Despite its much higher atomic weight, Gd has more than four times

the thermal neutron absorbing capabilities of boron. By restricting the boron content to less than 1%, and using Gd to attain equivalent boron content (Beq), the new alloys exhibit superior ductility, toughness, bendability and corrosion resistance compared to borated stainless steels [12]. In general, borated stainless steels are used only for strap on purposes and not primarily designed for any load bearing applications. Steels with boron content >1 wt.% show poor ductility and impact toughness due to the presence of elongated primary borides in the matrix [2].

## 2.2 Microstructures of borated stainless steels

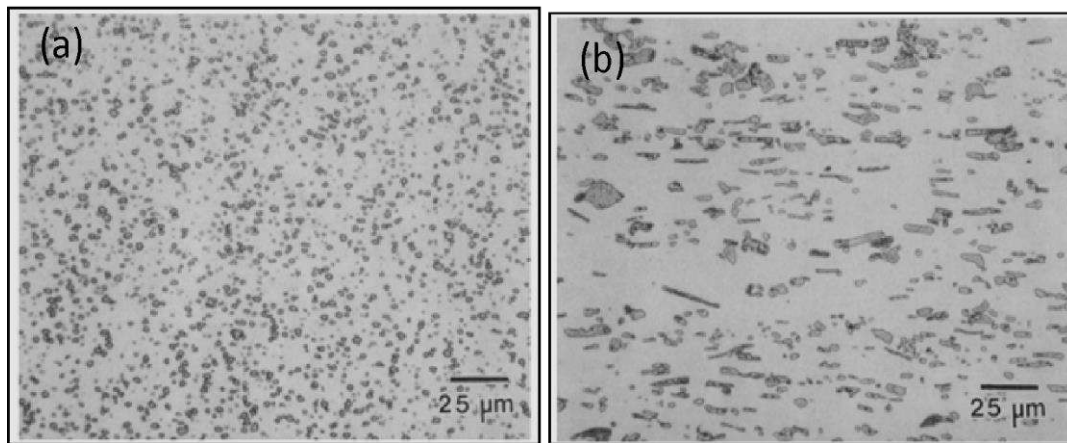


Fig.2.1 Microstructures of SS 304B4 in annealed condition (a) Grade A (powder metallurgy route) (b) Grade B (ingot metallurgy route) [7]

Microstructures of all borated stainless steels in annealed and quenched condition, irrespective of the type, consists of austenite matrix in which micron size  $\text{Cr}_2\text{B}$  type of borides are densely distributed as shown in Fig.2.1 [7]. In type A steels, the borides are comparatively smaller in size than in type B steels and more or less spherical in morphology [9]. There are not many variations in microstructural features of different

grades of borated stainless steels except for the volume fraction of borides which increase with boron content, as shown in Fig.2.2 [13,14].

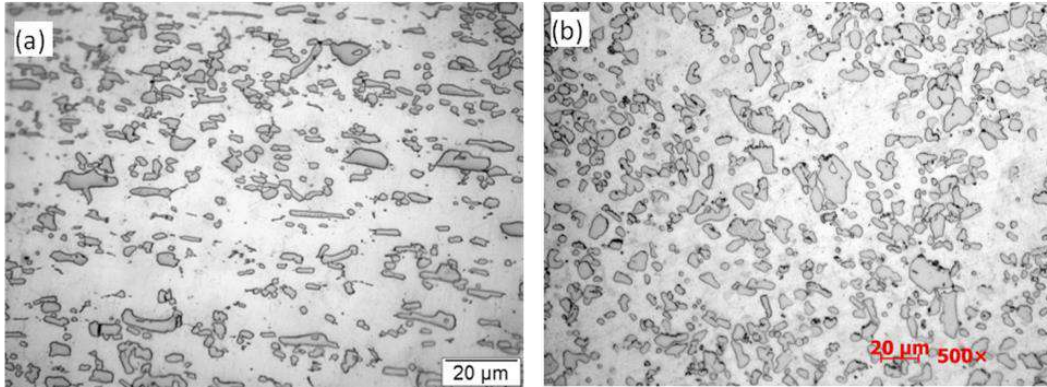


Fig.2.2 Microstructures of borated stainless steel in annealed condition (a) 304B4 (~1.2 wt.%B) SS grade B (b) 304B6 (~1.7 wt.%B) Grade B [13,14]

### 2.3 Evolution of phases on melting and re-solidification of borated stainless steels

Borated stainless steels show three distinct solidification behaviors, depending on the boron content, during DTA experiments. The solidification temperature range, type of phases formed and temperature at which phase transformations take place etc. vary with respect to boron content of the steel. 304B2 to 304B5 steels containing 0.5-1.5 wt.% boron show Type 1 behavior which is similar to those observed for off-eutectic alloys in binary systems (ex: Fe-C, Al-Si) as shown in Fig.2.3(a). Type 2 behavior is exhibited by steels 304B and 304B1 containing boron in the range of 0.20 - 0.49 wt.% as shown in Fig.2.3(b)[7].

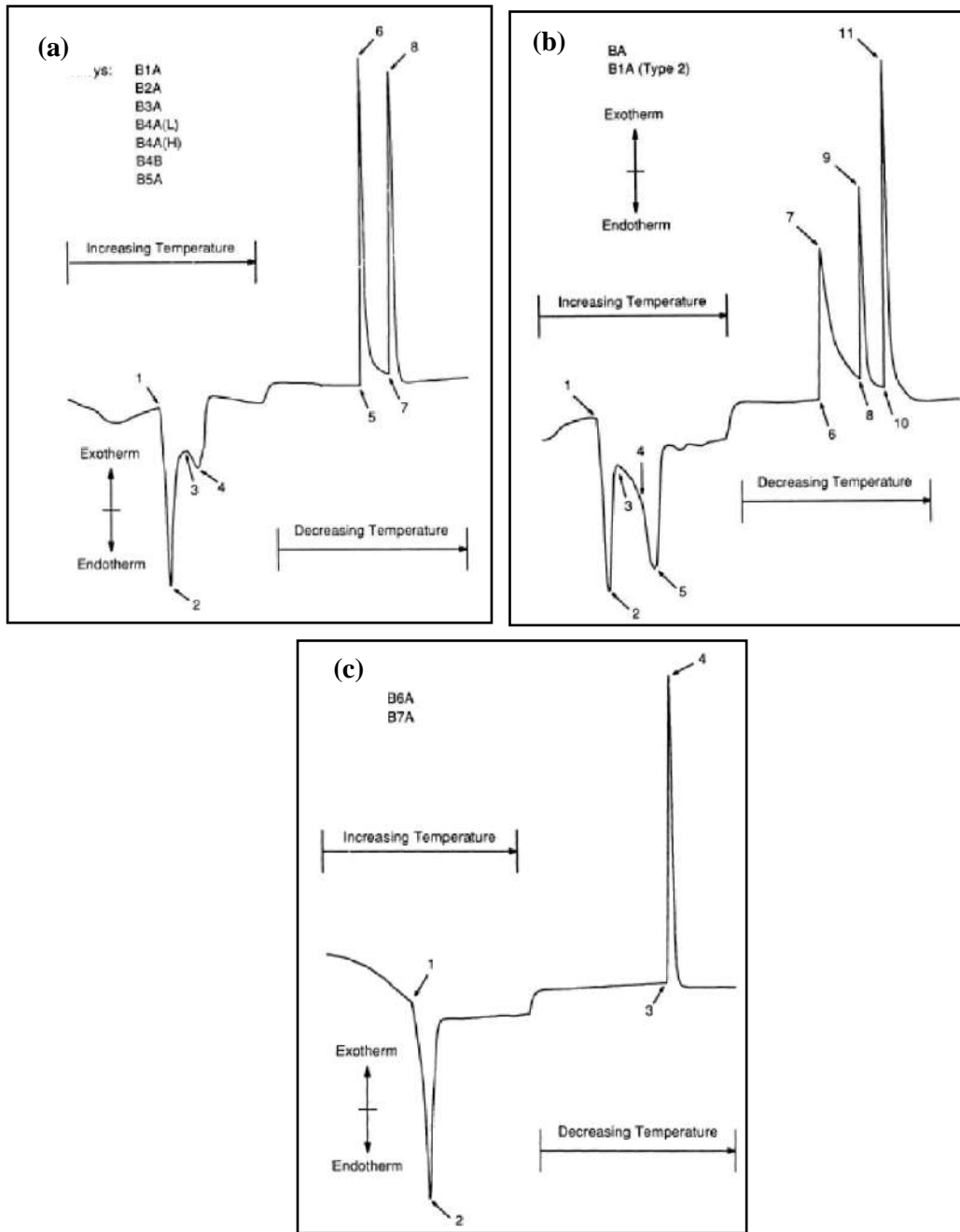


Fig.2.3 DTA thermograms obtained for different types of borated stainless steel (a) Type 1 (b) Type 2 (c) Type 3 [7].

304B6 and 304B7 steels exhibit solidification behavior similar to binary eutectic alloys as shown in Fig.2.3(c). It is reported that point 1 in Fig.2.3(a) corresponds to commencement of liquation of borides by eutectic reaction. Point 2 corresponds to completion of melting of eutectic. On continuous heating, the primary austenite starts melting at point 3 and the steel is completely liquid at point 4. During the cooling cycle of DTA experiment, solidification initiates with the formation of austenite at point 5 and continues until point 6. Point 7 indicates the formation of eutectic boride/austenite constituent which continues to solidify until the temperature associated with point 8 is reached. DTA curve shown in Fig.2.3(b) is substantially different from that shown in Fig.2.3(a). Points 1 and 2 in Fig.2.3(b) corresponds to initiation and completion respectively of liquation of borides. Points 3 and 5 represent initiation and completion of liquation of primary austenitic phase as shown in the figure. In between points 3 and 5 there is a pronounced break at point 4; the reason for this is unclear. Points 6 and 7 correspond to initiation and completion of solidification of primary austenite phase respectively during cooling cycle of DTA experiment. Points 8,9,10 and 11 indicate initiation and completion of solidification of eutectic borides in two stages. On comparing the DTA thermograms in Fig.2.3(a) and (b), it is found that *on heating* curve in Fig.2.3(b) shows clearer separation between the features corresponding to melting of eutectic and austenite as well as an extra peak exhibited on solidification. So far there is no clear explanation for the observed differences between the Type 1 and 2 behaviors though it is reported by many authors. Some authors state that the extra peak found in Type 2 behavior during cooling in low boron alloys is due to formation of divorced type of

eutectic borides but not supported by microstructural evidences. The most convincing explanation for this behavior is given by Robino et al. who suggested the intermediate peak may be due to formation of two distinct types of eutectics. The compositions of which are indistinguishable by analytical electron microscope as reported by Mehrabian and Flemmings for ternary systems [15]. The microstructure of as-solidified DTA sample consists of primary austenite dendrites with interdendritic eutectic constituents of irregular type [7]. Fig.2.3(c) shows Type 3 behavior exhibited by borated steel which resemble the behavior of binary eutectic alloy. Points 1 and 2 correspond to initiation and completion of melting of eutectic boride/austenite respectively on heating and points 3 and 4 corresponds to solidification of the eutectic boride/ austenitic constituents on cooling.

#### **2.4 Microstructure of 304B4 weldment**

At present, there are only a few studies reported on SS 304B4 weldments. These studies were carried out either on bead on plate weld pads prepared by autogenous GTAW process or by SMAW process using E308L, E309 electrodes [2, 7, 13]. In GTAW bead on plate welds, weldment consists of 3 distinct zones, namely, completely molten and solidified fusion zone (FZ), partially molten and solidified zone (PMZ) where the peak temperature lies in between solidus and liquidus temperatures and heat affected zone (HAZ) where the peak temperature is below the solidus [7]. Microstructure of fusion zone of SS 304B4 consists of primary austenite dendrite and interdendritic eutectic borides. PMZ shows regions of primary austenite grains which are intact as well as partially molten and solidified eutectic borides.

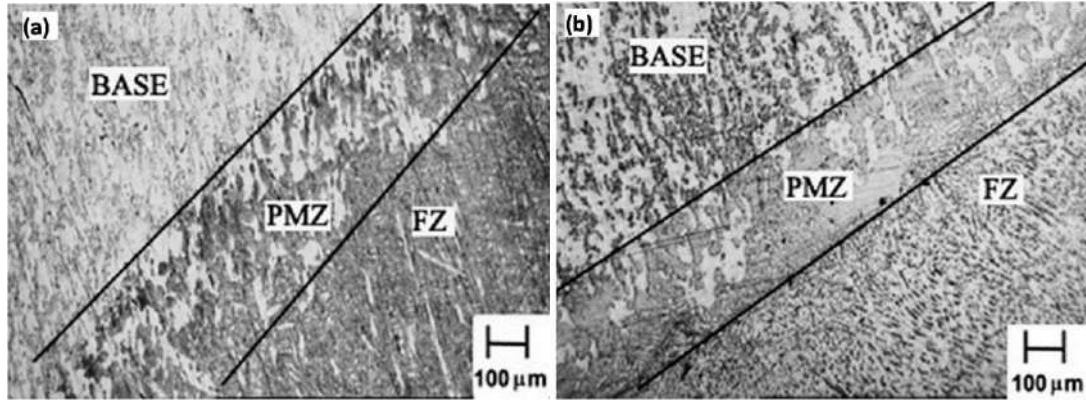


Fig.2.4 Microstructures of different zones of 304B4 SS weldment (a) taken from autogenous bead on plate welds made using GTAW process (b) taken from weldment prepared using E308L and SMAW process [16].

HAZ microstructure consists of coarsened borides in austenite matrix. Morphology of eutectic borides in fusion zone and PMZ were found to be highly irregular in nature as shown in Fig.2.4(a). Weldment microstructures of 304B4 prepared using E308L austenitic electrodes and SMAW process and autogenous GTA weldments are shown in Fig.2.4(a) and (b). It is reported that the fraction of eutectic borides in the PMZ of SMAW joint is lower than that present in the GTA weldment and is attributed to base metal dilution in 308 weld metal [16]. This can be contested since the dilution from molten base metal can affect the fraction of eutectic borides in the weld metal but not the fraction of eutectic borides in the PMZ. The observed differences may also be due to difference in the heat inputs employed during preparation the weld joints by two different processes. It is also reported in this study that the fusion zone microstructure of SMAW joint consists of duplex microstructure of austenite and vermicular ferrite. In this study as well as in the study carried out by Park et.al [2] on SS 304B3 weld joint prepared using ER308L filler wire and GTAW process there is no mention of the dilution of the fusion zone by the molten base metal.

## 2.5 Weldability

The term weldability refers to ability of the material to be welded under imposed fabrication condition into a suitably designed structure and to perform satisfactorily in the intended service [17]. It covers the aspects like ease of fabricability, resistance to metallurgical damage and resistance to premature failures of the welded components.

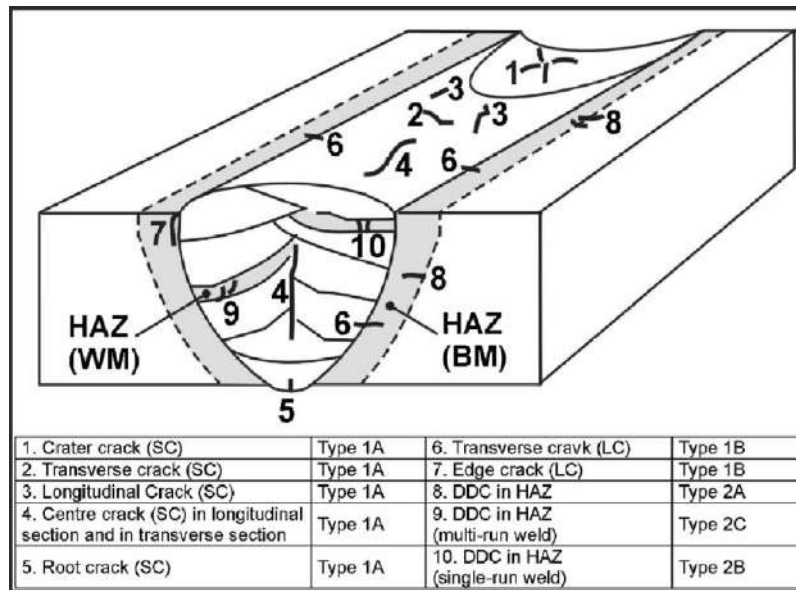


Fig.2.5 Schematic of a weld joint showing various types of hot cracks formed during welding [18]

Since producing a weld joint without cracks and fissures is a primary facet of weldability, many researchers focus on cracking studies on weld joints of structural materials to assess weldability [18]. A weld joint is susceptible to different forms of cracking which can be categorized based on the temperature range over which it occurs. Hot cracking refers to cracking of weld joints during the thermal cycle experienced by the fusion zone and the HAZ. The formation of hot cracks is attributed to the presence of intergranular/interdendritic liquid films as well as action of tensile stresses in the

weldment during the last stage of solidification. Various forms of hot cracks are solidification cracks, HAZ liquation cracks and weld metal liquation cracks [18] as shown schematically in Fig.2.5.

Solidification cracking refers to cracking in the fusion zone during solidification due to presence of liquid films along the interdendritic regions and residual tensile stresses. Liquation cracking refers to cracking in PMZ/HAZ lying either in base metal or weld metal (in multipass welds) due to presence of liquid films along the intergranular/interdendritic regions and residual tensile stresses generated during solidification of the welds. The liquation cracks can be divided into two parts, namely, *on heating* and *on cooling* liquation cracks. *On heating* liquation cracking is defined as cracking in PMZ/HAZ due to sudden drop in ductility of the material associated with incipient melting of grain boundaries due to the presence of low melting eutectics in intergranular/interdendritic (multipass welds) regions on heating the material close to its melting temperature during welding. A detailed description on mechanism of *on heating* and *on cooling* liquation cracking is given in section 2.5.3.

Other cracks that occur in weld joints in solid state at any temperature between solidus and  $0.5 T_H$  (homologous temperature) are ductility dip cracks, strain age cracks, reheat cracks and lamellar tears. Apart from these, cold cracks occur in solid state at a temperature close to room temperature assisted by the presence of diffusible hydrogen. Each of the cracking phenomena mentioned above are specific to alloy systems, microstructure and micro constituents developed during welding [19]. Since austenitic

stainless steels are prone to hot cracking, extensive literature is available on hot cracking susceptibility of this class of steel.

### ***2.5.1 Theory of weld solidification cracking***

Several theories on solidification cracking were propounded by my many authors in the past. The initial theories (Medovar) associated cracking with segregation and solidification range [20]. The wider the freezing range, the greater is the susceptibility to solidification cracking. However, this theory was not applicable to all systems and many exceptions were identified. A 'Generalised Theory' of cracking was proposed by Borland (1960). Borland classified solidification of a binary alloy into four stages according to distribution of the liquid and solid phases. In stage 1, the solid phase is widely dispersed, the liquid phase is continuously spread and both the phases can accommodate relative movement under the action of shrinkage stresses. In stage 2, solid phases are also continuous similar to liquid, but the solid dendrites are interlocked and only the liquid is able to move. At this stage, the liquid is capable to heal any crack that is formed. In stage 3, the solid crystals are in an advanced stage of development and the free passage of liquid is restricted. The liquid is present in very small quantity and isolated areas. At this stage, if the applied stress exceeds the threshold limit of fracture stress of the material, cracking can occur. This crack cannot be filled by the remaining liquid phase present as isolated pockets. The temperature range in this stage, during which the cracking occurs, is called the critical solidification range (CSR). In stage 4, complete solidification takes place and no cracking involving the liquid phase is possible [21].

Most of the theories on solidification cracking [22-23] effectively follow the concept of the formation of a coherent interlocking solid network that is separated by continuous thin liquid films and thus ruptured by the tensile stresses as stated by Borland. If sufficient amount of liquid metal is present near the cracks, it can “backfill” and “heal” the incipient cracks. Hence, it can be said that hot cracking occurs due to synergetic effect of both mechanical and metallurgical factors. The metallurgical factors considered contributing for weld solidification cracking and liquation cracking are discussed elaborately in the forth coming sections.

### ***2.5.2 Metallurgical factors responsible for weld solidification cracking***

Metallurgical factors known to affect the solidification cracking susceptibility of weld metals are (i) the solidification temperature range, (ii) the amount and distribution of liquid at the terminal stage of solidification, (iii) the primary solidification phase, (iv) the surface tension of the grain boundary liquid, and (v) the grain structure. All these factors are either directly or indirectly affected by the weld metal composition. The first two factors are affected by micro-segregation during solidification. Micro-segregation in turn can be affected by the cooling rate during solidification [24].

The solidification of alloys requires solute atoms to be redistributed between liquid and solid as indicated by the phase diagram. In alloy systems where the partition coefficient,  $k$ , is less than one, such as 0.03, 0.13 and 0.001 for S, P and B respectively [24], the liquid phase becomes increasingly enriched in solute as the temperature decreases within the solidification temperature. This redistribution occurs by mass transport of solute atoms between liquid and solid to maintain equilibrium at the interface. This mass transport can

take place both through the liquid via mixing and in the solid by diffusion. If mass transport is constrained in the solid, liquid, or both, then solidification occurs in a non-equilibrium mode. In a microscopic weld solidification (formation of cellular and dendritic subgrains), solid diffusion is considered insignificant and liquid mixing is complete. Equilibrium exists between the solid and the liquid only at the interface. This case is described schematically in Fig.2.6. Unlike the case of equilibrium solidification, all of the solute atoms rejected by the growing solid has to be accommodated into the liquid.

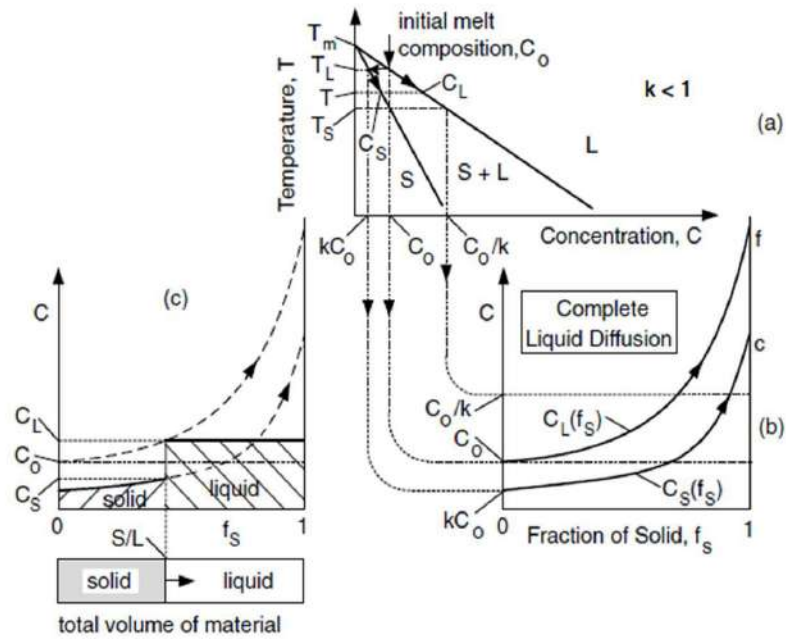


Fig.2.6 Schematic representation of micro segregation in welds (a) phase diagram of an alloy system (b) compositions of solid and liquid during solidification (c) composition profiles of solid and liquid during solidification [25]

Consequently,  $C_L$  increases more rapidly during solidification than in the case of equilibrium solidification. Since the solid grows from the liquid, its composition at the

S/L interface  $C_S$  also changes more rapidly than in the case of equilibrium solidification. When  $C_L$  rises beyond  $C_0/k$ ,  $C_S$  rises beyond  $C_0$  (Figure 2.6(b)).

The amounts of solute in the solid and liquid are represented by the two hatched areas in Figure 2.6(c), and sum of the hatched regions equals the amount of solute in the liquid before solidification. Figure 2.7 shows solute redistribution across a cell boundary at various stages for the case  $k < 1$ . Note that in all cases, the liquid composition is uniform. The composition of initial solid formed is  $kC_0$ . The solid composition gradually increases outward from the cell core and then rises rapidly at the end of solidification. In eutectic alloy systems, this may result in the formation of eutectic constituents along the subgrain boundaries

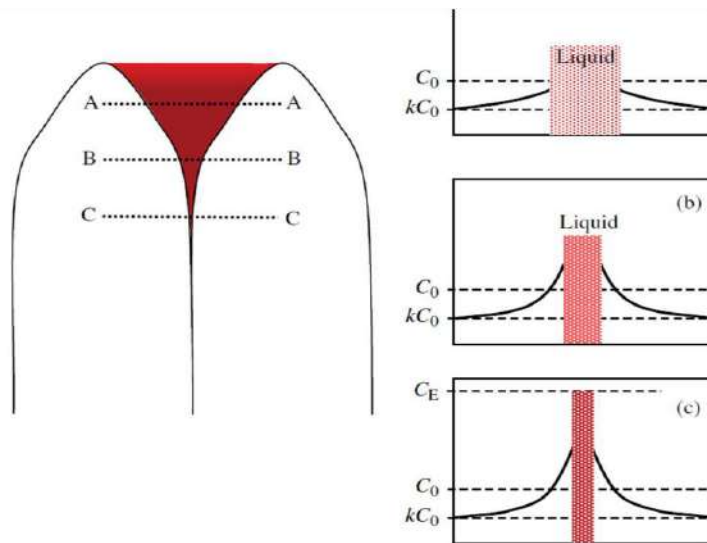


Fig.2.7 Schematic of a solute segregation during solidification of a subgrain in a weld metal [41].

(i) *Solidification temperature range*

Alloys with wide solidification ranges generally have extensive partially melted zones (PMZ) and hence are highly susceptible to solidification cracking as the PMZ is

weak and very amenable to cracking. Widening of freezing range can take place either due to the presence of impurity elements such as phosphorus and sulphur above acceptable limits or due to alloy elements such as Nb, Ti, B etc. In the case of impurity elements like sulphur and phosphorus, their segregation to grain boundaries, formation of FeS and FeP respectively and the terminal eutectic reaction contribute to solidification cracking [26]. The eutectic reactions taking place at the end of solidification generally widens the freezing range which further increases the risk of hot cracking. The effect of eutectic reactions on solidification temperature range and solidification cracking was thoroughly studied by Dupont et.al in many alloy systems such as Ni based super alloys and Nb stabilized austenitic stainless steel [27,28].

(ii) *Fraction and distribution of liquid during final solidification*

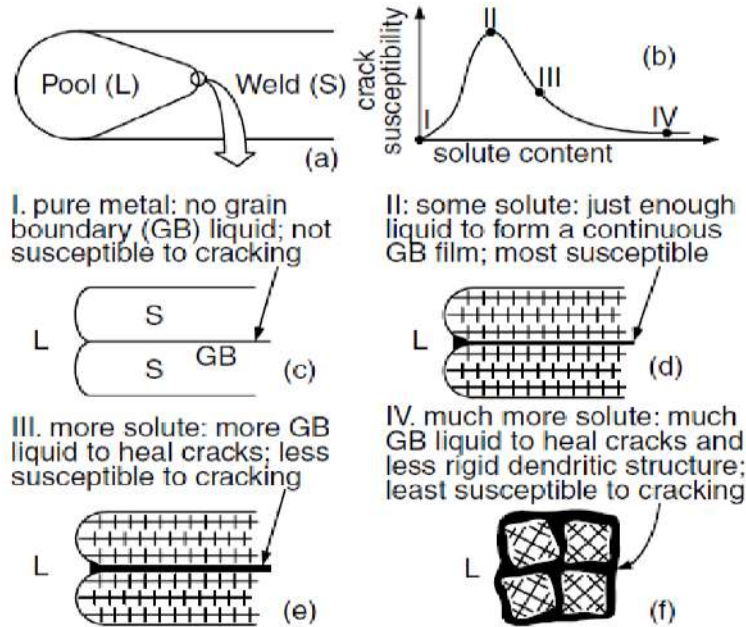


Fig.2.8 Effect of composition on crack susceptibility: (a) weld (b) crack susceptibility curve; (c) pure metal; (d) low solute; (e) more solute; (f) much more solute [49].

Several studies on the amount of liquid formed during last stages of solidification and its distribution in the as cast microstructure in many Al-Cu alloy systems is reported [29]. From these studies it is clear that the solidification cracking susceptibility is highest only at certain compositions between the pure metal and highly alloyed metal as illustrated schematically in Fig.2.8. Pure metal is resistant to solidification cracking because there are no low-melting eutectic constituents present at the grain boundaries. In highly alloyed materials, on the other hand, the fraction of eutectic liquid in the interdendritic regions can be high enough to “backfill” the solidification cracks [30]. At some points between these two composition levels the volume fraction of liquid can be just enough to form a thin and continuous grain boundary film with no extra liquid to heal the cracks. This makes the alloy highly susceptible to solidification cracking.

Though the amount of liquid formed in the solidifying weld metal is important, its distribution along the interdendritic region also contributes significantly to solidification cracking. For example, it is reported that certain Nb containing super alloys has solidification sequence  $L \rightarrow \gamma + \text{NbC} + L$  followed by  $L + \gamma + \text{NbC} \rightarrow \gamma + \text{NbC} + \text{laves eutectic}$  reaction, where the eutectic laves phase is distributed in the form of isolated pockets while the NbC eutectic is distributed in the form of continuous grain boundary films. The isolated distribution of the eutectic laves phase does not contribute to cracking; but the distribution of NbC does. Hence, the solidification ranges of such alloys have to be determined based on the temperature at which  $L \rightarrow \gamma + \text{NbC} + L$  reaction takes place [30].

(iii) *Primary solidifying phase*

The primary solidifying phase is an important criterion for determining the solidification cracking susceptibility of austenitic stainless steels and cast irons. In general during non-equilibrium solidification, the freezing range of stainless steels is extended due to the presence of impurity elements such as S and P thereby increasing the susceptibility for hot cracking. However, steels which purely solidify in primary austenitic mode are more susceptible to solidification cracking than the steels which solidify in primary ferritic mode. This is because solubility of the impurity elements like S and P are more in ferrite phase than in austenite and hence concentration of these elements in the remaining liquid metal becomes less when the first phase formed during solidification is ferrite [31-36]. Not all stainless steels, though, can be made resistant to solidification cracking by playing with mode of solidification. In stabilized 347 stainless steel, the major cause of hot cracking is the alloying element Nb itself and hence its composition is not amenable to alterations [37]. This is true also in the case of the borated stainless steel since boron has low partitioning coefficient for both austenite and delta ferrite with liquid metal, unlike S and P which have higher partitioning coefficient in delta ferrite than in austenite. Hence, boron cannot be effectively partitioned by delta ferrite even if the primary mode of solidification is ferritic.

(iv) *Wettability of the grain boundary liquid*

Wettability of the liquid is determined by both surface tension and viscosity of the liquid. If the surface tension between the solid grains and the grain boundary liquid is very low then it can be said that wettability of the liquid is high. As a consequence of this,

a liquid film will form between the grains and the solidification cracking susceptibility is increased. On the other hand, if the surface tension of the liquid is high, the liquid phase will appear as globular pockets and will not wet the grain boundaries. Such discontinuous liquid phase do not appreciably reduce the strength of the grain boundaries and therefore, are not harmful [38]. For example, FeS is present as thin films at the grain boundaries of steels while MnS is present as globules. Due to higher melting point and its globular morphology, MnS is considered to be far less harmful than FeS [39]. Effect of viscosity on wettability is indirect as it determines how a liquid flows. Viscosity is a thermo-physical property which is influenced by the composition of a liquid at a given temperature. For highly viscous liquids, the spreading time increases with increase in viscosity. This can affect the dynamic wettability of the liquid and capillary action [40]. Since the composition of liquid at the terminal stages of solidification is continuously changing due to segregation of alloying elements, viscosity and hence the wettability characteristics also vary dynamically.

(v) *Grain structure*

It is reported that a microstructure with fine equiaxed grains is often less susceptible to solidification cracking than that of coarse columnar grains [41-44], as equiaxed grains can deform to accommodate more contraction strains. That is, fine equiaxed grain structure is more ductile than columnar grain structure. Liquid feeding and healing of incipient cracks can be more effective in case of fine-grained material. In addition to this, in fine-grained material, the grain boundary area is much greater and therefore, harmful low-melting eutectics are less concentrated at the grain boundary.

It is understood that there are several factors affecting the solidification cracking susceptibility of an alloy. In order to evaluate the mechanism behind solidification cracking susceptibility of the alloy, it is important to choose appropriate method to isolate the mechanical factors from the metallurgical factors affecting the cracking.

### ***2.5.3 Mechanisms of HAZ Liquation Cracking***

As mentioned earlier in section 2.5 liquation cracks are formed as a result of grain boundary liquation in HAZ / PMZ formed in the base metal or in the previously deposited weld metal during multipass welding in the presence of shrinkage stresses. In general, two mechanisms are put forth to explain the liquation of grain boundaries, namely penetration mechanism and segregation mechanism.

#### *(i) Penetration mechanism*

The penetration mechanism requires both liquation phenomenon and grain boundary motion to occur simultaneously. Liquation can happen in a material due to enrichment of certain elements in the matrix as a result of compositional banding that occur during thermo-mechanical treatment of the base metal subsequent to ingot solidification. Liquation can also occur either in the grain interiors or grain boundaries due to the presence of second phase particle in these locations due to “constitutional liquation phenomenon” [41]. Constitutional liquation refers to melting of the interface surrounding a second phase particle due to interaction of the particle with the matrix during rapid heating as experienced during welding. As shown in Figure 2.9 [41] constitutional liquation of a particle and boundary motion occurs simultaneously.

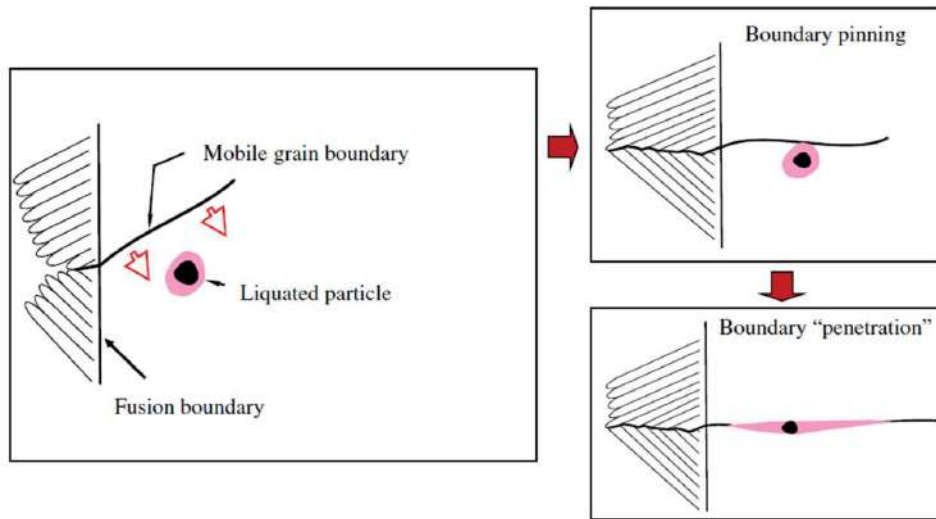


Fig.2.9 Schematic representation of penetration mechanism occurring in the HAZ of a weldment [41].

When the boundary encounters the liquated region surrounding the particle, it will be “pinned” down. Further, the liquid spread and penetrate the grain boundary in the partially melted zone depending on the amount of liquid formed, temperature profile and wettability characteristics of the grain boundary. Liquation cracking in alloy 718 is reported to occur due to constitutional liquation of NbC and penetration of the liquid along the grain boundaries of the PMZ [41].

(ii) *Segregation mechanism*

In the segregation mechanism, liquation of grain boundaries that are enriched in elements such as S, P, B, Ti, Si etc, which are known to bring down the melting temperatures, occurs in the PMZ during welding. These elements diffuse or segregate to the boundary at elevated temperature. A number of mechanisms are put forth to explain this segregation, this includes “Gibbsian” segregation, grain boundary sweeping, and pipeline diffusion. The mechanism is schematically explained in Fig.2.10 [41].

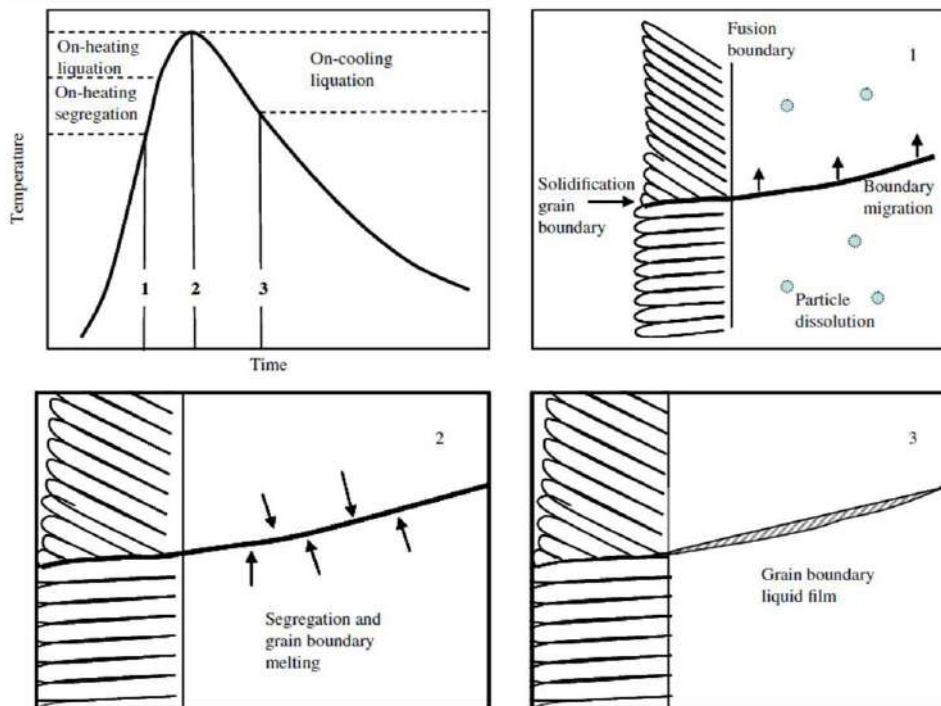


Fig.2.10 Mechanism of segregation occurring in HAZ liquation cracking [41]

In Gibbsian segregation, the segregation of impurity element such as S, P, Si to the grain boundaries occurs as the grain boundary energy is lowered as a result of accommodating these elements in to it. The enrichment of impurity elements at grain boundaries also take place as a result of dragging /sweeping of these element from the matrix by the boundaries of growing grains above homologous ( $0.5T_m$ ) temperature. This phenomenon is known as grain boundary sweeping. Yet another way by which segregation of impurity elements at grain boundary take place is by pipe diffusion along the grain boundaries. This happens because the interdendritic boundaries of weld region adjacent to the fusion line are highly segregated with alloying and impurity elements. The elements enriched along the interdendritic region of fusion zone diffuse into the grain boundaries of the PMZ as the diffusion rate is 10-100 times higher along the grain

boundaries than in the matrix. Liquation cracking in SS 304L is reported to take place due to segregation of impurity elements along the grain boundaries of HAZ [41].

In case of weld metal liquation cracking, liquation can take place either along segregated or migrated grain boundaries. Here, there is no requirement for movement of grain boundaries to cause liquation since the boundaries are already enriched with alloying element.

#### ***2.5.4 Factors influencing the liquation cracking susceptibility***

##### *(a) Composition:*

Chemical composition of base metal is the most influencing factor affecting the liquation cracking tendency of the alloy during welding. In general, controlling the level of impurity elements in the base metal is the only option available to reduce liquation cracking while welding. In case of alloys containing intentional alloying elements such as Ti, Nb, B which form precipitates like TiC, NbC or secondary precipitates and undergo constitutional liquation during welding, it is not possible to alter the composition of the alloy but to find some other solution to reduce hot cracking.

##### *(b) Grain Size*

In general, higher the grain size, higher is the susceptibility to HAZ liquation cracking. For material with coarse grain structure, grain boundary area is small and hence if liquid exists along the grain boundaries, strain localization occur over less boundary area which lead to higher stress concentration and increased cracking propensity. The increased grain boundary area resulting from a small grain size produces a stronger weld microstructure that can support the accumulated restraint on cooling. Even in the presence

of liquid films, increased boundary area helps in preventing strain localization and potential cracking.

*(c) Base Metal Heat Treatment*

Base metal heat treatment condition would be particularly important in the case of welding precipitation-strengthened materials, such as Ni-base super alloys. Welding such alloys in solution treated condition has the advantage of decreased susceptibility for cracking as the precipitates that cause constitutional liquation are not present and elements that promote cracking are already in solution. This condition also, minimizes intrinsic restraint by reducing the strength of the base material. Welding in the solution-annealed condition is also used to reduce weld solidification cracking.

*(d) Weld Heat Input and Filler Metal Selection*

Heat input during welding influence the temperature gradient in the HAZ of the weld joint. Since liquation cracking occurs over a fixed temperature range, weld heat input controls the extent to which liquation occurs. A sharp/steep temperature gradient in the HAZ (low weld heat input process) can reduce the amount of grain boundary melting in the HAZ compared to a shallow temperature gradient.

Another factor that has some effect on HAZ liquation cracking susceptibility is the strength and composition of the filler metal. Since a fraction of the restraint in the HAZ is associated with solidification shrinkage in the weld metal, lower-strength filler metals can generate less shrinkage stress that is translated to the HAZ or underlying weld metal. But this option cannot be taken at all times.

One more factor is the solidification temperature range of the filler metal which is again depended upon the chemical composition. To reduce the risk of liquation cracking in the PMZ, solidification of the weld metal should complete after the PMZ solidifies. This is because the restraint arising from shrinkage of weld metal and acting on the PMZ is substantially reduced [41].

## **2.6 Methods for evaluation of hot cracking**

Over past several years, numerous studies on weldability were carried out, various theories and mechanisms behind the hot cracking mechanisms were propounded and about 200 test techniques were developed [45]. There are weldability tests developed to assess a particular type of cracking in a specific material type. Some are developed for determining relative susceptibility of similar alloys whereas others are to predict whether or not cracking would occur in a real situation. Also, there are some tests which are primarily used for the optimization of alloy compositions and others used to develop and optimize weld procedures. There are some tests which are highly quantitative and designed to give a numerical indication of susceptibility, others tend to be go/no-go or crack/no crack types of test. Therefore, a universal test should take in to account of all the following possible variables:

1. Different alloy types, steels, aluminum alloys etc.
2. The different forms of hot cracks.
3. Weld metal cracking in autogeneous and multipass welds.
4. Base material HAZ cracking in single and multipass welds.
5. Visible and subsurface cracks.

## 6. Effects of variable strain as well as variable strain rate.

In practice, it is impossible to integrate all these variables in a single weldability test. Hence, it is up to the user to select one or combinations of tests based on the requirements. However, it is possible to broadly categorize them under two major groups: SELF RESTRAINT and EXTERNAL RESTRAINT tests.

**Self restraint tests:** These are tests in which the specimen loading occurs by stresses developed during preparation of a restrained weld joint. Self-restraint cracking tests are employed to reproduce the actual welding conditions as closely as possible in practical work. The configuration of test specimens and the related fixtures are designed to induce different restraints in the weld joint. Widely used methods includes the Houldcroft test, FISCO hot cracking test, and circular patch test etc.. Nevertheless, most self-restraint cracking tests are not suitable to reproduce cracking in materials with low cracking susceptibility. Moreover, the mechanical factors causing solidification cracking are unclear and not separated from the material factors [45].

**External restraint tests:** In these test techniques, an external augmented strain or stress is applied during welding. By this means, the effect of metallurgical factors and composition associated with solidification cracking can be distinguished from the mechanical factors. Consequently, these tests can be used for quantitative evaluation of cracking susceptibility that provides a comprehensive ranking for families of alloys. There are several types of externally loaded-cracking tests such as Varestreint test, Sigmajig test, Rapid tensile test, U-type test, hot ductility test etc.

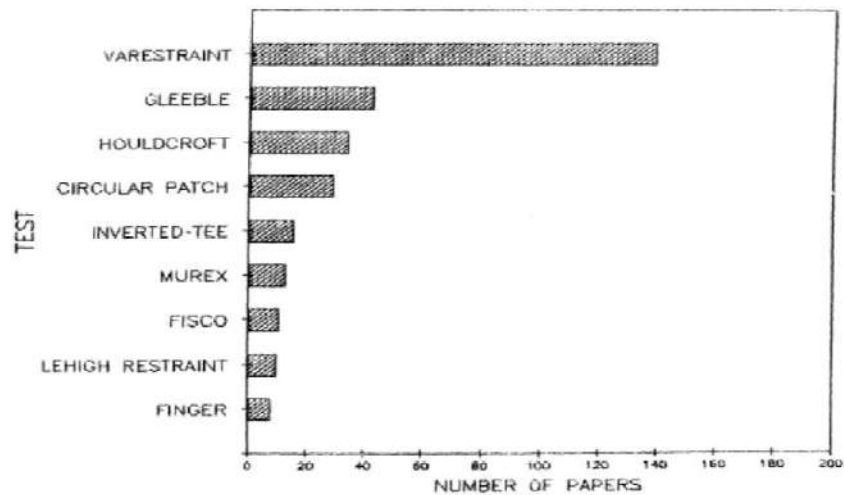


Fig.2.11 Statistics on utility of different types of hot cracking tests for weldability studies based on literature citations [45].

ISO standard 17641 gives the standardized tests for evaluating hot cracking susceptibility for an alloy [46]. The standard ISO 17641-2 is dedicated for SELF RESTRAINT hot cracking tests which includes test techniques such as T-joint, weld metal tensile and longitudinal bend. ISO 17641-3 is meant for EXTERNAL LOADED hot cracking tests which includes test techniques such as hot tensile, Varestraint and Flat tensile (PVR).

Approximately three hundred references in the available literature deal with the application of one or more hot cracking tests in their studies. Figure 2.11 shows the nine most often used tests, based on number of literature citations. The Varestraint and its modifications account for nearly half of the total [45]. Figure 2.12 further sub divides the Varestraint-type tests. Since Varestraint and hot ductility test methods are most widely used for evaluation of hot cracking tendencies. Next widely used method is “Gleeble™”

based hot ductility test method. The two methods are elaborated in the forth coming sections.

### 2.6.1 The Varestraint Test

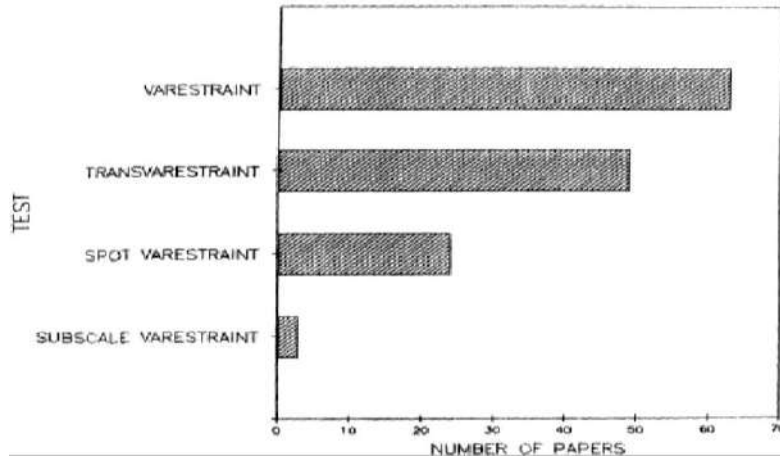


Fig.2.12 Statistics on the utility of different types of Varestraint tests for weldability studies based on citations [45].

The Variable restraint, or Varestraint test was developed in the 1960s by Savage and Lundin at Rensselaer Polytechnic Institute (RPI) [19]. Originally, it was a simple, augmented strain-type test that can isolate the metallurgical variables that cause hot cracking and now several variants are introduced and being used worldwide. The test itself has never been fully standardized and a variety of test techniques are in use today, although ISO 17641 do provide some guidance on the use of preparation of test specimens and results to be obtained from the test but there is no mention about the evaluation criteria [46]. There are three basic types of Varestraint tests, as shown in Figure 2.13. The original test was a longitudinal type, whereby bending strain is applied along the direction of the weld that is produced on the sample. This type of test produces cracking in both the fusion zone and adjacent HAZ. Since in some cases, it is desirable to

separate HAZ liquation cracking from solidification cracking, the spot and transverse tests were developed. The transverse test applies bending strain across the weld and generally restricts cracking to the fusion zone (there is little or no strain applied to the HAZ). The Transvarestraint, developed in 1971 [19], has nearly overtaken the original Varestraint test in popularity. From the frequency distribution chart shown in Fig.2.9, it can be conceived that the Varestraint test is used more frequently, is more useful than other methods and satisfies several criteria for hot cracking listed down by many researchers of this field to a large extent. Some of the test criteria given by Borland [21] are (i) Cheap and simple equipment (ii) Economical in material labor and time (iii) Direct correlation with fabrication requirement and service behavior (iv) Simple to conduct test, free from human errors (v) Capable of giving reproducible results (vi) Applicable to all welding processes and so on. By comparison of all the available hot cracking tests based on each of these criteria, it is understood that Varestraint tests has the following advantages over the other tests.

- 1 Latest version of Varestraint test setup is very compact and simple in operation.
- 2 Small size and simple geometry of the specimen used in Varestraint experiment makes it very economical method for hot crack testing
- 3 Varestraint test is capable to provide reproducible results on weldability of the material.
- 4 Varestraint tests are more sensitive to applied strain rather than small changes in welding parameter.

5 Quantitative measure of cracking sensitivity makes heat to heat or material to material comparison is very easy.

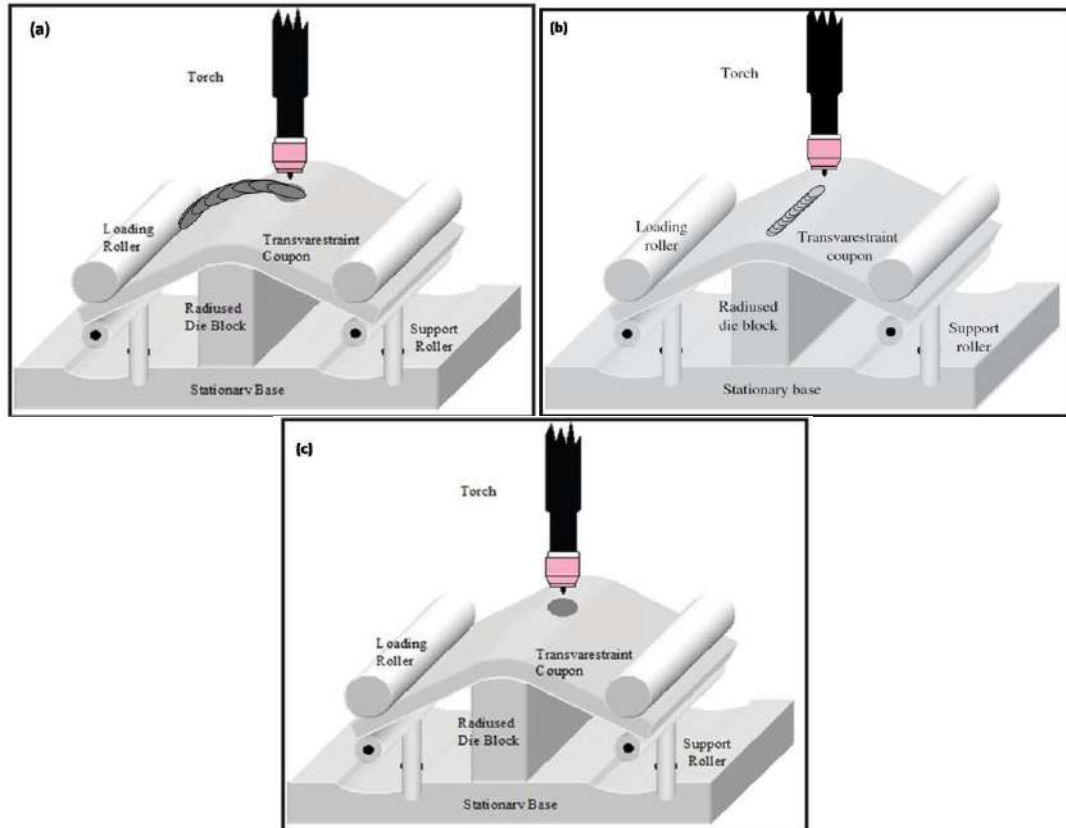


Fig.2.13 Schematic representation of different type of Varestraint tests (a) Longitudinal Varestraint test (b) Transverse Varestraint test (c) Spot Varestraint test [19].

Spot Varestraint test is an advanced version of standard Varestraint test which is generally applied to evaluate HAZ liquation cracking and ductility dip cracking and was further extended to study weld metal liquation cracking [19,47-52]. It is reported that there were some major issues with spot varestraint test. Some of them are (i) weld metal liquation cracking and DDC could not be distinguished, (ii) determination of the temperature range over which cracking occurred was difficult, and (iii) some materials only exhibited DDC at the highest achievable strain (~10%) so determining a threshold

strain was difficult. In the 1990s, Lin and Lippold at OSU developed test techniques that can quantitatively determine the crack-susceptible region (CSR) using Varestraint testing [48]. Lippold and Lin showed that double spot Varestraint tests could be effectively used to separate solidification cracks and ductility dip cracks [53]. Kikel and Parker [54] were able to compare the DDC susceptibility of filler metal Inconel52 and Alloy 690 with that of filler metals Inconel 82 and Alloy 625 using double spot Varestraint test technique in multipass 690 weldments. Double spot Varestraint test was used to compare base metal and weld metal liquation cracking susceptibility of Alloy 903 [49]. Ramriez determined liquation cracking sensitivity of IN740 using spot Varestraint and hot ductility tests [55]. Liquation cracking susceptibility of A286 steels have been determined using CSR which was determined by obtaining *on heating* and *on cooling* CSR using spot Varestraint tests [53]. Hence, there are several studies on liquation cracking susceptibility of many alloy systems using spot Varestraint test technique which show that the method is very versatile and capable for determination of weld metal liquation cracking occurring in multipass weldments.

### ***2.6.2 Hot ductility test***

The second most important technique used for evaluation of liquation cracking sensitivity of base metal is “Gleeble™” based hot ductility experiments. High temperature ductility can offer some information on a material’s weldability, since hot cracking is usually associated with an exhaustion of ductility in the material at high temperatures. In order to appropriately simulate the heating and cooling rates associated with welding, special equipment is developed to rapidly heat and cool small laboratory

scale samples. This equipment was developed by Savage and Ferguson at RPI in 1950s [56]. The machine is now produced commercially by Dynamic Systems, Inc. in Poestenkill, NY [57]. A schematic representation of test chamber in “Gleeble™” machine is shown in Fig.2.14.

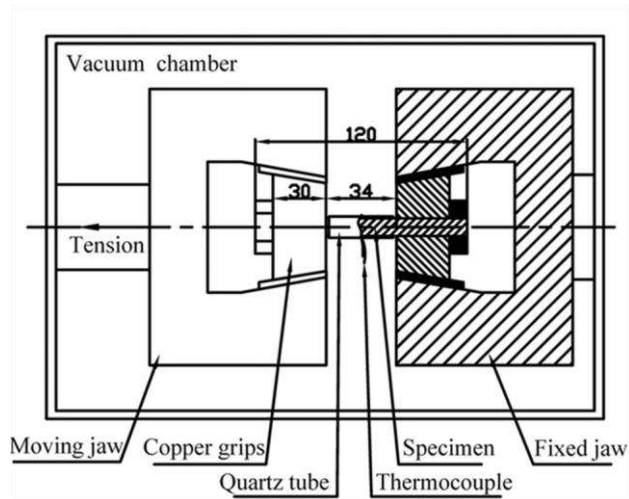


Fig.2.14 Schematic representation of vacuum chamber in which test specimen is loaded in a “Gleeble™” -1500D machine [58].

Some special features of “Gleeble™” for which the system is very popular is that it uses resistance heating ( $I^2R$ ) to heat small samples under precise temperature control and cools them by conduction through water-cooled copper grips. It also has quench systems for accelerated cooling. Heating rates up to  $10,000^\circ\text{C/s}$  are possible. The equipment is also capable of mechanically loading (either in load control or in stroke control modes) samples at any point along the programmed thermal cycle.

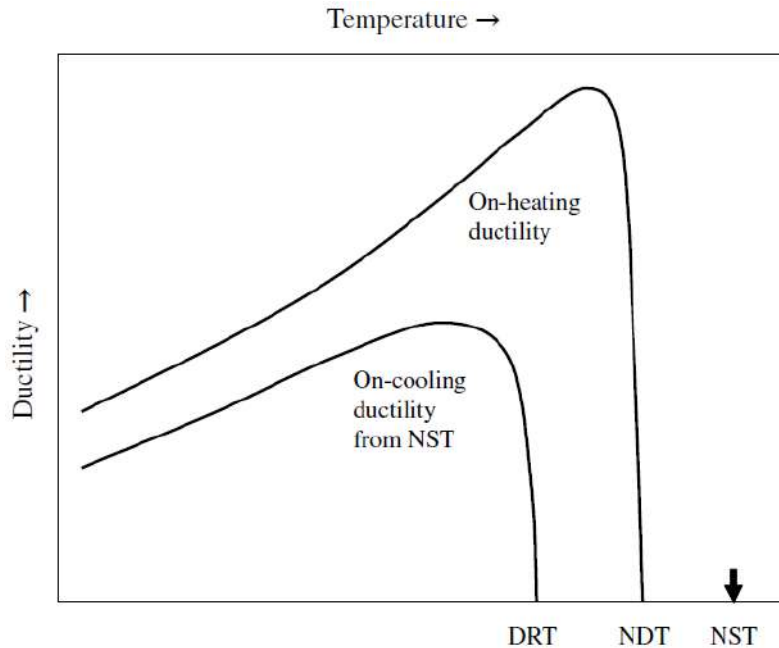


Fig.2.15 Schematic representation of hot ductility curves and locations of NDT, NST and DRT are indicated in the figure [44].

Hot ductility testing involves both “*on-heating*” and “*on-cooling*” tests which provides a unique ductility curve for a material. This curve shows several distinct features, as shown schematically in Figure 2.15. The ductility of a material increases *on heating*, followed by a sudden drop. This drop is associated with the onset of incipient grain boundary melting. The temperature at which ductility drops to zero is known as the Nil Ductility Temperature (NDT). This experiment is carried out in stroke controlled mode. The applied stroke rate is in the order of 25-50 mm/s to ensure that the test temperature is reasonably constant during application of the stroke. At NDT, the material still has measurable strength.

On further increase of temperature, the material loses its strength and the temperature at which the strength is zero is termed the Nil Strength Temperature (NST). Hence, after determining NDT, additional tests are conducted in load controlled mode at

temperatures above NDT, to determine the NST [44]. A minimum nominal load in the order of ~4 KN to grip the specimen is applied and held constant. The specimen is then continuously heated at a heating rate simulating welding thermal cycle approximately ~100-150°C/s (same as that used for determination of NDT) until it separates. The temperature at which the specimen is fractured with almost zero load (only the nominal load applied to hold the specimen) is termed as NST. In this condition failure of the specimen takes place due to complete liquation of grain boundaries.

To determine the *on-cooling* ductility curve, samples are first heated to a peak temperature almost equal to that of NST at the same heating rate employed for determining NDT or NST (without allowing to fracture) and subsequently cooled to a preset temperature and tested for remnant ductility by pulling the specimens. Tests are conducted for different specimens for different preset temperatures for fracturing the specimens by pulling (stroke control mode). The highest temperature at which measurable ductility is obtained for the specimen (~5%) is identified as the Ductility Recovery Temperature (DRT). At the DRT, liquid formed upon heating to the NST solidifies to such an extent that ductility recovers. For a material that is 100% resistant to hot cracking, DRT should be equal to NDT; but this does not happen in any of the alloy systems due to segregation induced and or constitutional liquation on heating to NST. The ductility recovery generally takes place below the *on heating* NDT [44]. The cracking susceptibility is calculated based on the difference between NST and DRT and the details are given in Chapter 3.

As in the case of Varestraint test, NDT, NST and DRT obtained from the hot ductility curves also can be used to define the CSR in the HAZ formed in the weldment. Unfortunately, there is no standardized procedure for generating hot ductility curves. ISO 17641-3 describes the for hot ductility test and the *on-heating* and *on-cooling* behavior but does not provide specifications on how the curves are generated and the assessment criteria.

Hot ductility and hot cracking behavior of modified 316 stainless steel evaluated by Lundin et al showed that the new “Gleeble<sup>TM</sup>” hot ductility criterion, Ratio of Ductility Recovery (RDR) - a measure of how fast the ductility recover on cooling as compared to its decrease on heating, shows a very good correlation with the Varestraint hot cracking test. The RDR criterion can be used to predict base metal HAZ hot cracking behavior [59]. There are several studies on phenomenon of hot cracking reported by many researchers which proved that hot ductility experiments produce reliable results from which the mechanism of cracking can be evaluated [60-63]. Hot cracking susceptibility of boron added 304 SS evaluated using hot ductility and varestraint tests by Shinoda et al showed that the NDR for steel containing 0.2 wt.% boron is higher than that containing greater than 0.6 wt.% B [6] .

## **2.7 Weldability of borated stainless steel**

The welding behavior of borated stainless steels is not extensively evaluated, although there were some investigations on the welding response of Grade B materials. From the studies carried out on experimental GTA welds fabricated using ER309L filler wires, weldability of SS 304B4 is reported to be good and comparable to other austenitic

stainless steels. However, EB welding of SS 304B4 produced several defects such as lack of fusion and porosities in the welds [8]. A few studies were carried out on the weldability of boron steels by the Nuclear Power Research Committee of the Japan Welding Engineering Society from 1964 to 1965. In this study Fisco weld cracking test was conducted and it is reported that borated stainless steel base metals containing 1.6 and 2 wt.% B can be welded without hot cracking by meticulously selecting proper welding procedure [64,65]. Ito and Ishii showed that for autogenous TIG welded 18Cr-15Ni steels containing different levels of boron up to 1.6 wt.% , cracking susceptibility is highest at 0.3wt.% boron and cracking did not occur when the boron content exceeded 0.5 wt.% though the amount of boron eutectic increased with increasing boron content [66]. Prozorovskii and Petrov reported that in autogenous TIG welds of 19Cr-12Ni steels containing up to 2 wt.% boron, hot cracking occurred only at boron contents of ~0.35 wt.%. [67]. However, using Varestraint and hot ductility test methods, Shinoda et.al studied the hot cracking susceptibility of AISI 304 stainless steels with boron varying from 0.2 to 1 wt.% and showed that susceptibility to cracking is greatest for the lowest boron addition, and it decreases on increasing the boron content up to ~0.5%. This study also showed that low phosphorus and sulphur contents result in lower cracking susceptibility. Shinoda et al., also showed that the cracking resistance of the higher boron steels results from eutectic healing of the cracks by backfilling [6]. Spalaris and Weyers reported on fabrication of control rods for nuclear reactors from conventional ingot processed 18Cr-12Ni-2B stainless steel which required special weld junction geometries to overcome cracking problems [68]. King and Wilkinson evaluated the welding behavior

and impact properties of 18Cr-10Ni-0.8B (essentially Grade B) steel weld joints [69] and Harrison et al. [70], discussed the general fabrication characteristics of borated stainless and showed that the steels can be readily fabricated. The results shown by King and Wilkinson were in agreement with early work by Prozorovskii and Petrov, and Shinoda with respect to eutectic back filling of hot cracks in borated stainless steels with higher boron contents. In an investigation of the behavior of Grade A alloys, Robino and Cieslak used differential thermal analysis to determine the melting and solidification temperatures and observed that the alloys solidify as irregular eutectics in a manner similar to Fe-C and Al-Si alloys. Their results revealed a decreasing solidification temperature range as a function of the increasing boron content [ $\sim 200^{\circ}\text{C}$  ( $392^{\circ}\text{F}$ ) for a 0.2 wt.% B alloy down to  $60^{\circ}\text{C}$  ( $140^{\circ}\text{F}$ ) for a 1.5 wt.% B alloy][9].

It is reported that during fabrication of neutron shield for prototype fast breeder reactor (PFBR), several numbers of trial coupons welded using 10 different variants showed fissures and cracks in the weld. However, a special grade  $\sim 1$  wt.% boron containing welding consumable was specifically developed for welding of borated steel components of IHX [4]. The welds produced using this electrode is expected to have very poor impact toughness but still were accepted as there is no requirement of impact properties for the SS 304B4 grade B steel as per ASTM A887 and the component fabricated is not a pressure boundary and hence meets the requirements of the codes. As of now there are only limited studies carried out on SS 304B4 weld joints made using borated electrode.

## **2.8 Research gaps in weldability study of borated stainless steel**

The commonality between all the researches carried out to evaluate weldability of borated stainless steels by various authors in the past is that most of them were performed on fusion zones produced autogenously on borated stainless steel base metals; only a few on weld joints. In practice, most of the components are fabricated using welding processes which involve filler additions. In this aspect, it is to be noted that the information available in literature on weldability of borated stainless steel is far from complete. In case where studies on weld joints are reported, simple butt welds were fabricated using 10-15 mm thick plates and standard E309 or E308 electrodes or filler metal in a laboratory for evaluation of mechanical properties. Even while addressing these results, there is not a single study in the present literature which focuses on the base metal dilution issues in the austenitic weld metal; either pertaining to weld metal mechanical properties or weldability aspects. It is to be reiterated that there is a clear demarcation on upper and lower limits (0.5-2wt.%) of boron content in stainless steel based on ease of welding. Base metal dilution in austenitic weld metals produced using E308/E309 electrodes while welding can result in boron concentrations in the range 0.2-0.5 wt.% in the weld metal which makes it highly susceptible for hot cracking. These aspects which are likely to be encountered during actual welding of borated stainless steels using standard and recommended austenitic electrodes are rather not covered adequately in the open literature. It is to be noted that base metal dilution of the weld metal which finally affects the weld metal composition can make the weld metal vulnerable for hot cracking. This is an important and relevant issue which can cause weld

metal cracking during fabrication of thick section components. However, little information is available in the open literature.

Boron added electrodes are available as special purpose electrodes which are potential candidates for welding borated stainless steel, although they are not classified in any codes or standards. At present, no studies on boron added electrodes for welding borated stainless steels are reported so far. Evaluation of weldability of these electrodes is indeed necessary to increase its utility for appropriate applications.

From the view point of weldability testing carried out on borated stainless steels, it is found that the different hot cracking susceptibility tests such as Varestraint, hot ductility, FISCO tests were used to evaluate the susceptibility of the steel independently. Back filling of the cracks formed by large volume of eutectic liquid present in the final stages of solidification is the major reason attributed to relatively good resistance of certain grades of borated stainless steels. However, the way in which the phenomena of back filling would be reflected in the results of various hot cracking tests is not addressed in the literature. It is expected that for a material in which back filling of the hot crack is an important mechanism of healing of crack, results of hot ductility tests using “Gleeble<sup>TM</sup>” may indicate that material highly susceptible; but this would not be the case for the results from a Varestraint test. However, no such comparative study is reported in literature to best of our knowledge.

## 2.9 Scope of the Thesis

From the literature available on borated stainless steels, it is found that most of the work reported on the weldability is confined to tests conducted on the base metal. However, welding of this steel is normally carried out using welding consumables like ER 309/308 which do not contain boron and susceptibility of the weld joint as a whole to hot cracking is not reported. Hence, in the present work solidification and liquation cracking susceptibilities of 304B4 weld joint prepared using E309 electrode are investigated along with that of base metal. Transvarestraint and spot Vareststraint tests were conducted to assess the susceptibility to hot cracking while hot ductility was assessed using “Gleeble<sup>TM</sup>” thermomechanical simulator. Further, it is found that there is no detailed microstructural characterization of the different zones (HAZ, Un-mixed zone, partially melted zone, dilution zone etc.) of the weld joints of this steel reported in literature. Therefore, an extensive study on the microchemistry of borides and microstructure of the weld joints also forms part of the current work. As use of special electrodes containing boron is also reported for fabrication of borated steel, evaluation of the cracking susceptibility of the weld joints made by these electrodes and their microstructural characterization are also included in the study. Based on the results obtained from the above mentioned studies, development of an alternate procedure for welding SS 304B4 using E309 electrode which is likely to reduce cracking during fabrication of components using SS 304B4 is also included in the scope of the present work.

# **CHAPTER 3**

## **MATERIALS AND EXPERIMENTAL DETAILS**

### **3.1 Introduction**

In this chapter details of materials and procedures followed for preparation of weld pads are described. Hot cracking experiments such as Vareststraint tests and hot ductility tests carried out are explained in detail with the aid of figures and pictures. Details of specimen preparation techniques used for metallography and subsequent characterization of eutectic borides are given along with details of different characterizations tools employed for microstructural analysis.

### **3.2 Materials**

AISI 304B4 SS grade B borated stainless steel plates of 12 mm thick and sheets of 3 mm thick with boron (B) specified in the range of 1.24 - 1.3 wt.% are the base materials used in the present investigation. Compositions of SS 304B4 plate and sheet used in this study are given in Table 3.1. These two heats are produced by ingot metallurgy route and subsequently hot rolled at 950-1150°C followed by solution annealing. Both the sheets and the plates were supplied by M/s.MIDHANI, Hyderabad, India.

Chemical compositions of standard undiluted E309 and non-standard E308BRN (boron added) Shielded Metal Arc Welding (SMAW) weld metal analyzed by Optical Emission Spectroscopy as per procedure specified by AWS A5.4 [71] are given in Table 3.2.

Table 3.1 Chemical composition of 304B4 SS base metal used in the study in wt.%

Elements	C	Cr	Ni	Mn	Si	P	S	N	B	Fe
ASTM A887 specification	0.08 max	18-20	12-15	2 max	0.75 max	0.045 max	0.03 Max	0.01 max	1-1.24	Balance
3mm thick Plate	0.06	17.7	13.75	1.70	0.55	0.018	0.004	0.014	1.30*	Balance
12 mm thick plate	0.02	18.05	12.29	1.7	0.55	0.027	0.0002	0.02	1.24	Balance

\* Boron content is slightly higher than that specified in the standard.

Table 3.2 Chemical compositions in wt.% of undiluted weld metal of E309 and E308BRN electrodes used in the present study.

Elements	C	Cr	Ni	Mo	Mn	Si	P	S	Cu	B	Fe
E309 AWS A5.4	0.15 max	22-25	12-14	0.75 max	0.5-2.5	1 max	0.04 max	0.03 max	0.75 max	-	Balance
E309	0.15	23	18	0.75	2	1	0.04	0.03	0.75	-	Balance
E308BRN	0.06	18.2	9.18	0.039	1.84	0.92	0.029	0.005	0.072	0.97	Balance

### 3.3 Procedures for weld pad fabrication

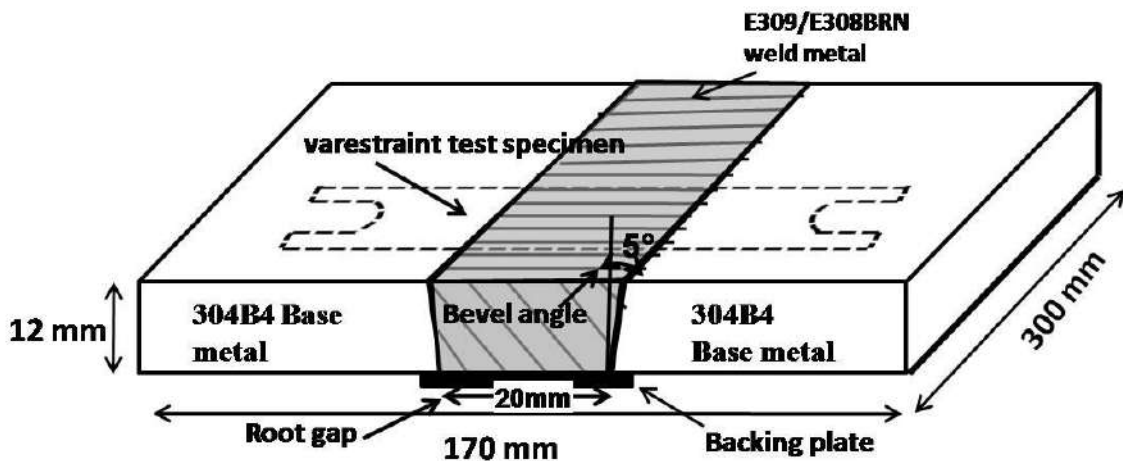


Fig.3.1 Schematic figure of weld joint prepared using E309 and 308BRN from which Varestraint specimens were extracted

AISI 304B4 SS weld pads of size 300x150x12 mm were fabricated using standard E309 and non standard E308BRN electrodes by SMAW process to extract Varestraint test specimens used for hot crack testing. The groove angle for the weld pads was limited to less than 5° and a root gap of 20 mm was maintained as shown in the Fig.3.1. Multipass welding was carried out using plain 304 SS backing plate while using E309 electrode and 304B4 SS backing plate in case of E308BRN electrode. Backing plates were necessary while welding these weld pads owing to large root gap between the plates. These weld pads were specifically designed in this way to extract Varestraint test specimens with sufficient width of weld metal which is more or less uniform across the thickness of the specimens so that hot cracking susceptibility of different parts of the weld joints can be evaluated using these specimens.

Table 3.3 Welding parameters used for weld pad fabrication using E309 and E308BRN electrode using SMAW process

Position	1G	1G
Polarity	DCEP	DCEP
Current	125 A	110 A
Voltage	25 V	20-25 V
Speed	1.6 mm/s	1.6 mm/s
Electrode	309	E308BRN
Electrode $\phi$	4mm	4mm

Welding parameters used for weld pad fabrication are listed in Table 3.3. The welds were examined by X-ray radiography as per the requirement of ASME section IX [72] to confirm that the welds are acceptable as per the ASME code.

### 3.4 Hot cracking test procedures

#### 3.4.1 Varestraint test specimens

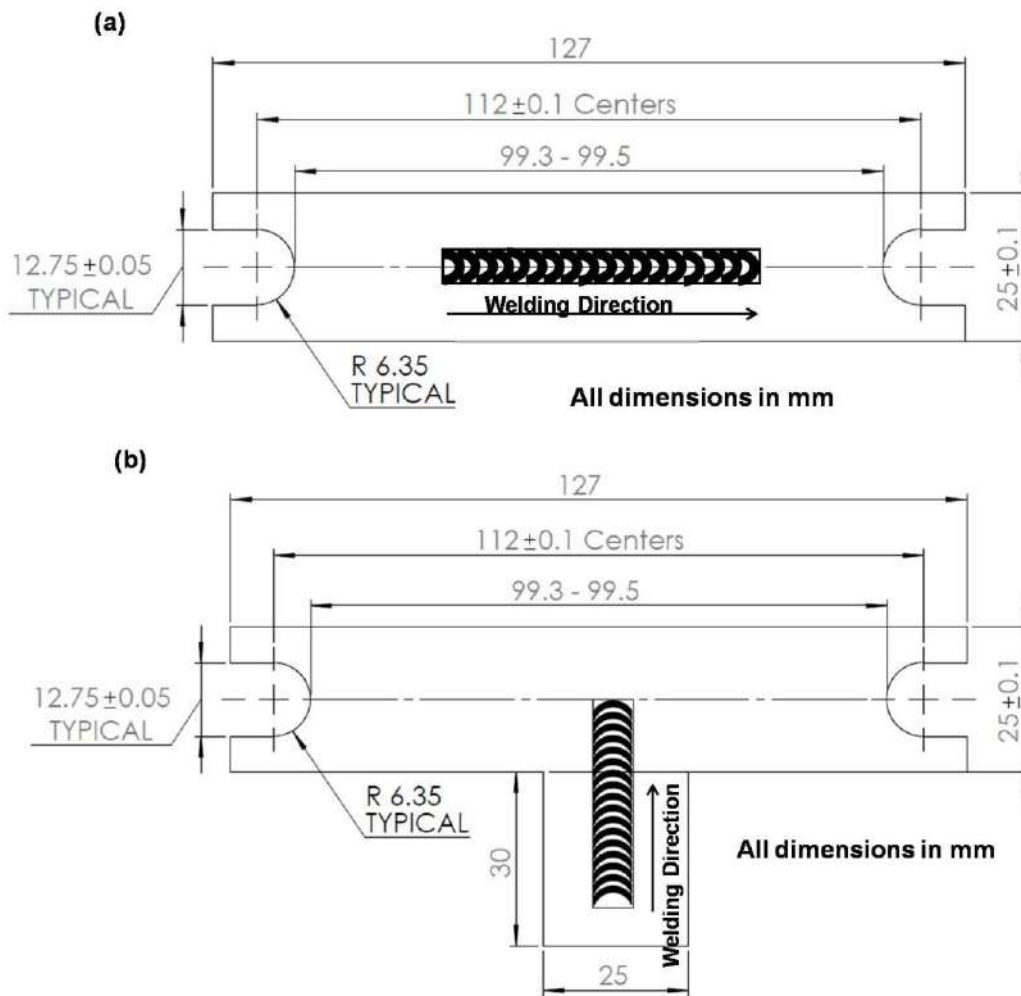


Fig.3.2 Schematic of (a) Longitudinal Varestraint test specimen (b) Transverse Varestraint Test specimen

Specimens of dimensions 127 x 25 x 3 mm were used for lab scale Varestraint tests.

Fig.3.2 shows the dimensions of the specimens used in this study.

### 3.4.2 Varestraint test procedure

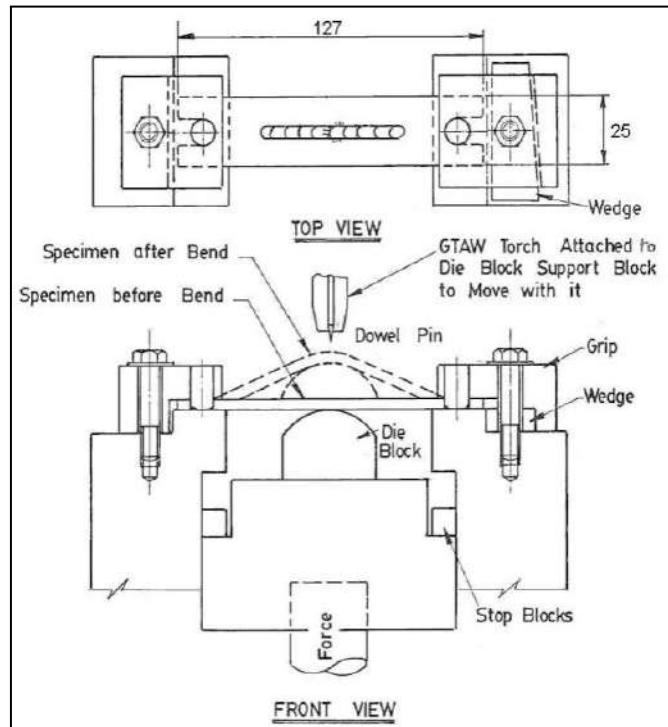


Fig.3.3 Schematic of Varestraint test set up used for hot cracking experiments [26].

Varestraint test is a simple external restraint test technique used for quantitative evaluation of hot cracking susceptibility of a material by application of bending strain. Varestraint test in this study was conducted as per ISO 17641-3 guide lines. Varestraint test facility used is illustrated schematically as shown in Fig.3.3.

The equipment consists of (1) a die block mounted on a pneumatically controlled cylinder (2) a clamp that holds specimen intact (3) Tungsten Inert Gas (TIG) welding torch connected to the TIG welding Power Source and whose motion is controlled by a variable speed motor, (4) proximity sensors to actuate the dynamic setup of the test. The specimen is placed on the anvil and locked in position by bolts. A die block of known radius of curvature is suitably mounted on the pneumatic ram just below the specimen.

Once the welding starts, the arc travels along the length from one end of the specimen towards the center at a preset speed. When it reaches the center, the pneumatic ram is automatically actuated so that the die block is plunged on to the specimen thereby straining the specimen and solidifying weld puddle. The die block movement occurs in 15 milliseconds so as to ensure that the specimen is strained while the weld is solidifying. This produces cracks along the instantaneous solid – liquid interface formed during melting of the specimen. The extent of cracking in the specimen depends on the susceptibility of the alloy to hot cracking. Depending on the strain to be imparted on the specimen, die blocks with different radius of curvature can be chosen. The vareststraint test can be conducted in three configurations (i) Longitudinal Vareststraint Test (LVT) (ii) Transverse Vareststraint Test (TVT) (iii) Spot Vareststraint Test (SVT). All these three types of tests can be executed in the same facility by varying settings of the machine. In LVT configuration, the direction of welding is along the length of the specimen as shown in Fig.2.13(a) in Chapter 2. In TVT configuration, the direction of welding is along the width of the specimen shown in Fig.2.13(b) in Chapter 2. In SVT mode, spot weld is produced by striking an arc and holding it at the same location using GTAW process for 40 seconds, allowing the thermal conditions in the spot to approach a steady state thereby allowing the weld pool diameter to stabilize [50]. At the end of this period, the arc is extinguished, the ram actuated so that the die block impinges on the specimen forcing it deform and conform to the die block. The augmented strain experienced by the specimen can be found using the relation  $\varepsilon \approx t/(2R+t)$ , where  $\varepsilon$  is the strain on the outer fiber,  $t$  is the specimen thickness and  $R$  is the radius of the die block. Five different die blocks

having radius of 640, 320, 160, 80 and 40 mm were used to obtain augmented strains of 0.25, 0.5, 1, 2 and 4%, respectively. The parameters used for LVT, TVT and SVT in the present study are given in Table 3.4. LVT is the original and primary method of vareststraint test, where both fusion zone and heat affected zone (HAZ)/partially melted zone (PMZ) are subjected to deformation. TVT is an advanced method of vareststraint test where exclusively fusion zone is subjected to strain for evaluation of solidification cracking susceptibility. SVT is also an improvement over LVT, using which HAZ/PMZ liquation cracking as well as ductility dip cracking can be determined in multipass welds.

Table 3.4 Welding parameters used during Transverse, Longitudinal and Spot Vareststraint test

<b>Parameters</b>	<b>Transverse/Longitudinal Vareststraint Test</b>	<b>Spot vareststraint test</b>
Position	1G	1G
Polarity	DCEN	DCEN
Current	80A	40 A
Voltage	10 V	10 V
Speed	4mm/s	-
Hold time	-	40 sec
Arc Length	1.6 mm	1.6 mm
Argon Shielding Gas	12 liters / min	12 liters / min
Augmented strain	0.25, 0.5, 1.0, 2.0 & 4.0 %	0.25, 0.5, 1.0, 2.0 & 4.0 %

(i) Crack length measurements:

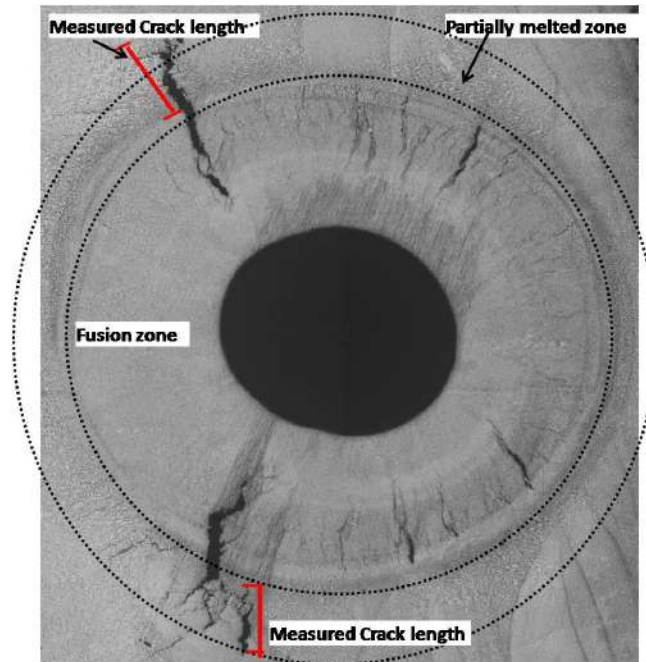


Fig.3.4 Macrostructure of spot Varestraint tested specimen showing the fusion zone and partially melted zone. Cracks that are considered for calculation of TCL and MCL are marked.

The crack lengths were measured directly on hot crack tested specimens using a stereo-microscope at 60× magnification. The hot cracking assessment parameters obtained from the test are: (i) Total Crack Length (TCL sum of the lengths of both fusion zone and HAZ cracks); (ii) Cracking Threshold ( $\epsilon$ )- minimum augmented strain at which cracks observed on the specimen (iii) Maximum Crack Length (MCL-longest crack among all the cracks). From the measured MCL, Brittleness Temperature Range (BTR) - which is an important measure of solidification cracking susceptibility is estimated using the cooling curve (Temperature vs Time) and speed of the welding.

In LVT, cracks present within the fusion zone and HAZ are considered for determining TCL. The TCL and cracking threshold strain ( $\epsilon$ ) are considered the most important measure for evaluation of hot cracking tendency [24, 26]. In the present study, in certain cases where there were no measurable number of cracks on the specimens after LVT, TCL was calculated using the crack lengths obtained from TVT specimens and threshold strain was identified from plots of TCL vs % augmented strain. The Vareststraint experiments to evaluate solidification and liquation cracking susceptibility in this study were designed as per the cases described in Table 3.5. In the TVT, the maximum crack length (MCL) and BTR are used for assessment of solidification cracking. In SVT method, the cracks formed in the HAZ/PMZ (Fig.3.4) are only considered for evaluation of liquation cracking susceptibility and the cracks present within the fusion zone are not considered. Crack length data is represented as a plot of average TCL vs % augmented strain. Average TCL is calculated from TCL values obtained from three specimens.

*(ii) BTR estimation:*

BTR of solidifying weld was evaluated by plunging a C-type (W-5%Re/W-26%Re) thermocouple in the solidifying weld puddle. Voltage-time data was collected using HP data logger model 34970A connected to the thermocouples. Temperature – time plots computed from voltage –time data was used to obtain the thermal profile of the weld. The temperature - time of the cooling curve can be converted into a temperature Vs distance using the relationship of distance = speed x time, the assumption here is that rate of solidification is equal to the welding speed at the center of the weld [25]. The crack length is mapped on to this temperature field as a function of distance from the molten

zone. The difference between the temperatures at the two ends of the longest crack gives the brittleness temperature range (BTR). A schematic representation of procedure for determination of BTR is given in Fig.3.5.

Table 3.5 Summary of Vareststraint experiments designed in this study.

Case No:	Type of tests	Cracking in Fusion zone	Cracking in HAZ/PMZ	Remarks
1	LVT	✓	✗	May be susceptible to solidification cracking
	TVT	✓	✗	Susceptible to solidification cracking
	SVT	-	-	Further investigation on liquation cracking using SVT is not required
2	LVT	✗	✓	Susceptible for liquation cracking
	TVT	✓	✓	More susceptible for liquation cracking than solidification cracking
		✗	✓	
SVT	-	✓	Further investigation on liquation cracking using SVT is required	
3	LVT	✗	✗	May not be susceptible for hot cracking
	TVT	✓	✗	Susceptible for solidification cracking
	SVT	-	-	Further investigation on liquation cracking using SVT is not required
4	LVT	✓	✓	May be susceptible for both solidification and liquation cracking
	TVT	✓	✗	Susceptible for both solidification and liquation cracking
		✓	✓	
SVT	-	✓	Further investigation on liquation cracking using SVT is required	

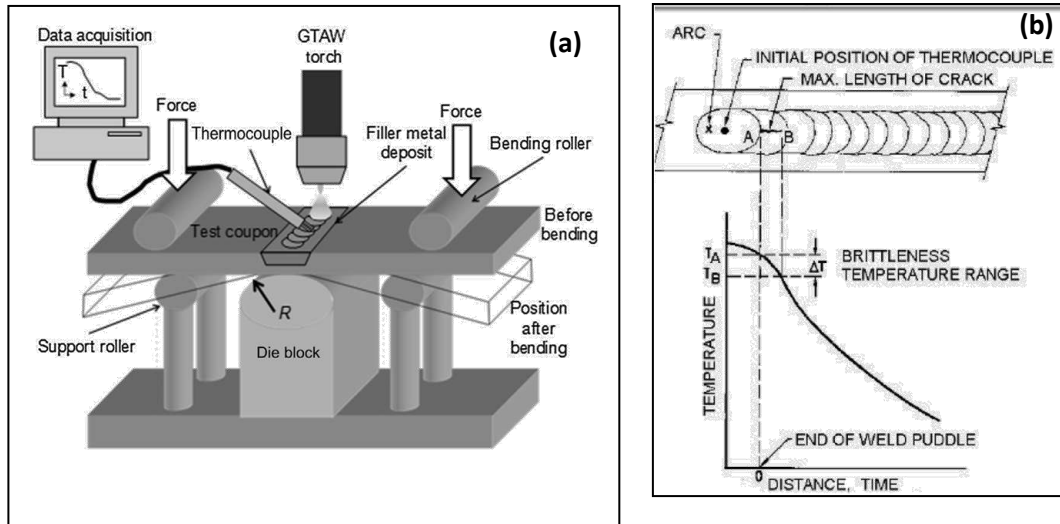


Fig.3.5 Schematic representation of procedure involved during BTR determination (a) acquiring weld thermal profile (b) Determination of BTR [24]

For BTR evaluation of PMZ, maximum crack length is obtained from the spot V restraint test conducted. However, to obtain variation of the peak temperatures with distance in the HAZs of the solidifying spot weld, a separate spot weld was made using same type of specimens used for spot V restraint testing. During the arcing time of this weld, the temperatures were recorded using three C-type thermocouples of 0.2 mm diameter percussion welded to the specimen around the spot weld area at an interval of 0.5 mm and connected to the data logger (HP data logger model 34970A). This spot weld was made at the predetermined distance from the welded thermocouples using same parameters as used for actual spot V restraint tests. Voltage-time data was collected using the data logger was converted to Temperature – time plots from which peak temperatures experienced at 0.5 mm distance in the HAZs were estimated. Thus, the temperature gradient ( $G_T$ ) in the HAZ of spot weld was determined for the test conditions. BTR for each of the test condition is obtained using the equations (1) and (2)

$$BTR = T_L - T_P \quad (1)$$

$$T_P = MCL * G_T \quad (2) [48]$$

Where,  $T_L$  is taken as on cooling liquidus temperature of 304B4 SS obtained from differential scanning calorimetry studies (described in section 3.5 in this Chapter).

### 3.4.3 Hot Ductility Experiments

Hot ductility tests:

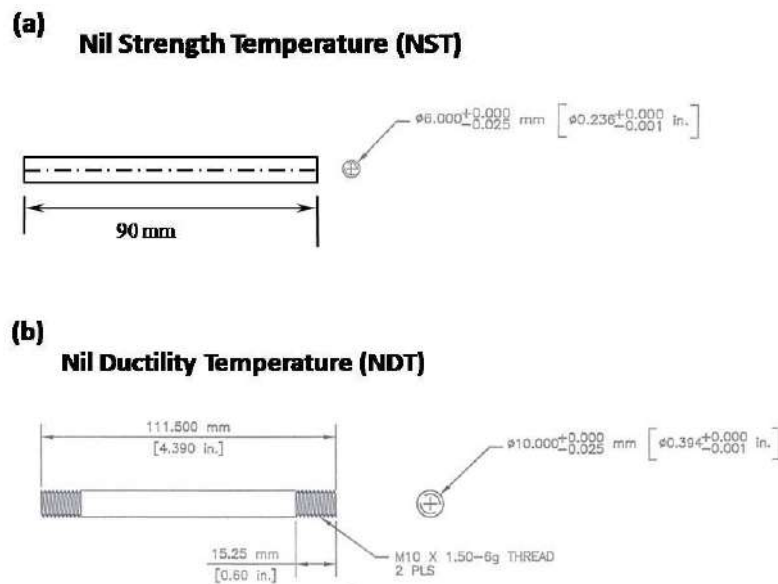


Fig.3.6 Sketches and dimensions of specimens used for hot ductility experiments (a) determination of Nil Strength Temperature (NST) (b) determination of Nil Ductility Temperature (NDT) and Ductility Recovery Temperature (DRT).

Hot ductility experiments were carried out on 304B4 SS base metal and partially melted 304B4 specimens using “Gleeble<sup>TM</sup>” thermo-mechanical simulator. Different types of specimens used in hot ductility experiments are as shown in Fig.3.6. Specimen dimensions are different for those used for determining Nil Strength Temperature (NST) and those used for determining Nil Ductility Temperature (NDT) and Ductility Recovery Temperature (DRT). In case of base metal, specimens extracted from 12 mm thick plate

were directly used for hot ductility experiments. Whereas, to determine the hot ductility of re-melted specimens, partial melting of SS 304B4 was achieved in the base metal specimens and then these specimens were used for the hot ductility experiment. For this, NST of base metal was first determined. At NST, strength is negligible because the temperature lies around the solidus temperature of the alloy where there is complete grain boundary melting in the specimen.

*(a) Determination of NST*

Thermal cycle employed to determine NST is shown in Fig.3.7(a). In the NST experiments, the specimens were gripped in a thermomechanical simulator and the experiment was conducted in load controlled mode with a nominal load of 4 kN (required to maintain the grip on the specimen during weld thermal cycle) and heated at 100°C/s, till fracture. The temperature at which fracture occurred is the NST. Three specimens were tested under the same conditions to ensure repeatability of the NST values.

*(b) Determination of NDT*

For determination of *on heating* NDT and *on cooling* DRT of base metal, specimens of 111 mm length and 10 mm diameter as shown in Fig.3.6(b), fabricated from base metal were used. NDT experiments were carried out in stroke controlled mode by pulling the specimens at the rate of 50 mm/s after the specimen reached the test temperature. The specimens were heated at the rate of 100°C/s (same as that used for the NST experiments). Tests for determination of NDT were started with peak temperature of simulation lower than NST. This peak temperature was varied in steps until the minimum

temperature at which percentage reduction in area (%RA) of the tested specimen was found to be zero.

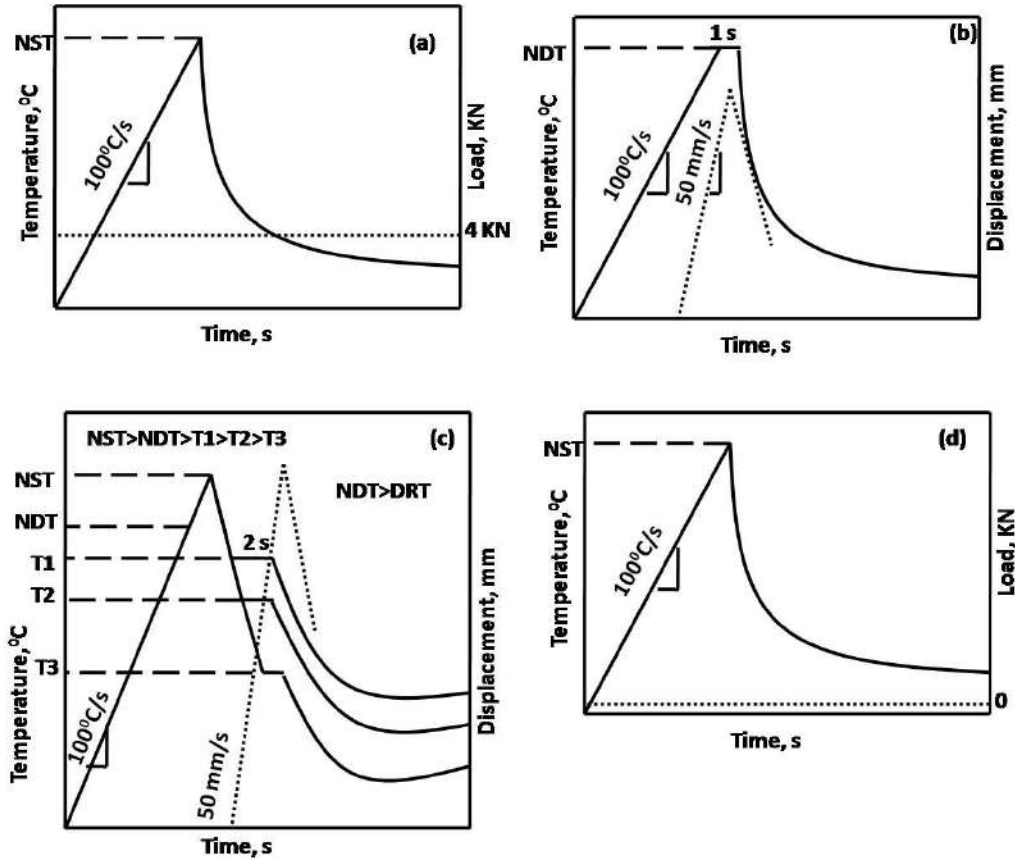


Fig.3.7 Schematic representation of load and temperature cycle experienced by 304B4 specimens during hot ductility experiments thermal cycle for (a) NST (b) NDT (c) DRT (d) Partial melting in hot ductility specimens.

For example, the first test temperature chosen was  $100^{\circ}\text{C}$  lower than NST (NST- $100^{\circ}\text{C}$ ) and it was found that %RA is  $\sim 30$  for tested specimen, then the subsequent test was conducted at a temperature  $50^{\circ}\text{C}$  below NST (NST- $50^{\circ}\text{C}$ ). The % RA for that sample after the test was found to be 0. Hence, the next specimen was tested at a temperature, NST- $60^{\circ}\text{C}$ . For that specimen, % RA was found to be  $\sim 10\%$ . By this mode, the minimum temperature, NDT at which %RA  $\sim 0$  was finally arrived. The thermal cycle and load

experienced by the specimen during *on heating* NDT experiment is explained schematically in Fig.3.7(b).

*(c) Determination of DRT*

*On cooling* DRT of the specimens is determined by cooling the specimen after it is heated up to NST at 100°C/s and then continuing the thermal cycle by switching over from heating to cooling. In the cooling part of the cycle, the specimens were cooled down to the desired test temperature at 40°C/s (closely simulating actual cooling rate experienced at PMZ/HAZ of the weld when cooling from the peak temperature). Consequently, the specimen was held there for 2 seconds for stabilization of temperature and rapidly pulled to failure at 50 mm/s. The thermal and load cycle experienced by the specimen during the *on cooling* experiments is schematically represented in Fig.3.7(c). The experiment was repeated for different temperatures (below *on heating* NDT) after cooling from NST and the maximum temperature at which the ductility is found to be ~ 5% is determined as DRT. In this way, the DRT for base metal specimens was determined. The susceptibility for hot cracking is based on the difference between NST and DRT which is termed as Nil Ductility Range (NDR). Cracking susceptibility is considered to be high for alloys with NDR greater than 50°C. Using NDR, % Cracking Factor (%CF) is calculated using equation (3) given below.

$$(\text{CF})\% = \frac{\text{NST} - \text{DRT}}{\text{NDT}} \times 100 \quad (3) [73]$$

*(d) Partial melting in hot ductility test specimens*

Partial melting in base metal specimens was accomplished by subjecting them to the same heating cycle employed for estimating NST and cooling down to room

temperature without application of any load (Fig.3.7(d)). Partial melting was accomplished separately in specimens used for determination of NST (Fig. 3.6(a)) and in those for determination of NDT and DRT (Fig. 3.6(b)) as well.

The procedure followed for evaluation of hot ductility behavior of base metal specimens viz, first determination of Nil Strength Temperature (NST), then, *on heating* Nil-Ductility-Temperature (NDT) and finally, the Ductility Recovery Temperature (DRT) were also applied to the specimens subjected to partial melting. Following hot ductility tests, Nil Ductility Range (NDR) and %CF were determined for partially melted specimens as described above for the base metal.

### **3.5 Differential scanning calorimetry (DSC) experiments**

DSC experiments were conducted to obtain temperatures of various phase transformations that occur upon heating and cooling. In this experiment a constant heating and cooling rate was maintained while acquiring the heat flow between reference and sample crucibles during the thermal cycles to interpret phase transformations in the specimen. A phase transformation will appear as upward (exothermic) or downward (endothermic) peak in the DSC output (voltage) versus temperature curves. DSC experiments involving heating and cooling cycle at a slow scan rate of  $10 \text{ K min}^{-1}$  were performed, up to the melting point on specimens extracted from the base metal and autogenous weld bead deposited on the base metal using GTA welding process. The slowest scan rate possible with the equipment was used so that results obtained can be considered close to those expected from equilibrium transformations.

### **3.6 Metallography**

Metallography specimens were sectioned from selected tested samples using abrasive cutting wheel. These specimens were then ground with standard emery papers and polished using clothes impregnated with diamond particles, up to one micron surface finish for metallographic examination. Weld specimens were etched electrolytically using 10% oxalic acid solution at 3V DC for 10-20 s while base metal specimens were etched using 60% Nitric acid at 1V DC for 2-3 s.

The borides present in the specimens, were extracted from the samples by anodic electrochemical dissolution of the austenite matrix in specimens at 3 V in an electrolyte consisting of 10% HCL in methanol for 48 hours [74]. After dissolution of the austenite matrix, the borides suspended in the electrolyte were collected using a precipitate extraction system equipped with vacuum pump - filtration set up supplied by “Millipore<sup>TM</sup>”. Filter paper of pore size 0.1 micrometer was used to filter out the suspended borides by pumping out the electrolyte through this filter paper for 3-4 hours. The filter paper containing the borides was dried in a desiccator.

### **3.7 Optical microscopy**

Metallographically prepared specimens were then observed in an optical microscope of make “Carl Zeiss<sup>TM</sup>”, equipped with “Axio observer Z1<sup>TM</sup>”, software. The software houses complete set of modules which are useful for quantitative metallography such as phase fraction analysis, grain size measurements etc.

### **3.8 Scanning Electron Microscopy (SEM)**

Specimens prepared for optical microscopy, were subsequently examined in a SEM. SEM used in this study is of make “CamScan™ 3200, UK with attached Energy Dispersive Spectrometer (EDS) equipped with “Oxford™” software. Semi-quantitative elemental distribution in selected specimens was carried out using SEM-EDS. Boride specimens collected after electrolytic dissolution were gold coated to make them electrically conductive and then analysed under SEM. Fractography was also carried out on selected hot ductility and Varenstraint tested specimens using SEM to identify the mechanism of fracture.

### **3.9 X-ray Diffraction Studies (XRD)**

To characterize the borides present in the base metal and re-melted 304B4, XRD studies were carried out on borides collected on the filter paper after electrolytic dissolution using X’pert MPD™ XRD equipment of Philips make using Cu–K<sub>α</sub> radiation with Ni filter in the angular range 20 to 80° at a step size of 0.02°. Standard JCPDS data base was used to identify the phases in the X-ray Diffractograms.

### **3.10 Transmission Electron Microscopy (TEM)**

TEM was used as a complementary tool for characterization of borides. For this, the precipitates extracted from the specimens were suspended in methanol and ultrasonically stirred so that agglomerated borides would be separated. However, it was not possible to separate them completely using ultrasound and we could get only slightly coarse particles for observation under TEM. These boride particles were then collected over a copper grid for observation under TEM. “Philips™” CM 200 microscope having

INCA™ energy dispersive spectrometer (EDS) attachment was used at operating voltages in the range of 120-200kV. The EDS spectra were quantified by Cliff-Lorrimer method using standard  $K_{AB}$  values. Efforts were also made to prepare thin foils of samples so as to image and identify the borides present in them. The borides were characterized on the basis of Selected Area Diffraction Patterns (SAD) and EDS obtained from them. The borides were identified by matching their SADs and microchemistry with that of standard crystallographic structures of borides available in JCPDS data book.

### **3.11 Electron Probe Micro Analysis (EPMA)**

Selected specimens from base metal, 304B4 SS fusion zone, weld joints, hot ductility and Vareststraint tested samples were characterized using Electron Probe Micro Analysis (EPMA) in JXA8230 JEOL™ EPMA operating at 15kV and 50nA probe current for identifying the elemental distribution in various phases. Selected area mapping of elements on these specimens were carried out to perform quantitative micro-chemical analysis of borides present in the various zones of a weldment.

### **3.12 Mechanical property evaluation**

#### *(i) Tensile properties*

Cylindrical tensile specimens of gage length 25 mm and L/D ratio of 6.25 as shown in Fig.3.8(a) were extracted from fabricated weld pads and base metal plates along the rolling direction. Tensile tests at room temperature were carried out according to ASTM standard E8-04 at a strain rate of  $10^{-4}$ /s [75].

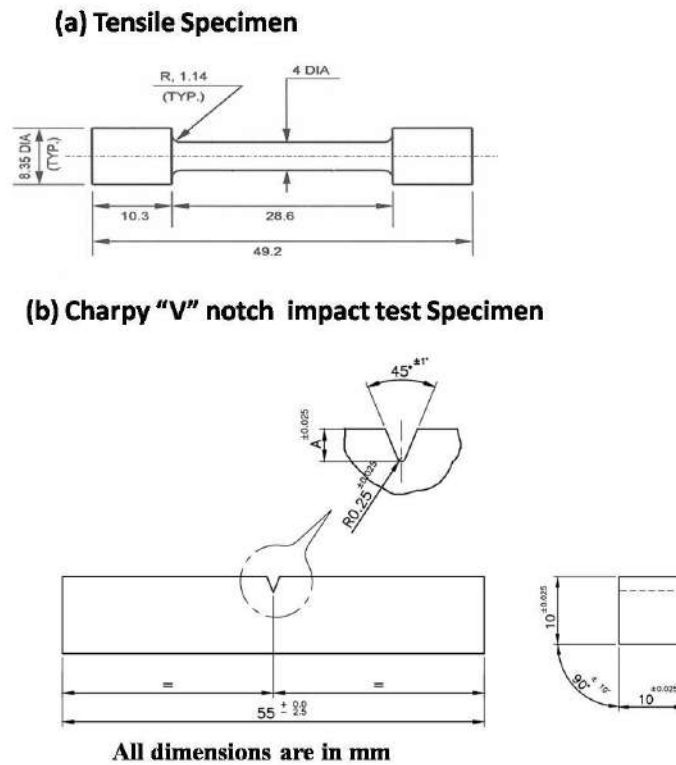


Fig.3.8 Drawings of specimens used for (a) Tensile test (b) Charpy “V” notch impact test

*(ii) Impact toughness*

Full size Charpy- “V” notch cross weld impact test specimens of dimension 55x10x10 mm as shown in Fig.3.8(b) were extracted from the fabricated weld joints and room temperature impact tests were carried out according to ASTM standard E-23 [76]. The notch was positioned exactly at the centre of the weld oriented along the welding direction. Impact tests were also carried out on specimens extracted from base metal plate in transverse-longitudinal (T-L) direction for comparison.

**3.13 Solidification simulations**

Phase transformations occurring in SS 304B4 base metal under equilibrium conditions were predicted using Thermo-Calc software version 6 using TCFE8 database.

Even though TCFE-8 database limits its applicability to steels containing trace amount of boron, references available in literature reported equilibrium phase diagrams calculation on hard facing alloys containing up to 3 wt.% of boron. The thermodynamic calculations showed good agreement with the experimental results in their study [77]. On this basis, equilibrium and non equilibrium calculations are performed for SS 304B4 containing 1.3 wt.% boron in the present study.

The results obtained from this simulation were used in conjunction with results from microscopy and XRD results to explain the microstructures of base metal, fusion zone and PMZ regions.

### **3.14 Scheil’s solidification simulation:**

Solidification path of SS 304B4 base metal, fused 304B4 SS and weld metals such as E309 and E308BRN used in this study was simulated using Scheil’s model in “Thermo Calc™” software version 6 with the TCFE8 database to predict the freezing temperature range. The software predicts the solidification sequence of various phases under non-equilibrium cooling conditions. The simulation was performed for 304B4 base metal and undiluted 309 weld metal using their respective chemical compositions given in Table 3.1. The basic assumption in Scheil’s model is complete mixing in liquid, no diffusion in solid and equilibrium at the interface [23].

The software uses the Scheil’s models [25] given below for calculations of composition of solid and liquid phases below the liquidus temperature of the alloy system until 0.99 fraction of solid is formed.

$$C_s = k C_0 (1 - f_s)^{k-1} \dots \dots \dots (4)$$

$$C_L = C_0 f_L^{k-1} \dots\dots\dots(5)$$

Where,  $C_S$  and  $C_L$  are composition of solid and liquid phases respectively,  $k$  is partitioning coefficient of the elements at a particular temperature,  $C_0$  is the initial composition of the liquid,  $f_s$  and  $f_L$  are fractions of solid and liquid respectively.

In solidification process using Scheil-Gulliver model, the condition at liquid -solid interface can be explained with a local equilibrium. By stepping with small decrements of the temperature one can determine the new composition of the liquid at that instance.

In summary this chapter gives details on different experiments used; specimens, simulations and evaluation methods. Apart from these general experiment details and specimen configurations, there are a few specific experiments conducted and characterization carried out to realize the objective of the work. These are given in the respective chapters. For example details of preparation of the weld joints with buttering using E309 electrode, then preparation of the weld joints using the same electrode and studies on cracking susceptibility of weld joint thus produced are not given here. They are given in Chapter 8 along with results of the tests carried out on this weld joint.

## CHAPTER 4

### HOT CRACKING SUSCEPTIBILITY OF SOLUTION ANNEALED AND FUSED SS 304B4

#### 4.1 Introduction

In this chapter the results of investigations on solidification and liquation cracking susceptibility of SS 304B4 base metal and fused SS 304B4 are presented and discussed. SS 304B4 contains ~1.24 wt.% of boron present almost entirely as chromium rich  $M_2B$  type of borides. Presence of boron in the form of borides decreases the hot ductility of borated stainless steel and increases the tendency for hot cracking especially in the steels with boron content in the range of 0.2- 0.5 wt.%. Cracking tendency for steels with boron content higher than 0.5 wt.% is comparatively lower than those with lower boron content as eutectic back filling of the cracks take place in the former [6]. This is verified by the Varestraint test and hot ductility tests conducted on the borated steel used in the present study. Further, in multipass welding, as used in fabrication of components, the weld metal can undergo repeated weld thermal cycles as welding progresses layer by layer making it susceptible to liquation cracking. Hence, susceptibility of the fused base metal to cracking during subsequent re-melting is also important. Accordingly, liquation cracking susceptibility and hot ductility of the fused metal is also carried out. This is accompanied by detailed microstructural evaluation of the base metal and fused metal, and that of the specimens after Varestraint and hot ductility tests. In addition to these, equilibrium and non – equilibrium phase transformations in SS 304B4 simulated using Thermo-Calc™

software are presented and compared with the results of Differential Scanning Calorimetry (DSC) studies as well as with the results obtained from the microstructural investigation of the base metal and fused metal. Based on all these, the differences in the hot cracking susceptibility of the wrought base metal and the fused metal of the same composition are explained.

## 4.2 Results

### 4.2.1 Equilibrium transformations-“Thermo-Calc<sup>TM</sup>” Simulation

Equilibrium transformation temperatures and phases existing in SS 304B4 alloy system was predicted using pseudo - binary phase diagram calculated using “Thermo-Calc<sup>TM</sup>” software. Based on the alloy composition given in Table 3.1 of Chapter 3, the calculated pseudo - binary phase diagram is shown in Fig.4.1. It is clear from the phase diagram that SS 304B4 with 1.24 wt.% boron, under equilibrium conditions solidifies in a sequence as listed below.

- i.  $L \leftrightarrow \gamma + L$  at Liquidus temperature (1310°C):
- ii.  $L + \gamma \leftrightarrow \gamma + M_2B + L$  at (1217°C);  $M_2B = (Fe, Cr)_2B$
- iii.  $L + \gamma + M_2B \leftrightarrow \gamma + M_2B + MnS$  at (1205°C):
- iv.  $\gamma + M_2B + MnS \leftrightarrow \gamma + Cr_2B + MnS$  at (987°C);
- v.  $\gamma + Cr_2B + MnS \leftrightarrow \gamma + Cr_2B + MnS + M_{23}C_6$  at (827°C);  $M_{23}C_6 = (Fe, Cr)_{23}C_6$

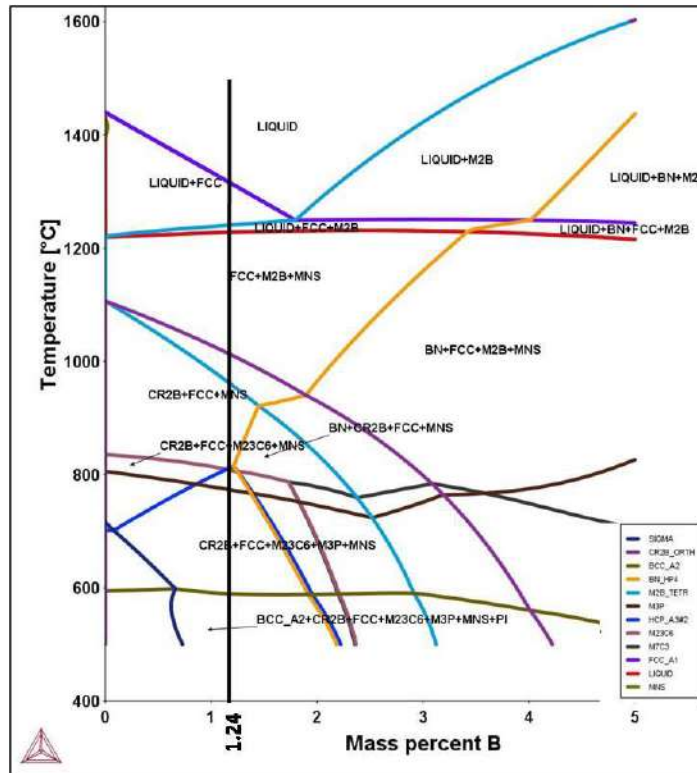


Fig.4.1 Pseudo-binary phase diagram of SS 304B4 generated using “Thermo-Calc™”, version 6 using TCFE8 database

In short, it can be stated that under equilibrium cooling conditions primary austenite is formed first from the liquid. Subsequently,  $M_2B$  type of borides are formed as a result of eutectic reaction which then undergo solid state transformation to  $Cr_2B$  type of borides at around  $987^\circ\text{C}$ . Hence, the equilibrium microstructure of 304B4 SS is predicted to consist of primary austenite and  $Cr_2B$  type of borides as major phases at room temperature.

#### 4.2.2 Non-equilibrium transformations

Although an equilibrium phase diagram helps in understanding the phase transformations in an alloy system, equilibrium solidification seldom occurs in practical

conditions. During welding, prevailing cooling rates and the consequent non equilibrium conditions in the weldment can cause the transformation sequence to deviate from those predicted by the equilibrium phase calculations. At high cooling rate, partitioning of solute elements in equilibrium phases is not complete and hence solute elements are enriched in the liquid phase more than that in equilibrium condition. As a result, the local liquid composition is different from that of the initial composition and the liquid is enriched in alloying elements such as boron, chromium, sulphur, phosphorus etc.. Also, the solidification progresses with local equilibrium at the solid-liquid interface.

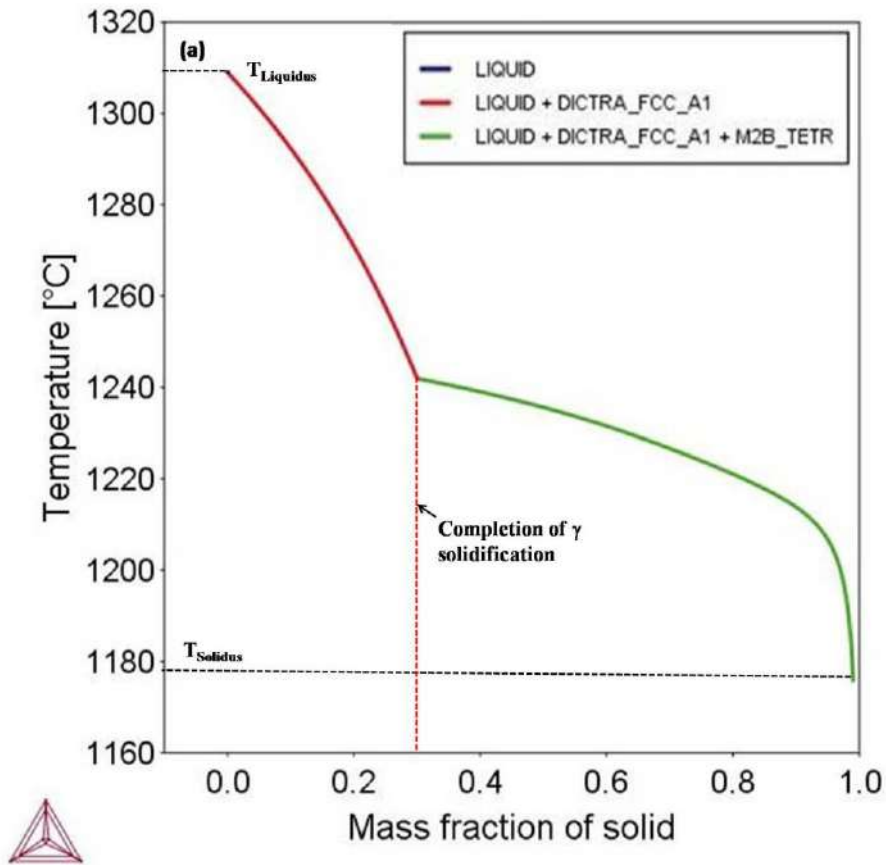


Fig.4.2 Non -equilibrium solidification simulation of SS 304B4 using Scheil's module

This type of solidification is modeled using “Scheil-Gulliver” module, which assumes complete mixing in liquid no diffusion in solid and equilibrium at the solid-liquid interface. The solidification simulation result for the present steel composition is presented in Fig.4.2. As it can be seen from the figure, the solidification starts at 1310°C, the liquidus temperature at which the mass fraction of solid is almost zero. At about 1240°C, around 30% of  $\gamma$  phase is formed; the remaining liquid is enriched in boron since its solid solubility in austenite is negligible. Below 1240°C down to temperature ~1180°C, super saturation of boron in the liquid decreases by precipitation of  $M_2B$  type of borides. The fraction of solid at 1180°C is 0.99 and this marks the solidus temperature of the steel.

In order to simulate the solidification sequence of interdendritic phases present in PMZ formed in fused SS 304B4, the composition of liquid obtained at 0.3 mass fraction of solid from the solidification simulation of base metal (Fig.4.2) is considered as initial composition (as this is composition of the liquid after austenite corresponding to 0.3 mass fraction is formed and this starts solidifying as eutectic phase in the interdendritic region) and the result of the same is shown in Fig.4.3. This is done to simulate the solidification temperature of the interdendritic liquid present in the fused 304B4 on re-melting while this zone is exposed to peak temperatures experienced by a PMZ during multipass welding. The figure shows that the solidification simulation of re-melted liquid phase and the solidus temperature calculated for this composition is about 1140°C. It is inferred that at ~1180°C, which marks the solidus temperature of the base metal (Fig.4.2), the fraction

of liquid in re-melted interdendritic liquid is still 0.1 and Cr<sub>2</sub>B type of boride is formed from the liquid at last stage of solidification.

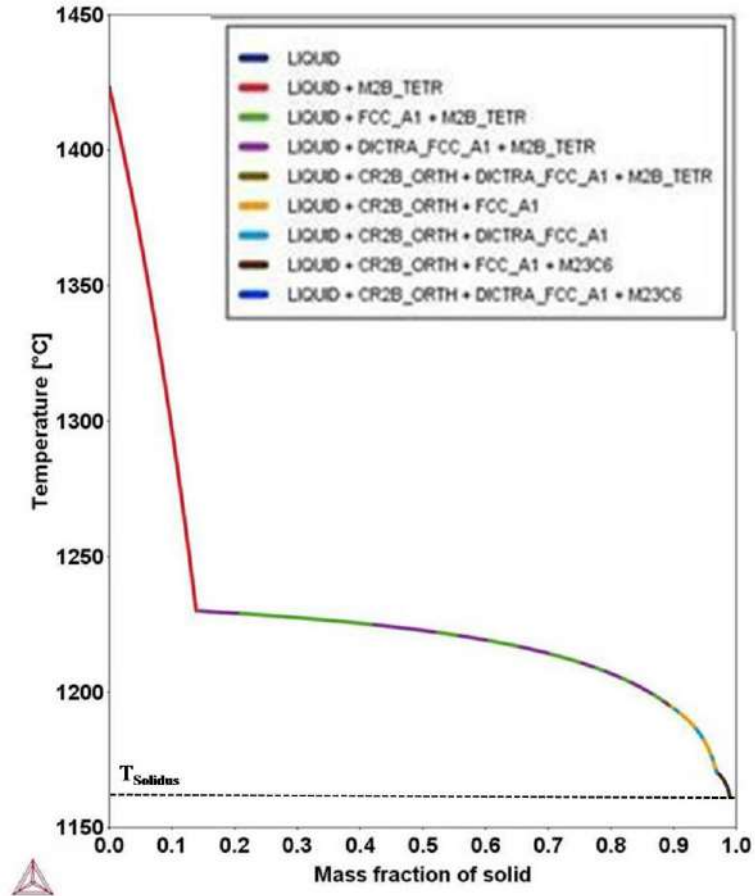


Fig.4.3 Scheil's solidification simulation of liquid phase in the interdendritic regions of PMZ in re-melted 304B4 SS of composition (19.84 wt.% Cr-11.53wt.% Ni-1.77 wt.% B - 0.025 wt.% C-0.357wt.% Si-0.031wt.% P-65wt.% Fe).

From the simulation studies, it is understood that under non-equilibrium cooling conditions, microstructure of SS 304B4 would consist of primary austenite and high temperature M<sub>2</sub>B type eutectic borides retained at room temperature. Such cooling conditions may lead to an increase in the freezing range of the steel. Also, the simulation of non-equilibrium cooling of re-melted interdendritic liquid in the PMZ shows that on

cooling, solidus temperature is further lowered below the solidus temperature predicted for non-equilibrium cooled SS 304B4 base metal.

#### 4.2.3 Phase transformations in 304B4 base metal during thermal cycle

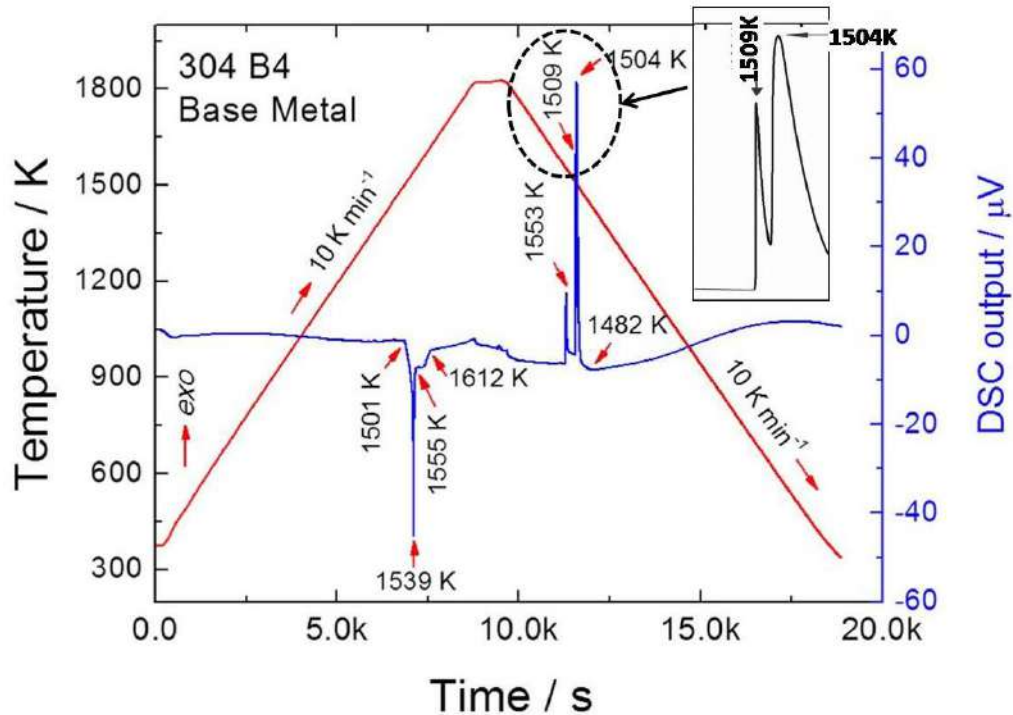


Fig. 4.4 On heating and On cooling DSC profile of 304B4 SS base metal heating up to its melting point and cooled down at 10 K/min.

DSC profiles of specimens extracted from 3 mm thick SS 304B4 base metal, the chemical composition of which is given in Table.3.1 of Chapter 3 is shown in Fig.4.4. The first deviation from baseline, observed at 1228°C (1501 K), marks the beginning of liquation (the solidus). It may be noted that the thermal arrest profile found upon slow heating (10 K/min) shows two stages. This can be qualitatively attributed to eutectic reaction  $\gamma + \text{Cr}_2\text{B} \leftrightarrow \text{L}$  involved during melting of the steel which completes at 1282°C (1555 K). Further liquation observed as a consequence of reaction  $\text{L} + \gamma \leftrightarrow \text{L}$  [6] and

liquation at 1339°C (1612K). Since the steel studied here is a multi-component alloy system, multiple eutectic phases formed during the liquation reaction such as  $\gamma$ +Fe<sub>2</sub>B,  $\gamma$ +Ni<sub>2</sub>B and  $\gamma$ +Cr<sub>2</sub>B type of borides [78] which can occur over a wide range of temperature as observed in this DSC profile.

In contrast, the cooling profile shows three distinct peaks qualitatively corresponding to the following reactions in sequence. A peak at 1280°C (1553 K) marks the *on cooling* liquidus temperature of the steel corresponding to nucleation of primary austenite from the liquid,  $L \leftrightarrow \gamma + L$ . Subsequent thermal arrest point at 1236°C (1509 K) would be an indication of nucleation of M<sub>2</sub>B type of boride as a consequence of eutectic reaction,  $L \leftrightarrow \gamma + M_2B$  on comparing with the transformation temperatures of the phases shown in pseudo binary phase diagram in Fig.4.1. The reason for formation of additional peak at 1231°C (1504 K) is not understood clearly though some authors [7, 8] have reported similar observations in low as well as high boron steels. On comparing the DSC profile with the predicted phase diagram in Fig.4.1, the third peak can be attributed to nucleation of MnS from the liquid but so far this is not reported in the literature. As reported by other authors in the literature, it can also correspond to the formation of two distinct, but similar, eutectic-like constituents, with the composition of the borides in the two eutectics being essentially indistinguishable by analytical microscopy [15].

It is observed that the predicted equilibrium transformation sequences and the DSC results deviate substantially with respect to transformation temperatures and phases. Above all, signature of solid state transformation of M<sub>2</sub>B borides to Cr<sub>2</sub>B borides is not observed in DSC profile.

#### 4.2.4 Phase transformations in fused 304B4 during thermal cycle

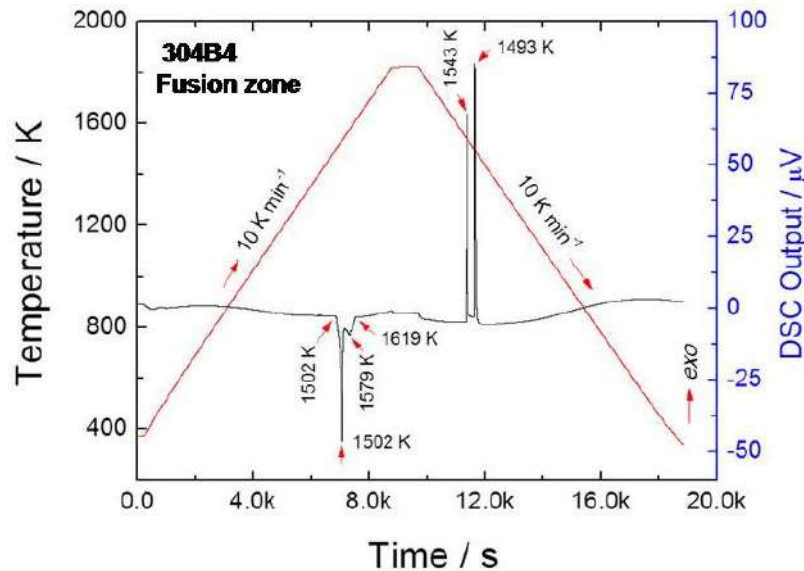


Fig.4.5 On heating and on cooling DSC profile of fused 304B4 SS heated up to its melting point and cooled thereafter at 10K/min.

DSC studies were carried out on specimens extracted from fusion zone of an autogenous GTAW bead on plate weld deposited on SS 304B4. On heating and on cooling DSC profile obtained for fused 304B4 is given in Fig.4.5. During heating, the onset of liquation is observed at 1229°C (1502 K) and an additional exothermic event was observed at 1306°C (1579 K). The first peak can be attributed to the melting of different eutectic phases present in the liquid. Exothermic arrest corresponding to complete liquation is found at 1346°C (1619 K) due to the melting of primary austenite.

On cooling, part of DSC thermogram of fused 304B4 shows two sharp peaks. The one corresponding to 1270°C (1543 K) represents nucleation of primary austenite from the liquid,  $L \leftrightarrow \gamma + L$  and the other corresponding to 1220°C (1493 K) represents the precipitation of borides via eutectic reaction  $L \leftrightarrow \gamma + M_2B$ . Equilibrium and non

equilibrium phase transformations occurring in 304B4 SS and fused 304B4 SS are summarized in Table.4.1

Table 4.1 Summary of transformation temperatures of 304B4 SS base metal, fused 304B4 and interdendritic liquid present in fused 304B4 SS

Temperature	304B4 base metal			Fused 304B4 SS			Interdendritic liquid
	Equilibrium-phase diagram	DSC <i>on heating</i>	DSC <i>on cooling</i>	Scheil's simulation	DSC <i>on heating</i>	DSC <i>on cooling</i>	Scheil's simulation
T <sub>liquidus</sub> (°C)	1310	1339	1280	1310	1306	1270	1425
T <sub>solidus</sub> (°C)	1205	1228	1236	1180	1229	1220	1140
M <sub>2</sub> B ↔ Cr <sub>2</sub> B	987	--	--	-	-	-	-

Over all, there is a close match between the transformation temperatures and phases formed in fused and SS 304B4 base metal except for an extra peak found in on cooling cycle of the base metal. In both the thermograms there are no indications of solid state transformation of M<sub>2</sub>B borides to Cr<sub>2</sub>B as found in the equilibrium phase diagram in Fig.4.1.

#### 4.2.5 Microstructure of SS 304B4 base metal

Optical microstructure of SS 304B4 base metal revealing austenite matrix consisting of coarse borides of size ~ 1-25µm distributed randomly in the matrix, is shown in Fig.4.6. The borides are coarse because they are primary borides formed during ingot solidification and subsequently broken down during hot rolling [79]. The SEM/EDS analysis of the borides extracted electrochemically from base metal (Fig.4.7) show that

the borides are predominantly enriched in Cr and contain some dissolved Fe; which is in agreement with that reported in literature [2].

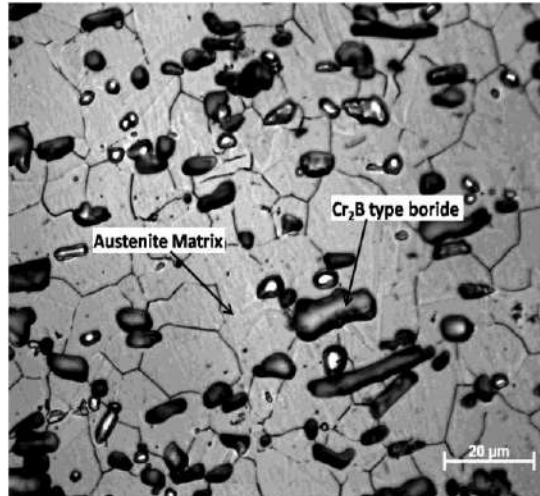


Fig.4.6 Microstructure of 304B4 SS base metal (solution annealed) obtained using optical microscope.

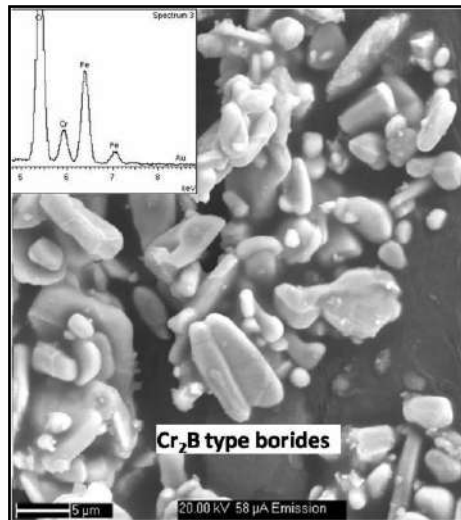


Fig.4.7 Microstructure of primary borides extracted from 304B4 SS base metal by electrolytic dissolution of matrix obtained using SEM. EDS spectrum of the boride is inset in the figure.

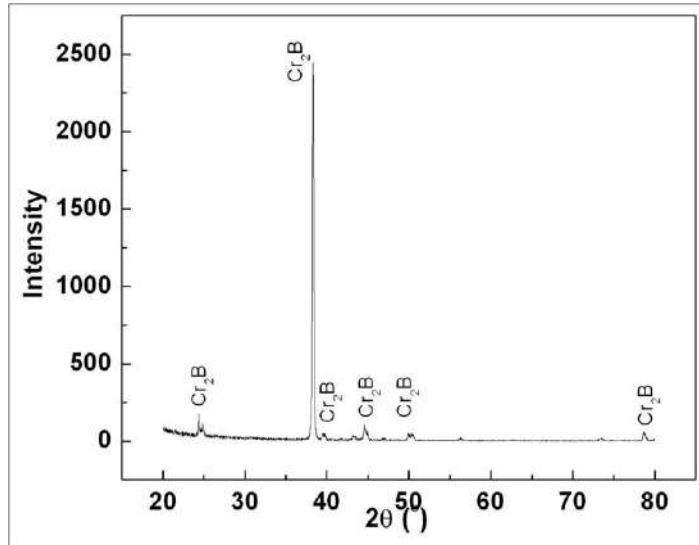


Fig.4.8 XRD profile obtained for base metal borides indicating that it is Cr<sub>2</sub>B type of boride.

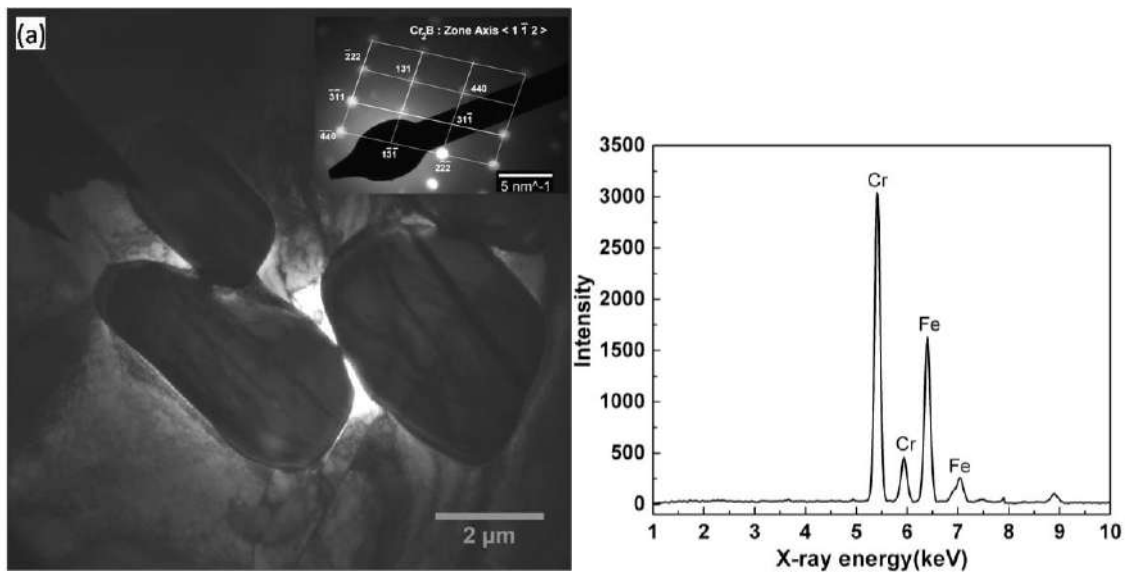


Fig.4.9 (a) TEM image of 304B4 SS base metal borides extracted by anodic dissolution (b) TEM/EDS taken on the extracted base metal borides.

The X-ray diffractogram of base metal borides shown in Fig.4.8 clearly confirms that these are Cr<sub>2</sub>B type of borides. This was further confirmed by Selected Area Diffraction (SAD) (Fig.4.9(a)) and EDS (Fig. 4.9b) analyses carried out on these precipitates while observing them under TEM. As expected, these borides though rich in Cr also contain some Fe and are of tetragonal crystal structure.

In summary, it is understood that SS 304B4 base metal predominantly contain Cr rich Cr<sub>2</sub>B type of boride in the microstructure.

#### 4.2.6 Microstructure of 304B4 fusion zone

The microstructures of the SS 304B4 fusion zone produced by autogenous GTA bead on plate welding and observed under optical and scanning electron microscopes are shown in Fig.4.10(a) and (b) respectively. The melting and re-solidification hypoeutectic microstructure consists of dendritic austenite and eutectic phase filling the interdendritic regions. SEM image (Fig.4.10(b)) reveals interdendritic eutectic phases of different morphologies and intradendritic precipitates with spheroidal morphology.

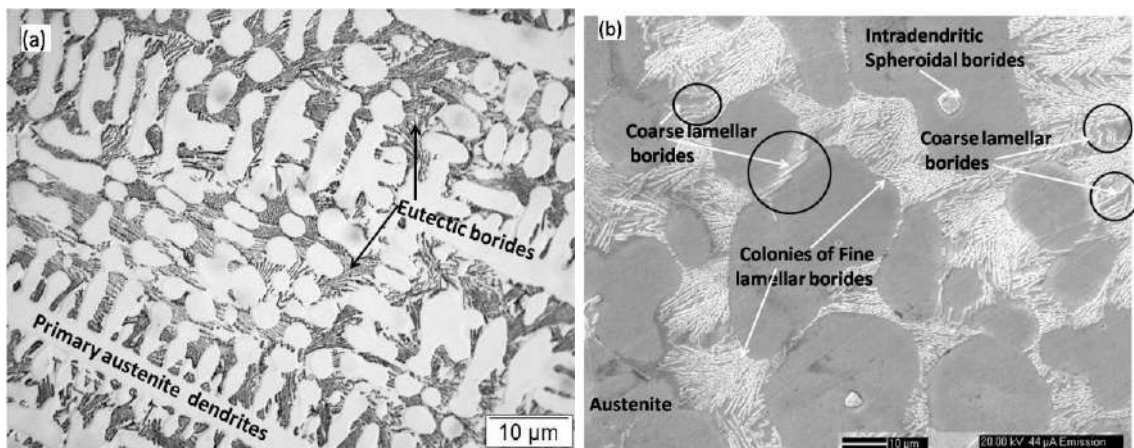


Fig.4.10(a) Microstructure of re-melted 304B4 showing austenite dendrites and interdendritic eutectic borides(b) SEM image of re-melted 304B4 showing borides of different morphologies

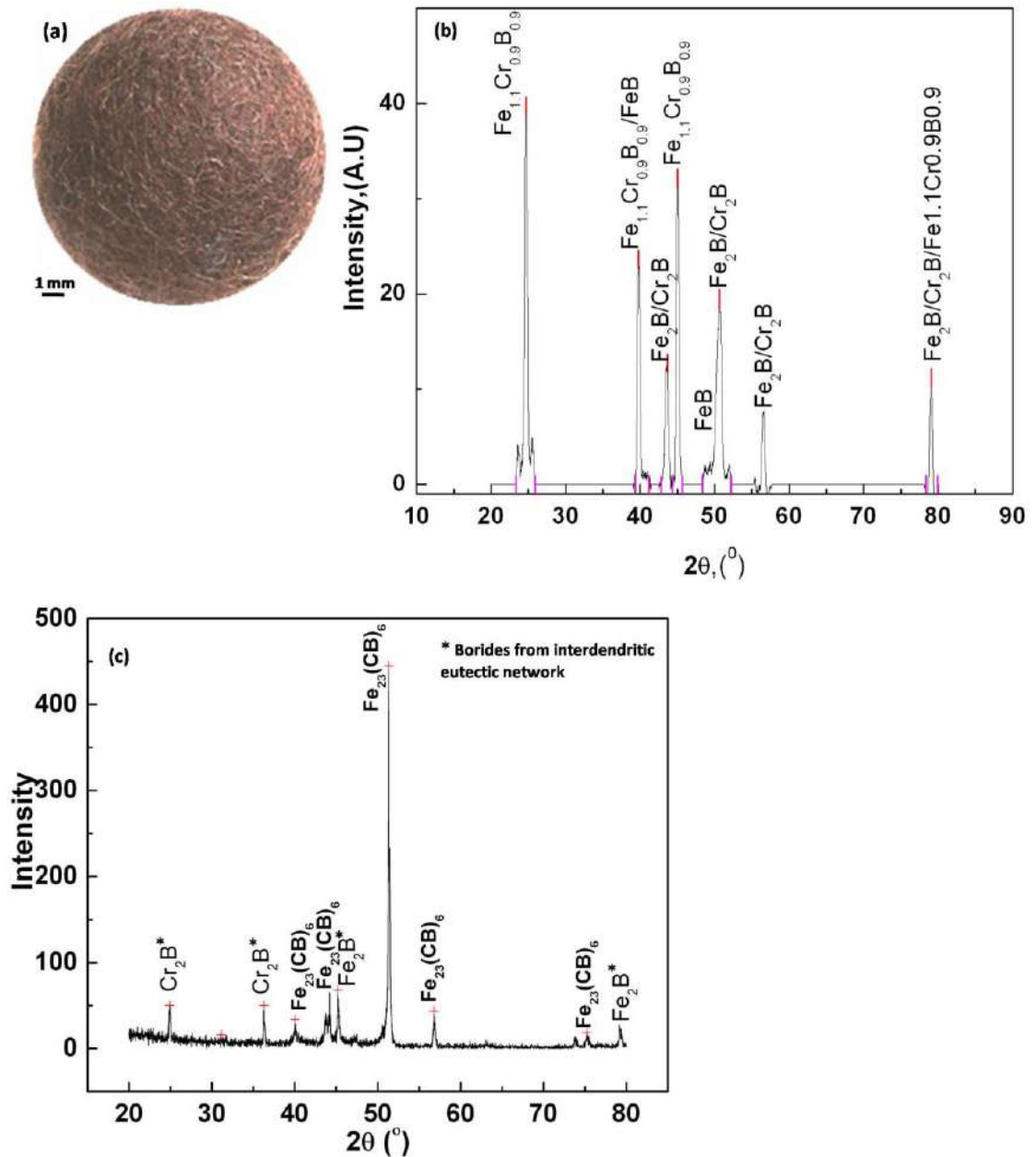


Fig.4.11 (a) Image of the porous mass of eutectic network left out after anodic dissolution and XRD analysis of (b) Interdendritic borides and (c) Intradendritic borides present in the re-melted 304B4 SS

The interdendritic eutectic network and intradendritic borides were extracted by electrochemical precipitation extraction process as described in section 3.6 of Chapter 3. The interdendritic eutectic network of borides remained as a porous mass as shown in

Fig.4.11(a) and the intradendritic borides settled at the bottom of the electrolyte as fine powder after dissolution of austenite phase. Hence, the interdendritic and intradendritic borides were more or less separated for further characterization using XRD and TEM.

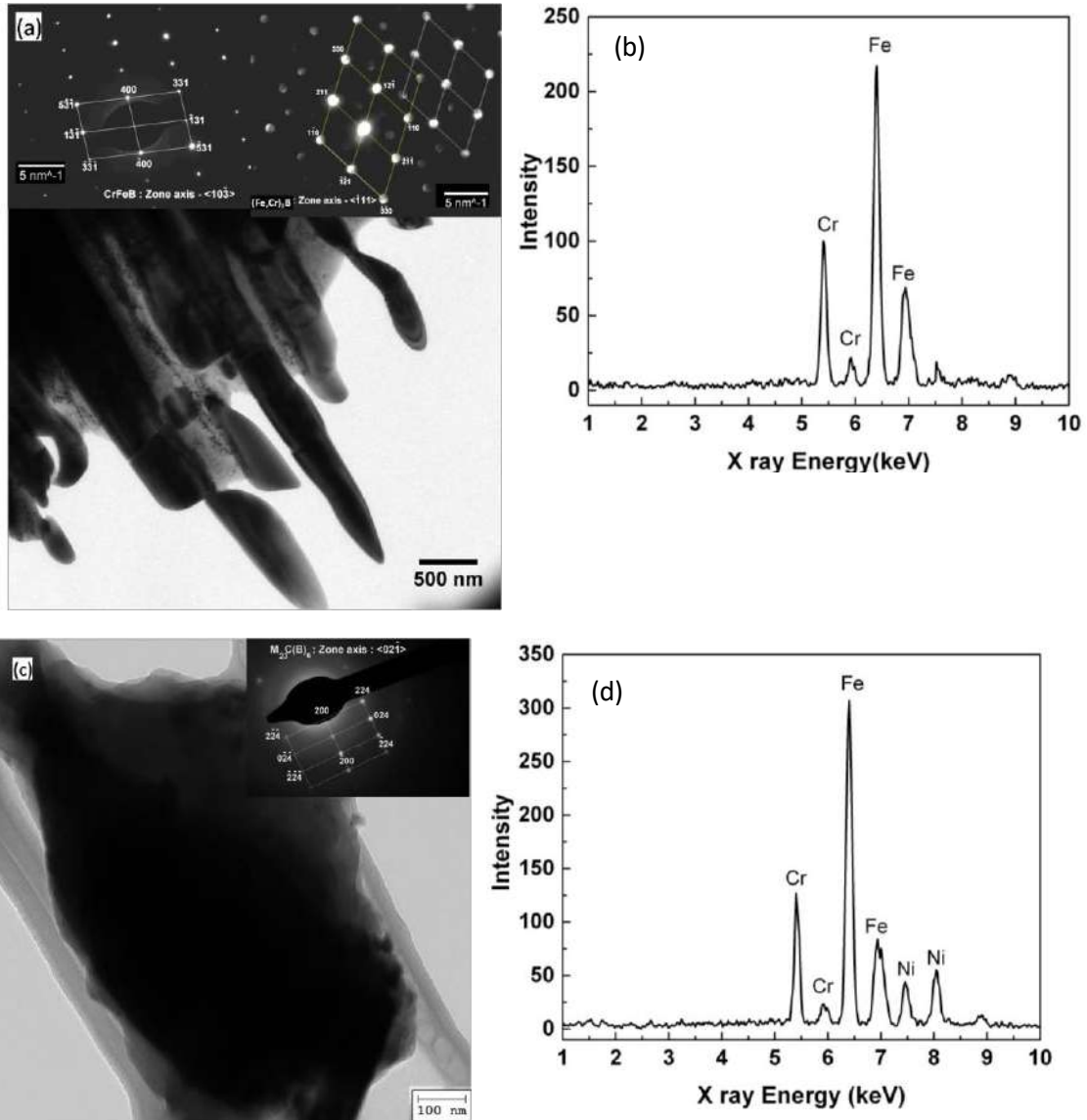


Fig.4.12 (a) TEM image of interdentritic borides (b) TEM/EDS analysis of borides shown in (a),(c) TEM image intradendritic spheroidal borides (d)TEM/ EDS analysis of boride shown in (c).

XRD results of eutectic phases extracted from fused SS 304B4 shown in Fig.4.11(a) and (b) reveals the different types of borides present in the interdendritic regions and intradendritic regions of the fused 304B4 SS, further confirmed through SAD and EDS analysis. The results shown in Fig.4.12(a),(b) and (c),(d) clearly convey that the re-melted alloy consists of predominantly Fe rich  $(\text{Fe,Cr})_2\text{B}$  of orthogonal crystal structure and  $\text{Fe}_{23}(\text{C,B})_6$  type of borides (FCC crystal structure) in the interdendritic and intradendritic regions respectively.

In brief, it can be stated that the microstructure of fused 304B4 consists of primary austenite and a complex mixture of borides such as  $(\text{Fe,Cr})_2\text{B}$  and  $\text{Fe}_{23}(\text{C,B})_6$  which are rich in Fe in addition to  $\text{Cr}_2\text{B}$  type borides. Table 4.2 summarizes the various types of borides present in 304B4 SS base metal and fused 304B4 found experimentally in this study and those predicted using “Thermo-Calc<sup>TM</sup>” and reported in literature.

Table 4.2 Comparison of types of borides present in 304B4 SS base metal and fused 304B4 SS with predicted using “Thermo-Calc<sup>TM</sup>” and that reported in literature.

	<b>Borides</b>				
	Predicted using “Thermo-Calc <sup>TM</sup> ”	Found experimentally		Reported in literature [6]	
<b>304B4 SS base metal</b>	$\text{Cr}_2\text{B}$	$\text{Cr}_2\text{B}$		$(\text{Cr,Fe})_2\text{B}$	
<b>Fused 304B4 SS</b>	$(\text{Fe,Cr})_2\text{B}$	Interdendritic	Intradendritic	Interdendritic	Intradendritic
		$(\text{Fe,Cr})_2\text{B}$	$\text{Fe}_{23}(\text{C,B})_6$	$\text{M}_{23}(\text{C,B})_6$	$\text{M}_{23}(\text{C,B})_6$

## 4.2.7 Hot cracking susceptibility

### 4.2.7.1 SS 304B4 Base metal

#### a. Longitudinal Varestraint Test (LVT)

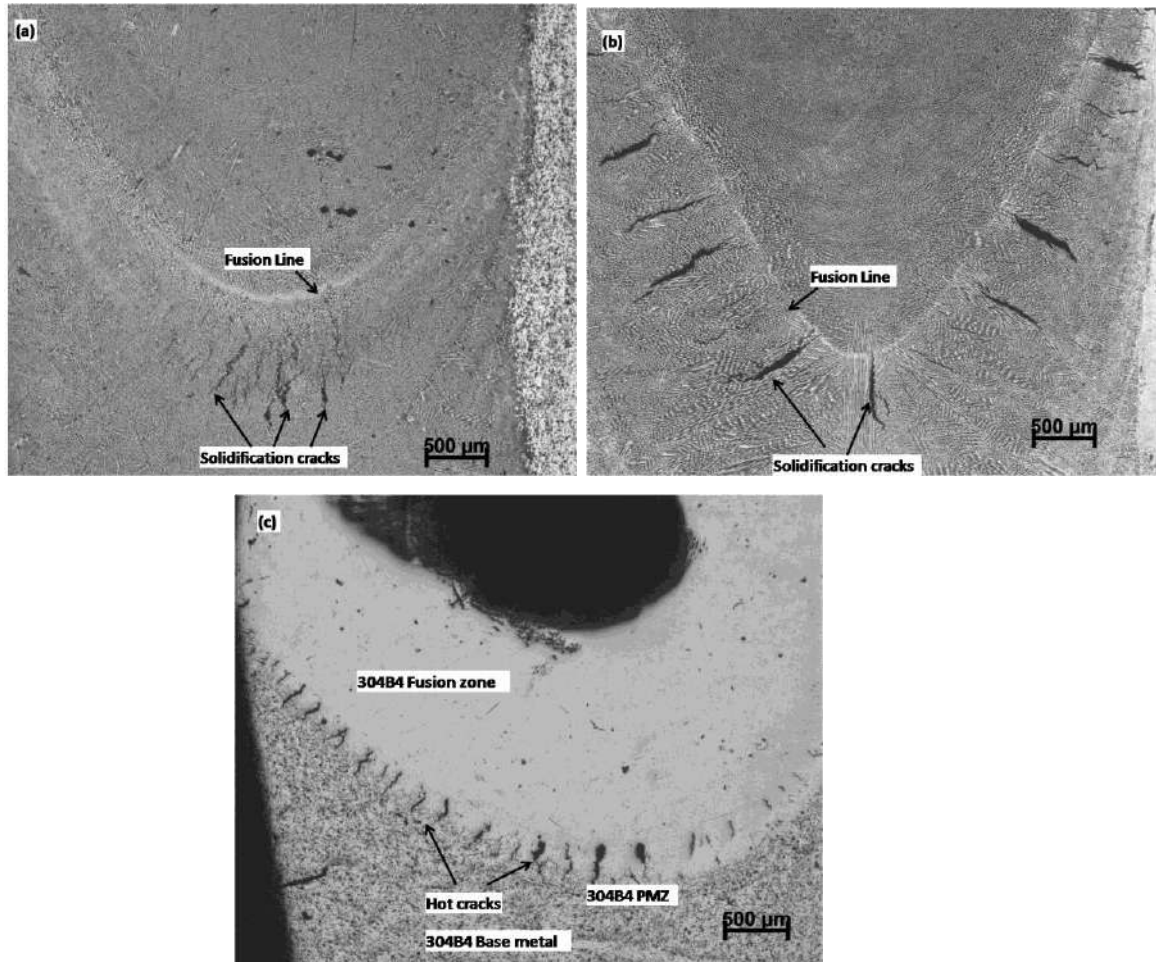


Fig.4.13 Macrostructure of (a) Longitudinal Varestraint specimen tested at 4% augmented strain (b) Transverse Varestraint specimen tested at 4% augmented strain showing solidification cracks in the fusion zone (c) Spot Varestraint specimen tested at 4% augmented strain showing hot cracks.

LVT was carried out on SS 304B4 base metal specimens prepared as per drawing shown in Fig.3.2(a) of Chapter 3. Fig.4.13(a) shows the macrostructure of a longitudinal varestraint specimen tested at 4% augmented strain with the location of cracks marked.

Even at the highest strain of testing, only a few fine cracks are seen indicating resistance of the base metal to solidification cracking. At lower strains of testing, even these cracks are not present. This result is in agreement with the information already available on resistance of solidification cracking of the borated stainless steel with boron content in 0.5-2.0 wt.% boron which is attributed to eutectic backfilling [6]. As this result is in agreement with that widely reported in literature, we are not discussing it further here.

b. *Transvarestraint test (TVT)*

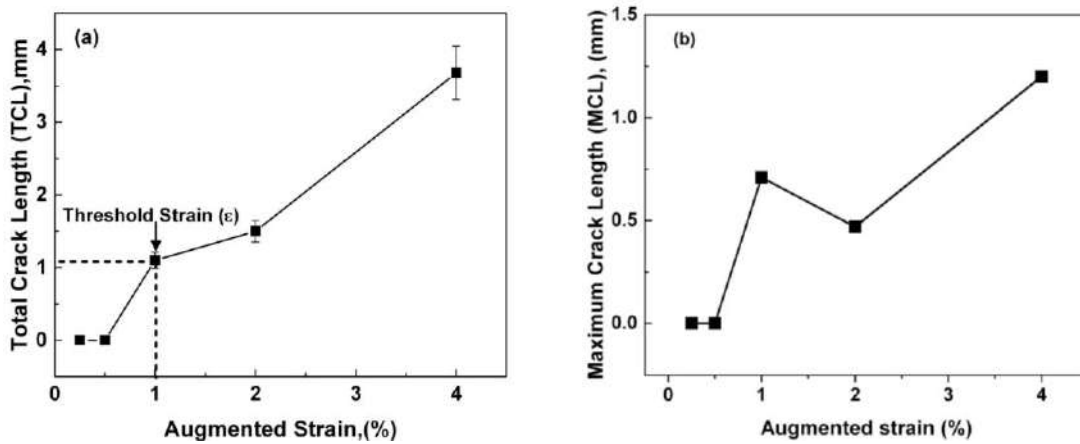


Fig.4.14(a) Total Crack Length Vs % Augmented strain (b) Maximum Crack Length Vs % Augmented strain obtained from SS 304B4 base metal TVT specimens.

TVT was carried out on SS 304B4 base metal specimens fabricated as per drawing shown in Fig.3.2(b) of Chapter 3. The macrostructure of SS 304B4 base metal transvarestraint specimen tested at 4% augmented strain (Fig.4.13(b)) shows significant number of cracks in the weld zone. Fig.4.14(a) and (b) shows Total Crack Length (TCL) and Maximum Crack Length (MCL) respectively plotted against augmented strain obtained from TVT specimens. The threshold strain for cracking is observed at 1% augmented strain. The results clearly show that the solidification cracking susceptibility

of SS 304B4 base metal to be on par with that of SS 304 stainless steel (TCL is ~2 mm and MCL is ~0.5 mm at 2% augmented strain) [6] from the MCL data. Brittleness Temperature Range (BTR) determined for SS 304B4 in the fusion zone using the procedure mentioned in section 3.4.2 of Chapter 3 is 192°C.

c. *Spot Varestraint test*

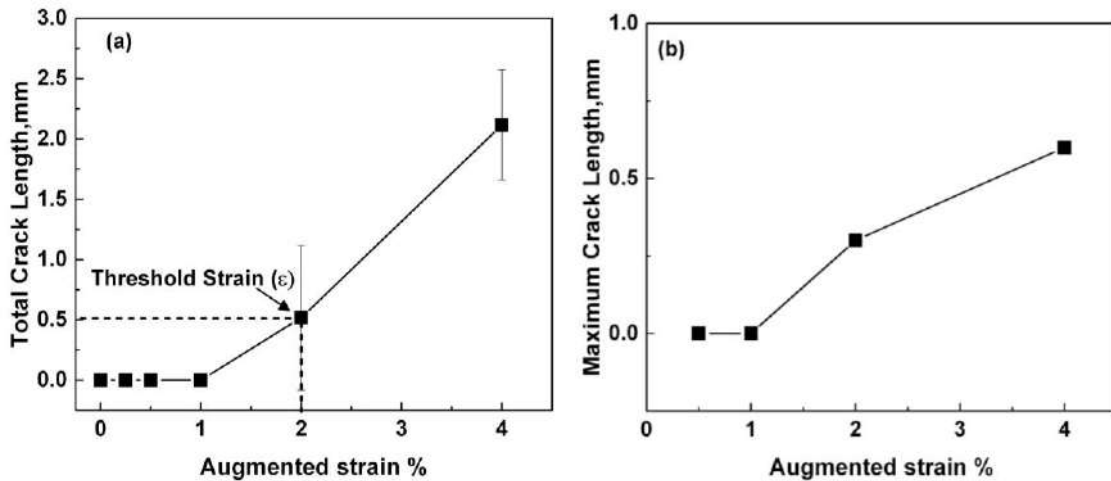


Fig.4.15(a) Total Crack length Vs % Augmented strain (b) Maximum Crack Length Vs % Augmented Strain obtained from 304B4 base metal SVT specimens

As pointed out in section 2.6.1 of Chapter 2, spot Varestraint test is more sensitive towards determination of liquation cracking tendency in a material. Hence, spot Varestraint tests were conducted on specimens prepared from SS 304B4 base metal as per procedure described in 3.4.2 of Chapter 3. Fig.4.13(c) shows the macrostructure of spot Varestraint specimen tested at 4% augmented strain. The Figure shows a few measurable number of cracks in the base metal PMZ adjacent to weld zone. Total Crack Length (TCL) and Maximum Crack Length (MCL) against % augmented strain obtained from spot Varestraint test conducted on SS 304B4 base metal is shown in Fig.4.15(a) and (b). Threshold strain ( $\epsilon$ ) for cracking is found to be 2% as shown in TCL data. Brittleness

Temperature Range (BTR) determined for the PMZ formed in base metal during spot vareststraint tests is found to be 214°C.

*d. Hot ductility tests*

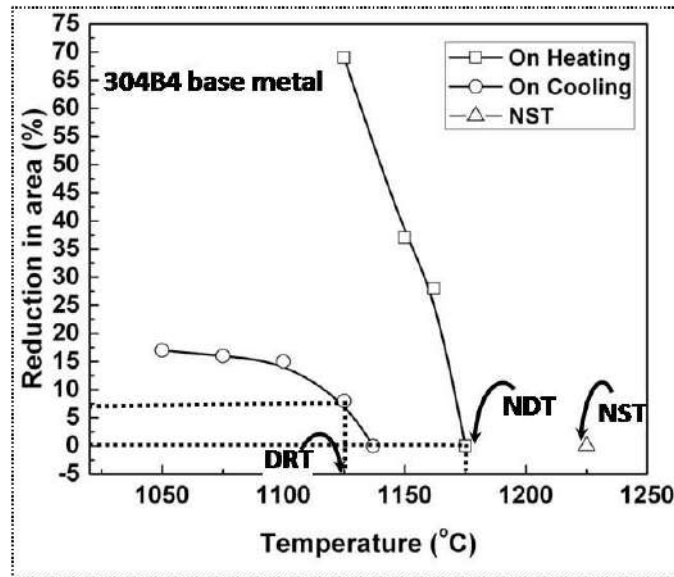


Fig.4.16 Hot ductility curve obtained for 304B4 SS base metal from hot ductility experiments carried out using “Gleeble<sup>TM</sup>” thermomechanical simulator

As mentioned in Chapter 2, hot ductility results can compliment Vareststraint test results used for determination of liquation cracking sensitivity in base metal PMZ. Hot ductility experiments were conducted using “Gleeble<sup>TM</sup>” thermo-mechanical simulator using specimens fabricated from base metal as per the dimensions given in Fig.3.6 of Chapter 3. The results of hot ductility test carried out using 304B4 SS base metal specimens is summarized in Table 4.3. Accordingly, the Nil Ductility Range (NDR) [NDR = NST-DRT] for 304B4 base metal is 95°C. The Cracking Factor (%CF) calculated using equation (3) for the base metal was found to be 8.1%.

Table 4.3 summary of hot ductility test results of 304B4 SS base metal

<b>Specimen</b>	<b>NST</b>	<b>NDT</b>	<b>DRT</b>	<b>NDR</b> (NST-DRT)	<b>CF (%)</b>
<b>Base metal</b>	1220°C	1168°C	1125°C	95	8.5%

#### 4.2.7.2 Fused SS 304B4

For fused SS 304B4, solidification cracking susceptibility was assumed to be similar to that of the base metal since complete re-melting and solidification takes place in the fusion zone during Varestraint tests. Hence, solidification cracking studies (tests involving LVT and TVT) were not carried out and only liquation cracking studies (spot Varestraint tests) were conducted on fused SS 304B4 specimens. This is because the microstructure of the fusion zone is different from that of the base metal and hence microstructure of PMZ formed in the fusion HAZ is expected to be different and hence its susceptibility to liquation cracking.

##### a. *Liquation cracking*

##### [1] *Spot Varestraint tests*

##### (i) *Preparation of fused 304B4 SS specimens for SVT*

Fused SS 304B4 specimens were prepared by making an autogenous GTA bead on plate weld on the base metal specimen as shown schematically in Fig.4.17. The welding parameters used for the bead on plate weld are given in Table 3.3. SVT was carried out on the autogenous weld bead as per the procedure described in section 3.4.2 of Chapter 3.

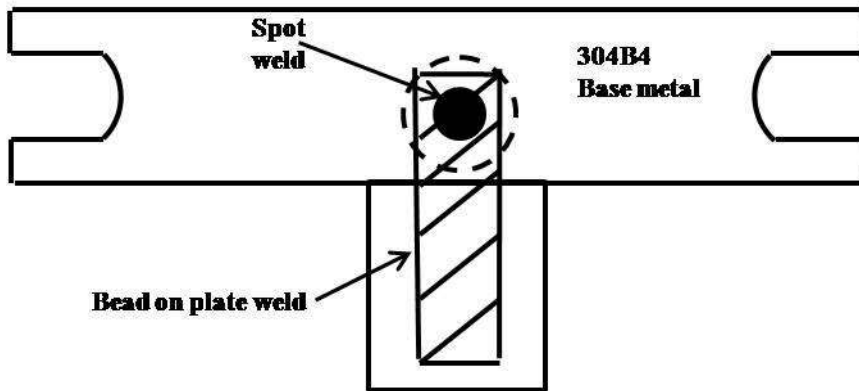


Fig.4.17 Schematic of re-melted 304B4 SS specimen with bead on plate weld used for SVT.

*(ii) Cracking susceptibility*

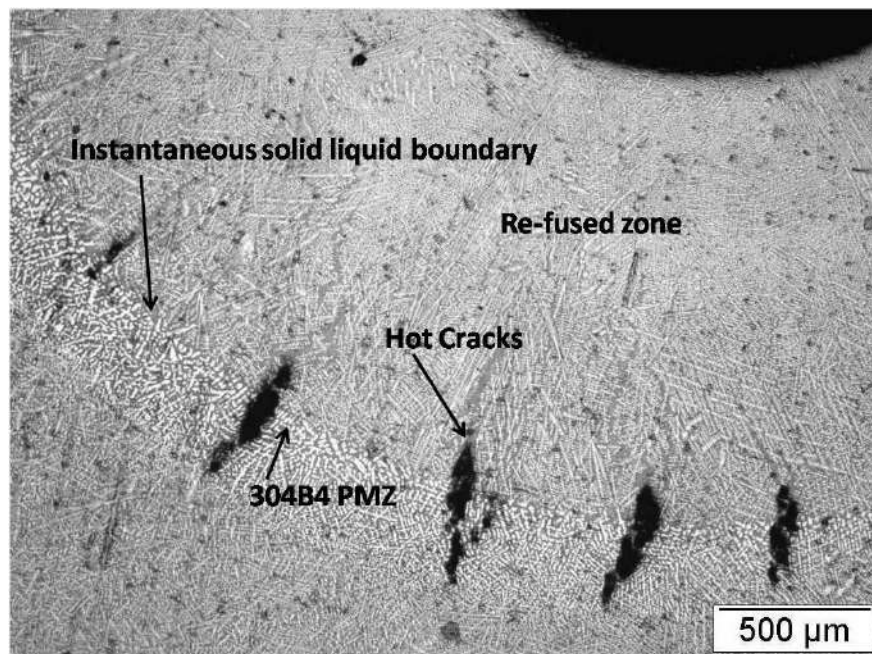


Fig.4.18 Macrostructure of spot Varestraint specimen tested at 4% augmented strain showing hot cracks.

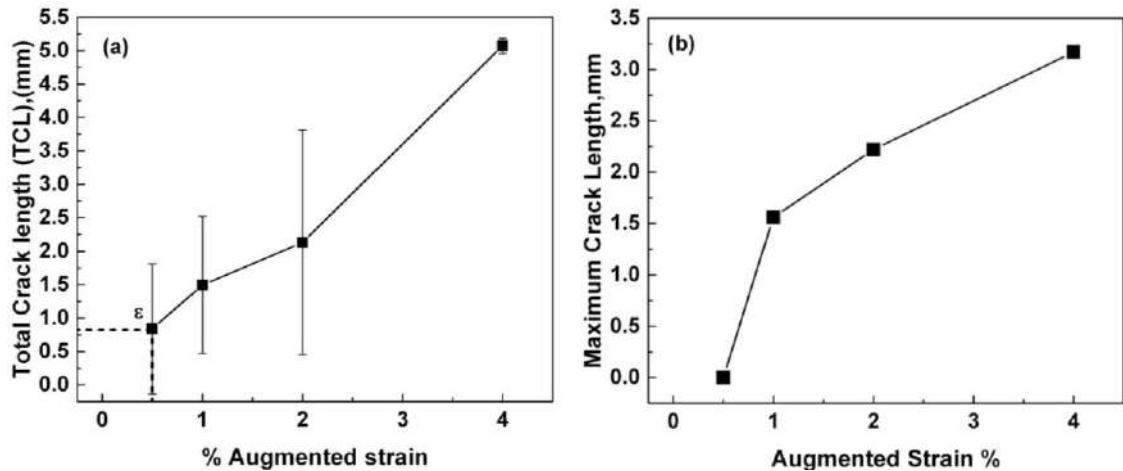


Fig.4.19 (a) Total Crack Length Vs %Augmented Strain (b) Maximum Crack Length Vs %augmented strain obtained for re-fused 304B4 SS specimens from spot Varestraint test.

The macrostructures of spot Varestraint test specimens subjected to 4% augmented strain containing hot cracks is shown in Fig.4.18. Total Crack Length (TCL) and Maximum Crack Length (MCL) plotted against % augmented strain from spot Varestraint tests conducted on fused SS 304B4 is shown in Fig.4.19(a) and (b). Threshold strain for cracking is found to be 1% which is lower than that obtained for base metal. This clearly indicates that liquation cracking susceptibility for PMZ lying in fused 304B4 is higher than the base metal.

Also, the TCL and MCL values obtained from the specimen are higher than that obtained from base metal specimens. Brittleness Temperature Range (BTR) determined for PMZ in fused 304B4 determined using spot Varestraint tests is found to be 224°C which is higher than base metal shows that PMZ in fused SS 304B4 has higher susceptibility for liquation cracking than the base metal.

[2] *Hot ductility tests*

Hot ductility experiments similar to that of SS 304B4 base metal were carried out on specimens prepared using partially melted SS 304B4 as described in section 3.4.3 (d) of Chapter 3 and the results of the same are summarized in Table 4.4. *On heating* and *on cooling* hot ductility curves obtained for fused SS 304B4 is shown in Fig.4.20.

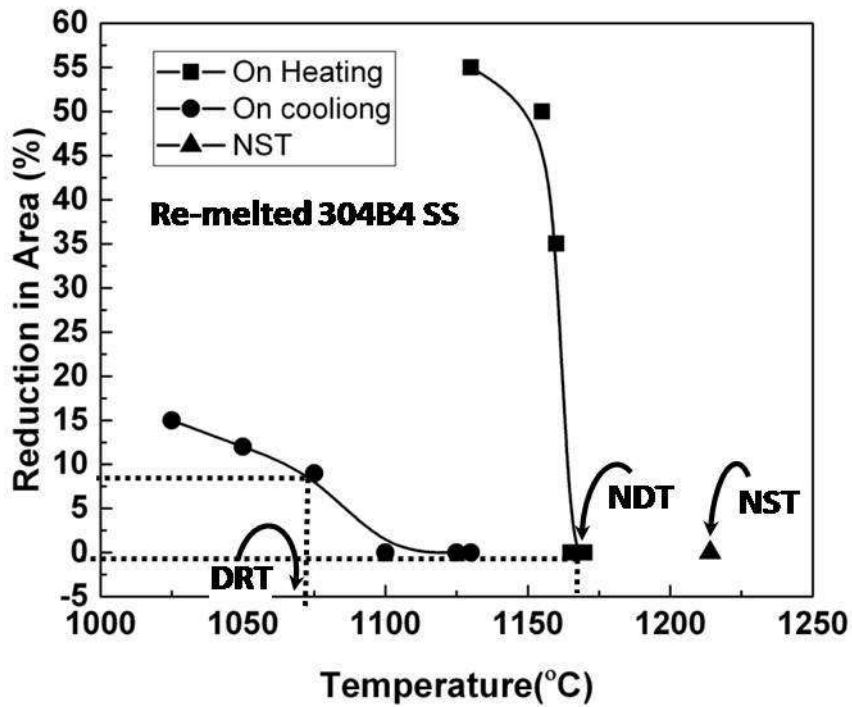


Fig.4.20 Hot ductility curve obtained for re-melted 304B4 SS from hot ductility experiments using “Gleeble™” thermo mechanical simulator.

Table 4.4 Summary of hot ductility test results of re-melted SS 304B4.

Sample	NST	NDT	DRT	NDR (NST-DRT)	CF (%)
PMZ simulated specimen	1214°C	1165°C	1075°C	139	12%

The NST and NDT values obtained for fused specimen are 1214°C [1487 K] and 1165°C [1438K] respectively which are almost similar to that obtained in base metal specimens. However, DRT obtained for fused specimen is 1075°C [1348 K] which is considerably lower than that obtained in base metal. Accordingly, the value of Nil Ductility Range (NDR) [NDR = NST-DRT] for fused specimen is 139°C. The cracking factor (%CF) calculated using equation (3) for fused 304B4 is 12%.

Overall, from the results of hot ductility experiments it is observed that the susceptibility for liquation cracking of fused 304B4 is higher than the base metal.

#### ***4.2.8 Microstructural features of hot cracks in Varestraint tested specimens***

##### ***4.2.8.1 Transvarestraint tested specimens of SS 304B4 base metal***

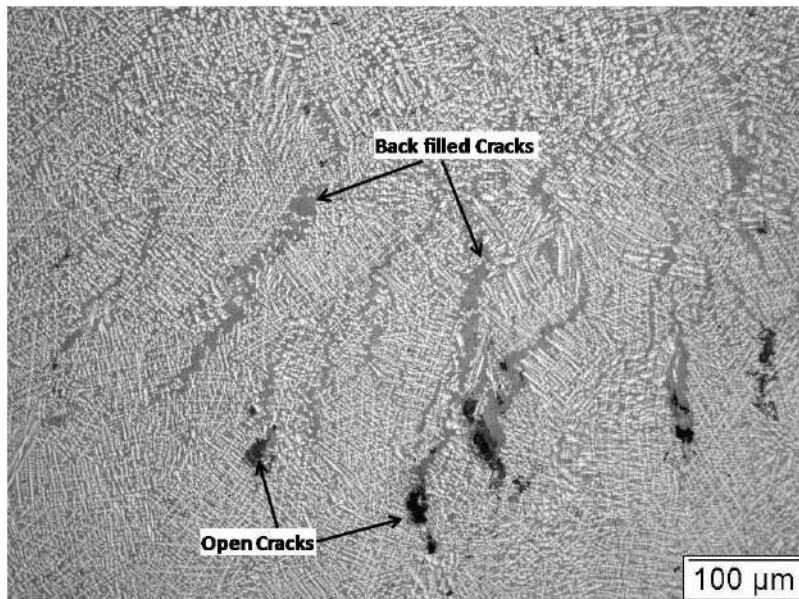


Fig.4.21 Microstructure of 304B4 SS specimens subjected to TVT showing prominent backfilled cracks in the fusion zone

Microstructure of TVT specimen subjected to 4% augmented strain is presented in Fig.4.21. The microstructure shows that the fusion zone consists of austenite dendrites

and interdendritic eutectic borides. Also, it shows solidification cracks present along the interdendritic regions partially backfilled by the eutectic constituents.

#### 4.2.8.2 Spot Varestraint tested specimens of SS 304B4 base metal

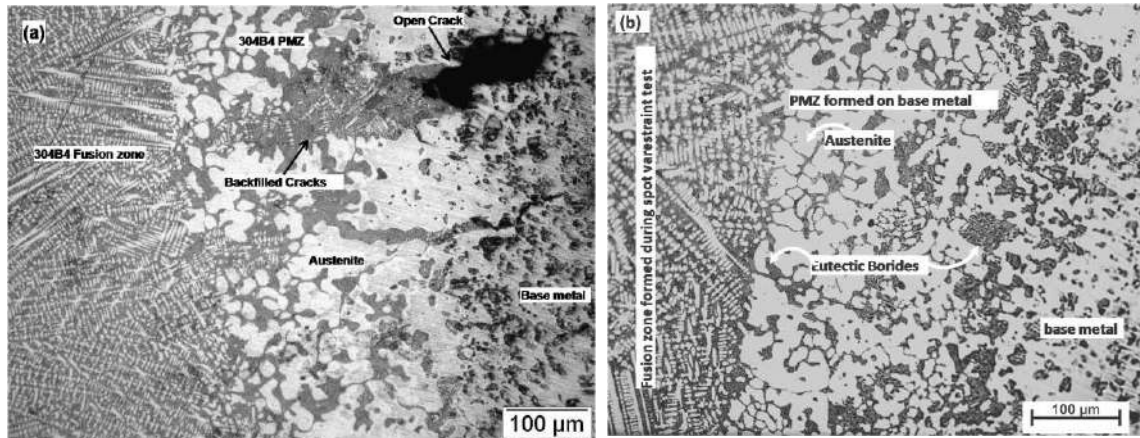


Fig.4.22 Microstructure of 304B4 SS specimen (a) subjected to augmented strain during SVT showing PMZ formed in the base metal region and back filled cracks (b) not subjected to strain during SVT.

Figure 4.22(a) shows the microstructure of SS 304B4 fusion zone and PMZ in base metal obtained from the spot Varestraint test. Most of the cracks in the fusion zone and PMZ are backfilled by eutectic liquid. Only a small portion of the cracks are open and they lie in the base metal. It can be seen that PMZ microstructure consists of austenite grains intergranularly separated by heavily liquated grain boundaries. It may be noted that the liquation in this region has not occurred uniformly as the distribution of borides is non uniform. Fig.4.22(b) shows the microstructure of base metal PMZ that was not subjected to augmented strain during spot varestraint test. The areal fraction of eutectic phases present exclusively in the PMZ region was estimated to be  $\sim 0.3$  using *Image J* software.

#### 4.2.8.3 Spot Varestraint tested specimens of fused SS 304B4

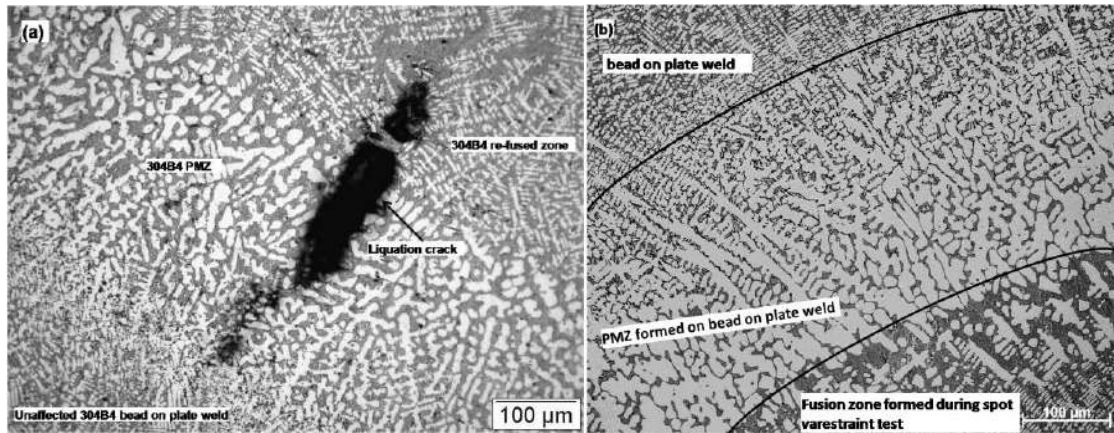


Fig.4.23(a) Microstructure of fused 304B4 SS specimen subjected to SVT shows hot crack extending from re-fused zone to the PMZ formed in the fused region (b) microstructure of PMZ formed on fused 304B4 SS not subjected to augmented strain.

Figure 4.23(a) shows the microstructure of re-fused region and PMZ in fused 304B4 after spot Varestraint test at 4% augmented strain. From the figure it is discernable that the weld metal has solidified as austenite dendrites with austenite/ boride eutectic in the interdendritic regions. It is also observed that the austenite dendrites in the PMZ are coarser than that present in the re-fused zone or in the unaffected bead on plate weld. The microstructure also shows that the PMZ region predominantly consists of open cracks partially back filled in the re-fused zone. Fig.4.23(b) shows the PMZ formed on fused 304B4 SS (bead on plate weld) during SVT without application of augmented strain. The areal fraction of interdendritic eutectic in the PMZ was estimated to be  $\sim 0.19$  using *Image J* software.

## 4.2.9 Microstructures of hot ductility tested specimens

### 4.2.9.1 SS 304B4 base metal

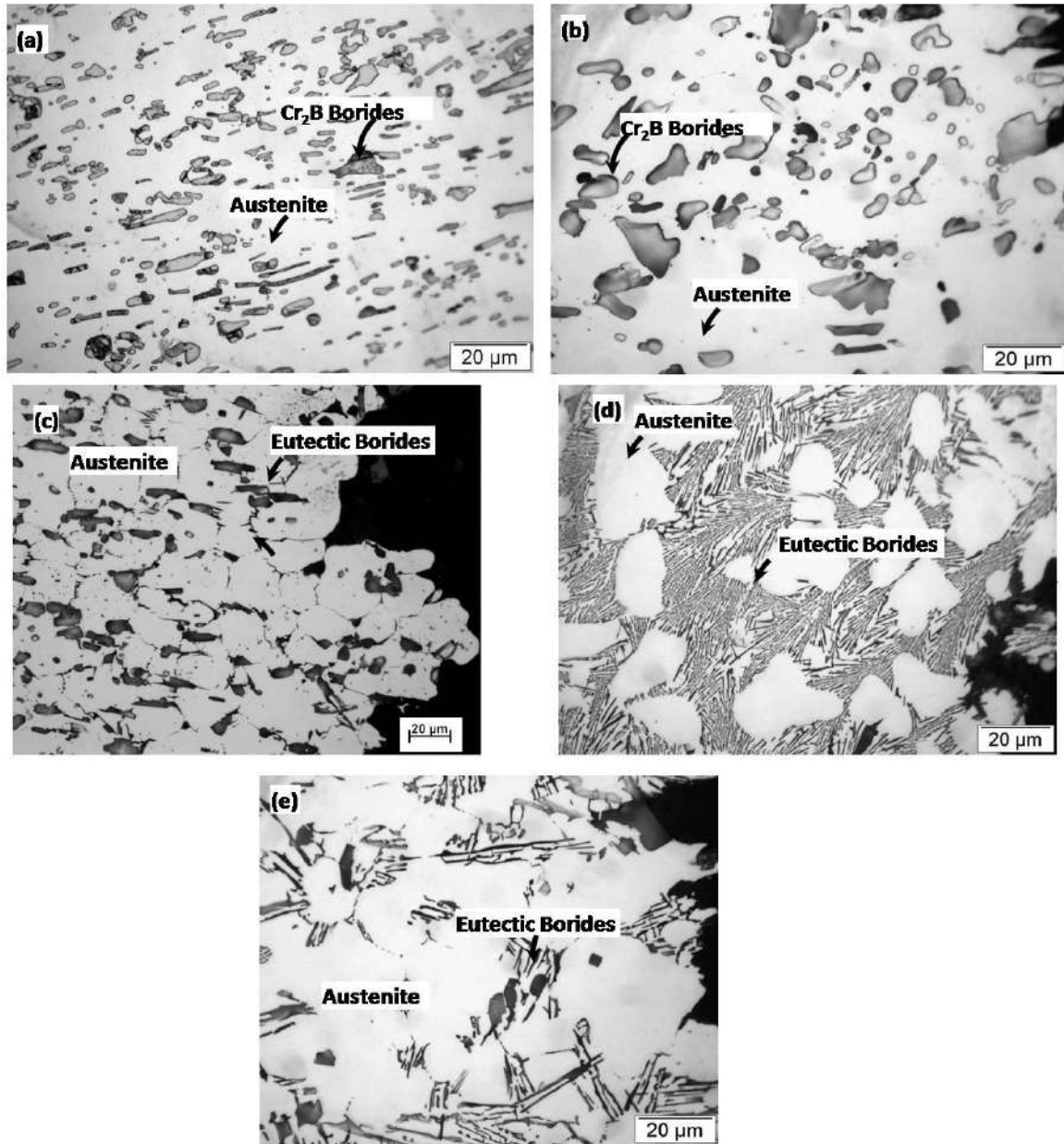


Fig.4.24 Microstructures of (a) 304B4 base metal (b) hot ductility tested base metal specimens at NDT (1165°C), (c) NST (1220°C), (d) Above DRT (1150°C), (e) At DRT (1125°C)

(Fig.4.24(a) and (b)) show coarsening and agglomeration of borides in NDT specimens while NST specimen shows complete grain boundary liquation. The DRT specimens tested at 1150°C and 1125°C show higher level of eutectic boride than the NST specimen. However, the 1125°C specimen shows a lower volume fraction of eutectic boride than the 1150°C specimen (Fig.4.24(c) and (d)). These observations are attributed to the testing temperature and hold time. In the NST specimens, the incipient grain boundary liquation is reflected in the microstructure. In the DRT specimens the 2 s hold is considered to be adequate to cause grain boundary liquation which, on quenching, shows up as the fine “finger print” morphology eutectic phase. Microstructure of DRT specimens tested at 1150°C and 1125°C shown in Fig.4.24(c) and (d), show drastic changes in the fraction of eutectic borides between them. This can be explained as follows. Due to very high heating rate given in the hot ductility tests, the NST temperatures determined from these tests is expected to be much higher than the solidus temperature for the alloy. However, for determination of DRT, a hold time of 2 s is given at the test temperature before the specimen is fractured, if the test temperature is above DRT, then it is likely that this temperature would also be above the solidus temperature of the alloy and isothermal holding, even for a short time of 2 s, can allow continued melting of the alloy at the test temperature, producing high volume fraction of eutectic phases and retained on subsequent cooling. In contrast, the DRT is expected to be lower than the solidus temperature and all the liquid phase formed during heating from NDT to NST and subsequent cooling has already solidified at the DRT, where testing is conducted. Accordingly, it is reasonable to expect that volume fraction of the eutectic phase is

expected to be minimum for the NST specimen and maximum for the specimen tested above DRT and in between these two for specimen tested at DRT. A careful examination of microstructures given in Fig. 4.24 (b)-(d) indicates that the above arguments holds true.

#### 4.2.9.2 Fused SS 304B4

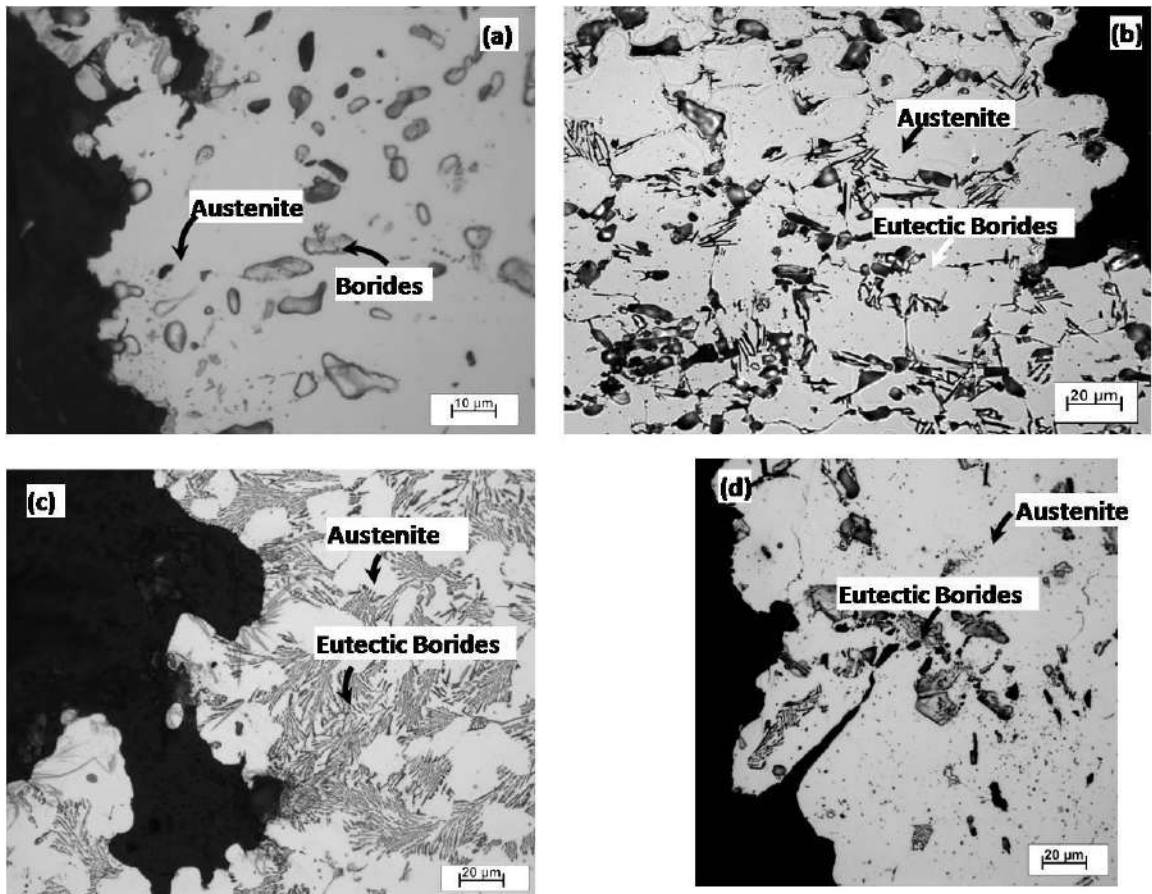


Fig.4.25 Microstructures of hot ductility tested re-melted 304B4 SS specimen (a) NDT (1165°C) (b) NST (1214°C) (c) above DRT (1100°C) (d) at DRT (1075°C).

Since it is not possible to simulate completely molten and re-solidified microstructure as we observe in the weld fusion zone using the “Gleeble™” thermo mechanical simulator. Partial melting and subsequent re-solidification of the material was achieved without any significant physical damage to the specimen, by subjecting the

specimen to a thermal cycle with a peak temperature of NST of the base metal as described in section 3.4.3(a) of Chapter 3. As already shown in Fig. 4.24 (c), microstructure of the partially melted specimen, consists of partially melted and re-solidified boride eutectic and un-melted primary austenite grains. Specimens with this simulated microstructures were subsequently used to determine NST, NDT and DRT for the (partially) fused SS 304B4. The specimen tested at NDT show coarsening of eutectic borides and cracking at boride matrix interfaces is observed at the fracture edges as seen in Fig.4.25(a). The microstructure of NST specimen of fused 304B4 shows partial melting of borides and complete grain boundary liquation and is shown in Fig.4.25(b). The microstructures of specimens tested at 1100°C and at DRT (1075°C) are shown in Fig.4.25(c) and (d) respectively. The eutectic fractions in Fig.4.25(c) is higher than that found in the NST specimen shown in Fig.4.25(b). For the specimen tested at DRT, the microstructure near the fracture surfaces shows areal fraction of eutectic borides is lower than that of the specimen tested above DRT. These observations are similar to those seen in the microstructures of specimens tested for hot ductility of base metal and the same explanation given for the results obtained for base metal is valid here too.

#### ***4.2.10 Fracture surfaces of hot ductility tested specimens***

##### ***4.2.10.1 SS 304B4 base metal specimens***

The fractographs of SS 304B4 base metal hot ductility specimens are shown in Fig.4.26. Fracture surface of NST specimen (Fig.4.26(a)) indicates complete grain boundary liquation which manifests as smooth surfaces evident in the fractograph. Fracture surface of specimen tested at NDT shows isolated locations of incipient liquation

in the matrix as indicated in Fig.4.26(b). Fractograph of specimen tested at DRT shows ductile mode of fracture as shown in Fig.4.26(c).

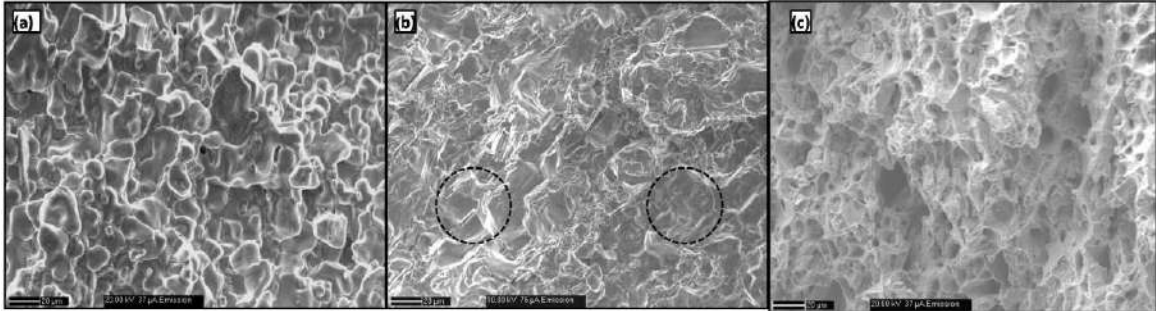


Fig.4.26 Fracture surfaces of SS 304B4 base metal specimens tested at (a) NST (b) NDT (c) DRT

#### 4.2.10.2 Fused SS 304B4 specimens

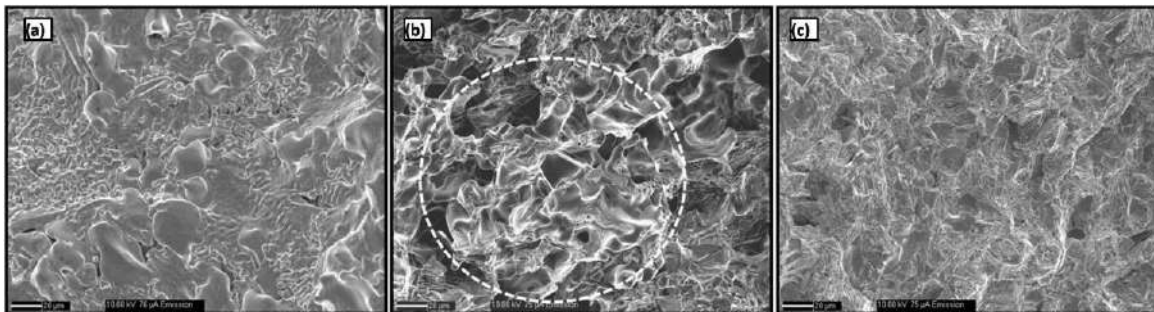


Fig.4.27 Fracture surfaces of hot ductility tested re-melted 304B4 specimens (a) NST (b) NDT (c) DRT

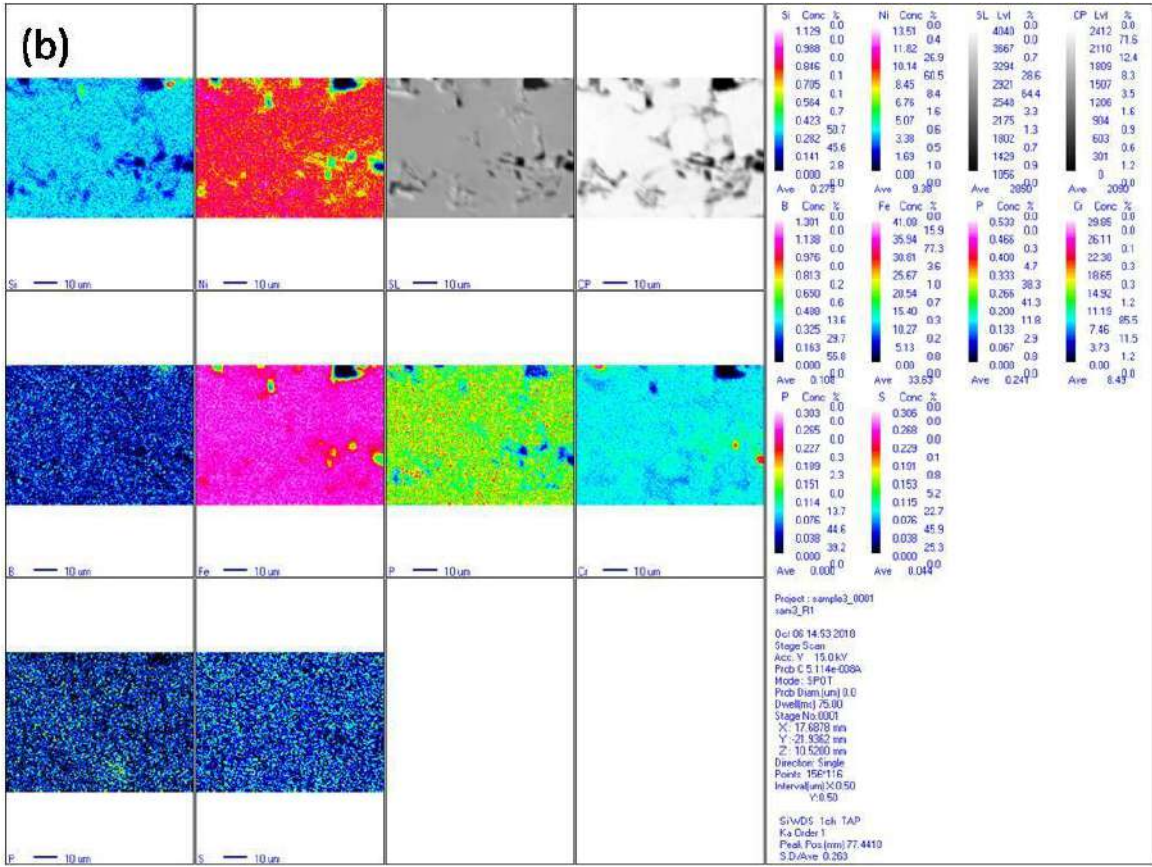
Fractographs obtained on the fracture surfaces of fused 304B4 hot ductility specimens are shown in Fig.4.27. Fused 304B4 specimens tested at NST show smooth surface features indicative of partial melting at the time of fracture as shown in Fig.4.27(a). In contrast, surface of specimen fractured at NDT shows predominantly cleavage mode of fracture with only isolated locations of liquation (encircled region of Fig.4.27(b)). Fracture surface of the specimen (Fig.4.27(c)) tested at DRT is similar to that of the specimen tested at NDT confirming the solidification is almost complete. The

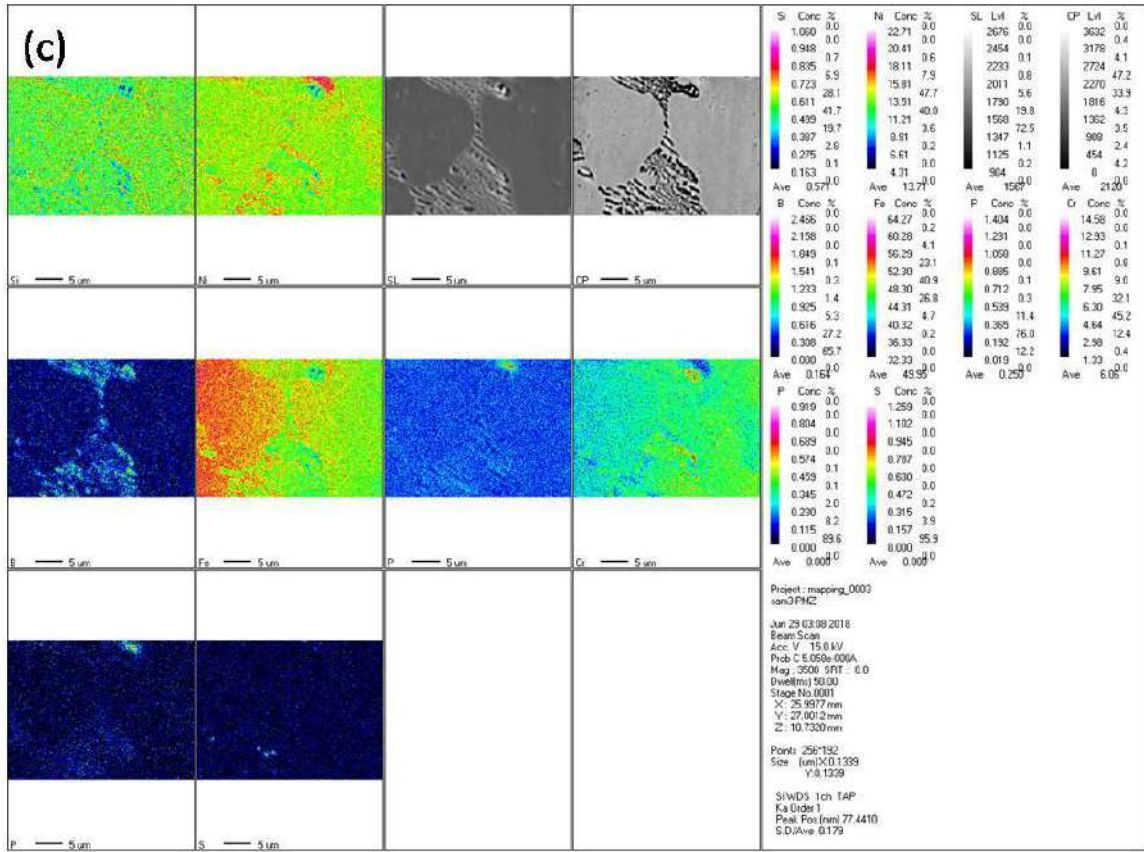
fractographs clearly show the existence of liquid film along the grain boundaries in NST specimen and some liquated regions in NDT specimen. Fracture surface of DRT specimen show features more or less devoid of liquid film.

#### *4.2.11 Electron Probe Micro Analysis (EPMA) of Hot ductility tested specimens*

Microchemistry of borides and austenite matrix of hot ductility tested specimens and SS 304B4 base metal were analyzed using EPMA technique and the elemental mapping obtained on each of the specimens are shown in Fig.4.28. Even though adequate characterization of base metal borides were carried out using SEM, XRD and TEM and the results of the same are discussed in the previous sections, EPMA on base metal specimen was carried out for comparison purposes. The elemental mapping obtained on base metal (Fig.4.28(a)) clearly indicate that borides present in the base metal consist of almost equal weight (0.3) fractions of Cr and Fe whereas those present in base metal NST specimens are rich in Fe and lean in Cr as shown in Fig.4.28(b). Also, the *on cooling* base metal specimens after heating up to NST shows that the borides are lean in Cr as shown in Fig.4.28(c). The elemental distribution in various phases of the fused specimen tested at NST is shown in Fig.4.28(d). It can be noted that the elemental distribution in this specimen is significantly different from that of the base metal. It is to be noted that the borides in this specimen seem to contain significant amount of Ni in addition to Fe and Cr. There also appears to be enrichment of Cr in the austenite matrix close to the boundaries where borides are present in the interdendritic region.







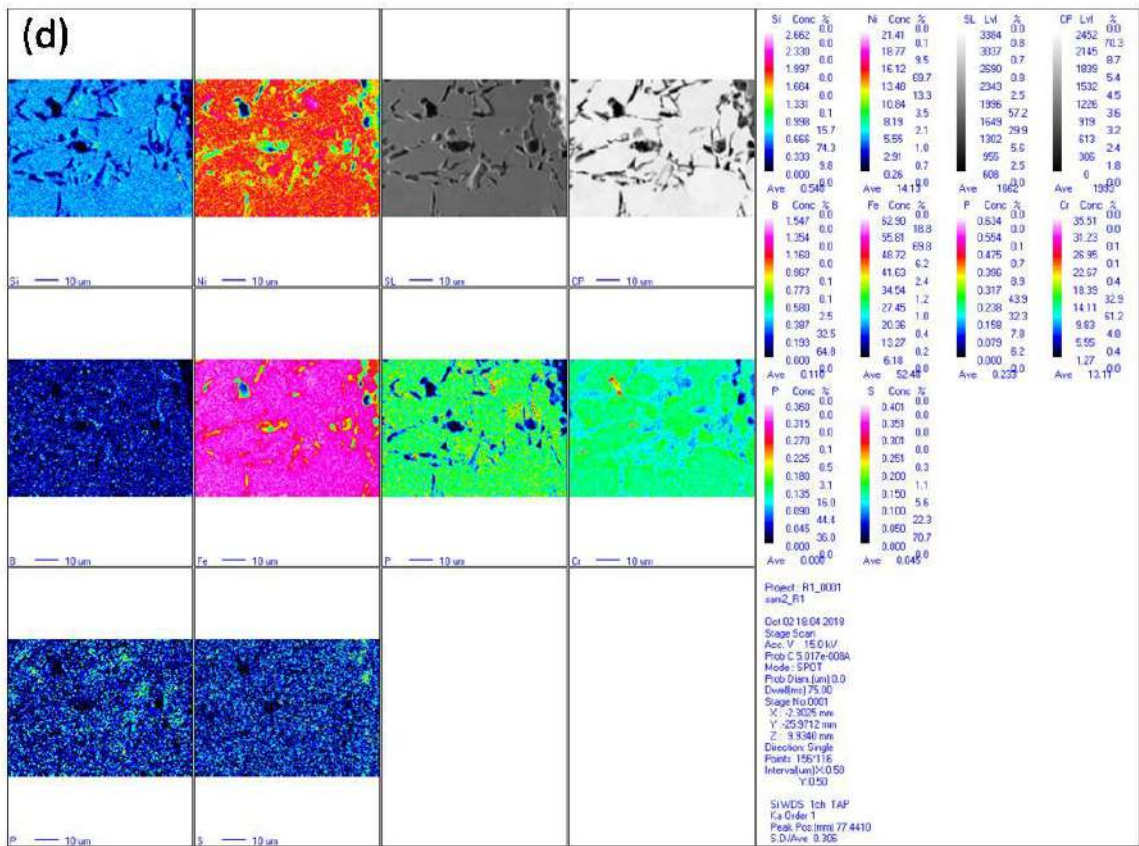


Fig.4.28 Elemental mapping performed using WDS/EPMA on (a) SS 304B4 base metal (b) SS 304B4 specimen tested at NST (c) SS 304B4 specimen on cooling from NST (DRT) (d) re-melted SS 304B4 specimens tested at NST.

Thus, EPMA analysis clearly reveals that the borides originally present in the base metal undergoes significant changes in the chemistry during melting and re-solidification that takes place during welding.

### 4.3 Discussion

#### 4.3.1 Equilibrium and non equilibrium transformations in SS 304B4

A comparison of equilibrium solidification with “Scheil-Gulliver” prediction show notable differences in the solidification sequence, transformation temperatures and phases formed during solidification of fused SS 304B4 from that of the 304B4 base

metal. From the equilibrium phase diagram in Fig.4.1, it can be observed that  $M_2B$  ( $(Fe,Cr)_2B$ ) type boride is stable at high temperature whereas,  $Cr_2B$  type boride is stable phase at room temperature. The results of XRD analysis and SAD obtained from TEM studies carried out on electrolytically extracted base metal borides shown in figures 4.8 and 4.9 conforms to the predictions of pseudo-binary phase diagram calculated for SS 304B4. In contrast, the non equilibrium prediction by Scheil's simulation (Fig.4.2) shows only  $M_2B$  ( $(Fe,Cr)_2B$ ) type of borides retained at lower temperature. It is to be noted that  $Cr_2B$  and  $M_2B$  type of borides show different crystal structures. The results of XRD analysis and SAD obtained from TEM studies carried out on electrolytically extracted borides from fused SS 304B4 produced by autogenous GTAW bead on plate weld shown in Fig.4.11 and 4.12 also partially complies with the Scheil's simulation shown in Fig.4.2. It is to be noted that Scheil's simulation shows only  $M_2B$  ( $(Fe,Cr)_2B$ ) type of borides to be formed during non-equilibrium cooling of SS 304B4 whereas, the characterization of borides extracted from fused SS 304B4 by XRD and TEM shows the presence of  $Fe_{23}(C,B)_6$  type of boride in addition to  $(M_2B)$   $(Fe,Cr)_2B$  type of borides that are rich in Fe. Formation of  $Fe_{23}(C,B)_6$  type of boride is not reported so far in the fusion zone of borated stainless steel. It is observed that  $Fe_{23}B_6$  forms very rapidly in other boron containing steels [80] and metallic glass forming compounds even on splat cooling [81]. It may be noted that carbides of type  $M_{23}C_6$  do not form as primary carbides from liquid metals whereas  $Fe_{23}B_6$  form first from liquid metal readily because these borides are of greater stability than the corresponding carbides and silicides [82]. The fusion zone consists of borides rich in Fe and lean in Cr as shown by the composition of Fe in  $M_2B$

((Fe,Cr)<sub>2</sub>B) type of boride in Fig.4.12(b) which is in agreement with the prediction by Scheil's solidification simulation. Formation of M<sub>2</sub>B type borides during solidification is also reflected in the *on cooling* DSC profile of base metal (Fig.4.4) with peaks at 1236-1240°C [1509-1504K] corresponding to formation of this phase. Also, lack of additional peak at lower temperatures indicates no further transformation of M<sub>2</sub>B borides to Cr<sub>2</sub>B during cooling as seen from Table 4.1. Similar transformation behavior except for small variations in temperatures are noticed for fused SS 304B4 in the DSC profile shown in Fig.4.5. Such observations in base metal and fused SS 304B4 are because cooling at 10 K/min during DSC experiment though comparatively slower than weld cooling rate, does not result in thermodynamic equilibrium at liquid – solid interface. This leads to appreciable segregation of solute elements and formation of non equilibrium phases.

Similar situation exists during solidification of weld metal also. High cooling rate experienced by the weld metal during solidification does not provide sufficient time for the equilibrium to be established. This in turn causes enrichment of solute elements in to remaining liquid. This ultimately, results in change in the composition of the remaining liquid metal from that of the nominal composition of the initial molten metal and segregation in the solidified metal. The solidification of solute enriched liquid is dictated by the local equilibrium at the solid –liquid interface. Overall, high temperature phases formed during solidification are retained down to room temperature in the weld metal. This leads to evolution of weld metal microstructure with phases which are not present in the base metal though composition of the base metal and the weld metal are the same. As a result of such non equilibrium transformations occurring in the weld zone, the

solidification range of the weld is 135°C which is increased by 45°C from the equilibrium freezing range (90°C) as shown in Fig.4.2.

#### ***4.3.2 Influence of non equilibrium transformation on hot cracking susceptibility***

The NDR and percentage cracking factor (% CF) determined for base metal using NDT, NST and DRT parameters obtained from hot ductility tests shows that the steel is highly susceptible to liquation cracking in the PMZ during welding. The large NDR is attributed to suppression of DRT sufficiently below the *on heating* NDT. The delay in ductility recovery in the specimen exposed to NST is clearly due to lowered solidus temperature of the Fe-rich eutectic borides. The observations are in line with the increased solidification temperature range of SS 304B4 obtained during non-equilibrium solidification simulation shown in Fig.4.2. As it is apparent from the microstructures of hot ductility tested specimens shown in Fig.4.24, the fraction of eutectic borides present at a temperature 25°C above the DRT is significantly higher than the fraction of eutectic borides present at DRT. This is precisely due to formation of Fe-rich eutectic borides formed *on cooling* from NST as shown in Fig.4.28(b). This shows that the non equilibrium cooling occurring in PMZs of 304B4 base metal increases the risk of liquation cracking.

Comparing NDR (139°C) and % CF (12%) of fused specimens with that of base metal reveals that there is a substantial increment of ~84% in %CF and NDR for fused specimens. The NDR is clearly proportional to the solidification range predicted by Scheil's model for the re-melted eutectic liquid shown in Fig.4.3 Microchemistry of eutectic borides present in the specimen above DRT shows that the borides are highly

enriched in Fe. Therefore, the hot ductility results of SS 304B4 base metal and fused specimens shows that the alloy is highly susceptible for liquation cracking in PMZ that is formed in the base metal and further more in the PMZ formed in fused 304B4.

#### ***4.3.3 Effect of back filling in hot cracks formed in SS 304B4***

It is found that though solidification range for 304B4 base metal is as high as 135°C (Fig.4.2), the solidification and liquation cracking susceptibility observed in the Varestraint test results as shown in Figs.4.13 and 4.14 is low. This behavior is attributed to effective back filling of the eutectic liquid in the cracks formed during solidification by capillary action as also observed and reported by Shinoda et al. in austenitic stainless steels containing 0.5-2 wt.% boron [6]. It may be appropriate to mention here that in case of alloys like 304B4 with near eutectic composition (Fig.4.1) where appreciable volume fraction of eutectic phase is expected to form during solidification, “Gleeble<sup>TM</sup>” hot ductility tests and Varestraint tests give contrasting results while assessing the susceptibility for hot cracking. Hot ductility tests give the temperature range over which the material is susceptible for cracking but does not consider the possibility of back filling whereas Varestraint test results reveals the net result of the combined effect of cracking and back filling.

Now coming to the liquation cracking susceptibility of fused 304B4, it is reasonable to expect fused zone to have higher susceptibility to hot cracking than the base metal because of segregated microstructure which would readily re-melt on reheating. This is precisely what is revealed from the comparison of the results of the spot Varestraint test conducted on the 304B4 base metal and on fused specimens prepared by

making autogenous bead on plate welds on the specimen. In contrast to hot cracking susceptibility results found on base metal of 304B4, the results of hot ductility and spot Varestraint tests carried out on fused specimens are consistent and both indicate high susceptibility to liquation cracking on the basis of NDR and BTR values respectively. The following reasons can be attributed to higher liquation cracking susceptibility of re-melted 304B4 SS than the base metal. Eutectic  $M_2B$  borides is formed during solidification of base metal in the bead on plate weld as indicated by the solidification simulation of SS 304B4 base metal in Fig.4.2 and observed in XRD and TEM analysis (figures 4.11 and 4.12). During SVT carried out on bead on plate weld, the eutectic  $M_2B$  borides undergoes liquation *on heating* cycle in the PMZ region formed around the spot weld as indicated in the *on heating cycle* of DSC analysis of fused SS 304B4 in Fig.4.5 and the same is confirmed by liquation indicated by the fractograph of re-melted 304B4 SS after NDT test in Fig.4.27. These liquated  $M_2B$  boride eutectic has considerably increased the solidification temperature range as predicted in the Scheil's solidification simulation in Fig.4.3. In addition to lower solidus temperature noticed for the fusion zone during re-melting of eutectic phases, poor back filling of the cracks by eutectic liquid also seems to contribute to higher cracking susceptibility of fused specimen during spot Varestraint test than that of the base metal.

#### ***4.3.4 Mechanism of liquation cracking in PMZ***

In general backfilling of the liquation cracks formed in PMZ of a weld is assumed to occur due to liquid of eutectic composition flowing from the solid liquid interface just ahead of the crack [83] and can be seen in the microstructure shown in Fig.4.22. Details

of mechanisms of formation of liquid in the PMZ of base metal and fused 304B4 based on the equilibrium phase diagram and non equilibrium solidification simulation depicted in Fig.4.1 and 4.3 respectively and subsequent backfilling in the liquation cracks are explained based on the microstructures shown in figures 4.29 and 4.30. Though pseudo binary phase diagram cannot be used for calculations of quantitative analysis of phase fractions, it is used here to qualitatively compare and understand the transformations occurring in the PMZ. The compositions of liquid phases anticipated in the PMZ of base metal and bead on plate weld (fusion zone) in SVT are marked in the phase diagram in Fig 4.29. Figure 4.29 also shows a schematic representation of the temperatures experienced by the various zones in specimens of spot Varestraint tests conducted on base metal and autogenous bead on plate weld with the corresponding microstructures and the temperature profiles experienced at these locations.

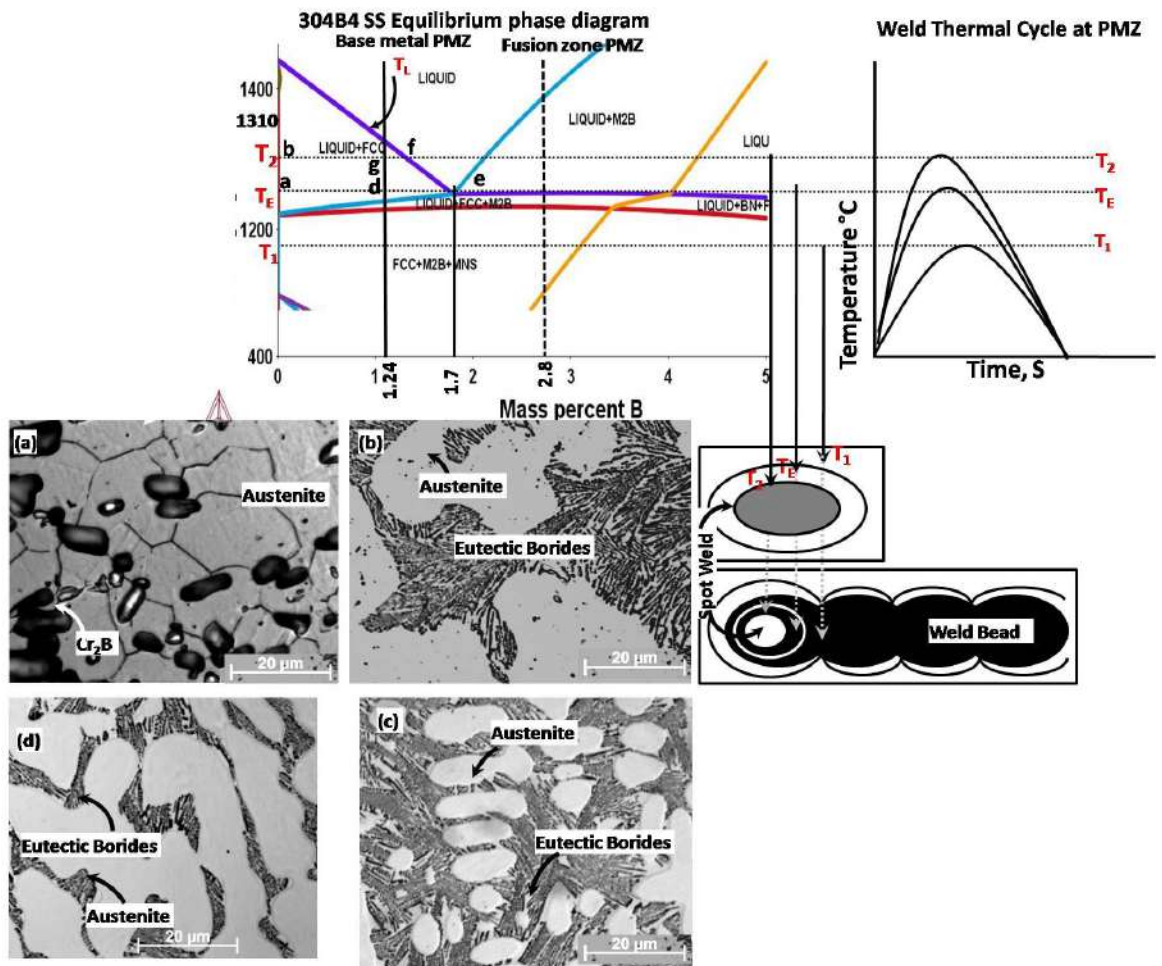


Fig.4.29 Schematic representation of thermal cycle and phase transformations experienced by various regions of 304B SS PMZ with respect to the weld thermal cycle and its corresponding microstructures (a) 304B4 SS base metal (b) PMZ in base metal (c) unaffected region of 304B4 SS bead on plate weld (d) PMZ in bead on plate weld formed during spot Vareststraint test

(i) Base Metal PMZ

Microstructure in Fig.4.29(a) shows that the location is exposed to temperature less than  $T_E$  and the morphology and distribution of borides is similar to that observed in the base metal microstructure. The microstructure in Fig.4.29(b) represents a location where the peak temperature during welding is between  $T_E$  and  $T_2$ ; we observe “finger print” morphology typical to eutectic solidification surrounded by boride free austenite

phase. According to equilibrium phase diagram, the temperature ( $T_E$ ) is 1240°C. Upon heating, the liquation of the borides occurs via the eutectic reaction  $\gamma + Cr_2B \leftrightarrow L$  at 1240°C during heating while during cooling this eutectic liquid solidifies and the proeutectic austenite remains. With reference to phase diagram in Fig.4.29, the fraction of liquid at  $d$  is  $ad/ae$  as per lever rule. In PMZ, where the temperatures lie between  $T_E$  and  $T_2$ , as the peak temperature rises above  $T_E$ , the composition of liquid changes along the liquidus line from point  $e$  at  $T_E$  to significantly above  $T_E$ , say point  $f$ . The fraction of the liquid at  $T_2$ ,  $bg/bf$  is much greater than at  $T_E$  ( $ad/ae$ ) resulting in more liquation by melting of austenite phase surrounding the eutectic liquid. The boron content of the liquid in the PMZ range between 1.24 to 1.7 wt.% as observed in Scheil's simulation shown in Fig.4.2. During the cooling part of the weld thermal cycle, some fraction of austenite is nucleated from the liquid and finally eutectic phase is formed on reaching  $T_E$ . Since the PMZ experiences a range of temperatures from  $T_E$  to  $T_2$ , the extent of melting of austenite increases on approaching  $T_2$ . Therefore, base metal PMZ consists of unmelted austenite, austenite nucleated from the liquid and the eutectic phase mixture shown in Fig.4.29 (b) exposed to peak temperatures between  $T_2$  and  $T_E$  respectively. In addition, grain growth is also observed in extent being more towards the fusion line possibly due to higher temperatures and the liquid penetrated along the boundary region which can be seen in Fig.4.22(b). Though grain growth can hinder back filling of cracks present in the PMZ by the liquid from fusion zone, it appears that since the fraction of eutectic liquid in PMZ is high (0.30) (estimated using PMZ microstructures shown in Fig 4.22(b)), backfilling of cracks is unaffected.

*(ii) Bead on Plate weld/Fusion zone PMZ*

The microstructure in 304B4 SS bead on plate weld consists of dendritic austenite and interdendritic mixture of eutectic phases as shown in Fig.4.29(c). In the PMZ formed on bead on plate weld, as shown in section 4.2.2, the interdendritic liquid has hyper eutectic composition due to further segregation occurring during re-melting. The boron content in the PMZ changes from 1.77 to 2.8 wt.% as the solidification in the interdendritic liquid progresses. During SVT, as the temperature rises above  $T_E$ , the interdendritic eutectic phase which has hyper eutectic composition undergoes complete liquation and dendritic austenite remains in the PMZ. During cooling, the borides precipitate from the liquid and finally on reaching  $T_E$ , the remaining liquid solidifies as eutectic phase. The volume of this liquid is less than the original volume of liquid present in the bead on plate weld since up to 0.12 fraction of  $M_2B$  type of boride form as primary phase and  $\gamma + M_2B$  borides transform to from the liquid as shown in Fig.4.3, the non equilibrium cooling further enriches the liquid in boron. Hence, the fraction of liquid reduces to 0.53 ( $f_{\text{liquid}}$  in the fusion zone 0.65-0.12) on re-melting from 0.65 fraction that was present in the fusion zone of bead on plate weld. Since simultaneous grain growth occur at these peak temperatures, liquid formed in the interdendritic region of the PMZ penetrate [41] along the boundaries and hence reduce the volume fraction of grain boundary area and effective amount of liquid present in this region as shown in the Fig.4.23(b). The grain growth leads to decreased number of channels for liquid and obstruct the flow of liquid [25,41] within the PMZ formed in bead on plate weld a shown in Fig.4.29 (d) as compared to the fusion zone microstructure shown in Fig.4.29(c).

Quantitative measurements of areal fractions of eutectic liquid in fusion zone and PMZ obtained using image J software are  $52\pm 3\%$  and 19% respectively.

However, it is also important to note the microstructural differences between the PMZ formed in base metal, PMZ formed in fused specimen and the original microstructures from which the PMZs are formed. The fraction of eutectic liquid formed in the PMZ of base metal is dependent on the volume of boride precipitates available at that location. If the density of boride particles per unit area is high, the volume of eutectic liquid formed is also correspondingly high. Whereas, the fraction of liquid formed in the bead on plate weld occurs in the interdendritic regions as borides are not present elsewhere in the microstructure. Hence, on comparison of areal fractions of eutectic phase present in Fig.4.29 (b),(c) and (d) it is clearly evident that eutectic fraction is qualitatively higher in base metal PMZ than PMZ formed on bead on plate weld. These observations are consistent with the simulations performed using Scheil's model.

*(iii) Backfilling of the cracks in PMZ by the liquid*

Figure 4.30(a) shows the PMZ formed in fused specimen during spot Vareststraint testing conducted at 2% strain, Figure 4.30 (b) is the PMZ formed on a similar specimen that was not subjected to augmented strain. On comparing Fig.4.30(a)&(b), it is quite discernable that qualitative area fraction of eutectic liquid in the PMZ microstructure of Vareststraint specimen tested at 2% augmented strain is higher than that present in the microstructure taken from specimen without application of strain. This is possible only if cracks formed in this zone are healed by the molten metal in the re-fused zone drawn into this zone by capillary action. From these observations it can be deduced that eutectic

liquid from the re-fused zone is drawn by capillary action into interdendritic regions of PMZ due to differences in liquid potential present at the time of straining during the Varestraint experiment. On comparing the specimen tested at 2% augmented strain (Fig.4.30(a)) with that of specimen tested at 4% strain (Fig.4.23(a)), it is observed that complete backfilling has not occurred in the latter specimen. This is attributed to inadequate fraction liquid flowing from the re-fused and within the PMZ regions of bead on plate weld.

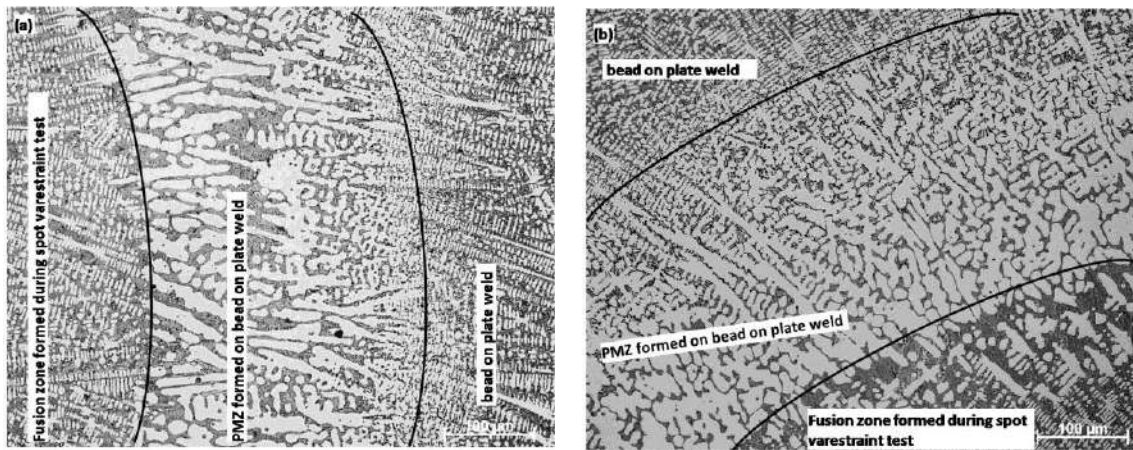


Fig.4.30 Microstructure of PMZ formed in 304B4 SS bead on plate weld (a) after applying 2% strain during spot varestraint test (b) without applying strain.

From the macrostructure of 304B4 SS weld joint produced using standard E309 electrode explained clearly in section 1.2 of Chapter 1, PMZ is formed in base metal and un-mixed zone. The microstructure of PMZ of un-mixed zone is similar to that of PMZ formed during SVT of bead on plate weld. Hence, PMZ formed on fused region formed in this alloy during multipass welding on subsequent re-melting, is susceptible to liquation cracking. This is because the borides present in the re-melted regions differ in chemistry, morphology and volume fraction from those present in the base metal. As a

result of variation in the chemistry of borides, NDR determined for fused specimen is 50°C higher than the base metal. Also, reduction in the volume fraction of the eutectic liquid and the coarsening of dendrites in PMZ formed in fused region on reheating makes backfilling difficult.

From the above study, it is quite discernable that high liquation cracking sensitivity of the re-melted fusion zone (un-mixed zone in multipass welding) may also be a reason for extensive cracking observed during fabrication of components made from this steel by multipass welding using E309 consumables, in spite of choosing base metal composition that facilitate back filling of the crack and welding consumable that is resistant to hot cracking.

#### **4.4 Summary**

1. Solidification and liquation cracking susceptibility of SS 304B4 evaluated using Varestraint tests show low cracking susceptibility for the alloy due to effective back filling of the eutectic borides in the hot cracks formed during solidification.
2. Hot ductility experiments reveal higher susceptibility for liquation cracking in the PMZ formed in fused zone than that formed in SS 304B4 base metal.
3. Liquation cracking susceptibility of PMZ formed in SS 304B4 base metal determined using hot ductility and Varestraint tests show contradictory results. Varestraint test results reflect the combined effect of back filling and high solidification temperature range for the alloy, while the hot ductility test results reveals only the effect of large solidification range for the alloy.

4. Melting and subsequent solidification of the SS 304B4 results in significant changes in the chemistry, morphology, volume fraction and distribution of the borides in the steel. Borides present in the fused zone or PMZ of the steel is rich in Fe and lean in Cr. Differences observed in the hot ductility behavior of the PMZ and hot cracking susceptibility of PMZ and fused zone (assessed using Varestraint testing) from those of the base metal can be attributed to this.

5. Though volume fraction of the eutectic phase in the 304B4 fusion zone is high after first melting, its volume fraction significantly comes down on partial re-melting, which in turn makes back filling of the cracks formed in the final stages of solidification difficult. This also could be contributing to high cracking susceptibility of PMZ formed on fused zone of this steel.

## **CHAPTER 5**

### **WELD METAL LIQUATION CRACKING IN SS 304B4 WELD**

#### **JOINT PREPARED USING E309 ELECTRODE**

##### **5.1 Introduction**

In the previous chapter, results of the studies on liquation cracking susceptibility of PMZs formed in SS 304B4 base metal and fusion zone are presented along with that of the solidification cracking susceptibility of the steel. In multipass welding, deposition of every layer of weld metal on previously deposited weld metal can produce a PMZ in the fusion zone or weld metal. In fact, total area of PMZs formed in the weld metal is likely to be much more than that of the PMZs formed on base metal on either side of the weld metal. As base metal PMZ, the PMZs formed in the weld metal can also be susceptible to liquation cracking. Since the standard welding consumable recommended for welding borated stainless steel (in the present study SS 304B4) is E309, which has a composition different from that of SS 304B4 and does not have intentional addition of boron in the welding consumable, there is an additional complication of dilution of the weld metal by the base metal which introduces boron into the weld metal making it susceptible to liquation cracking. To the best of our knowledge, no work on the effect of dilution from the borated stainless steel base metal on the cracking susceptibility of the weld joints is reported so far; even though multipass welding of borated stainless steel with E309 electrode is very common for fabrication of components from this class of steel. Hence, in this chapter focus is on the hot cracking susceptibility of the weld metal of SS 304B4 weld joint prepared using E309 electrode. For this purpose, specimens extracted from

weld pads fabricated using E309 were used. Microstructural variation observed in the present study form the basis for the discussions. Solidification cracking studies on 309 weld metal is carried out as this would not be meaningful because the undiluted E309 weld metal is inherently resistant to solidification cracking.

## 5.2 Preparation of Spot Varestraint Test specimens

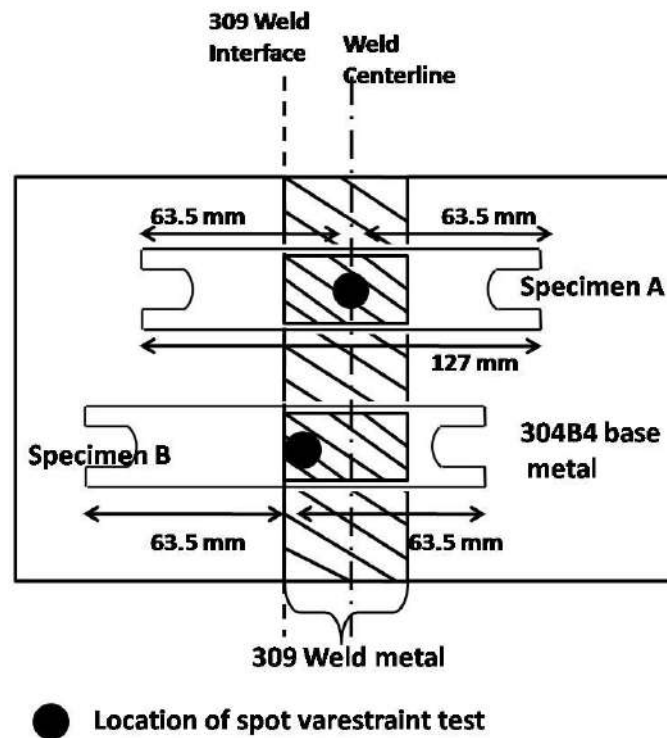


Fig.5.1 Schematic representation of extraction of Varestraint test specimens from 304B4 SS weld joint prepared using E309 electrode and location of spot Varestraint test conducted on the specimens.

Specimens for spot Varestraint tests were extracted from the weld joint prepared using E309 electrode and parameters mentioned in Table 3.3 of Chapter 3. Two types of specimens were prepared from the weld joints; one with the center of the weld joint matching with the specimen center and another with one of the fusion boundary of the weld joints falling near the center of the specimen. Extraction of these two type of

specimens and the location of the spot weld on the specimen for the spot Varestraint test are schematically shown in Fig. 5.1. In the former, spot weld during testing is made on the weld metal with minimum dilution from the base metal while in the latter, it is made at location where effect of dilution from the base metal is expected to be maximum.

Spot Varestraint tests were conducted as per the procedure mentioned in section 3.4.2 and parameters mentioned in Table 3.4 of Chapter 3.

### 5.3 Results

#### 5.3.1 Microstructures of different zones of SS 304B4 weld joint prepared using E309 electrode

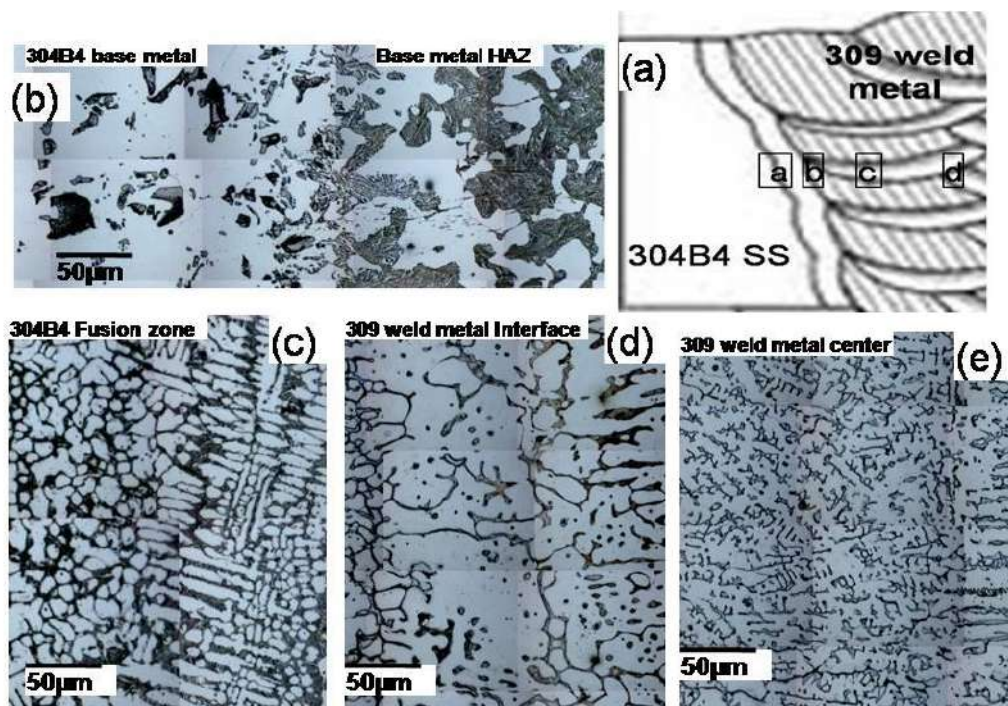


Fig.5.2 (a) Schematic of 304B4 SS weld joint. Microstructure of various zones of 304B4 SS weld joint prepared using 309 electrode (b) base metal PMZ (c) 304B4 unmixed zone (d) 309 weld metal affected by base metal dilution (e) undiluted 309 weld metal.

Fig.5.2 (a) shows the various zones of the weldment and Fig.5.2(b) to (e) show their microstructures. Fig.5.2(b) shows the microstructure of unaffected SS 304B4 base metal and the partially melted zone (PMZ) formed during weld thermal cycle. Figure 5.2(c) shows the un-mixed zone which is a thin layer of molten and re-solidified SS 304B4. Formation of unmixed zone is attributed to significant difference in melting points between the base metal and the weld metal [84,85]. Fig.5.2(d) shows the microstructure of 309 weld metal diluted by base metal and is a continuation of the un-mixed zone. It comprises of austenite dendrites and interdendritic eutectic phases. At the center of the weldment, undiluted 309 weld metal comprising of only austenite dendrites and delta ferrite is observed (Fig.5.2(e)). Therefore, it can be stated that the weld joint prepared using E309 consumable consists of an array of zones with considerable variation in the microstructures.

### ***5.3.2 Microstructural features of 309 weld metal diluted by base metal***

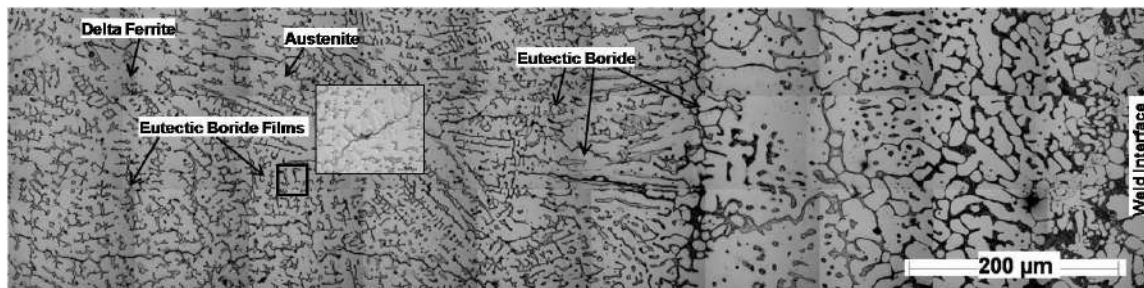


Fig.5.3 Microstructure of 309 weld metal affected by base metal dilution. The image shows the weld interface at the right side and weld center towards the left. Bright contrast is austenite, grey contrast is delta ferrite and dark contrast is eutectic phase.

Figure 5.3 shows microstructural variations caused by the dilution of 304B4 base metal in the weld metal in more detail; with the effect of dilution decreasing from the weld interface to the weld center. It can be observed that area fraction of eutectic borides

(dark contrast) decrease from weld interface towards the center of the weld metal. On the other hand, fraction of delta ferrite (grey contrast) increases from the interface towards the weld center which can be clearly seen from Fig.5.3. Hence, we could observe that the delta ferrite present near the interface is very low whereas, high fraction of skeletal/lacy delta ferrite is present towards the weld metal center. In other words, it can be said that near the weld interface the solidification mode is primary austenitic whereas slightly away, it changed to primary ferritic mode. This is a clear effect of modifications occurred in weld metal chemistry due to base metal dilution.

**5.3.3 Dilution of weld metal by the base metal in the weld joint made using E309 Electrode**

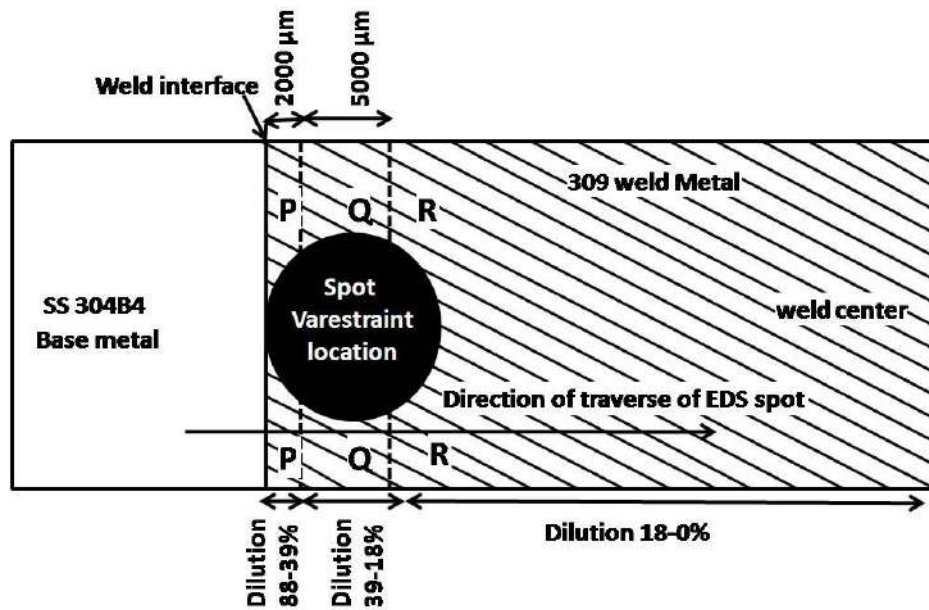


Fig.5.4 Schematic of SS 304B4 weld joint prepared using E309 electrode showing the locations of spot varestraint test, direction of spot EDS analysis and different zones in the weld metal diluted by base metal.

From the semi quantitative spot EDS analysis, performed at an interval of 100  $\mu\text{m}$  across the weld interface of SS 304B4 weld joint produced using 309 electrode, dilution of the weld metal by base metal was estimated. Figure 5.4 shows a schematic of SS 304B4 joint prepared using E309 electrode indicating the location of spot Varestraint test, direction of traverse of EDS spot across weld interface. The weld metal, including the spot which was re-melted during spot Varestraint test is broadly divided into P,Q and R in Fig.5.4 and wt.% of Fe, Cr and Ni estimated from SEM-EDS at these locations are given in Table 5.1.

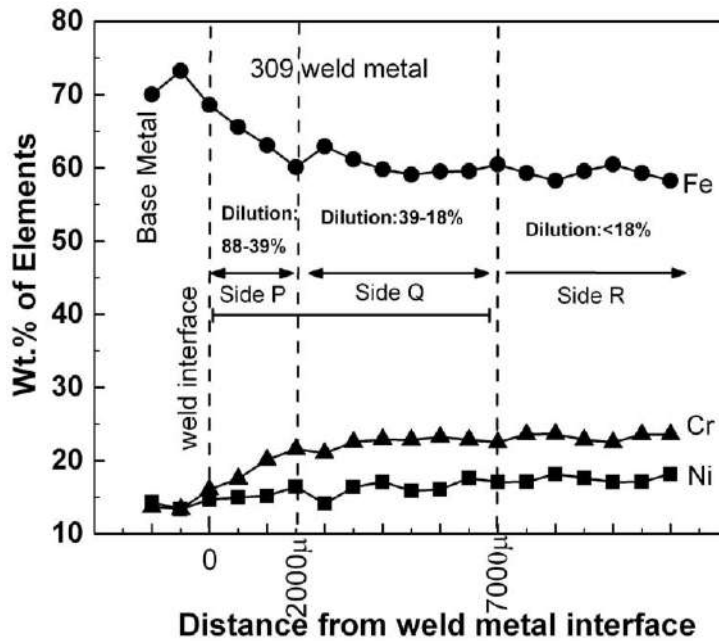


Fig.5.5 Semi quantitative spot EDS analysis of elements : Fe, Cr, Ni across the weld interface shows percentage of base metal dilution in sides P, Q and R of weld metal affected by base metal dilution.

As the alloy composition is estimated from EDS results, not considering all elements (especially light elements C and B not included), the wt.% for various elements given in Table 5.1 is only indicative; not absolute. The % dilution of P, Q and R regions

in weld metal were estimated using the average Fe concentration reported in Fig. 5.5 and Fe content of the base metal and that of undiluted weld metal of E309. The reason for choosing Fe content in the weld metal for calculation of dilution ratio though Cr and Ni is also present in the weld metal is that since Cr forms borides its concentration in matrix may be less and difference in the Ni content of base metal and weld metal is quite low. As the distance from the fusion boundary increases the dilution level decreases from ~88% at the fusion boundary to 39% at the location corresponding to dotted vertical line shown as boundary for P side. Similarly, it varies from 39 to 18% in the Q side and decreases further in the R region.

Table-5.1 Semi quantitative EDS analysis of various regions of 309 weld metal affected by base metal dilution in wt.%.

Elements	Base metal	E309 weld metal	309 weld metal diluted by base metal		
			P side		Q side
			Close to weld interface	2000 $\mu\text{m}$ from interface	7000 $\mu\text{m}$ from interface
Cr	13.79	23.56	15.61	21.37	22.48
Fe	70.4	58.26	68.62	62.92	60.46
Ni	14.12	18.17	13.83	13.2	17.05
B	1.24	0			
% Dilution			<b>88</b>	<b>39</b>	<b>18</b>
Estimated boron content based on dilution ratio			<b>1.09</b>	<b>0.484</b>	<b>0.223</b>

In fact, from the estimated dilution ratios, expected approximate boron content at each point of the analysis was calculated and given in Table.5.1. It is found that in region P, close to weld interface, the calculated boron content ranges between 1- 0.48 wt.%

corresponding to 88-39 % of base metal dilution. In region Q, the calculated boron content is between 0.48 - 0.22 wt.% corresponding to base metal dilution levels ~39 - 18% respectively. In region R, the calculated boron content corresponding to dilution level less than 18% is lower than 0.22 wt.%.

### 5.3.4 Ferrite Number (FN)

Ferrite number (FN) measured across the weld interface is shown in Fig.5.6. It can be observed that ferrite content increased from 0.14 in the base metal to 11 FN in 309 weld center. In the weld zone where base metal dilution is less than 18%, FN is found to be more than 7. In general, it may be noted that it is recommended to have 3-10 FN in the weld metal of austenitic stainless steel to minimize the risk of hot cracking during welding.

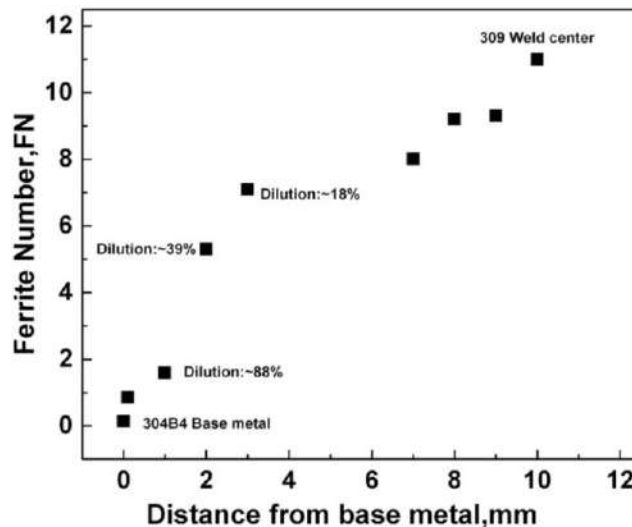


Fig.5.6 Shows ferrite number measured across weld metal interface from base metal to weld center.

### 5.3.5 Scheil's Solidification simulation

#### a) Solidification range

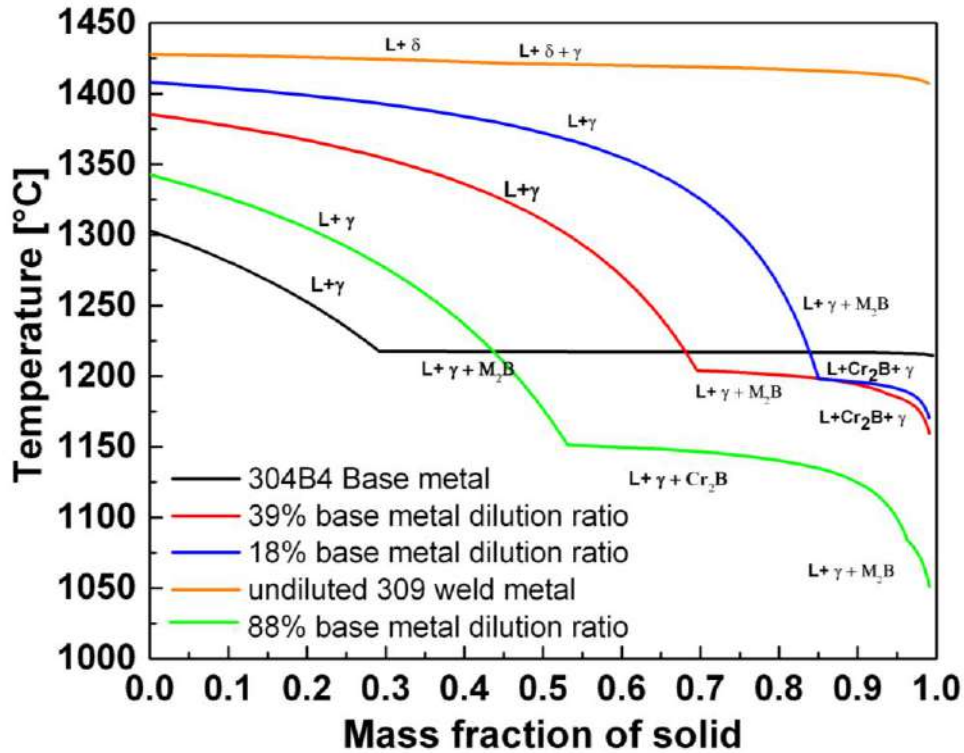


Fig.5.7 Comparison of solidification temperature range of SS 304B4 base metal to that of weld metal affected by base metal dilution and undiluted 309 weld metal simulated using Scheil's solidification model.

Solidification temperature range of weld metal is a significant parameter which is directly associated with its hot cracking susceptibility. The higher the solidification temperature range, the wider is the mushy zone where solid and liquid co-exists and hence higher is the cracking susceptibility. The solidification simulation using Scheil's model was performed for 304B4 base metal and undiluted 309 weld metal using their respective chemical compositions given in Table.3.1 of Chapter 3. Chemical composition for 309 weld metal diluted by base metal was taken from EDS spot analysis data obtained

for calculation of dilution ratio and the estimated boron content given in Table.5.1. The predicted temperature ranges for solidification of SS 304B4 base metal is 95°C. Similarly, solidification ranges predicted for undiluted 309 weld metal is 27°C and that for 39% and 18% diluted 309 weld metals are 226 and 238°C respectively as estimated from Fig.5.7. It is clear that this temperature range is significantly higher in SS 304B4 than undiluted weld metal from E309 electrode. Further, dilution of E309 weld metal by base metal increases the solidification temperature range for the weld metal even beyond that of the 304B4 as shown in Fig.5.7.

b) *Fraction of eutectic liquid in the weld metal*

Mass fraction of eutectic liquid for different weld compositions were estimated from the analysis performed using Scheil's solidification model in Thermo-Calc™ software. The mass fraction of eutectic liquid formed during solidification of base metal and undiluted 309 weld metal is found to be 0.35 and 0.09 respectively. The eutectic liquid fractions estimated for 309 weld metal with 88, 39 and 18% base metal dilution is 0.5, 0.27 and 0.13 respectively. The calculated boron content in the weld region corresponding to 88, 39 and 18% dilution is 1.09, 0.48 and 0.22 wt.% respectively.

***5.3.6 Effect of base metal dilution in weld metal on its liquation cracking susceptibility***

Fig.5.8(a) and (b) shows the plot of Total Crack Length (TCL) Vs percent augmented strain and Maximum crack length Vs percent augmented strain respectively for spot Varestraint test conducted on Type A and B specimens. Scatter in crack length data for the three specimens tested at same strain level is indicated by the error bar in the plot. Maximum crack length obtained in Type B specimen is found to be ~4.6 mm, which

shows that the crack has propagated even in to the unliquated (during spot Varestraint test) region of the weld metal. Threshold strain for cracking in type B specimen is 1% whereas for type A specimen is 2%.

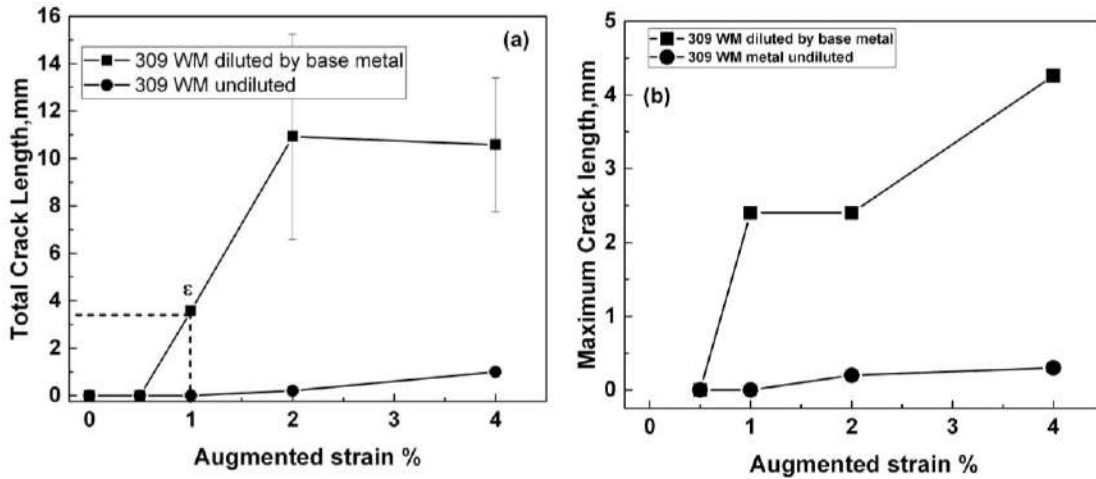


Fig.5.8 Plot of (a) Total Crack Length Vs % augmented strain (b) Maximum Crack Length Vs % augmented strain obtained for 309 weld metal diluted by base metal (Type B)

### 5.3.7 Macroscopic Cracking characteristics:

Macrostructures in Fig.5.9 (a) and (b) show hot cracks in the specimens after spot varestraint test conducted at 4% augmented strain on specimens extracted from SS 304B4 weld pad fabricated using E309 electrode. In the specimen A shown in Fig.5.1, location of spot is almost undiluted E309 weld metal and there are little or no cracks whereas in specimen B, the spot Varestraint test was conducted at a location where dilution is significant from the base metal and cracking is found to be high. From Fig.5.9(a), it is quite interesting to note that cracks are observed to be localized at a particular region around the spot; that is more cracks are present at certain distance away from the weld interface. As already shown in Fig. 5.4, the spot Varestraint tested region in Fig. 5.9 (a)

can be divided into three zones P, Q and R respectively based on the extent of dilution. It is interesting to note that the number density of cracks observed in these zones varied widely as shown in the graph beneath the Fig.5.9(a). In region P, there are some fine cracks which are backfilled by eutectics, the boron content corresponding to this location ~1 wt.%. In region Q, it may be noted that the cracks are long and wide where the boron content is ~0.4 to 0.2 wt.%. Also, it is discernable that the longest crack propagates up to quite a distance away from the liquated region formed during spot Varestraint testing. In region R, no cracks are observed, boron content at this location is estimated to be less than 0.2 wt.%. On an average, the crack density is very high at a location ~3000  $\mu\text{m}$  away from the weld interface. Figure 5.9(b) shows type A specimen with a very few cracks in the weld metal HAZ. This spot is very close to region R of type B specimen shown in Fig.5.9(a). Accordingly, effect of dilution from base metal is low and as expected with regions having high delta ferrite content in the weld metal and low boron level, resistance to cracking of this zone is high.

From the results, it is clear that the cracking susceptibility of the weld metal produced by welding 304B4 SS with E309 electrode varies depending on the dilution from the base metal. It is high at the intermediate dilution level and as expected, low in the undiluted weld metal. In the high dilution zone, backfilling of the eutectic liquid effectively reduces the cracking.

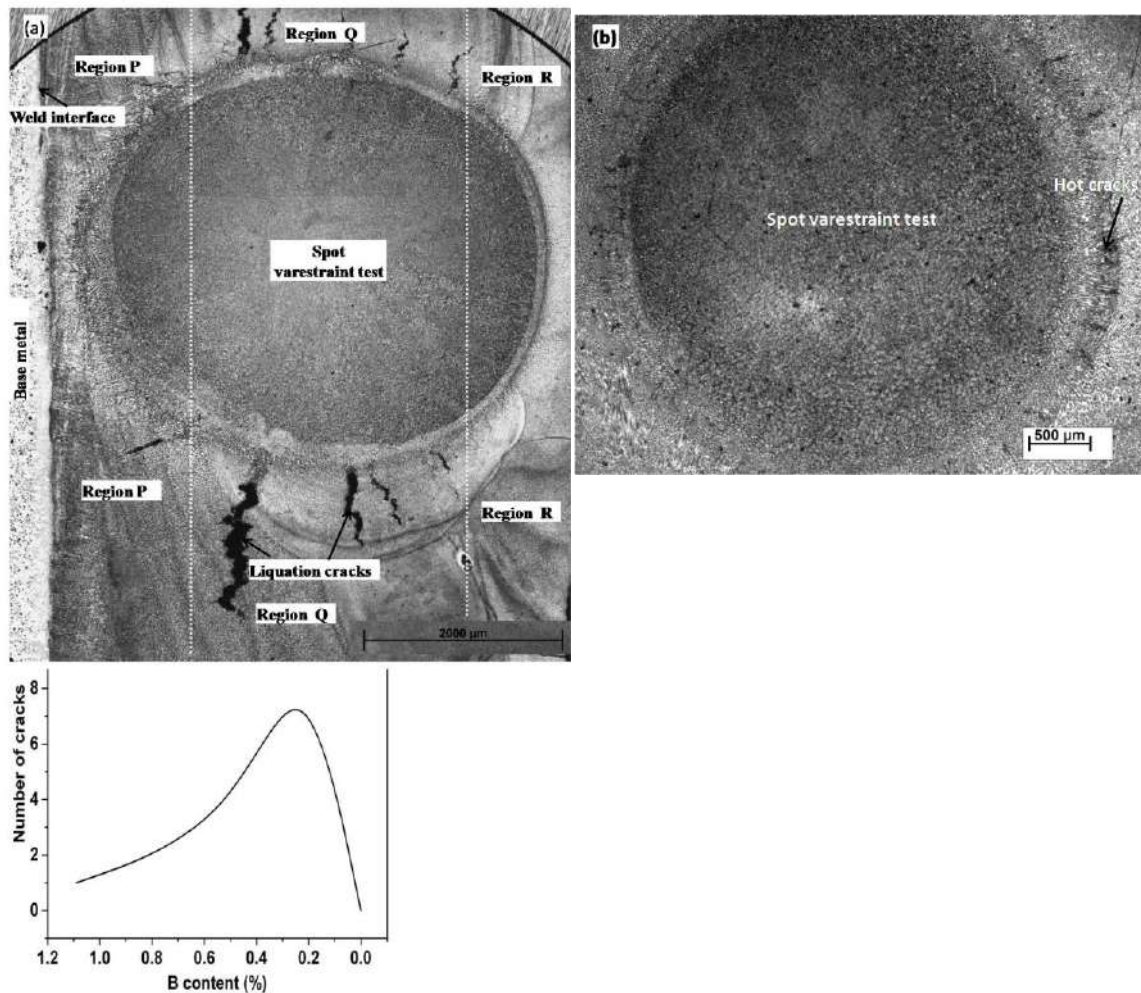


Fig.5.9(a) Macro-cracks observed on (a) weld metal affected by base metal dilution (Type -B)(b) undiluted 309 weld metal (Type A).

### 5.3.8. Microstructures of specimens after spot Vareststraint test

Figures 5.10(a), (b), (c) and (d) shows microstructures taken from Type B specimen. Fig.5.10(a) shows low magnification image of Type B specimen after spot Vareststraint test indicating the locations of the high magnification microstructures.

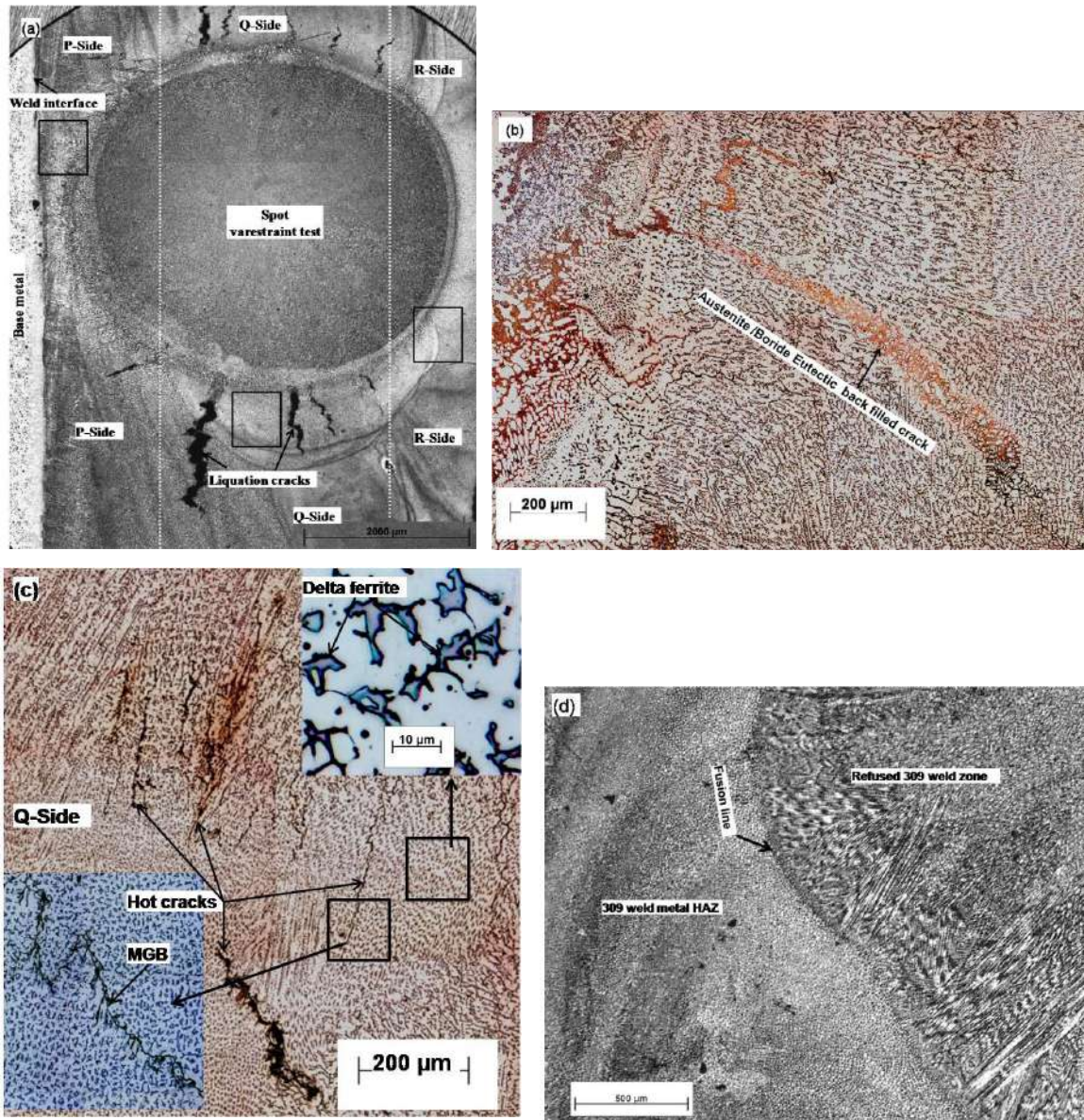


Fig.5.10(a) Microstructures of spot Varestraint tested Type B specimen at low magnification.(b) Microstructure at region P (close to weld interface) (c) Microstructure at region Q (slightly away from the interface) (d) Microstructure of region R (opposite to P)

Fig.5.10(b) is the high magnification image of region P which shows liquation cracks back filled by eutectics in this region. Fig.5.10(c) is the high magnification image of region Q which shows wide and lengthy cracks along the migrated grain boundaries in

spite of presence of delta ferrite in the austenite matrix. Region R opposite to P (approximately 180° apart) is close to the centre of the weld and is equivalent to undiluted 309 weld metal. Fig.5.10(d) shows the microstructure of region R close to weld center; it consists of only austenite and delta ferrite. In this region neither borides nor cracks are observed. On comparison to region P, this region indicates a good resistance to hot cracking. Fig.5.11 shows microstructure of undiluted 309 weld metal (Type A specimen) consisting of austenite and delta ferrite which is similar to that of microstructure of region R shown in Fig.5.10 (d) and resistant to hot cracking.

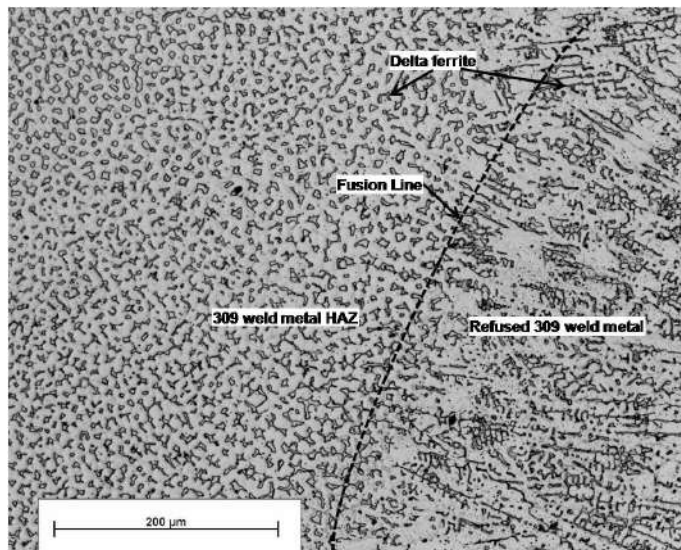


Fig.5.11 Microstructure of undiluted 309 weld metal (Type A specimen) taken from spot Varestraint tested specimen.

### ***5.3.9 Brittleness Temperature Range (BTR)***

From the spot Varestraint tested Type B specimen, BTR could not be determined using MCL and the method described in section 3.4.2 of Chapter 3, as the crack originated at the fusion boundary of the re-melted zone (spot weld) had extended far into unliquated region of the weld in a brittle manner along the interdendritic region of the

previously deposited weld metal. In this zone, crack consists of two parts, one formed by liquation and the other that extends and propagates from the first part in a brittle manner. Using fractographs of a hot crack, it is possible to differentiate between the liquation region of the crack and the brittle portion of the crack in the weld metal. Hence, a fine slice of the cracked region, covering the entire length of the crack starting from fusion line was removed carefully from the top surface of hot crack tested specimen as shown schematically in Fig.5.12(a). The sliced region was subsequently thinned down to ~ 200 micrometer by polishing as shown in Fig.5.12(b) (center). The thin specimen containing hot crack was separated into two halves by removing the small portion of the metal at the back end of the crack tip. “Egg crate” morphology (locations 1 and 2 marked in Fig.5.12(b)) indicated liquation cracking while the solid state interdendritic fracture indicated (at location 3 in Fig.5.12(b)) ductility dip cracking. Accordingly, the length of liquated region is estimated to be 2.9 mm and this was used to estimate BTR. BTR for this zone was determined to be 283°C. In contrast, cracking in the undiluted weld metal, is almost negligible which makes BTR too small to be estimated from the experiments.

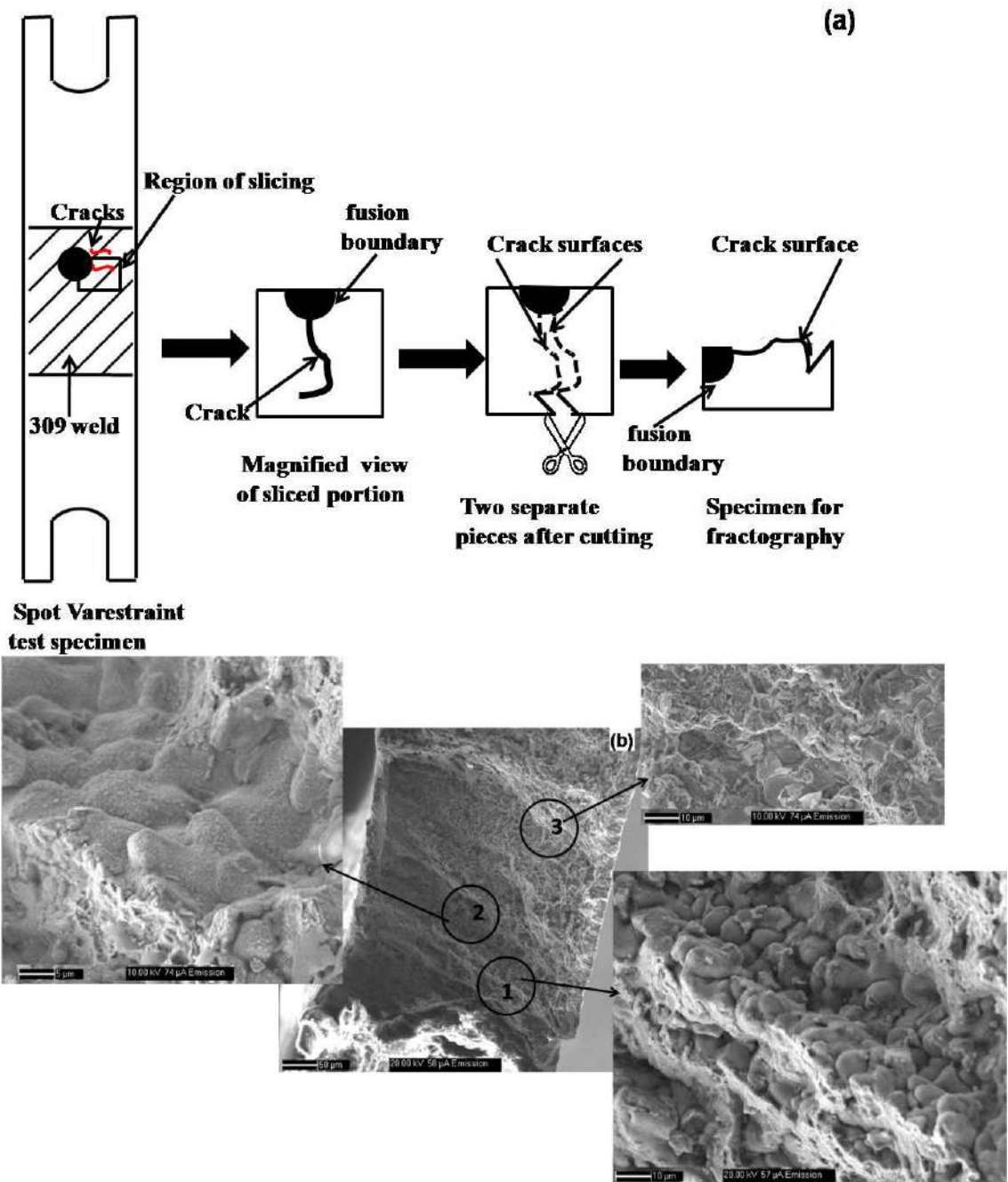


Fig.5.12 (a) Schematic representation specimen preparation for fractography (b) top view of crack surface of 309 weld metal PMZ obtained from hot crack tested specimen of weld metal diluted by base metal. Regions 1 & 2 shows typical “egg crate” fracture morphology pertaining to liquation of grain boundaries and region 3 shows interdendritic fracture typical of ductility dip cracking.

### 5.3.10 Qualitative analysis of microchemistry of borides

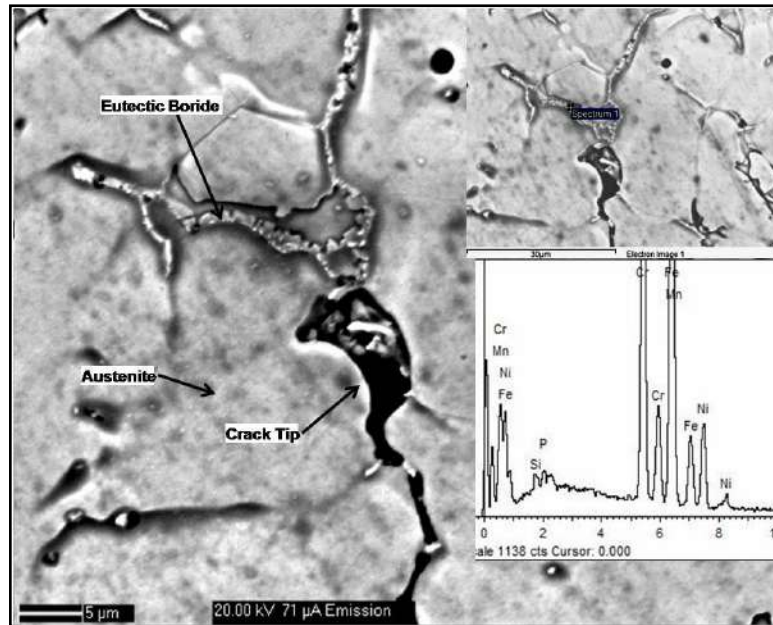


Fig.5.13 SEM image of region Q of 309 weld metal diluted by base metal shows thin films of eutectics along MGB and spot EDS on the eutectic in the inset of figure reveals segregation of impurity elements along with Cr borides.

Figure 5.13 shows the SEM microstructure near the crack tips present in region Q of the weld joint tested for cracking susceptibility in Type B specimen. This image shows a thin film of eutectic along the reheated grain boundaries just above an open crack. Qualitative EDS analysis of the eutectic film shows that the eutectic phases are enriched in Cr, P and Si.

## 5.4 Discussion

### 5.4.1 Effect of base metal dilution on weld metal

From the microstructural characterization of SS 304B4 weld joint prepared using E309 electrode, it is clearly evident that it is composed of base metal PMZ, unmixed

304B4, weld metal diluted by base metal, the dilution varying with distance from the fusion boundary, and an almost undiluted E309 weld metal towards the centre of the weld. This variation in dilution results in continually changing microstructure. Close to weld interface (region P) since dilution from base metal is high (88 - 39%), boron content estimated in this region is ~1- 0.48 wt.% whereas away from the interface (region Q), base metal dilution is between 39-18% and corresponding boron content estimated is 0.48 - 0.22 wt%. Boron content > 0.48 wt.% in the weld metal leads to a larger volume fraction of eutectic phases whereas regions with critically low boron ( $0 < B < 0.2$  wt.%) content result in formation of thin films of eutectic phases in the weld metal as observed in Fig.5.13. In the weld metal, eutectic films are found to be present along the migrated grain boundaries (MGB) as shown in the inset of the Fig.5.3. Just as the volume fraction of eutectic phases, the volume fraction of delta ferrite retained in the weld metal is also affected by base metal dilution level as seen in Fig.5.6.

#### ***5.4.2 Cracking susceptibility***

The crack susceptible microstructure appears to comprise of austenite dendrites and thin films of eutectic borides in interdendritic regions as shown in Fig.5.10. In the microstructures of tested specimens, the liquation cracks were predominantly present in weld metal (not the fusion zone produced by spot Varestraint test; but the weld metal of the weld joint) at a location slightly away from the original weld interface as shown in Fig.5.8(a) where delta ferrite is present and the fraction of eutectic borides is less than those present near the fusion line. The open cracks are also attributed to presence of thin films of eutectic borides along the migrated grain boundaries (MGBs) which were not

liquated during spot Varestraint testing. From Fig.5.10 and Table 5.1, it is clear that the estimated boron content in Q side where severe cracking is observed, is found to be between the range 0.48 -0.22wt.%. These results are consistent with those reported by Shinoda et.al. [6] which indicate susceptibility to cracking is high if the boron content is between 0.2-0.5 wt.% and it is low at higher boron levels.

In Fig.5.10(a), it can be seen that, in region P, it is not that cracks did not form, in contrast, there was effective backfilling of the cracks due to large volume of the eutectic formed because of high boron content in this region. In region P, the fraction of eutectic liquid formed during solidification is ~0.27 as calculated from solidification simulation shown in Fig 5.7 whereas, that formed in region Q is only ~0.13. On comparison of solidification ranges of the two regions, P region (215°C) is found to have marginally lower value than the Q region (245°C). Therefore, the high cracking susceptibility of Type B specimen is attributed to synergistic effect of wide solidification range and insufficient eutectic liquid to back fill the cracks at region Q.

In addition to liquation cracking, further propagation of cracks along the grain boundary also could be contributing to the length of the cracks found in the region Q of weld metal. A close look at the cracks (Fig.5.10(b)) reveals cracks in Q side progressed beyond the liquation zone along the MGBs. The MGBs move easily through the weld metal microstructure when volume fraction of eutectic constituents is not sufficient to “lock” grain boundary motion [41]. During multipass welding, multiple thermal cycles promote additional boundary migration and segregation. During migration, impurity and interstitial elements segregate in the boundary as they have high diffusivities. From the

microstructure shown in Fig.5.10(a) it is quite discernable that the crack present in the weld metal PMZ has propagated beyond the PMZ into weld metal not liquated by the thermal cycle of spot Varestraint testing. This shows that the crack which initiated in the PMZ due to liquation of eutectic has propagated along the MGB into the unaffected weld metal due to poor cohesive strength of the MGB which is typical of ductility dip cracking which occurs without liquation of grain boundaries. From the EDS analysis of eutectic phases present in the cracked regions of 309 weld metal shown in Fig.5.13, it is understood that along with chromium borides, phosphorous and silicon are also segregated to the MGB. High impurity and interstitial concentration at the MGBs lower the cohesion between grains and can lead to grain boundary sliding under low strain, subsequently resulting in intergranular cracking [86]. This also could be a reason behind saturation of TCL at 2% augmented strain as shown in Fig.5.9. Also, since ductility dip cracking takes place in solid state which is evident from the fractographs shown in Fig.5.13, there is no eutectic liquid present at these locations which can aid in healing of the cracks. Thus, hot cracking that occurs in the weld metal HAZ produced in multipass welding of 304B4 SS using E309 consumable is a combination of liquation and ductility dip cracking. Crack initiation being influenced by liquation of thin films of eutectic along the interdendritic regions and further propagation of the crack aggravated by the presence of boride precipitates and segregation of tramp elements along the MGBs in the weld metal.

#### ***5.4.3 Effect of Delta ferrite on liquation cracking susceptibility***

It is well known that austenitic stainless steels with 5–30% ferrite are quite resistant to hot cracking during welding [25]. Also, it is reported that ferrite- austenite (FA) /ferrite (F) solidification mode is a better index of resistance to hot cracking than residual ferrite content after welding [33,87-88]. It is stated by many authors that higher solubility of S, P and other impurity elements in ferrite results in interdendritic regions with low volume fraction of low melting eutectic during final stages of solidification [89]. Not only this but also many mechanisms are put forward in favor of delta ferrite in reducing hot cracking susceptibility in austenitic stainless steels. Nominal delta ferrite content in 309 weld metal is ~15% and it solidifies in F mode [90]. Delta ferrite content measured across the weld interface of SS 304B4-309 weld joint shows that the delta ferrite content at weld metal region affected by base metal dilution (Q-region) is 7 FN. Delta ferrite morphology observed from the weld microstructures were found to be skeletal and lathy (lacy) resulting from the F mode of solidification [91] and also comply with the Scheil's solidification simulation shown in Fig.5.7. In spite of presence of delta ferrite, cracking propensity at this region is found to be very high because the partitioning coefficient of boron in delta ferrite is only 0.125 and in austenite it is as low as 0.001 at 1654K [24]. This demonstrates that the presence of delta ferrite during solidification of boron containing steels do not have any advantages towards reducing the hot cracking susceptibility by scavenging boron. Ferrite profile taken across the weld interface shows that ferrite number gradually increases on moving from weld interface to weld metal center, as shown in Fig.5.6. It can also be understood from the figure that as the base

metal dilution ratio decreases from the weld interface towards the centre of the weld, the delta ferrite content correspondingly increases. Also, from the microstructure shown in Fig.5.10(b) it is quite discernable that there is sufficient volume of delta ferrite formed during solidification in weld metal affected by base metal dilution. It is worth noting that ferritic mode of solidification or presence of delta ferrite in the weld metal has no effect on reducing the hot cracking susceptibility of boron containing stainless steel.

#### ***5.4.4 Effect of Sulphur, phosphorus and silicon on liquation cracking susceptibility***

Presence of sulphur, phosphorus and silicon in the weld metal is generally considered as detrimental for weldability of stainless steels because of segregation of these elements to the last solidifying liquid and formation of low melting eutectic there by increasing the susceptibility to hot cracking [25]. From the present study, it is understood that presence of eutectic borides in weld metal overrides the effect of eutectics such as Fe-FeS or Fe-FeP formed from segregated sulphur or phosphorus. Also, it is understood that since the volume percent of delta ferrite in the weld metal ranges from 2 – 11, S and P even if present will be scavenged by the delta ferrite since the partitioning coefficient of S and P in delta ferrite is 0.091 (at 1638 K) and 0.23 (at 1523 K) respectively [24-26]. Similar observation is quoted by Shinoda et.al in his studies carried out on two sets of boron modified SS 304 containing different levels of sulphur and phosphorus contents. It is concluded that segregation of impurity elements is not the major factor controlling the solidification cracking of boron containing steels [6] But their presence synergistically increase the cracking propensity by their segregation along the MGBs which aid ductility dip cracking in the weld metal.

## 5.5 Summary

1. SS 304B4 weld fusion zone prepared using E309 electrode is composed of base metal PMZ, un-mixed zone, 309 weld metal affected by base metal dilution and undiluted 309 weld metal. The microstructures of these zones are distinctly different from each other and hence their hot cracking susceptibility is also different.
2. In the fusion zone, base metal dilution level decreases on moving from the weld interface towards the weld center. Since the boron content present in the fusion zone is dependent on dilution level, the microstructures vary continuously from the weld interface to the weld center. Fusion zone near the weld interface consists of more eutectic phase due to high boron concentration whereas slightly away from the interface has only thin films of eutectic and delta ferrite due to relatively less boron content. No borides are present in the undiluted E309 weld metal at the center.
3. Part of the fusion zone of SS 304B4 weld made using E309 welding consumable, which is affected by base metal dilution and containing ~0.2-0.48 wt.% boron is highly susceptible to liquation cracking during multipass welding. High cracking susceptibility of this part of the fusion zone is attributed to synergistic effect of large freezing range and insufficient eutectic borides to aid back filling of hot cracks.
4. Other major factor contributing to high cracking susceptibility is the extension of liquation cracks further as ductility dip cracking assisted by presence of thin films of eutectic boride and segregation of P and Si along the migrated grain boundaries of the weld metal.

5. Presence of delta ferrite during solidification of fusion zone does not show any advantage in reducing liquation cracking susceptibility because partitioning coefficient of boron from liquid metal to delta ferrite is very low; unlike for impurity elements like S and P.

## **CHAPTER 6**

### **HOT CRACKING SUSCEPTIBILITY OF THE WELD METAL IN SS 304B4 WELD JOINT PREPARED USING BORON ADDED E308 ELECTRODE**

#### **6.1 Introduction**

In the previous chapter, study on weld metal liquation cracking susceptibility of SS 304B4 weld joint prepared using E309 electrode is presented. The reasons behind the high cracking susceptibility of the weld joint prepared using standard E309 electrode are elucidated. It is shown that base metal dilution played a major role in altering the weld metal chemistry which ultimately leads to liquation cracking in the weld metal during multipass welding. It is also shown that the cracking susceptibility is high for that part of the weld metal where boron is in the range of 0.4 to 0.2 wt.% due to dilution from the base metal, which is in agreement with the literature reports [6]. In Chapter 4, it is shown that SS 304B4 base metal containing 1.3 wt.% boron is quite resistant to solidification and liquation cracking tendency. The results obtained from the work done so far, it is expected that hot cracking in borated stainless steels can be greatly reduced by choosing electrodes containing boron similar to that of the base metal. Accordingly, this chapter details the hot cracking susceptibility of SS 304B4 weld joint prepared using E308BRN electrode that contains ~1 wt.% boron. Only transverse and longitudinal V-restraint tests were conducted. Attempts to perform SVT using the welding parameters mentioned in Table 3.4 resulted in melt through of the specimens. As per Table 3.5, since LVT

specimens did not show any cracks in the HAZ region, further investigations on liquation cracking susceptibility was not carried out.

## 6.2 Varestraint test specimens

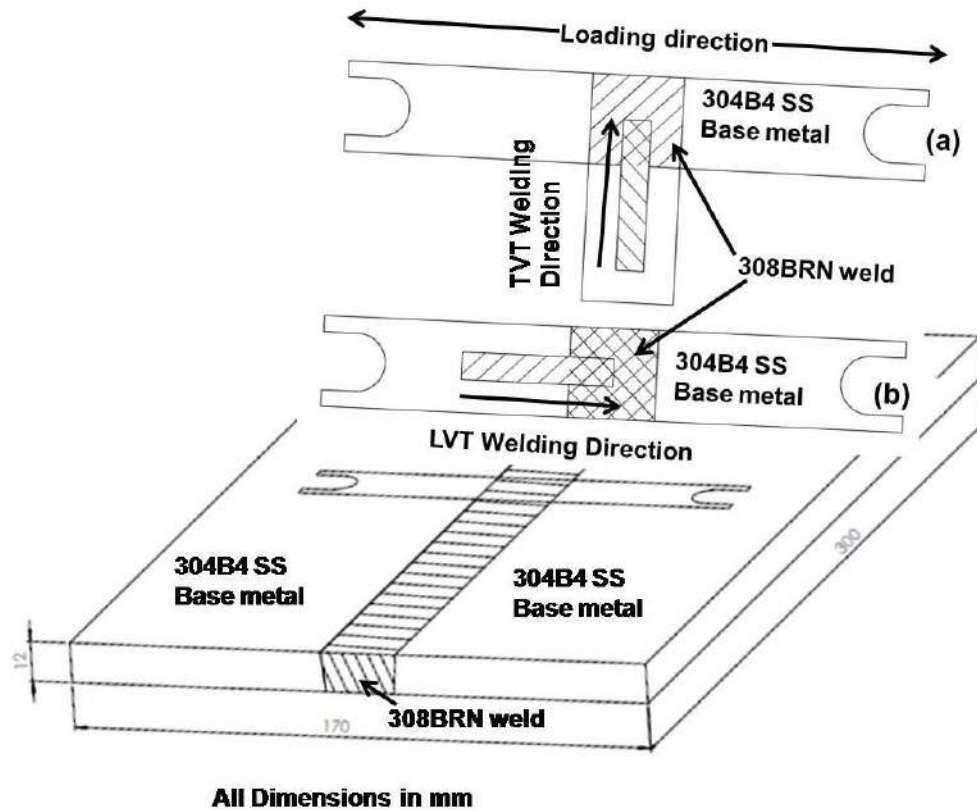


Fig.6.1 Schematic of extraction of hot crack specimens from the weld joint used for (a) Transvarestraint (TVT) (b) longitudinal Varestraint test (LVT) showing the direction of autogenous TIG welding and loading during testing.

Varestraint test specimens used for evaluation of 308BRN weld metal was extracted from the weld joint prepared using E308BRN electrode and parameters mentioned in Table 3.3 in section 3.3 of Chapter 3. The schematic representation of

positions on weld pad from which specimens were extracted is shown in Fig.6.1.

Varestraint tests were conducted using these specimens as described in Chapter 3.

## 6.3 Results

### 6.3.1 Microstructure of 308BRN weld metal

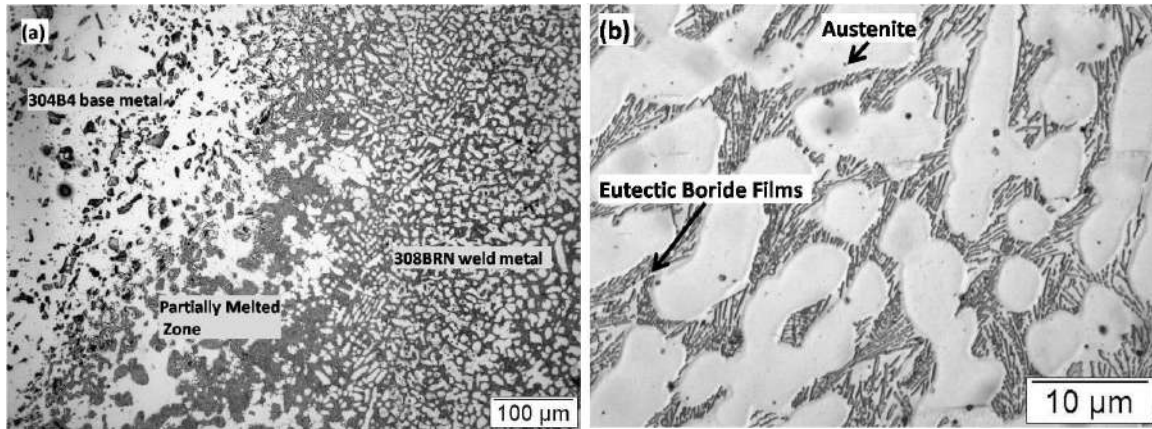


Fig.6.2 (a) Microstructure of 308BRN weldment at low magnification and (b) high magnification image of 308BRN weld metal microstructure .

Figure 6.2 (a) shows the microstructure of 308BRN weldment consisting of weld metal, fusion boundary and HAZ, and (b) shows the high magnification microstructure of 308BRN weld metal. The weld metal microstructure is composed of primary austenite dendrites with interdendritic austenite/ boride eutectic constituents. The volume fraction of the eutectic phases obtained using *Image J* software is  $\sim 0.32 \pm 0.02$ . The value reported is an average of readings taken from 10 images obtained from different locations of the weld metal. No variation in the microstructure along the width of the weld metal, as seen in the case of weld metal produced by E309 weld metal (Chapter 5) is seen in the case of weld metal produced by E308BRN.

### 6.3.2 Hot cracking susceptibility

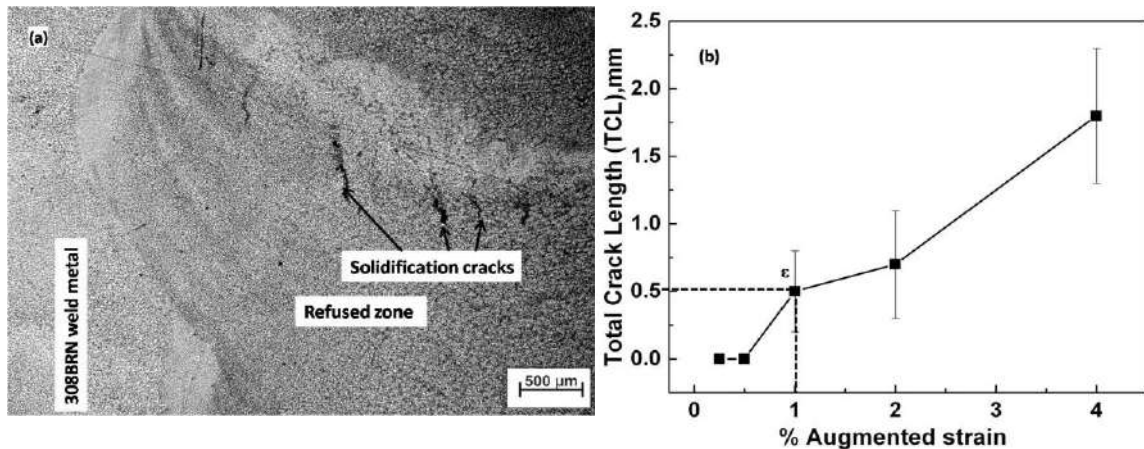


Fig.6.3(a) Macrostructure of longitudinal Varestreint tested specimen (b) plot of Total crack length(TCL) vs % augmented strain

The results of longitudinal and transverse Varestreint tests are given in Fig.6.3 and Fig.6.4 respectively. Fig.6.3(a) shows the macrostructure of longitudinal Varestreint tested specimens, figure (b) shows variation of average Total Crack Length (TCL) with respect to % augmented strain obtained from longitudinal test.

Similarly, Fig.6.4(a) shows the macrostructure of TVT specimen, figures (b) and (c) show variation of average Total Crack Length (TCL) and Maximum Crack Length (MCL) respectively with respect to % augmented strain obtained in TVT. In Fig.6.3(a) (LVT) shows no cracking in the weld metal HAZ (HAZ formed in the weld metal of the joint during LVT) while both Fig.6.3(a) and Fig. 6.4(a) show clear susceptibility for solidification cracking (TVT). Hence, the results suggest 308BRN weld metal is prone to solidification cracking; but not so much to HAZ liquation cracking of weld metal.

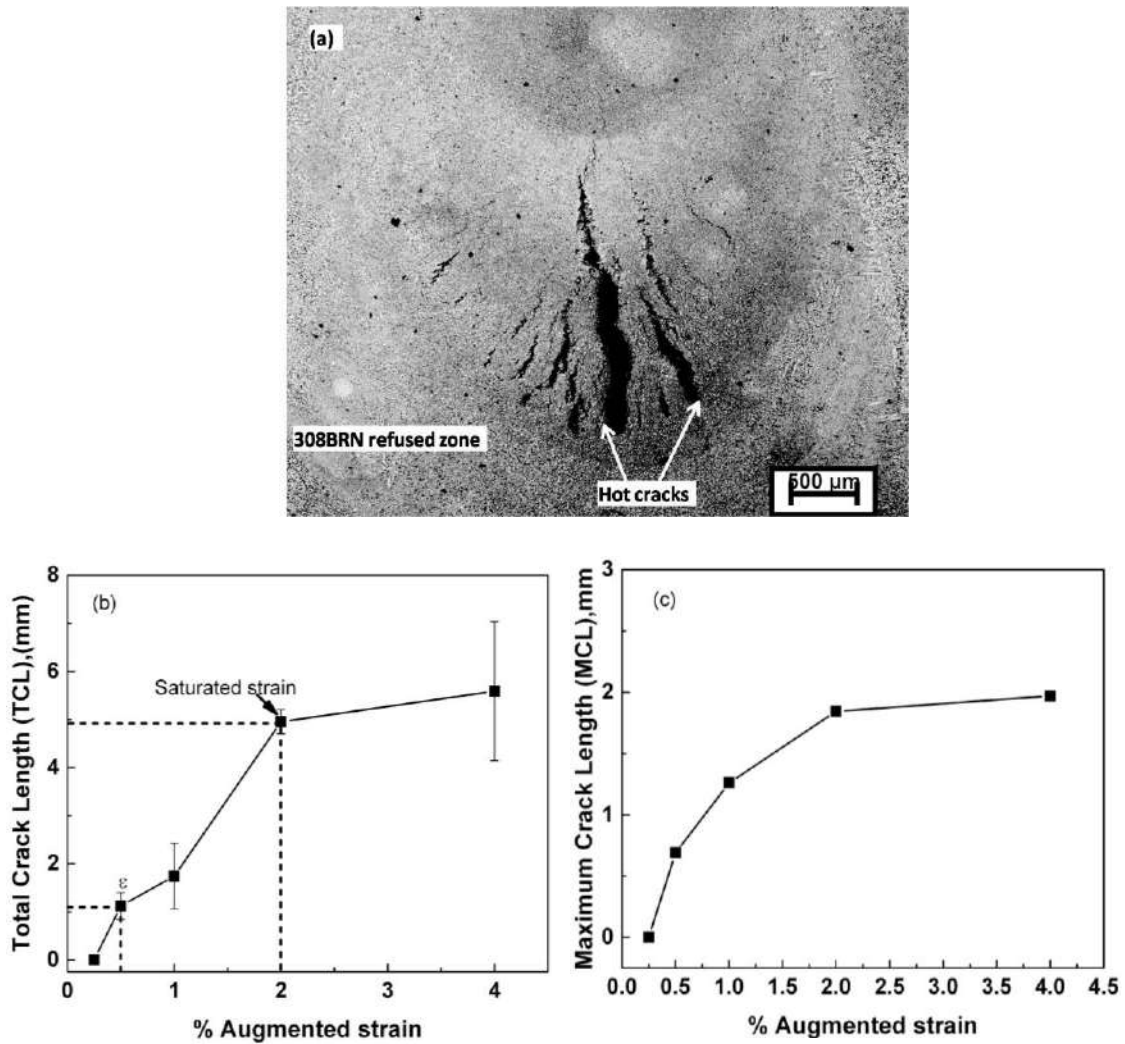


Fig.6.4(a) Macrostructure of transverse restraint tested specimen (b) Total Crack Length (b) (c) Maximum Crack Length (MCL) obtained from crack length measurements carried out on transverse restraint tested specimens extracted from 304B4 SS joined using E308BRN plotted against % augmented strain.

Further a comparison of results of TVT shown in Chapter 4 for base metal (Fig.4.13 and Fig. 4.14) and with Fig.6.4 shows solidification cracking susceptibility of the weld metal produced by E308BRN weld metal is more than that of the base metal.

Even threshold strain to obtain crack is lower for weld metal (0.5%) than for the base metal (1.0%). Further, it may be noticed that both maximum crack length and total crack length saturated at 2% strain. This shows that an augmented strain of 2% is sufficient to open up the entire length of liquated region in the solidifying weld metal.

### ***6.3.3 Microstructures of Vareststraint tested specimens***

Microstructures in Fig.6.5 show the solidification cracks in 308BRN weld metal after TVT at various magnification and augmented strains of 4 and 1 %. Fig.6.5(a) taken at low magnification shows the microstructure of TVT specimen at 4% augmented strain. Figure 6.5(b) shows the microstructure of the specimen tested at 4% augmented strain at high magnification. The cracks are present along the interdendritic regions of re-fused zone formed during test. In these microstructures, it is observed that backfilling was confined to few fine cracks; there is no eutectic backfilling occurred in the major cracks. Figure 6.5(c) shows solidification cracks observed on 308BRN weld metal specimen tested at 1% augmented strain; many of the fine cracks are backfilled and one centre line crack is almost 90% back filled. However, from the microstructures taken from TVT specimens, it is seen that backfilling by eutectic is effective only in small and fine cracks but not in long and wide ones.

From the results of LVT tests presented above it clear that weld metal of E308BRN weld metal resistant to weld metal liquation cracking but susceptible to solidification cracking. This is in contrast with the results of the cracking susceptibility of weld metal in the weld joints of 304B4 SS made with E309 consumable, which is presented in Chapter 5, where weld metal HAZ is susceptible to liquation cracking.

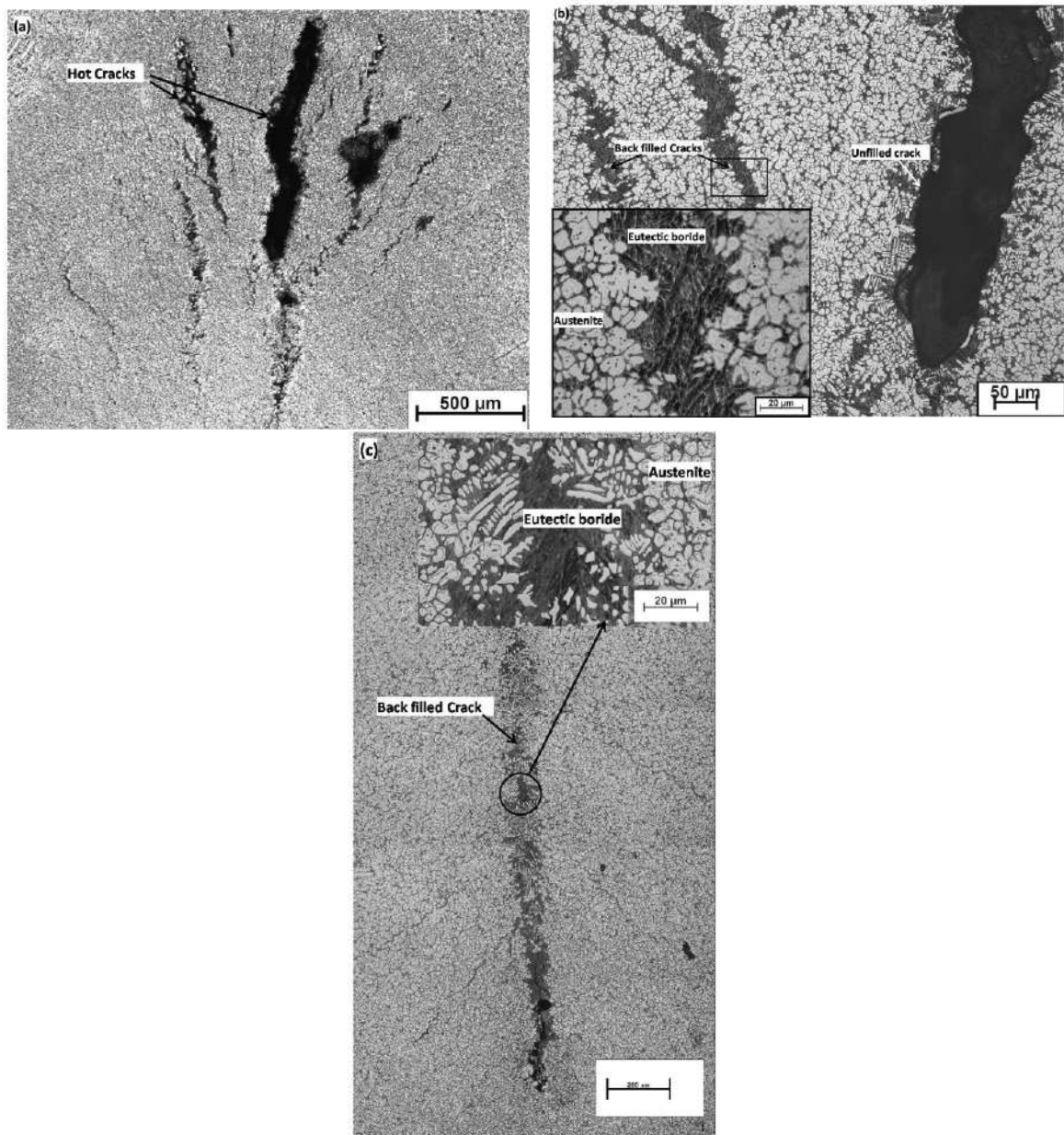


Fig.6.5 Microstructures obtained from 308BRN weld joint specimens after transverse restraint tested specimens at (a) 4% augmented strain (low magnification) (b) 4% augmented strain (high magnification) (c) 1% augmented strain.

**6.3.4 Micro chemical analysis of re-fused zone using Electron Probe Micro Analyzer (EPMA)**

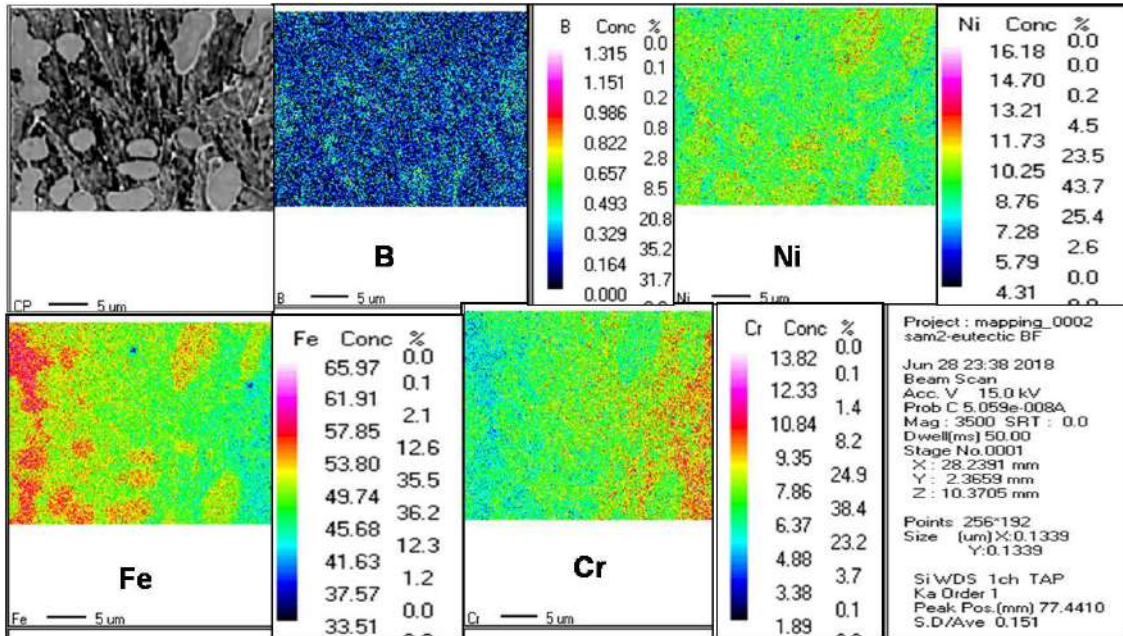


Fig.6.6 Elemental mapping performed on 308BRN weld metal using EPMA shows Fe rich eutectic borides present in the interdendritic regions.

Results of micro chemical analysis carried out on E308BRN transverse restraint tested specimens using EPMA is shown in Fig.6.6. The elemental mapping obtained in the austenite and eutectic phases present in the specimen shows clear indications that the eutectic boride found in 308BRN weld metal is predominantly non equilibrium Fe rich borides in which Cr content varies from 7-12 wt.% .

### 6.3.5 Solidification simulation

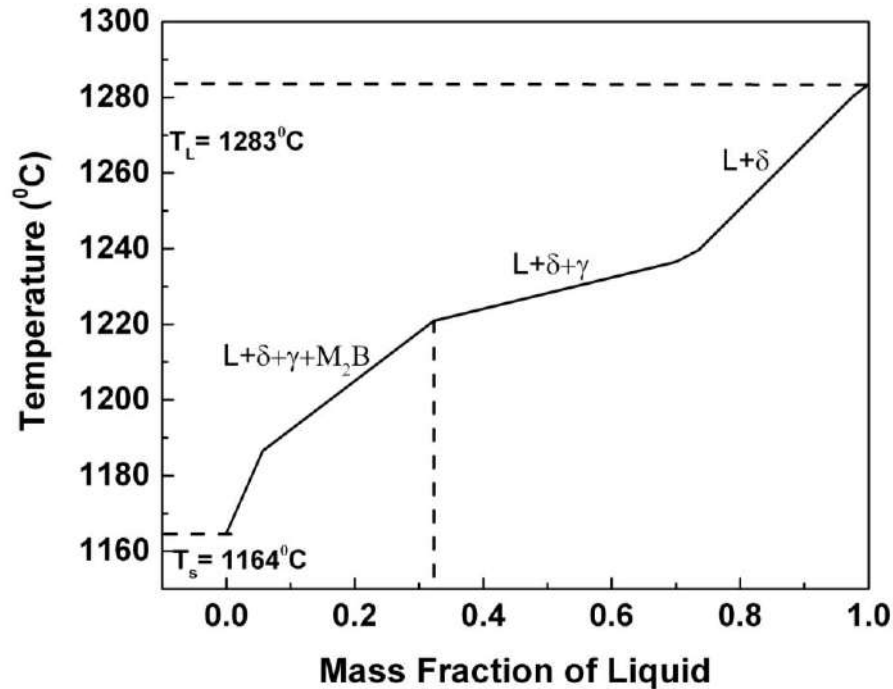


Fig.6.7 Temperature vs fraction of liquid curves generated for 308BRN weld metal predicted using Scheil's solidification simulation module.

Temperature (T) - Fraction of liquid ( $f_L$ ) curves generated for 308BRN weld metal compositions using Scheil's solidification simulation is shown in Fig.6.7. It is observed that the freezing range of 308BRN weld metal is  $120^\circ\text{C}$  whereas that of 304B4 base metal is  $130^\circ\text{C}$  as shown in Fig.4.2 of Chapter 4. This suggests that 308BRN may have a more or less similar propensity for solidification cracking as that of the base metal.

### 6.4 Discussion

E308BRN weld metal consists of austenite dendrites and a continuous network of interdendritic austenite /boride eutectic constituents as shown in Fig.6.2. In this weld joint, boron content of the weld metal is only marginally lower than that of base metal and hence, there is little scope altering the boron content in the weld metal due to effect of

dilution by base metal. Therefore, a uniform microstructure could be observed from the weld interface to the center of the weld metal. The area fraction of eutectic phase in the weld metal is estimated by *Image J* is around 0.32 which is uniformly distributed.

From the LVT results, it is found that there is no significant cracking in these specimens in the weld metal HAZ (Fig.6.3(a)). Hence, it can be stated that 308BRN weld metal is considerably resistant to weld metal liquation cracking. In TVT, the direction of strain is perpendicular to the solidifying weld pool. The solidifying interdendritic liquid is unable to accommodate the augmented strain, resulting in the solidification cracks as observed in Fig.6.4(a). The threshold strain for cracking was ~0.5% (Fig.6.4(b)). Values of TCL and MCL saturated at 2% augmented strain which implies that the cracking is independent of applied strain beyond 2% augmented strain, in other words, it can be said that the crack length has reached the maximum extent of liquated portion in the weld region. In general, the observed range of threshold and saturated strain for fully austenitic stainless steel and Ni based alloys are 0.5-2% and 5-7% respectively [19]. In the present study, for E308BRN weld metal the strain at which the total crack length is saturated (~2% strain) falls in the regime of expected threshold strain (0.5-2%) for fully austenitic alloys. This shows the relative cracking susceptibility of the E308BRN weld metal is higher than other fully austenitic alloys.

Also, it is observed that majority of the cracks were long and wide in the specimens tested at 2 and 4% augmented strain specimens. Fine cracks are relatively found to be few and many of these are completely backfilled by the eutectic constituents as shown in Fig.6.5(b). It is also observed in these microstructures that the wide cracks

are hardly backfilled by the eutectics. It is reported that backfilling of the cracks by eutectic liquid takes place by the phenomenon of capillary action [83]. Thus, the backfilling mechanism follows flow of liquid in the crack, assisted by capillary action which is a function of liquid density/viscosity, column radius/length and surface energy [93]. The height (h) of the liquid drawn into the column is given by equation 4 which is derived from Jurin's law [94].

$$h = \frac{2\gamma_{LV}}{D_L g R} \cos \theta \quad (4)$$

Where,

h = Capillary rise of liquid in the column

D<sub>L</sub> = Density of Liquid

γ<sub>LV</sub> = Surface tension

R = Radius of the column

g = Acceleration due to gravity

θ = Contact angle between liquid and column

Basic assumptions made before applying equation (4) to our case is that temperature is uniform across the solid- liquid interface so that there is no fluctuation of density of liquid and surface tension is constant. The assumptions are reported to be quite reasonable since only small fraction of liquid is drawn from the liquid metal ahead of the solid- liquid interface of the weld pool [83]. Except for the parameter radius of column (R), all the other parameters remain constant for the specimens tested at different augmented strain levels. The parameter R corresponds to the width of the crack in the

context of backfilling of hot cracks during Varestraint testing. Fig.6.8 shows the widths of longest cracks plotted against corresponding augmented strain observed in transvarestraint tested specimens. It is evident from Fig.6.8 that with increase in augmented strain, crack width increases. Comparison of the microstructures of TVT specimens tested at 1% and 4% augmented strain (Fig.6.4), clearly show that at low augmented strains where the cracks are short and narrow, back filling by eutectic is more or less complete. However, at high augmented strain, where the cracks are very long and wide, backfilling is sparse. This shows that effective backfilling by eutectic liquid occurs more in the case of fine and narrow cracks than in the cracks that are wide and long. From the results it can be inferred that in case of near eutectic alloys, where the fraction of eutectic liquid formed is as high as 0.3, hot cracking is likely to occur when high restraints are imposed during welding. At low restraint levels, solidification cracks formed in the welds are healed by backfilling of eutectic liquid.

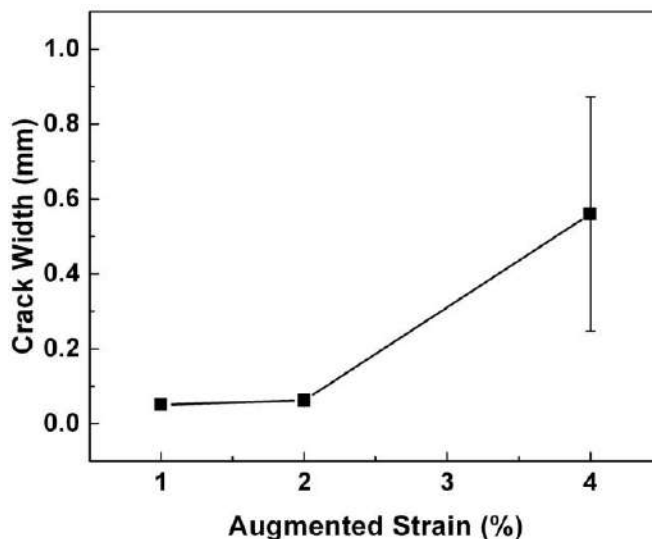


Fig.6.8 A plot of widths of the longest cracks observed in the transvarestraint tested specimen at various % augmented strain.

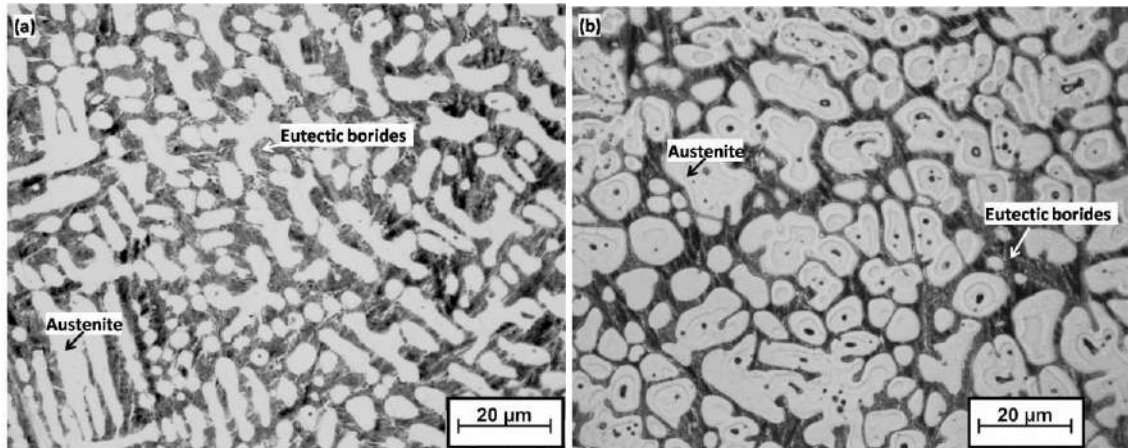


Fig.6.9 Microstructures of fusion zone of Varestraint test specimens (a) 304B4 SS base metal (b) 308BRN weld metal.

The above results are in contrast to transvarestraint test results conducted on 304B4 base metal containing 1.3 wt.% boron which has very low hot cracking sensitivity owing to extensive backfilling of the cracks by the eutectic constituents, discussed in Chapter 4. This is attributed to the abundant amount of liquid of eutectic composition-estimated to be ~0.41-0.44 area fraction from the fusion zone microstructure shown in Fig.6.9(a). In the present study, 308BRN weld metal microstructure shown in the Fig.6.9(b) contains ~0.31-0.32 area fraction of eutectic liquid which is found be insufficient to back fill the cracks in the re-fused zone at higher augmented strain. Also, Scheil's solidification simulation in Fig.6.8 shows that the solidification range of 308BRN weld metal is similar to that of 304B4 base metal but the fraction of terminal liquid in 308BRN weld metal is ~0.3 fraction whereas that of 304B4 base metal is ~0.5. Thus, the results from the analysis of microstructure complement the results of Scheil's simulations. Further, it is already shown in Chapter 4 that there is a considerable enlargement in freezing range for re-fused borated stainless steel due to formation of

kinetically favored Fe rich eutectic borides during solidification. Since the melting temperature of Fe rich borides are lower than equilibrium Cr rich borides [95], the propensity for hot cracking is further enhanced. In the present study, comparison of base metal and 308BRN weld metal boride microchemistry examined using EPMA/WDS also shows that the borides present in this weld metal are rich in Fe as compared to base metal borides. On the whole, there are multiple factors as discussed above which contribute to solidification cracking phenomenon in E308BRN. From the results of LVT, it is already known that susceptibility of 308BRN weld metal to liquation cracking is low. Hence, spot Varestraint tests were not conducted on weld metal of E308BRN not only because it is difficult to make a spot weld of sufficient duration because of the excess penetration, but also because of the low susceptibility of the re-fused weld metal to liquation cracking is already confirmed by the LVT.

Comparing the MCL values of 308BRN weld metal and 304B4 base metal obtained from TVT at 4% augmented strain, the base metal has a value lower by ~0.5 mm. This shows that although the MCL value of the weld is higher than base metal, it is still lower than that obtained for the weld metal produced by E309 weld metal (Fig. 5:9). Hence, this electrode can be used where moderate restraints are expected to be present during welding.

## **6.5 Summary**

1. Boron containing E308BRN weld joint is found to be more susceptible to solidification cracking than 304B4 SS metal (since the threshold strain for cracking in

308BRN weld is lower than that of the base metal) and less susceptible to liquation cracking than the E309 weld metal affected by the dilution from 304B4 SS.

2. Boron content of 308BRN weld metal is only marginally lower than that of 304B4 base metal and hence, the solidification range estimated for 308BRN weld is more or less similar to that of the base metal. Also, the eutectic borides formed in 308BRN weld metal are rich in Fe and hence the solidus temperature of the weld metal is further decreased. As a consequence, the overall temperature range of solidification for the weld metal is increased making it susceptible to solidification cracking.

3. The fraction of eutectic liquid formed during solidification of E308BRN weld metal is lower than that formed during solidification of 304B4 SS base metal due to differences in their boron content. This is one of the reasons behind ineffective backfilling occurring in E308BRN weld.

4. A comparison of the Maximum and Total crack lengths measured for different cracking tests conducted on weld joints of SS 304B4 using E309 and E308BRN consumables indicate, resistance to hot cracking is better for E308BRN weld metal than for E309 weld metal affected by dilution from base metal. Hence, for applications involving moderate restraints, use of E308BRN consumable for joining 304B4 SS can be recommended.

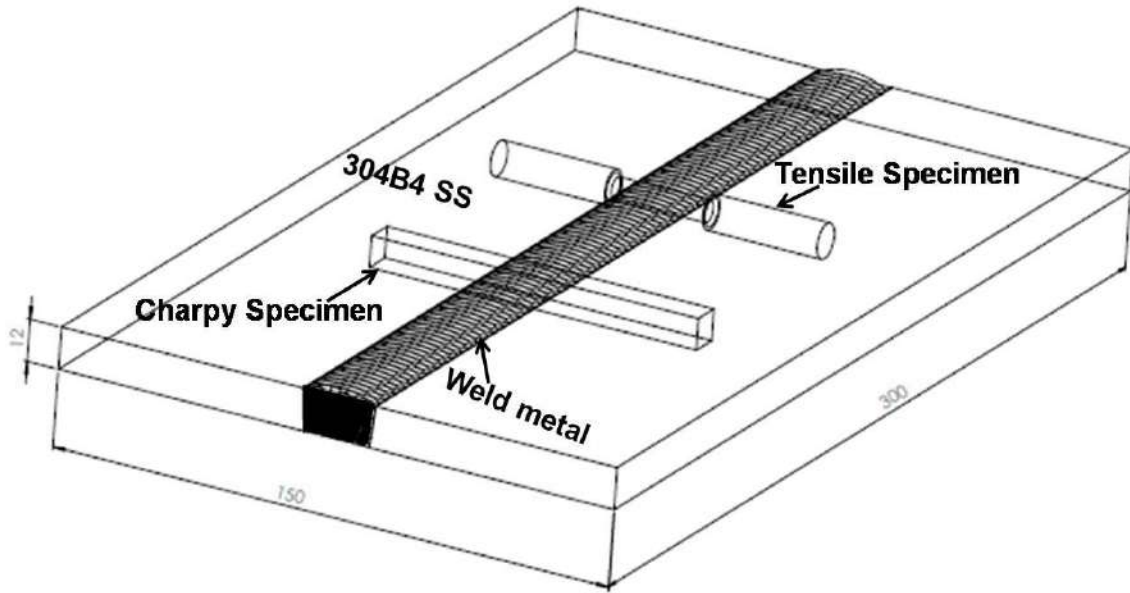
## **CHAPTER 7**

### **MECHANICAL PROPERTIES OF SS 304B4 WELD JOINTS**

#### **PREPARED USING E309 AND E308BRN ELECTRODES**

##### **7.1 Introduction**

In chapters 5 and 6, results of hot cracking susceptibility of weld joints prepared using E309 and E308BRN electrodes are presented and the metallurgical reasons for the same are discussed in detail. From the results obtained so far, it is quite clear that the weld joint prepared using E309 electrode is more susceptible to cracking than the weld joint prepared using E308BRN. In this chapter, the mechanical properties of these weld joints are presented and discussed. It may be noted that mechanical property requirement for the borated stainless steels are not very stringent unlike for other austenitic stainless steels as this class of steels are used mainly for neutron shielding and not for load bearing applications. Tensile and impact properties of the weld joints prepared using E309 and E308BRN electrodes were evaluated and compared with the base metal properties as per ASTM standards. The details on welding parameters and chemical compositions of weld metal produced from these welding electrodes are given in Chapter 3. To evaluate the mechanical properties, cross weld tensile and impact specimens were extracted from the weld joints as shown in Fig.7.1.



**All dimensions in mm**

Fig.7.1 Schematic representation of cross weld tensile and impact specimens extracted from the weld joints

**7.2 Results**

**7.2.1 Tensile properties**

Typical stress vs strain curves obtained from tensile tests conducted for base metal and weld joints made using E309 and E308BRN electrodes are shown in Fig.7.2. Tensile and yield strengths and % elongation obtained for 304B4 SS base metal are 660 and 320 MPa and 50% respectively. The base metal tensile properties satisfies the minimum requirements (Min. YS and UTS, 205 and 515 MPa respectively) specified for SS 304B4 base metal by ASTM A 887 as shown in Table 2.2 of Chapter 2. It is found that the base metal has good ductility whereas both the weld joints showed poor ductility. The cross weld tensile specimens taken from 309 weld pad failed in the part of the weld metal

highly diluted by the base metal (near the fusion boundary in the weld metal) whereas, the specimens taken from 308BRN weld pad failed in the partially melted zone (PMZ) as shown in the Fig.7.3. For weld joints made using E308BRN electrode, the UTS is comparable to that of the base metal; but for the weld joints made using E309, it is significantly lower than that of the base metal.

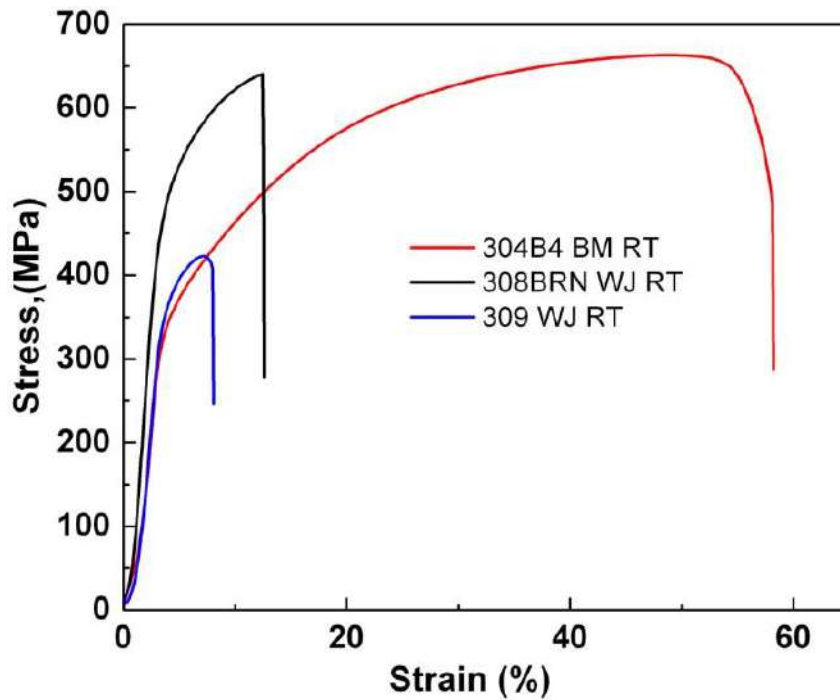


Fig.7.2 Stress-strain curves of SS 304B4 base metal, SS 304B4 weld joints prepared using E308BRN and E309 electrodes tested at room temperature.

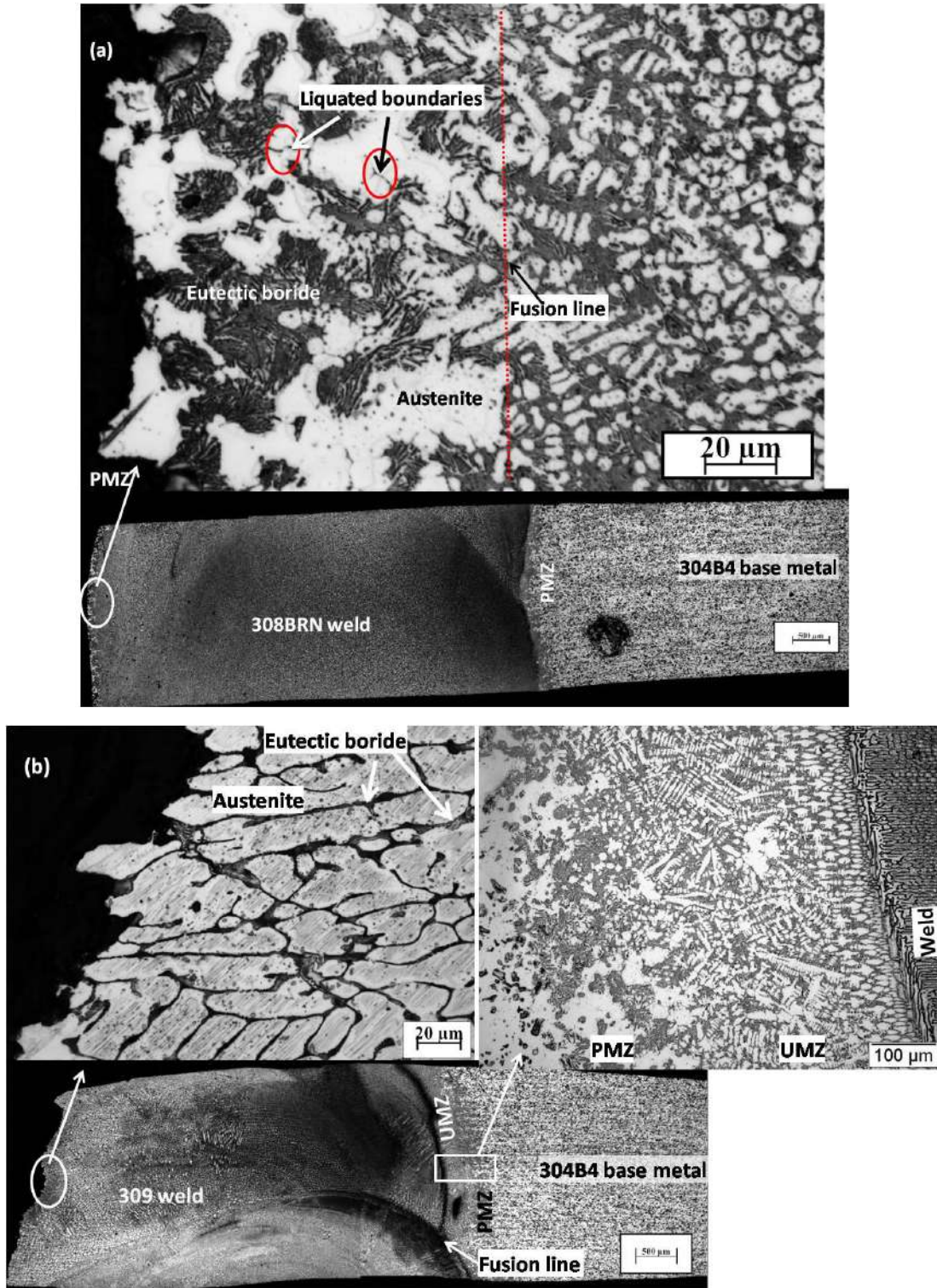


Fig.7.3 Microstructures at the fracture location of (a) E308BRN weld joint (b) E309 weld joint specimens taken after room temperature tensile test.

### 7.2.2 Impact properties

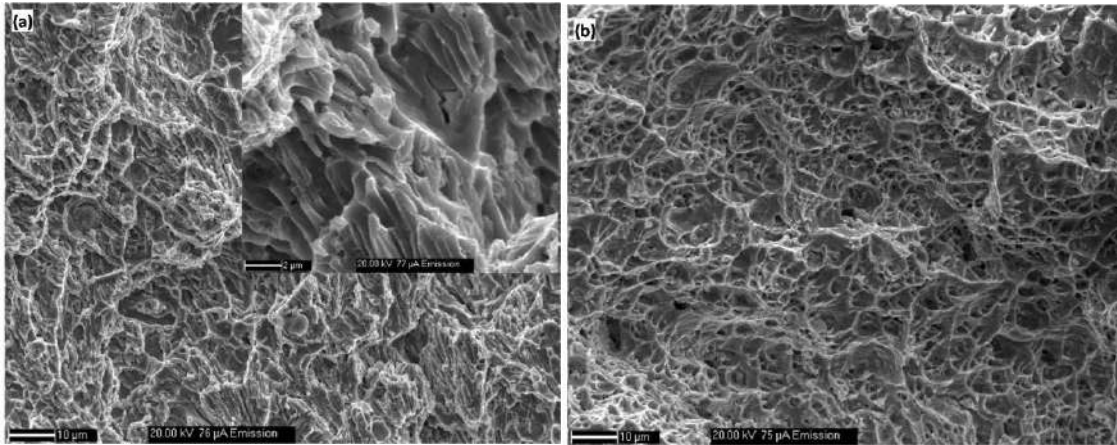


Fig.7.4 Fracture surface of (a) E308BRN weld joint (b) E309 weld joint specimens taken after room temperature impact test.

The impact toughness of 309 weld metal and 308BRN weld metal at room temperature is 50 and 10 J respectively. The toughness obtained for SS 304B4 base metal is 20 J. It is to be noted that location of the “V” notch is at the center of the weld metal in both the cases. The impact toughness of 309 weld metal may not be uniform and is expected to be lower at the weld interface than at the weld center because of base metal dilution which leads to formation of network of eutectic borides along the interdendritic boundaries (explained in Chapter 5). At the center of E309 weld metal, boron content in the weld metal would be negligible.

The fractographs of impact tested specimens of the weld joints are shown in Fig.7.4. Fractographs show cleavage facets in E308BRN weld specimens whereas E309 weld metal shows dimple morphology (Fig.7.4). The difference in the fractographs of the two weld metals can be attributed to presence of borides in the weld metal produced by

E308BRN electrode and absence of it in the notch (fracture) location of the weld metal produced by E309 electrode.

### 7.2.3 Microhardness survey across the weldments

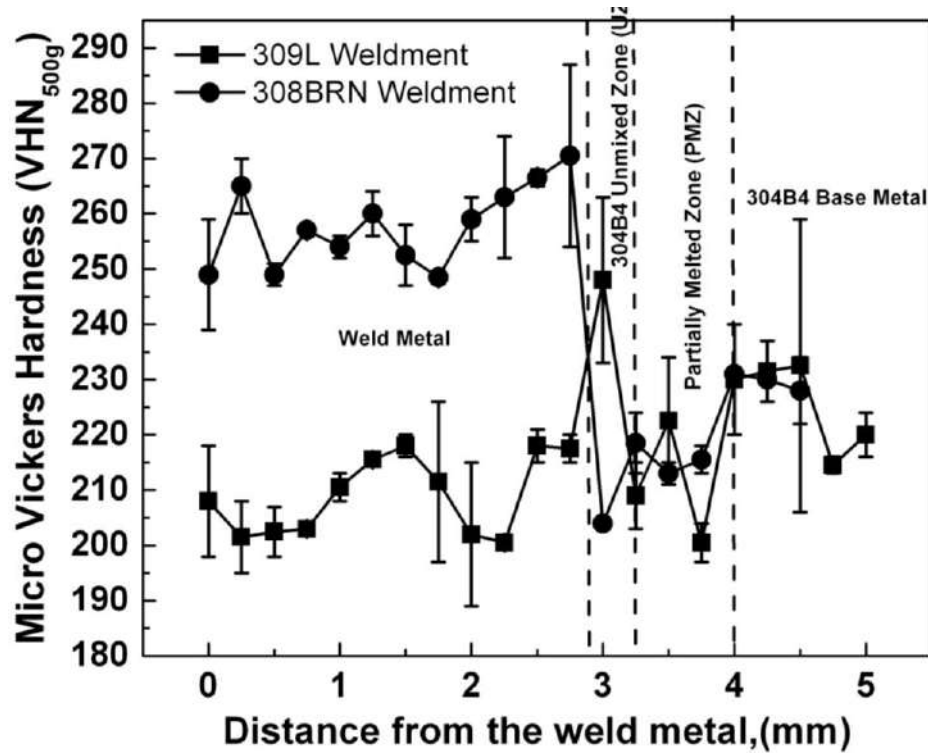


Fig.7.5 Microhardness profiles taken across weld joints prepared using E308BRN and E309 electrodes.

The microhardness profile taken across the weldments prepared using E309 and E308BRN is shown in Fig.7.5. The hardness of E308BRN weld metal ( $250 \pm 30$  VHN) is higher than that of the base metal ( $\sim 220$  VHN) and for E309 weld metal it ( $210 \pm 20$  VHN) is marginally lower. At the weld-base metal interface, where there exists a partially melted zone (PMZ) sandwiched between weld and the base metal as shown in Fig.7.3, the hardness is found to be as low as  $200 \pm 10$  VHN for both E309 and E308BRN. Similarly hardness is low in the E309 weld joint in the weld zone close to fusion boundary where

dilution is maximum ( $200 \pm 10$  VHN). It may be noted that in both the weld joints, during tension tests, fracture took place at the location of minimum hardness.

### **7.3 Discussion**

Room temperature tensile and impact properties specified for SS 304B4 as per ASTM A 887 are already mentioned in section 2.1 of Chapter 2. The minimum yield and tensile strength requirements specified for 304B4 SS in solution annealed condition is 205 and 515 MPa respectively. The minimum requirement of tensile elongation specified for grade A and B steel is 27 and 16% respectively. Impact toughness at room temperature for 304B4 grade A steel in solution annealed condition is specified around 41 joules whereas for grade B steel there is no value specified. Though, weld joint prepared using 308BRN is having yield strength closely matching with that of the base metal, its impact toughness is significantly lower than that obtained for the base metal.

In 308BRN weld joint, though weld metal composition is similar to that of the base metal, there is significant variation in hardness of the base metal and the weld metal as shown in Fig.7.5. Hardness of the weld zone is at least 50-70VHN more than the base metal and this can be attributed to as cast microstructure of the weld zone consisting of austenite and interdendritic eutectic constituents as shown in Fig.7.3(a). Also, it is evident from Fig.7.5 that there is a hardness dip in the PMZ region which suggests that the region has lower strength than the other regions of the weldment since the austenite grains are surrounded by the eutectic phases. During tension testing of the joint, fracture occurred at the PMZ where hardness is low. Owing to the constraint effect of the adjacent zones of higher hardness, deformation of relatively soft PMZ is restricted leading to fracture at this

location with limited ductility. By correlating the microstructure adjacent to the fracture location in Fig.7.3(a) and the stress- strain curve in Fig.7.2, it is evident that the failure has taken place with little elongation due to linkage of voids (generated due to constraint effect) at eutectic-matrix interface in the PMZ. Since PMZ is the location in the weldment where complete grain boundary liquation occurs as shown in the Fig.7.3(a), propagation of cracks occurs easily along the grain boundary.

In the case of E309 weld joint, the yield strength recorded closely matches with that of the base metal, as shown in Fig.7.2. The failure has occurred in the part of the weld metal highly diluted by the base metal. Figure 7.3(b) shows austenite dendrites and interdendritic eutectic borides in the microstructure adjacent to the failure location. The interdendritic eutectic phases are formed due to presence of boron in the weld metal as a consequence of base metal dilution of the boron free E309 weld metal during welding. Its chemistry is different from that of both base metal and undiluted weld metal. As already mentioned, the fracture location in tension test is the location of minimum hardness. Further adjacent to this location, there is an increase in the microhardness value (Fig.7.5) immediately after the weld interface in 304B4 unmixed zone as shown in microstructure of weldment extracted from 309 weld pad in Fig.7.3(b). Again the constraint effects resulting from adjacent regions of higher hardness is promoting a low ductility fracture of the part of the joint which is low in hardness.

The poor ductility of E309 weld joint can also be attributed to embrittling effect of eutectic borides present in the interdendritic regions as shown in the microstructure (Fig.7.3(b)). Figure 7.6 shows SEM image of tensile specimen extracted from 309 weld

joint near the fracture location. It can be observed that the voids are present along eutectic – austenite interfaces which indicate that the failure has taken place due to weakening of interdendritic regions by the presence of eutectic borides.

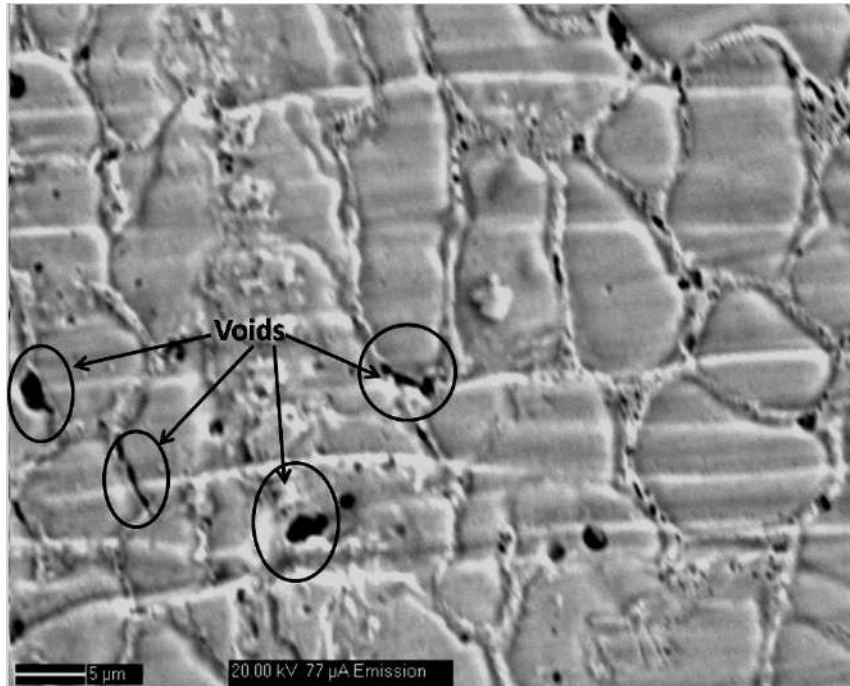


Fig.7.6 SEM image of tensile tested specimens extracted from 309 weld joint showing voids in the interdendritic regions near the fracture location.

Impact toughness obtained from 304B4 weld joint with the notch at 309 weld center was 50 J which is consistent with the value ~54 J reported for all weld E309 weld metal impact toughness at room temperature [96]. It seems at weld metal center, the base metal dilution being negligible as mentioned earlier; the weld metal impact toughness remained similar to undiluted 309 weld metal. The microstructure of 309 weld metal adjacent to the fracture location reveals only austenite dendrites and delta ferrite as shown in Fig.7.7. At the same time it is to be noted that the impact toughness value at the weld

joint interface may be less than that observed at weld center due to eutectic boride network observed at this region as shown in Fig.7.3(b). Impact toughness value (10 J) of E308BRN weld metal also shows that it is highly embrittled by the interdendritic eutectic phases as shown in the weld metal microstructure of 308BRN in Fig.7.3(a).

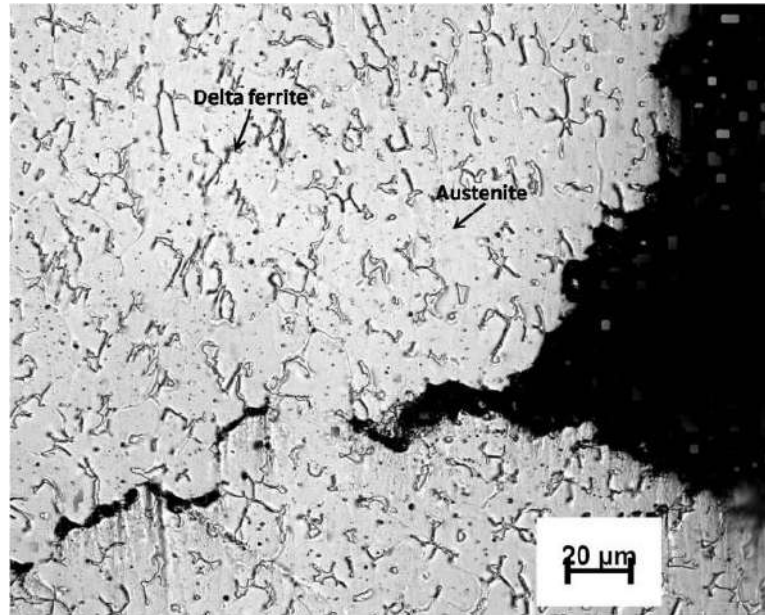


Fig.7.7 Microstructure of 309 weld metal taken adjacent to fracture location on impact tested specimen

As per the AWS A5.9 mechanical property requirements of typical E309 all weld metal is 400 MPa yield strength, 575 MPa tensile strength, impact toughness 55 J at room temperature and 35% elongation. Weld joint ductility and UTS values are lower than that is specified for the all weld metal for reasons given above. In case of 308BRN weld joint, tensile and yield strength satisfies the AWS requirements of E309 whereas, elongation and impact toughness criteria are not satisfied. Impact toughness of weld metal at the weld center in weld joint prepared using E309 shows superior toughness than weld joint

prepared using E308BRN. However, as already revealed from the results presented in Chapters 5 and 6, SS 304B4 weld joints prepared using E309 electrode shows higher susceptibility for hot cracking than the weld joint prepared using E308BRN. Although, using E309 consumable for welding 304B4 SS suffers from this drawback, in view of utilizing the benefit of superior toughness offered by this weld joint, and being a standard welding consumable widely used for welding austenitic stainless steels, it is worth exploring the options for reducing the cracking susceptibility of weld joints made by E309 consumable.

#### **7.4 Summary**

1. Weld joint of 304B4 made with E309 electrode has low strength compared to that of the base metal and the fracture occurs in the weld metal close to the interface where dilution is high. In the case of weld joints made by E308BRN electrode, UTS of the weld joints more or less matches with that of the base metal and fracture location is the PMZ of the base metal. Ductility is low for both the weld joints compared to that obtained for base metal.
2. Impact toughness of the weld joint made with E309 electrode with notch at at the weld center (50J) is significantly higher than that of the base metal (20 J); while that of the weld joints made with E308BRN is significantly lower (10 J).
3. In the case of E309 weld joints, difference in hardness between the base metal and the weld metal is not large though both composition and microstructure of the weld metal is significantly different from that of the base metal. In the case of E308BRN weld joint, hardness of the weld metal is consistently higher than that of the base metal. In both the

weld joints, specimens fractured during tension test at the location of minimum hardness of the weld joint; in the weld metal close to the fusion boundary, where effect of dilution from base metal is maximum, in the case of E309 weld joint and in the PMZ formed in the base metal for E308BRN weld joint.

4. Poor impact toughness observed in E308BRN weld metal is attributed to as cast structure of the weld metal consisting of continuous network of eutectic borides along the interdendritic regions. Whereas, good impact toughness shown by E309 weld metal is due to presence of only austenite - ferrite duplex microstructure and no traces of eutectic boride at the weld center. However, as the microstructure and composition varies across the weld metal, it is likely that there could be variation in toughness across the weld metal in the case of weld joints made by E309 welding consumable.

# **CHAPTER 8**

## **MODIFIED WELDING PROCEDURE TO REDUCE HOT CRACKING IN SS 304B4 WELD JOINT PREPARED USING E309 ELECTRODE**

### **8.1 Introduction**

In the previous chapter, it was shown that the mechanical properties of SS 304B4 weld joints prepared using E308BRN electrodes closely satisfies the minimum strength requirements of tensile properties specified for SS 304B4 base metal as per ASTM standard A887; but impact toughness value obtained for 308BRN weld metal is very low as compared to the base metal. Though, in the standards, for SS 304B4 there is no mention about impact toughness requirements for grade B steel while for grade A steel impact toughness value of 41 joule is recommended. This indicates that the toughness of the weld metal produced by E308BRN electrode is much lower than the desired value of toughness for base metal of grade A borated stainless steel. In Chapter 6, it was shown that weld joints prepared using boron added electrode-E308BRN showed better resistance to hot cracking in weld metal than E309 weld metal. Nevertheless, the study also indicated that the hot cracking susceptibility evaluated by Varestraint test carried out on weld metal produced by E308BRN consumable is more than that of the SS 304B4 base metal. In other words, it can be inferred from the results presented in Chapter 6 that the weld joints prepared using E308BRN electrode would be susceptible to hot cracking while welding under high restraint forces. Further, it is to be noted that E308BRN is a non standard electrode and with a boron content of ~1 wt.%, there is little scope for improving

the resistance to solidification cracking in 308BRN weld metal. In case of weld joint prepared using E309 electrode, though the weld joint does not meet the minimum tensile strength requirement of the base metal, the impact toughness obtained in the weld metal is on par with the base metal. Hence, this electrode is a good choice for welding borated stainless steel components for which minimum impact toughness is desirable as in the case for grade A borated stainless steel for which minimum impact toughness is specified in the standard.

Further, a critical analysis of the results reported in Chapter 5, hot cracking susceptibility of weld joints prepared using E309 welding consumables reveals the possibility of improving the hot cracking resistance of the weld joints by adopting a welding procedure with buttering. For both buttering and welding E309 welding consumable can be used. In this chapter, this new welding procedure is described and it is shown that this procedure can indeed reduce the cracking susceptibility of the weld joint considerably.

## **8.2 Modified welding procedure for joining SS 304B4 using E309 electrode**

The modified welding procedure adopted for welding SS 304B4 using standard E309 electrode is described schematically in Fig.8.1. The difference between the conventional welding procedures followed for welding SS 304B4 and the modified welding procedure is that an extra step of buttering is included in the latter. In this welding procedure, the edge surfaces are to be first buttered with E309 SS welding consumable as shown in Fig.8.1.

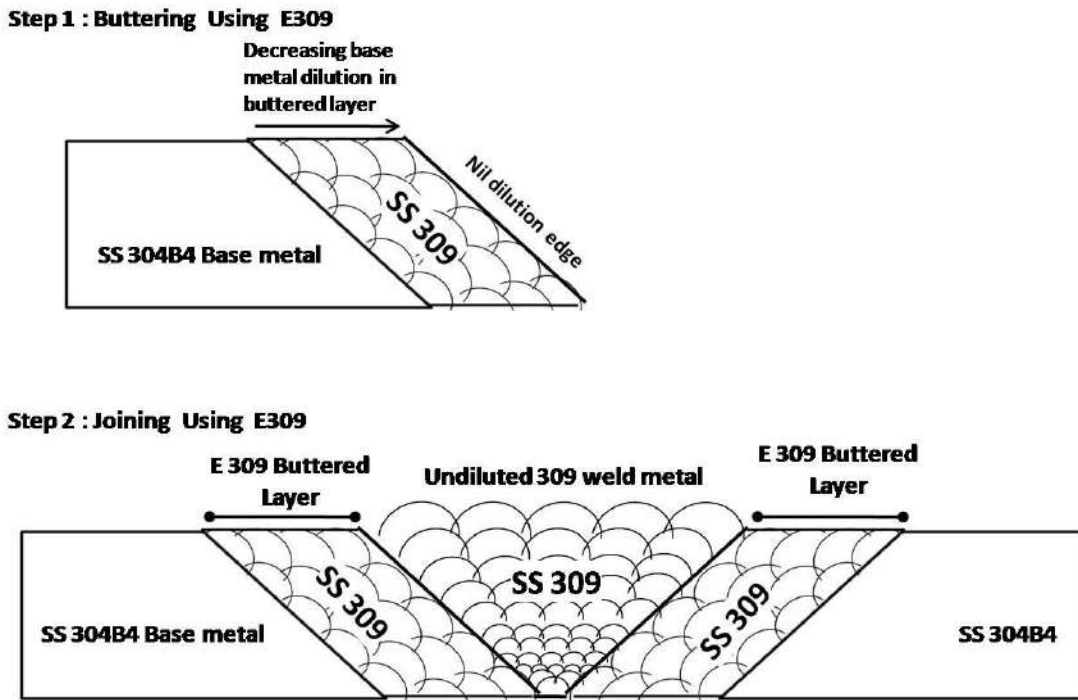


Fig.8.1 Schematic representation of modified welding procedure adopted for welding 304B4 SS using E309 electrode.

The welding parameters, current- 120 A and voltage- 25 V were used during the buttering process. The thickness of the buttered layer should be such that on the faces prepared after machining of the buttered layer, dilution from base metal should be negligible per se 7 mm. Since there is no joining involved during buttering, residual stresses generated during buttering would be less. Hence, though the fusion zone microstructure of the buttered layer could be susceptible, risk of cracking would be less. Further, during buttering there is much better control of heat input and hence, dilution from base metal can also be minimized in the buttered layer. Subsequently, welding is carried out using the plates with edges prepared with buttered layers as shown in Fig. 8.1. Now in the actual joining of plates, only melting of the free surface of the buttered layer,

which is for all practical purpose is same as the fused E309 welding consumable, occurs. Hence, risk of cracking is expected to be reduced.

In order to demonstrate this hypothesis, hot cracking specimens were prepared from the weld joints made as described above and susceptibility of the fusion zone in which melting and mixing of both buttered layer and welding consumable take place during actual joining, is evaluated .

### 8.3 Preparation of spot Varestraint test specimen from the weld joints prepared with buttering

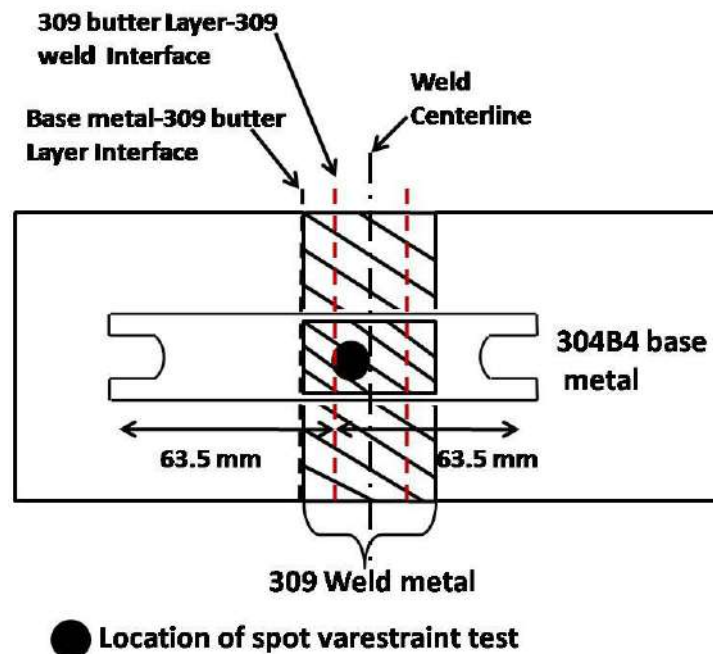


Fig.8.2. Schematic representation of locations on weld pad prepared after buttering from which spot Varestraint test specimens were extracted and spot Varestraint test was conducted.

Spot Varestraint test specimens used in this study was extracted from SS 304B4 weld joint prepared using E309 electrode and modified welding procedure. The welding parameters used for preparation of the weld joint are same as those given in Table 3.3 of

Chapter 3 for weld pad preparation using E309 electrode. The schematic representation of position on weld pad from which specimens were extracted is shown in Fig.8.2.

The specimens used for evaluation of weld metal liquation cracking susceptibility were extracted from weld pad in such a way that the fusion zone near the interface between the buttered layer and the weld metal is at the center of the V-restraint specimen. The purpose is to specifically study the susceptibility of this zone which would have been diluted with the fused portion of the buttered layer. Rest of the weld metal would be fused E309 electrode with no dilution. Results of hot cracking susceptibility of this zone (undiluted 309 weld metal) are already given in Chapter 4.

## **8.4 Results**

### ***8.4.1 Microstructure of the weld joint prepared after buttering***

Figure 8.3 shows the macrostructure of SS 304B4 weld joint (prepared using modified welding procedure) and the microstructures of individual zones of the weld joint. From the Fig.8.3(a) it is evident that there are two interfaces in the weld joint, (i) an interface between SS 304B4 base metal and 309 buttered layer and (ii) an interface between the E309 buttered layer and 309 weld metal. Figure 8.3(b) shows the microstructure of PMZ formed on 304B4 base metal which consists of partially molten and solidified austenite grains and completely molten and solidified eutectic phases. Figure 8.3(c) shows the microstructure of un-mixed zone (UMZ) formed next to PMZ which consists of austenite dendrites and interdendritic network of eutectic phases. In Fig.8.3(d), the region of 309 butter layer close to the interface-1 in which substantial base

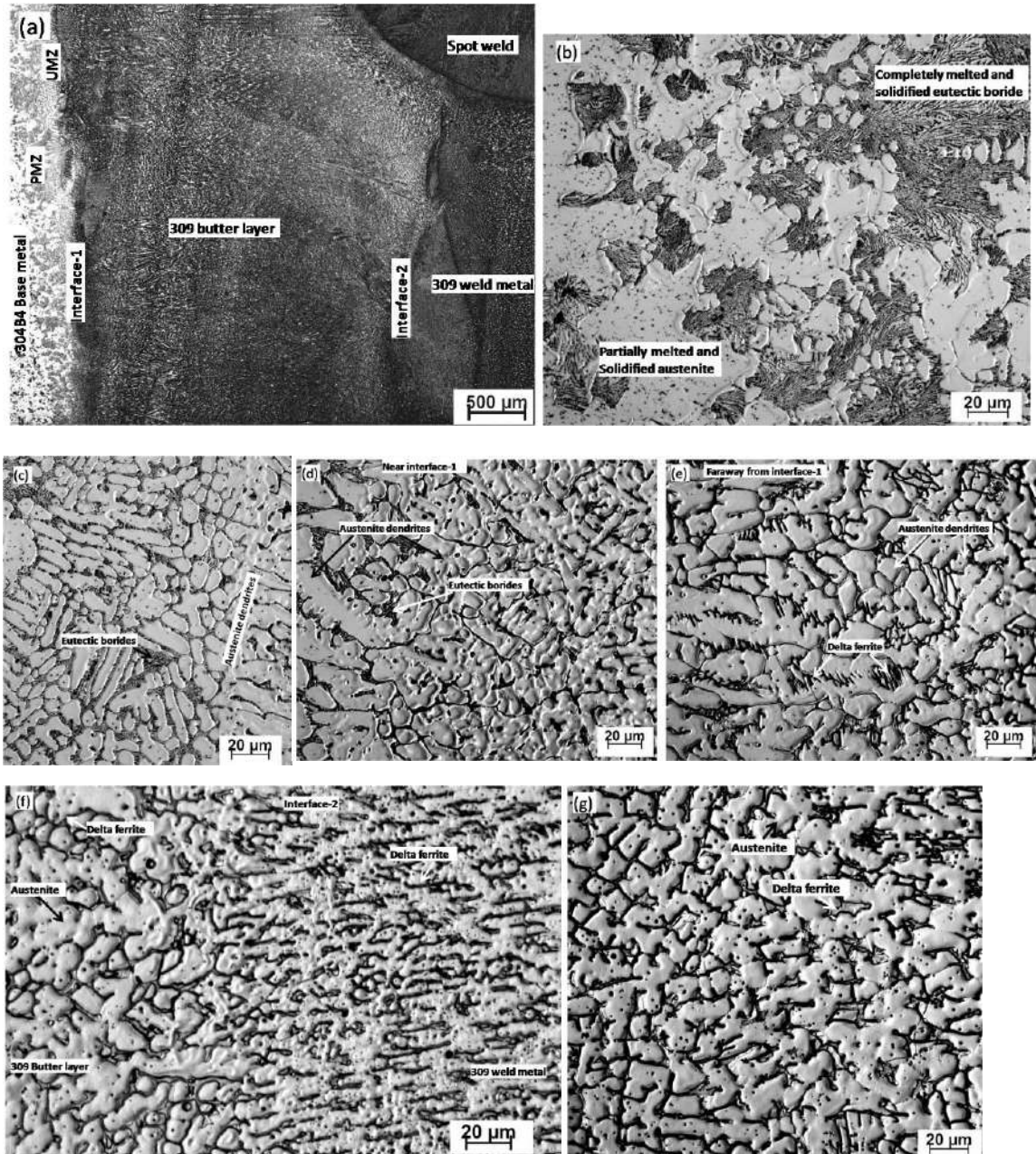


Fig.8.3 (a) Macrostructure of 304B4 SS weld joint prepared using modified welding procedure (b) Microstructure of PMZ formed on 304B4 SS base metal (c) Microstructure of UMZ formed next to PMZ Microstructures of 309 butter layer (d) near (e) far away from 304B4 SS base metal- 309 butter layer interface (interface -1) (f) Microstructure of interface between 309 butter layer and 309 weld metal (interface-2) (g) Microstructure of 309 weld metal.

metal dilution has occurred is shown. The microstructure consists of austenite dendrites and a mixture of eutectic phases and delta ferrite in the interdendritic region (as discussed in Chapter 5). The microstructure in Fig.8.3(e) shows the butter region far away from the interface -1 which consists of austenite dendrites and delta ferrite. The microstructure in Fig.8.3(f) shows the interface between the E309 butter layer and the weld metal. This microstructure consists of high fraction of delta ferrite. The microstructure of 309 weld metal deposited after buttering (Fig.8.3(g)) shows only austenite dendrites and delta ferrite.

#### ***8.4.2 Quantitative analysis of cracking susceptibility***

Figure 8.4(a) shows the macroscopic cracking features in specimen after spot Varestraint test at 4% augmented strain. Figs.8.4 (b) and (c) show plots of Total Crack Length (TCL) vs % augmented strain and Maximum Crack Length (MCL) vs % augmented strain respectively of weld joint prepared using E309 electrode with and without buttering (taken from Chapter-5 ). The macrostructures in Fig.8.4(a) show a few cracks in the re-fused region and one or two cracks on the weld metal PMZ region of 309 butter layer which lies on left side of interface-2 .Whereas, there are no cracks in the E309 weld metal PMZ which lies on the right side of the interface-2. A comparison of the crack length data shown in Fig. 8.4(b) and (c) shows that TCL and MCL obtained for the weld joint prepared using modified welding procedure is lower than that for the direct joint, thus, indicating lower susceptibility of the buttered joint to cracking. The MCL at threshold strain ( $\epsilon_2$ )(1% ) is 0.5 mm for the joint prepared using buttering layer whereas the same ( $\epsilon_1$ ) is ~ 2.5 mm for the joint prepared using without buttering as shown in the

figure. This shows the liquation cracking susceptibility of the weld joint prepared using modified welding procedure is lower than that prepared without buttering.

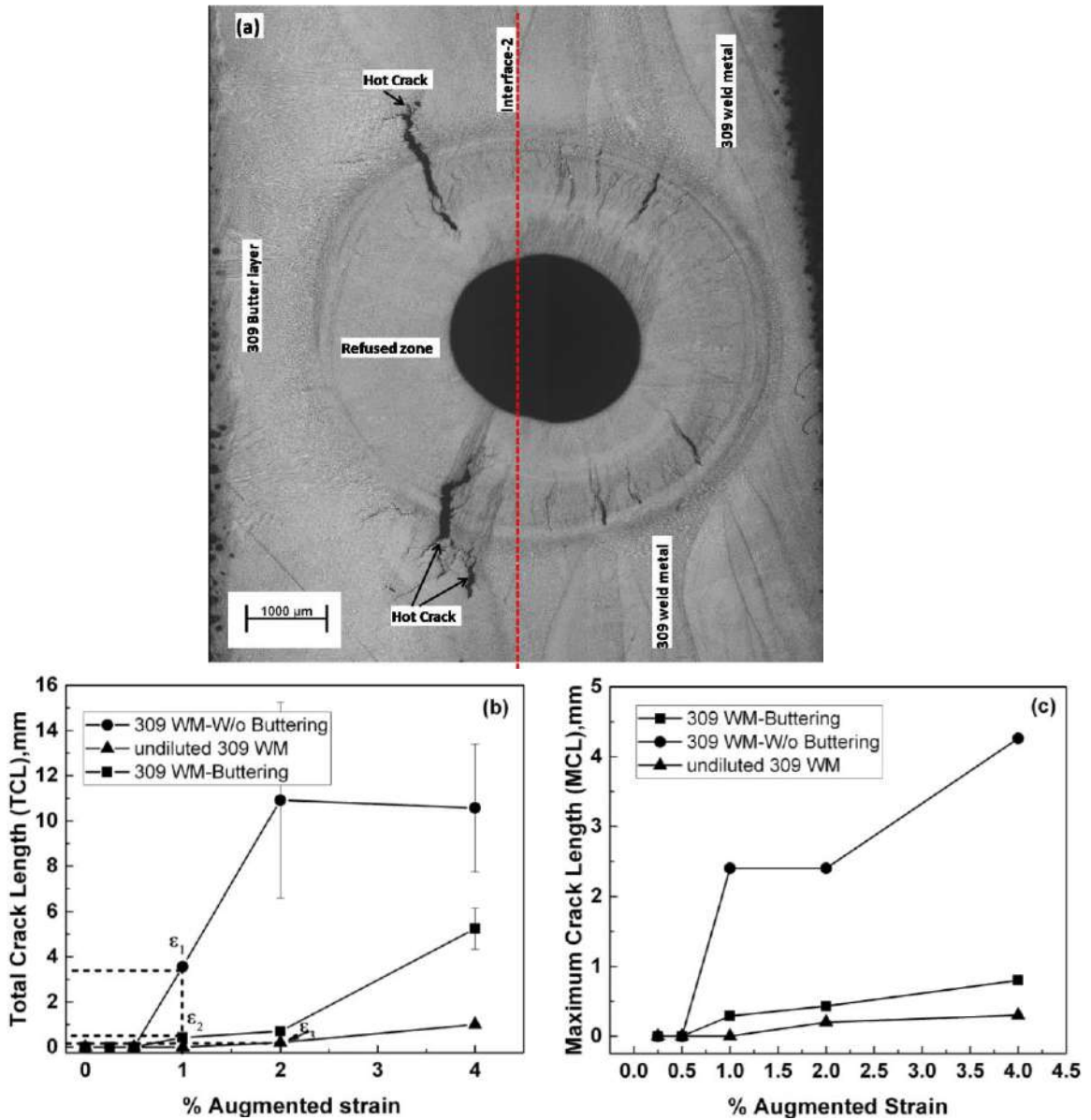


Fig.8.4 (a) Macrostructure of spot Varestraint tested specimen extracted from weld joint prepared using E309 after buttering. Plots of (b) Total Crack Length (TCL) vs % augmented strain (c) Maximum Crack Length (MCL) vs % augmented strain of weld joints prepared using E309 with, without buttering and undiluted 309 weld metal.

### 8.4.3 Microstructures of Specimens after Spot Varestraint Test

Figure 8.5(a) shows low magnification microstructure of spot Varestraint tested specimen where a few liquation cracks are present in the weld metal PMZ.

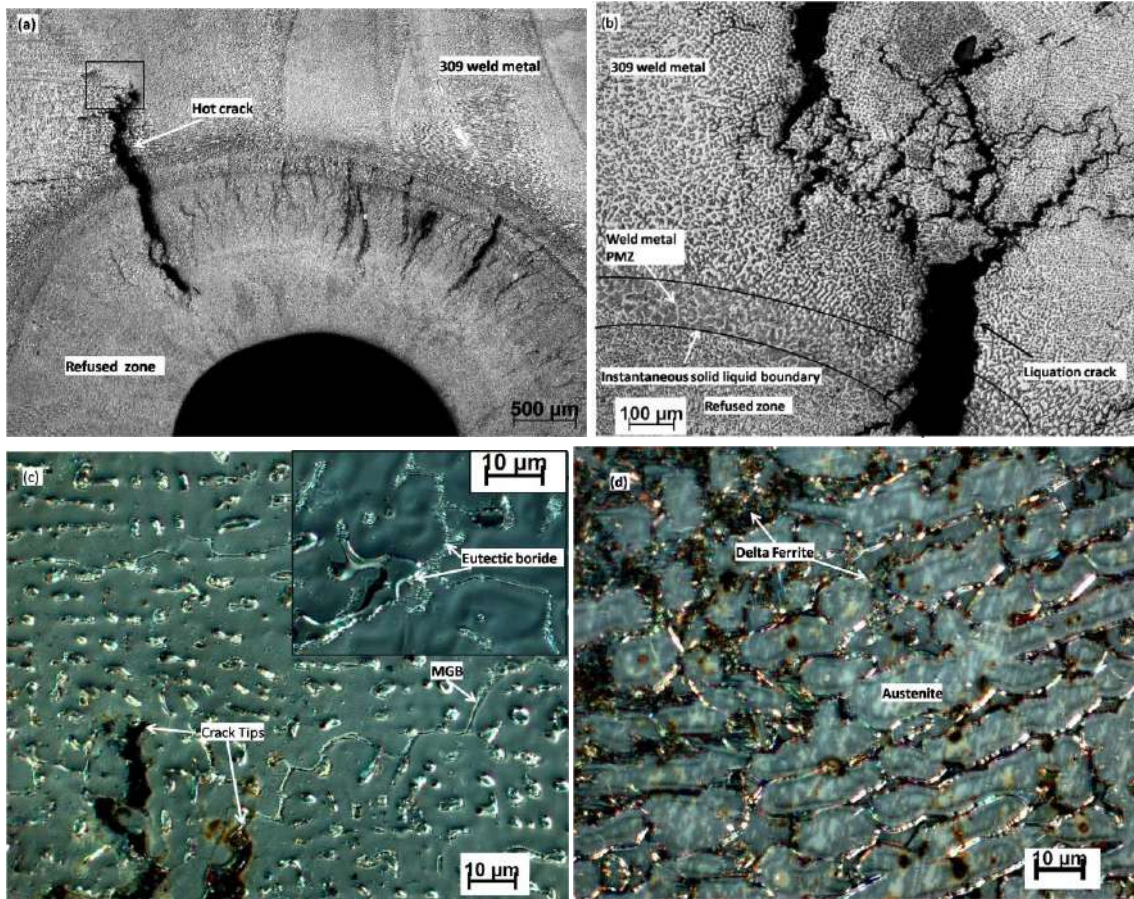


Fig.8.5(a) Macrostructure of spot Varestraint tested specimens showing a liquation crack taken at low magnification (b) Microstructure of the liquation crack present in 309 weld metal taken at high magnification (c) Polarized light contrast microstructure of 309 weld metal showing MGBs taken at the crack tips and the inset to the figure shows features pertaining to eutectic films along the MGB at high magnification (d) Polarized light contrast microstructure of 309 weld metal showing austenite and delta ferrite at the location where liquation cracks are not present.

Fig.8.5(b) shows the microstructure of spot Varestraint tested specimen at 4% augmented strain. From the microstructure it appears that the liquation cracks have

occurred along the Migrated Grain Boundaries (MGBs) in 309 butter layer. The microstructure in Fig.8.5(c) (magnified image of area demarcated in Fig.8.5(a)) shows presence of eutectic constituents along the MGBs below the crack tip. The microstructure taken in polarized light clearly differentiates the MGBs and cracks present in 309 weld metal, and also reveal the morphology of the eutectic constituents present along the MGBs. The microstructure in Fig.8.5(d) shows polarized light image of 309 weld metal PMZ where no liquation cracks are present (right side of the interface-2). The microstructure clearly shows that at this location only austenite dendrites and interdendritic and lacy ferrite are present with no indications of eutectic constituents.

## **8.5 Discussion**

From the study carried out so far and presented in the previous chapters, the reason behind liquation cracking occurring while using boron free welding consumable is clearly understood. The formation of thin films of eutectic borides due to base metal dilution in weld metal is the primary cause for liquation cracking in the weld joints. Also, the problem of hot cracking remains unsolved even after using boron containing consumable since the weld joints are susceptible for cracking at high restraints. Further, impact toughness of the weld joint made by this welding consumable is considerably inferior to those produced from E309 electrode and the base metal. Based on this understanding obtained from the previous studies, a modified welding procedure is proposed. The idea behind this welding procedure is that the risk of hot cracking can be considerably reduced if a susceptible microstructure can be avoided during actual welding, when residual stresses generated can facilitate cracking. Results indeed confirm

this hypothesis. The microstructure of the zone that is likely to be crack prone (near the interface between the butter layer and the weld metal) in the modified joint is almost free of borides and its cracking susceptibility is considerably lower than that observed for similar zone (the interface between base metal and weld metal) in the direct joint between 304B4 plates using E309 consumable. This is shown in Fig 8.4, a comparison of TCL data obtained for the spot Varestraint test conducted for the two zones as mentioned above in the weld joints prepared with and without buttering along with that of the undiluted weld metal of E309 electrode. From this figure it is quite discernable that liquation cracking susceptibility of weld joint prepared using the modified welding procedure is far lower than the other.

Ideally the liquation cracking susceptibility (MCL value) in the weld joint prepared using the modified welding procedure should have been similar to that of undiluted 309 weld metal but it is found to be slightly higher than that of the latter. This is because; boron is present in the E309 weld metal as result of dilution from the butter layer which can have some boron because of dilution from the base metal. This is clearly evident from the signatures of eutectic constituents present along the MGBs in the microstructure shown in Fig.8.5 in the weld metal near the interface between the buttered layer and weld metal. In addition to this, weld puddle produced during spot Varestraint test could not be accurately restricted within the interface between the butter layer and weld metal (interface-2, Fig.8.3(a)). It can be observed that the spot weld has slightly moved towards the butter layer as shown in Fig.8.3(a). This could be the possible reason behind the observed cracking susceptibility of weld joint prepared using modified

welding procedure which is slightly higher than the undiluted 309 weld metal. On the other hand, it should be noted that the cracking susceptibility of the weld joint has substantially reduced as compared to the direct joint prepared without buttering. Further, it is also possible that the TCL and MCL values of the weld joint produced using the modified procedure can be further reduced if proper care is taken during machining of buttered layer and subsequent testing. It may be possible that hot cracking resistance of the SS 304B4 weld joint can be made comparable to that of undiluted 309 weld metal using the modified welding procedure by carefully controlling the steps involved during weld joint fabrication process.

It is to be noted that no comparison is made between the hot cracking in the weld metal of E308BRN weld joint and that in the weld metal of weld joints made with E309 consumable with and without buttering. This is because, in the case of weld metal made of E308BRN, it is the solidification cracking of the fused metal, while in the other case, it is liquation cracking of the fusion zone HAZ that manifest as hot cracking of the weld joints. Solidification cracking is studied mainly using TVT while liquation cracking of the HAZ formed in the fusion zone is studied using spot Varestraint tests. Direct comparison of the results from these two different tests is appropriate and hence not attempted.

## **8.6 Summary**

1. The modified welding procedure involving buttering developed for welding SS 304B4 using standard E309 electrode significantly reduced cracking susceptibility of the weld joint.

2. The idea behind the design of modified welding procedure is that even though base metal dilution takes place in the butter layer resulting in formation of eutectic borides, tensile stresses responsible for cracking, generated during buttering would not be as high as that formed during welding. Subsequently, final welding is carried out between dilution free E309 buttered surfaces using 309 electrode where, weld metal microstructure produced is resistant to hot cracking.

3. Hence, buttering of the joint surface with E309 for sufficient thickness is recommended as an alternate procedure to join borated stainless steel to bring down the risk of hot cracking. Thickness of the buttered layer should be such that after edge preparation for subsequent welding, the surfaces to be welded together should be free of dilution (typically more than 5 mm).

## CHAPTER 9

### CONCLUSIONS, CONTRIBUTIONS AND SCOPE FOR FUTURE

#### RESEARCH

##### 9.1 Conclusions

In the preceding Chapters, results of extensive hot cracking and hot ductility tests carried out on AISI 304B4 base metal and the weld joints produced using E309 and boron containing E308BRN consumables are presented and discussed. It is shown that AISI 304B4 base metal is fairly resistant to both liquation and solidification cracking; two variants of the hot cracking. It is also shown that effective backfilling of the microcracks by the eutectic liquid is the major mechanism by which cracking is avoided in this steel. These are in agreement with published literature available on the cracking susceptibility of this steel.

It is found that fused 304B4 is susceptible to cracking during re-melting, which is unavoidable during multipass welding. Further, in the fusion zone of SS 304B4, because of the non equilibrium cooling conditions that persist, the borides present in the interdendritic regions are rich in Fe ((Fe,Cr)<sub>2</sub>B), unlike those present in base metal, which are predominantly Cr rich. Hence, the eutectic reaction during re-melting and subsequent solidification is completed at temperatures as low as ~1180°C. Further, it is found that because of partial melting of austenite and eutectic borides in the PMZ formed in fusion zone during subsequent re-melting, the boron content in liquid metal in this PMZ changes to hyper eutectic composition which is more than the nominal boron content of the alloy. Hence, there is reduced volume fraction of eutectic phase that makes complete backfilling

of the cracks difficult. All these contribute to higher cracking susceptibility of the PMZ formed in the fusion zone than that of the PMZ formed in the base metal.

The present study also reveals that in the multipass 304B4 weld joint, prepared using E309 electrode, the standard consumable recommended for welding this alloy, part of the weld metal diluted by the base metal is highly susceptible to liquation cracking. This is because dilution from base metal introduces boron into the weld metal resulting in the formation of thin films of eutectic boride/austenite constituents along interdendritic regions of the weld metal where dilution is significant. Further, as the boron content is low (compared to base metal), the volume fraction of the eutectic phase is not sufficient to heal the cracks by back filling. Thus, making the part of the diluted weld metal containing boron typically in the range of 0.2-0.4 wt.%, highly susceptible to liquation cracking during multipass welding. Away from the fusion boundary, towards the center of the weld joint, effect of base metal dilution on E309 weld metal is almost negligible and this part of the weld metal is found to be highly resistant to liquation cracking. Overall, it is shown that while joining of SS 304B4 using E309 electrode, due to dilution from the base metal, weld metal is highly prone to liquation cracking during multipass welding. This explains the severe hot cracking observed during welding of thick sections of 304B4 stainless steel during fabrication of components made of this steel.

Evaluation of hot cracking susceptibility of weld metal produced by joining 304B4 base metal using boron containing E308BRN electrode reveals that this weld metal is less susceptible to cracking than that produced using E309 electrode. Unlike the latter, this weld metal is more susceptible to solidification cracking than liquation

cracking. Though boron content in E308BRN (~1 wt.%) is only marginally lower than that of base metal (1.3 wt.%), weld metal is more prone to cracking than the base metal. Effective back filling of the cracks does not occur because of the large solidification range for the weld metal and low volume fraction of the eutectic liquid in the final stages of solidification. This is revealed from the hot cracking tests conducted using Transverse Vareststraint Test on the weld metal at different strain levels. Results indicate that risk of hot cracking during welding of 304B4 steel using boron containing electrode is low only under conditions of low restraints.

Mechanical properties evaluated for the weld joints prepared using E309 and E308BRN electrodes show that the ductility is poor due to the presence of continuous network of eutectic borides along the interdendritic regions of the weldments. On comparing the mechanical properties of the weld joints, it is found that weld joints prepared using E309 electrode offers better toughness than that prepared using E308BRN electrode; but its strength is lower than that of the latter and the base metal.

A new procedure, that can significantly bring down the risk of liquation cracking in the weld metal while welding borated stainless steel using E309 electrode is demonstrated in this study. This procedure involves an extra step of buttering first on the faces of the base metal to be joined using E309 electrode and then subsequent joining of the buttered faces (after proper edge preparation) using the same electrode. Using spot Vareststraint tests conducted on the weld metal thus produced, it is shown that the liquation cracking susceptibility of such welds is significantly lower than the weld metal produced by direct joining of the 304B4 plates using the same electrode. Hence, this procedure is

recommended for welding of 304B4 base metal using E309 electrode to produce weld joints with reduced risk of cracking and reasonably good weld metal toughness.

## **9.2 Contributions**

Following are the contributions from the present study towards an improved understanding of the hot cracking that occur during welding of borated stainless steels.

1. In addition to morphology and volume fraction, chemistry of the borides also changes during melting and solidification of borated stainless steels during welding making the fused metal more susceptible to liquation cracking than the base metal. Thus, making the multipass welds of this steel prone to hot cracking. Results reported on hot cracking susceptibility tests carried out on the base metal in the present literature does not reveal this.
2. The weld metal produced from E309 electrode, in spite of its high delta ferrite content, is also highly susceptible to liquation cracking during multipass welding due to dilution from the base metal. As a result, the borated stainless steel weld joints made using this electrode is also prone to cracking if appropriate steps are not taken to control base metal dilution during welding.
3. Use of boron containing electrodes for welding of borated stainless steels has a beneficial effect of reducing the risk of cracking; but does not eliminate it. Weld metals produced using this consumable is also prone to solidification cracking at considerably high restraints.
4. Present results agree with the published literatures available on hot cracking susceptibility of the borated stainless steels which attribute the low susceptibility of SS

304B4 to cracking to back filling of the cracks by the eutectic liquid. At the same time it also explains the cracking observed during multipass welding of this steel.

5. A new welding procedure that involve buttering and subsequent welding using E309 welding consumable which significantly reduces the risk of cracking is demonstrated and recommended for welding of borated stainless steel.

### **9.3 Scope of future research**

1. Present study showed that buttering of the weld faces to be joined and subsequent joining of the buttered surfaces, both using E309 electrodes, significantly brings down the risk of cracking during welding of SS 304B4. However, there is a need to optimize the thickness of the buttered layer in such a way that the part of the buttered faces which undergo melting and liquation during welding is free from dilution from base metal.

2. From the study it is understood that the delta ferrite formed during solidification does not play any role in preventing hot cracking in borated stainless steels. Hence, it is planned to weld the SS 304B4 using the newly proposed procedure that involve buttering and E308 electrode which is cheaper than E309 electrode. If found successful, replacing E309 with E308 can bring down the increased cost of fabrication emerging from the additional steps of buttering and machining present in the proposed new procedure.

3. Stainless steels containing higher boron levels such as 304B7 SS would be preferred for many nuclear applications where high levels neutron shielding is required. Therefore, weldability studies as carried out presently in SS 304B4 can be further extended for evaluation of hot cracking susceptibility of 304B7 stainless steel welds leading to development of improved procedures to mitigate the same.

## REFERENCES

1. “Standard specification for borated stainless steel plate”, sheet and strip for nuclear applications, 2000, ASTM, A887-89
2. “Effect of PWHT on mechanical properties of borated stainless steel GTA weldments for nuclear shield”, Park. T. D, Baek. K. K and Kim. D. S, Metals and Materials, 1997, 3, :46-50.
3. “Welding technology for stainless steel containing 1.2% boron content-case study”, Kulkarni. N. V, Galgali. V. S, Proceedings of 20th Annual Conference of Indian Nuclear Society, 2010, 61-65.
4. “An Overview of Welding Aspects and Challenges during Manufacture of Intermediate Heat Exchangers for 500mwe Prototype Fast Breeder Reactor”, Prabhat Kumar, Aravinda Pai, Procedia Engineering, 2014, 86, 173–183.
5. “Development of fast breeder reactor technology in India”, Puthiyavinayagam. P, Selvaraj. P, Balasubramanian. V, Raghupathy. S, Velusamy. K, Devan. K, et al., Progress in Nuclear Energy, 2017, 101, 19–42.
6. “Hot cracking susceptibility of boron modified AISI 304 austenitic stainless steel welds”, Shinoda. T, Miyake. H, Matsuzaka. T, Matsumoto. T and Kanai. H, Materials Science and Technology, 1992, 8, 913-921.
7. “Fusion Welding of Advanced Borated Stainless Steels Final Report: CRADA #CR1042C”, Robino. V and Cieslak M .J, Sandia National Laboratories, February 1994.

8. "Effect of boron content and processing on mechanical properties and microstructure of borated stainless steel", Martin. J .W, Carpenter Technology internal report K86007, Sep 23,1988.
9. "High-Temperature Metallurgy of Advanced Borated Stainless Steels", Robino. C .V, Cieslak. M .J, Metallurgical And Materials Transactions A, 1995, 26(7), 1673-1685.
10. "Boronated stainless steels for thermal neutron shield", Yamamoto. S, Honda. M, Journal of Thermal and Nuclear Power, 1990, 41(9), 79-87.
11. Web reference: ITER News line "Borated steel plate successfully fabricated"  
<https://www.iter.org/newsline/113>
12. "Review of the Development and Testing of a New Family of Boron and Gadolinium-Bearing Dual Thermal Neutron Absorbing Alloys – 13026", Schmidt. M .L, Del Corso. G .J, Klankowski. K .A, Lherbier. L .W and Novotnak. D .J, WM2013 Conference, February 24 – 28, 2013, Phoenix, Arizona USA.
13. "Studies on shielded metal arc welding of 304B4 stainless steel", Arivazhagan. B, Srinivasan. G, Albert. S .K and Bhaduri. A. K, Proceedings of National Welding Seminar, 2011.
14. "Investigation on Microstructure and Impact Properties of Borated Stainless Steel for High Density Storage Racks", Fei Xue, Zhifeng Luo, Weiwei Yu, Zhaoxi Wang, Lu Zhang, Advanced Materials Research, 2011, 197-198, 1520-1523.
15. "Macroseggregation in ternary alloys", Mehrabian. R and Flemings. M .C, Metallurgical and Materials Transactions B, 1970, 1(2), 455–464.

16. “Microstructure and Mechanical properties of Borated Stainless Steel (304B) GTA and SMA welds”, Raja Kumar. G, Ram. G .D. J, Rao. S .R. K, La Metallurgia Italiana , 2015, 5, 47-52.
17. Welding Handbook, Vol. 3, 7th ed., American Welding Society, Miami, FL, 1980, 170–238.
18. “Hot cracking tests—an overview of present technologies and applications”, Thomas Kannengiesser and Thomas Boellinghaus, Weld World, 2014, 58, 397–421, DOI 10.1007/s40194-014-0126-y.
19. “Recent Developments in Weldability Testing”, Lippold. J .C, Book: “Hot cracking phenomena in welds”, Springer-Verlag, Berlin Heidelberg, 2005, ISBN 3-540-22332-0, 271-290,
20. “On the nature of weld hot cracking”, Medovar. B. I , Avtom Svarka, 1954, 7 (4),12–28.
21. “Generalized theory of super-solidus cracking in welds (and Castings)”, Borland. J. C., British Welding Journal, 1960, 508–512.
22. “On the mechanism of hot cracking of welds”, Toropov. V .A, Metallo Obra Metallov, 1957, 6, 54–58.
23. “Factors which influence weld hot cracking”, Apblett. W .R, Pellini. W .S., Weld Journal 1954, 33(2), 83s–90s.
24. “Welding Metallurgy”, Sindo Kou, Second Edition, 2003, John Wiley & Sons, Inc. ISBN: 0-471-43491-4.

25. "Welding metallurgy of stainless steels", Folkhard. E., New York: Springer Verlag;1988
26. "Solidification cracking in austenitic stainless steel welds", Shankar. V, Gill. T. P. S, Mannan. S. L and Sundaresan. S, Sadhana, 2003, 28,359–382.
27. "Solidification and weldability of Nb bearing super alloys", DuPont. J. N, Robino. C V, and Marder. A. R, Welding Journal, 1998, 77, 417s-431s.
28. "Modeling solute redistribution and microstructural development in fusion welds of Nb bearing superalloys", DuPont. J. N, Robino. C.V, and Marder A. R, Acta Materialia, 1998, 46, 4781-4790.
29. "Partially Melted Zone in Aluminum Welds Liquation Mechanism and Directional Solidification", Huang. C and Kou. S, Welding Journal, 2000, 79, 113s-120s.
30. "The Hot Tearing Tendencies of Aluminium Casting Alloys", Lees. D. C. G, The Journal of the Institute of Metals, 1946, 72, 343-365.
31. US Patent 2240672, Scherer. R, Riedrich. G, Hougardy. H, 1941.
32. "A new explanation for role of  $\delta$ -ferrite improving weld solidification crack susceptibility in austenitic stainless steel", Matsuda. F, Nakagawa. H, Uehara. T, Katayama. S, Arata. Y, Transactions of Japan Welding Research Institute, 1979, 8, 105–112.
33. "The effect of  $\delta$  - ferrite on the hot cracking of stainless steel", Hull. F .C, Welding Journal, 1967, 46, 399s–409s

34. "A fundamental study of the beneficial effects of  $\delta$  ferrite in reducing weld cracking", Brooks. J .A, Thompson. A. W, Williams. J .C, Welding Journal, 1984. 63, 71s–83s.
35. "The effects of phosphorus, sulfur and ferrite content on weld cracking of type E309 stainless steel", Brooks. J .A, Lambert Jr. F .J, Welding Journal, 1978, 57, 139s–143s.
36. "Solidification crack susceptibility in weld metals of fully austenitic stainless steels (report II) – effect of ferrite, P, S, C, Si, and Mn on ductility properties of solidification brittleness", Arata. .Y, Matsuda. F, Katayama. S, Transactions of Japan Welding. Research. Institute, 1977, 6, 105–116.
37. "Welding Type 347 stainless steel – an interpretive report", Thomas Jr. R. D and Messler Jr. R.W, WRC Bulletin, 1997, No. 421.
38. "Evaluation of ductility characteristics and cracking susceptibility of Al alloys during welding", Nakata. K and Matsuda. F, Transactions of Japan Welding. Research. Institute, 1995, 24(1), 83-94.
39. "Effects of alloying additions on hot cracking of austenitic stainless steels", Hull. F.C, Proc. ASTM, 1960, 60, 667–690.
40. "Effects of surface wettability and liquid viscosity on the dynamic wetting of individual drops", Longquan Chen and Elmar Bonaccorso, Physical review E, 2014, 90, 022401-022409.

41. "Welding Metallurgy and Weldability", John. C. Lippold, Ohio State University  
Published by John Wiley & Sons, Inc., Hoboken, New Jersey,2015.
42. "Liquation cracking in partial penetration aluminium welds: assessing tendencies to liquate, crack and backfill", Huang. C, Cao. G and Kou. S, Science and Technology of Welding and Joining, 2004, 9:2, 149-157, DOI: 10.1179/136217104225017071.
43. "Effect of additional element on weld solidification crack susceptibility of Al-Zn-Mg alloy (report II)", Matsuda. F, Nakata. K, Tsukamoto. K, Arai. K, Transactions of Joining and Welding Research Institute, 1983, 12(2), 253– 262.
44. "Effect of Additional Element on Weld Solidification Crack Susceptibility of Al-Zn-Mg Alloy (Report III)-Enhancement of Beneficial Effect of Zirconium on Improvement of Crack Susceptibility by Application of Electromagnetic Stirring", Matsuda. F, Nakata. K, Tsukamoto. K and Uchiyama. T, Transactions of Japan Welding. Research. Institute, 1984, 13(1), 57-66.
45. "Test methods for evaluating hot cracking: review and perspective", Goodwin. G .M, Oak Ridge National Laboratory, DE90 009820.
46. "Destructive tests on welds in metallic materials – Hot cracking tests for weldments – Arc welding processes", Draft European International Standard. Pr EN ISO 17641.
47. "Dynamic observation of solidification and solidification cracking during welding with optical microscope", Matsuda. F, Nakagawa. H, Sorada .K, Transactions of Japan Welding. Research. Institute, 1982, 11 (2), 67–77.

48. "An investigation of heat-affected zone liquation cracking, part 1 – a methodology for quantification" Lin. W, Lippold. J .C, Baeslack. W .A, Welding Journal, 1993, 71(4), 135s–153s.
49. "Liquid metal embrittlement of the heat-affected zone by copper contamination", Savage.W .F, Nippes. E .F, Mushala. M. C,. Welding Journal, 1978, 57 (8), 237s–245s.
50. "Microcracking in multipass Weld metal of alloy 690 Part 1 – Microcracking susceptibility in reheated Weld metal". Nishimoto", Saida. K and Okauchi. H, Science and Technology of Welding and Joining, 2006, 11(4), 455 -461.
51. "Microcracking in multipass weld metal of alloy 690 Part 2 – Microcracking mechanism in reheated weld metal", Nishimoto. K, Saida. K, Okauchi. H and Ohta. K, Science and Technology of Welding and Joining, 2006, 11(4 ), 462-470.
52. "A Study of Heat-Affected Zone and Weld Metal Liquation Cracking in Alloy 903", Baeslack -III .W. A, Lata. W .P and. West. S .L, Welding Journal, 1993, 67 (4), 77s-87s.
53. "A methodology for quantifying heat-affected zone liquation cracking susceptibility", Lippold. J .C, Lin. W, PhD Thesis,. 1994, Columbus, OH: Edison Welding Institute;.
54. "Ductility-dip cracking susceptibility of filler metal 52 and alloy 690", Kikel. J .M, and Parker. D .M, Trends in Welding Research V, Metals Park, OH: ASM International; 1999, 757–762.

55. “High temperature behavior of Ni-base weld metal Part II – Insight into the mechanism for ductility dip cracking”, Ramirez. A .J, Lippold. J .C, Materials Science and Engineering A, 2004, 380, 245–258.
56. “An investigation of the hot ductility of high-temperature alloys”, Nippes. E .F and Savage. W .F, Welding Journal, 1955, 34 (4), 183s–196s.
57. Gleeble® Systems: Defining a New Era in Thermal-Mechanical Physical Simulation and Testing. Poestenkill, NY: Dynamic Systems Inc. Available at <http://gleeble.com>.
58. “Hot Cracking Phenomena in Welds- Testing for Susceptibility to Hot Cracking on Gleeble™ Physical Simulator”, Dr. Stan T. Mandziej, BAM, Berlin, March 4-5, 2004.
59. “Hot Ductility and Hot Cracking Behavior of Modified 316 Stainless Steels Designed for High-Temperature Service”, Lundin. C .D, Qiao. C .Y .P, Gill. T .P .S and Goodwin. G .M, Welding Journal, 1993,72, 189s–200s.
60. “Effect of multiple postweld heat treatment cycles on the weldability of Waspaloy”, Qian. M, Lippold. J .C, Welding Journal, 2002, 81 (11), 233s–238s.
61. “Microstructural evolution in the HAZ of Inconel 718 and correlation with the hot ductility test”, Thompson. R .G, Genculu. S, Welding Journal, 1983, 62(12), 337s–345s.
62. “Welding metallurgy and Weldability of nickel-base alloys”, DuPont. J. N, Lippold. J .C, Kiser.S .D, Wiley Hoboken, NJ, 2009.

63. "Standardization of Gleeble Hot Ductility Testing: Part II: Experimental Evaluation", Lundin.C .D, Qiao. C .Y .P and Lee. C. H, In: Patterson, R. A. (Hrsg.) Weldability of materials, ASM International Materials Park, Ohio, 1990, 9–22.
64. Nuclear power research committee of Japan welding engineering society Report 1. Welding Technology, 1964, 12(12), 61-70.
65. Nuclear power research committee of Japan welding engineering society Report 11. Welding Technology, 1965, 13(11), 53-65.
66. "Crack susceptibility of austenitic stainless steel deposited metal during solidification", Ito. K and Ishii. K, Journal of the Japan Welding Society, 196; 36(4): 294-305.
67. "Problems in arc welding austenitic steels alloyed with boron" Prozorovskii. E .V, and Petrov .G .L, Avt. Svarka ,1966,, 1, 18-27.
68. "Welding of fuels and controls for dresden nuclear power station", Spalaris. C .N, and Weyers. J .W, Welding Journal, 1959, 38(8), 760-765,.
69. "Boron-containing stainless steels for nuclear fuel storage and transportation", King. K .J, and Wilkinson. J, Stainless Steels "84,1984., Institute of Metals, London.
70. "Processing of boron containing stainless steels for nuclear industry", Harrison. A .H, King. K .J and Wilkinson. J, The journal of Nuclear Engineer 1990, 32(1), 3-9.
71. "Specifications for stainless steel electrode for shielded metal arc welding", AWS A5.4-92. USA: American welding society; 1992. (ISBN 087171 385 3).

72. ASME Boiler & Pressure Vessel Code, by The American Society Of Mechanical Engineers, Two Park Avenue, New York, NY 10016-5990, Copyright © 2017.
73. “Welding of material grade TP347 modified”, Musech. H, Nuclear Engineering and Design, 1985, 85(2), 155–161.
74. “Dissolution kinetics of NbC particles in the heat-affected zone of type 347 austenitic stainless steel”, Li. L and Messler. R .W, Metallurgical and Materials. Transactions. A, 2002, 33, 2031-2042.
75. ASTM E8-04, Standard Test Methods for Tension Testing of Metallic Materials.
76. ASTM E-23, Standard Test Methods for impact Testing of Metallic Materials.
77. “Wear resistant coatings of boron-modified stainless steels deposited by Plasma Transferred Arc”, Erich Sigolo, Juliano Soyama Guilherme Zepon, Claudio Shyinti Kiminami, Walter José Botta, Claudemiro Bolfarini, Surface & Coatings Technology, 2016, 302, 255–264.
78. “Borides in stainless steel”, Hideo Kaneko, Taji Nishizawa and Akira Chiba, Journal of Japanese institute of metals, 1966, 30(2):157-163.
79. “Materials Development for Indian Nuclear Power Programme: an Industry Perspective”, M. Narayana Rao, Energy procedia, 2011, 7, 199-204.
80. “Time-resolved X-ray diffraction study on solidification of Fe-B and Fe-C eutectic alloys”, Akitoshi Mizuno, Jin Tamura, Shinji Kohara et.al, Materials Science Forum, 2012, 706-709, 1703-1706.

81. "Synergistic stabilization of metastable  $\text{Fe}_{23}\text{B}_6$  and  $\gamma\text{-Fe}$  in undercooled  $\text{Fe}_{83}\text{B}_{17}$ ", Quirinale. D. G, Rustan. G .E, Kreyszig. A, Goldman. A .I, Applied Physics Letters, 2015, 106, 24197-4, doi: 10.1063/1.4922802.
82. "Formation and reactivity of borides, carbides and silicides I. Review and introduction", Glasson. D .R and Jones. J .A, Journal of applied chemistry, 1969, 19, 125-137.
83. "Evaluation of Backfilled Solidification Cracks in Austenitic Stainless Welds in Relationship to Evaluation of Hot Cracking", Lundin. C .D, Lee. C .H and Qiao. C .Y .P, Welding journal, 1993, 7, 321-328.
84. "A comparative evaluation of welding consumables for dissimilar welds between 316LN austenitic stainless steel and alloy 800",Sireesha. M, Albert. S .K, Shankar. V, Sundaresan. S, Journal Nuclear Materials, 2000,279, 65–76.
85. "Study of weld interface phenomena in a low alloy steel", Savage. W .F, Nipes. E. F, Szekeres. E .S, Welding Journal, 1976, 5, 260–268.
86. "Effects of constitutional liquation in 18 Ni maraging steel weldments", Pepe. J. J, Savage. W .F. Welding Journal, 1967, 46(9), 411–422.
87. "Hot cracking of austenitic stainless steel weld metal", Masumoto. I, Takami. K, Kutsuna. M, Journal of Japan Welding Society, 1972, 41, 1306–14.
88. "Effect of welding processes on microstructural and mechanical properties of dissimilar weldments between conventional austenitic and high nitrogen austenitic stainless steels", Vashishtha Himanshu, Ravindra. V, Sumitra Sharma Taiwade, Patil Awanikumar. P, Journal of Manufacturing Processes 2017, 25, 49–59.

89. "Some aspects of cracking in welded Cr–Ni austenitic steels", Borland. J .C, Younger. R .N, British Welding Journal, 1960, 7, 22–59.
90. "Effect of rapid solidification on stainless steel weld metal microstructures and its implications on the Schaeffler diagram", David. S .A, Vitek. J .M, Reed. R .W, Hebble. T .L, Welding journal, 1987, 66(10), 289s–300s.
91. "Weld cracking in duplex stainless steel (Report II) – modeling of cellular dendritic growth during weld solidification", Matsuda. F, Nakagawa. H, Lee. J .B, Transactions of Japan Welding. Research. Institute, 1989, 18, 107–117.
92. "Solidification of undercooled Fe–Cr–Ni alloys part II – Microstructural evolution", Koseki. T, Flemings. M .C. Metallurgical and Materials Transactions-A, 1996, 27(10), 3226–3240.
93. "Introduction to Ceramics", Kingery. W .D, Bowen. K .H and Uhlmann. D .R, JohnWiley & Sons Publication Second Edition, 1976 177-216.
94. "An account of some experiments shown before the Royal Society; with an enquiry into the cause of some of the ascent and suspension of water in capillary tubes", James Jurin, Philosophical Transactions of the Royal Society of London, 1718, 30, 739–747.
95. "Effect of Boron Additions to Austenitic Stainless Steels - Part II: Solubility of boron in 18%Cr, 15%Ni austenitic steel", Goldschmidt. H .J, Journal of the Iron and Steel Institute, 1971, 209(11), 910-911.
96. "Welding consumables for joining and cladding stainless steels and Ni based alloys", ESAB technical handbook for stainless steel welding.

## LIST OF ABBREVIATIONS & ACRONYMS

1	ASTM	American Society for Testing and Materials
2	BM	Base Metal
3	BTR	Brittleness Temperature Range
4	CF	Cracking factor
5	CSR	Crack Susceptible Region
6	DCEN	Direct Current Electrode Negative
7	DCEP	Direct Current Electrode Positive
8	DDC	Ductility Dip Cracking
9	DRT	Ductility Recovery Temperature
10	DSC	Differential Scanning Calorimetry
11	DTA	Differential Thermal Analysis
12	EDS	Energy Dispersive Spectroscopy
13	EPMA	Electron Probe Micro Analysis
14	FA	Ferrite-Austenite
16	FN	Ferrite Number
17	GTAW	Gas Tungsten Arc Welding
18	HAZ	Heat Affected Zone
19	IHX	Intermediate Heat Exchanger
20	JCPDS	Joint committee on Powder Diffraction Standards
21	LC	Liquation Cracking

22	LVT	Longitudinal Vareststraint Test
23	MCL	Maximum Crack Length
24	MGB	Migrated grain Boundary
25	NDR	Nil Ductility Range
26	NDT	Nil Ductility Temperature
27	NST	Nil Strength Temperature
28	PMZ	Partially Melted Zone
29	RA	Reduction in Area
30	RDR	Ratio of Ductility Recovery
31	SAD	Selected Area Diffraction
32	SC	Solidification Crack
33	SEM	Scanning Electron Microscope
34	SMAW	Shielded Metal Arc Welding
35	SVT	Spot Vareststraint Test
36	TCL	Total Crack Length
37	TEM	Transmission Electron Microscope
39	TVT	Transverse Vareststraint Test
40	UMZ	Un-Mixed Zone
41	UTS	Ultimate Tensile Strength
42	Vareststraint	Variable Restraint
43	VHN	Vickers Hardness Number
44	WM	Weld Metal

45 XRD X-Ray Diffraction

46 YS Yield Strength